TECH LIBRARY KAFB, NM
0062641

1. NASA CR 112308

2. U/U

# Final Report

for

# 4. ICICLE Feasibility Study, FINAL REPORT

6. Contract NAS5-21039

5. July 1970

Prepared by

7. Advanced Technology Laboratories
Defense Electronic Products
3. RCA
Camden, New Jersey 08102

FACILITY FORM 602

N70-34012 (ACCESSION NUMBER)
300 (PAGES)
CR-112308 (NASA CR OR TMX OR AD NUMBER)
(THRU)
1 (CODE)
28 (CATEGORY)

RECEIVED
NASA STI FACILITY
INPUT BRANCH
AUG 1970

for

Goddard Space Flight Center
Greenbelt, Maryland 20771

Reproduced by the
CLEARINGHOUSE
for Federal Scientific & Technical
Information Springfield Va. 22151

Final Report

for

# ICICLE Feasibility Study

Contract No.: NAS5-21039

Goddard Space Flight Center

Contracting Officer: J.A. Maloney
Technical Monitor: T.A. Cygnarowicz

Prepared by

Advanced Technology Laboratories
Defense Electronic Products
RCA
Camden, New Jersey 08102

Project Manager: P.E. Wright

for

Goddard Space Flight Center
Greenbelt, Maryland 20771

## ABSTRACT

A feasibility study and conceptual definition of an Integrated Cryogenic Isotope Cooling Engine System (ICICLE) have been completed. This investigation included a study of the possible applications of such a system and the performance requirements thus identified. The basic system configuration studied was based on a heat driven cryogenic refrigerator operated from a radioisotope heat source and thermally coupled with heat pipes.

On the basis of the study, several conclusions can be drawn.

- The principal potential requirement for ICICLE systems would be for IR radiometric systems and laser or low noise microwave communications systems.
- The use of a heat driven cryogenic refrigerator based on the thermodynamic cycle of R. Vuilleumier is a feasible approach to achieving 3 to 5 year unmaintained life.
- Typical capacity and temperature requirements for potential applications would range from 0.30 W to 7.00 W at temperatures of 60° K to 120° K. The most useful single requirement would be for 5.0 W at 77° K.
- A refrigerator to deliver 5.0 W to 77° K would weigh 7.0 lb and would require 200 to 250 W of driving energy at 900° K.
- A plutonium-236 fuel capsule could deliver the required driving energy and is the preferred heat source by virtue of technical parameters and relevant existing technology.
- The best available multifoil insulation technology is required at the hot end of the system.
- Sodium heat pipe is the preferred thermal link between isotope and VM hot cylinder.
- A fail-safe thermal switch coupling the heat source to space or the hot heat pipe is required in the system.
- The preferred heat sink for the system is a heat pipe radiator using ammonia heat pipes. This radiator will be 25 inches square.

- Cryogenic heat pipes are a feasible method of coupling between the refrigerator and experiments to be cooled. If distances are short, conductive coupling may be preferred.
- The configuration of the host spacecraft has important impact on the final system configuration. The flexibility of configuration of the ICICLE is an important factor. Preferred configuration can be identified only within the framework of a specific spacecraft.
- For example, ICICLE could integrate into Tiros M. It would require a 400 W isotope, 15 W of electrical power, and would weigh approximately 50 lb.

The most important subsystems which remain to be developed are the long life VM engine, cryogenic heat pipe, heat pipe radiator, and isotope heat source. In addition to development of these components, the flight of preliminary experiments with heat pipes could generate important data leading to ultimate flight of a complete system.

## FOREWORD

This technical report describes the parametric data and preferred feasible system configuration investigated under contract NAS 5-21039. The work was administered by the Goddard Space Flight Center, Greenbelt, Maryland. Mr. Thomas A. Cygnarowicz was the NASA technical officer.

The investigation was completed by the RCA Advanced Technology Laboratories in Camden, New Jersey, under the direction of P. E. Wright, Manager, Advanced Mechanical Technology. B. Shelpuk, Engineering Leader, Thermodynamics, was project leader. Principal investigators were M. S. Crouthamel, VM refrigeration and thermal switching; P. F. Joy, Jr., heat pipes; W. Harbaugh, heat pipes; R. Williams, spacecraft requirements and thermal interfaces; and B. Shelpuk, radioisotopes and system integration.

TABLE OF CONTENTS


| Section | | Page |
|---|---|---|
| | ABSTRACT | ii |
| | FOREWORD | iv |
| 1 | INTRODUCTION | 1-1 |
| 2 | ICICLE COOLING REQUIREMENTS STUDY | 2-1 |
| | A. Types of Systems Requiring Cryogenic Cooling | 2-1 |
| | 1. Meteorological | 2-1 |
| | 2. Communications | 2-3 |
| | 3. Earth Resources | 2-7 |
| | B. Conceptual Design of Detector Cryogenic Platform | 2-7 |
| | 1. Focus Sensitive Detector System | 2-7 |
| | 2. Focus Insensitive Detector System | 2-10 |
| | 3. Structural Requirements of Thermal Isolation Mounts | 2-12 |
| | C. Heat Loads | 2-15 |
| | 1. Electrical | 2-15 |
| | 2. Detector Subassembly Heat Leak | 2-15 |
| | 3. 3-Axis Rigid Thermal Isolation Mount Heat Leak | 2-17 |
| | 4. 2-Axis Rigid Thermal Isolation Mount Heat Leak | 2-20 |
| | 5. Flexible Conductor Heat Leak | 2-20 |
| | 6. Heat Pipe Heat Leak | 2-20 |
| | D. Conceptual Design for a Cooled Parametric Amplifier | 2-25 |
| | 1. Parametric Design for a Cooled Parametric Amplifier | 2-25 |
| | 2. Cooling | 2-25 |
| | 3. Number of Cooled Parametric Amplifiers Required in a Spacecraft | 2-27 |
| | 4. Temperature Requirements | 2-29 |
| | E. Laser Communication | 2-29 |
| | F. Determination of ICICLE System Heat Loads | 2-29 |
| | G. Conclusions to Section 2 | 2-33 |
| 3 | VUILLEUMIER THEORY AND PRACTICE | 3-1 |
| | A. Introduction | 3-1 |
| | B. Idealized VM Performance | 3-2 |
| | 1. Derivation of Performance Equations for Ideal VM Cycle | 3-2 |

TABLE OF CONTENTS (Continued)


| Section | | Page |
|---|---|---|
| | 2. Heat Pumping Versus Phase Angle and Volume Ratio | 3-9 |
| | 3. Heat Pumping Versus Volume Ratio and Void Volume at Phase Angle of 90° | 3-11 |
| | 4. Off Design Operation of VM Engines | 3-12 |
| | C. VM Sizing Parameters Study | 3-19 |
| | 1. Introduction | 3-19 |
| | 2. Description of Reference Design | 3-19 |
| | 3. Mass Distribution in Reference Design | 3-23 |
| | 4. Loss Equations for Hot and Cold Cylinder | 3-30 |
| | 5. VM Parameter Calculations | 3-36 |
| | D. Symbol Glossary | 3-43 |
| | E. References for Section 3 | 3-48 |
| 4 | RADIOISOTOPE FEASIBILITY | 4-1 |
| 5 | HEAT PIPES | 5-1 |
| | A. General Heat Pipe Theory | 5-1 |
| | 1. Introduction | 5-1 |
| | 2. Liquid and Vapor Flow Dynamics | 5-2 |
| | 3. Optimization Techniques | 5-18 |
| | 4. Vapor Flow Operational Limits | 5-22 |
| | 5. Heat Transfer | 5-25 |
| | B. High Temperature Heat Pipe | 5-30 |
| | 1. Fluid Flow and Thermodynamic Design | 5-30 |
| | 2. Fluid Selection | 5-32 |
| | 3. Wick Design | 5-35 |
| | 4. Containment Material | 5-36 |
| | 5. Design Calculations | 5-38 |
| | 6. Operational Summary | 5-51 |
| | 7. Temperature Drop | 5-51 |
| | 8. Summary | 5-67 |
| | C. Ambient Temperature Heat Pipes | 5-68 |
| | 1. Primary Heat Pipe - General Description | 5-68 |
| | 2. Constant-Temperature Operation | 5-68 |
| | 3. Working Fluid | 5-71 |
| | 4. Material | 5-71 |
| | 5. Thermodynamic Design | 5-72 |
| | 6. Temperature Drops | 5-73 |
| | 7. Summary | 5-75 |
| | D. By-Pass Heat Pipes | 5-75 |
| | E. Ambient Radiator | 5-78 |
| | 1. Selection of Ambient Radiator Surface Finishes | 5-78 |
| | 2. Radiator Configuration | 5-81 |
| | 3. Thermal Analysis and Optimization | 5-82 |

TABLE OF CONTENTS (Continued)


| Section | | Page |
|---|---|---|
| | F. Low-Temperature Heat Pipe | 5-95 |
| | 1. Fluid Selection | 5-95 |
| | 2. Design | 5-110 |
| | G. References | 5-129 |
| 6 | THERMAL INSULATION REQUIREMENTS | 6-1 |
| 7 | ICICLE THERMAL CONTROL | 7-1 |
| | A. Thermal Control Requirements | 7-2 |
| | 1. Cryogenic Temperature Range | 7-2 |
| | 2. Ambient Temperature Range | 7-2 |
| | 3. High Temperature Range | 7-3 |
| | B. Thermal Switch Selection Criteria | 7-12 |
| 8 | THERMAL INTERFACE DESIGN | 8-1 |
| | A. Hot Heat Pipe to VM Hot Cylinder Interface | 8-1 |
| | 1. Conduction Coupling | 8-3 |
| | 2. Radiation Coupling | 8-6 |
| | 3. Recommendation | 8-7 |
| | B. Ambient Temperature Interface | 8-10 |
| | 1. Location of Interface | 8-10 |
| | 2. Interface Techniques to Heat Sink Flange | 8-11 |
| | C. Cryogenic Temperature Interface | 8-13 |
| | D. References | 8-14 |
| 9 | ICICLE SYSTEM INTEGRATION | 9-1 |
| | A. General | 9-1 |
| | B. Integration of ICICLE Components on an ITOS-D or ITOS-E Spacecraft | 9-3 |
| | 1. Location | 9-3 |
| | 2. Weight | 9-4 |
| | 3. Refrigeration Load | 9-4 |
| | 4. Spacecraft Dynamics | 9-4 |
| | 5. Heat Leaks to Spacecraft | 9-8 |
| | 6. Electrical Interface | 9-8 |
| | 7. System Tradeoffs | 9-9 |
| | C. ICICLE Failure Mode Analysis | 9-10 |
| | 1. Heat Source | 9-10 |
| | 2. Heat Sink Assembly | 9-11 |
| | 3. Refrigerator | 9-13 |
| | 4. Cryogenic Subsystems | 9-13 |

## LIST OF ILLUSTRATIONS


| Figure | | Page |
|---|---|---|
| 2-1 | Temperature dependence of HgCdTe photoconductor | 2-3 |
| 2-2 | 3-axis detector mounting scheme | 2-8 |
| 2-3 | 3-axis thermal isolation mount | 2-9 |
| 2-4 | 2-axis rigid thermal isolation mount | 2-11 |
| 2-5 | Heat conducted in flexible copper braid vs. cross-sectional area per unit length for various thermal gradients | 2-12 |
| 2-6 | Design concept of focus insensitive detector system | 2-13 |
| 2-7 | Design concept for a VHRR system | 2-14 |
| 2-8 | Heat leak vs. AWG wire size for copper wire of various lengths | 2-18 |
| 2-9 | Flexible conductor heat leak vs. cross-sectional area | 2-21 |
| 2-10 | Heat leak vs. insulation outer to inner radius ratio | 2-22 |
| 2-11 | Thermal radiation barrier for multilayer insulation edge | 2-23 |
| 2-12 | Insulation edge heat leak vs. heat pipe OD | 2-25 |
| 2-13 | Integrated parametric amplifier | 2-26 |
| 2-14 | Parametric amplifier mounting concept | 2-26 |
| 2-15 | Satellite communications system concept | 2-28 |
| 3-1 | Ideal VM-cycle engine, block diagram | 3-2 |
| 3-2 | Schematic diagram of Vuilleumier-cycle refrigerator | 3-4 |
| 3-3 | Open cycle energy balance | 3-5 |
| 3-4 | Dimensionless ideal heat absorption per cycle as a function of phase angle with swept volume ratio as a parameter for a $T_c$ of 25°K | 3-9 |
| 3-5 | Dimensionless ideal heat absorption per cycle as a function of phase angle with swept volume ratio as a parameter for a $T_c$ of 77°K | 3-10 |
| 3-6 | Dimensionless ideal heat absorption per cycle as a function of phase angle with swept volume ratio as a parameter for a $T_c$ of 125°K | 3-10 |
| 3-7 | Dimensionless ideal heat absorption per cycle as a function of swept volume ratio with temperature-weighted dimensionless void volume as a parameter for a $T_c$ of 25°K | 3-12 |
| 3-8 | Dimensionless ideal heat absorption per cycle as a function of swept volume ratio with temperature-weighted dimensionless void volume as a parameter for a $T_c$ of 77°K | 3-13 |

LIST OF ILLUSTRATIONS (Continued)


| Figure | | Page |
|---|---|---|
| 3-9 | Dimensionless ideal heat absorption per cycle as a function of swept volume ratio with temperature-weighted dimensionless void volume as a parameter for a $T_c$ of 125°K | 3-14 |
| 3-10 | Dimensionless ideal heat absorption per cycle as a function refrigeration temperature for various optimized refrigerators | 3-15 |
| 3-11 | Dimensionless ideal heat absorption per cycle as a function of ambient temperature for various optimized refrigerators | 3-16 |
| 3-12 | Dimensionless ideal heat absorption per cycle as a function of heat source temperature for various optimized refrigerators | 3-17 |
| 3-13 | RCA VM engine | 3-20 |
| 3-14 | RCA VM engine, full size cross-sectional view | 3-21 |
| 3-15 | Full size, two view reference design | 3-22 |
| 3-16 | Mass fraction distribution in reference design vs. crank angle | 3-25 |
| 3-17 | Mass fraction flow rate in reference design vs. crank angle | 3-26 |
| 3-18 | Cold regenerator dimensionless flow rate at ambient ($M_{rca}$) and cold ($M_{rcc}$) ends | 3-28 |
| 3-19 | Hot regenerator dimensionless flow rate at ambient ($M_{rca}$) and cold ($M_{rcc}$) ends | 3-28 |
| 3-20 | Dimensionless pressure and pressure ratio vs. crank angle | 3-29 |
| 3-21 | Regenerator gas and matrix temperature profile at various times during a cycle | 3-33 |
| 3-22 | Shuttle loss mechanism | 3-35 |
| 3-23 | $Q_c$ net vs. scale factor | 3-38 |
| 3-24 | $Q_h$ net vs. scale factor | 3-41 |
| 3-25 | Weight vs. scale factor for VM | 3-41 |
| 3-26 | Power vs. scale factor | 3-42 |
| 3-27 | $Q_h$ net/$Q_c$ net vs. scale factor | 3-42 |
| 4-1 | Fuel capsule temperature required to transfer 250 W to the receiver | 4-2 |
| 4-2 | Power decay with time for various isotopes | 4-4 |
| 5-1 | One-dimensional fluid flow model | 5-5 |
| 5-2 | Heat pipe geometry | 5-9 |
| 5-3 | Working-fluid figure of merit as a function of temperature for $N_2$, $O_2$, $NH_3$, Cs, K, Li, and Na at zero g | 5-22 |
| 5-4 | Pertinent fluid properties | 5-26 |
| 5-5 | Heterogeneous conduction model | 5-27 |

LIST OF ILLUSTRATIONS (Continued)


| Figure | | Page |
|---|---|---|
| 5-6 | Figure of merit as a function of temperature for potassium, sodium, lithium, and cesium | 5-33 |
| 5-7 | Sonic limit as a function of temperature for potassium, sodium, and lithium | 5-35 |
| 5-8 | Power throughput capability as a function of length for sodium in stainless steel heat pipes with mesh wicks, diameter of 1.0 in, and wall thickness at 0.05 in. at a temperature of 627°C and a temperature drop of 25°C with wick structure as a parameter | 5-39 |
| 5-9 | Power throughput capability as a function of length for sodium in stainless steel heat pipes with mesh wicks, diameter of 1.5 in, and wall thickness at 0.05 in. at a temperature of 627°C and a temperature drop of 25°C with wick structure as a parameter | 5-40 |
| 5-10 | Power throughput capability as a function of weight for 6-in long stainless steel sodium heat pipes with mesh wicks, wall thickness of 0.050 in. at a temperature of 626°C and a temperature drop of 25°C with mesh gage and outside diameter as parameters | 5-40 |
| 5-11 | Power throughput capability as a function of weight for 12-in-long sodium in stainless stell heat pipes with mesh wicks, wall thickness of 0.050 in. at a temperature of 627°C with mesh gage and and outside diameter as parameters | 5-41 |
| 5-12 | Power throughput capability as a function of weight for 24-in-long sodium in stainless steel heat pipes with mesh wicks, wall thickness of 0.050 in. at a temperature of 627°C with mesh gage and outside diameter as parameters | 5-41 |
| 5-13 | Power throughput capability as a function of weight for 48-in-long sodium in stainless steel heat pipes with mesh wicks, wall thickness of 0.050 in. at a temperature of 627°C with mesh gage and outside diameter as parameters | 5-42 |
| 5-14 | Power throughput capability as a function of weight for 72-in-long sodium in stainless steel heat pipes with mesh wicks, wall thickness of 0.050 in. at a temperature of 627°C with mesh gage and outside diameter as parameters | 5-42 |
| 5-15 | Power throughput capability as a function of weight for 98-in-long sodium in stainless steel heat pipes with mesh wicks, wall thickness of 0.050 in. at a temperature of 627°C with mesh gage and outside diameter as parameters | 5-43 |

LIST OF ILLUSTRATIONS (Continued)


| Figure | | Page |
|---|---|---|
| 5-16 | Power throughput capability as a function of outside diameter for 12-in-long sodium in stainless steel heat pipes with mesh wicks at an optimum number of wraps, wall thickness of 0.050 in. at a temperature of 627°C with mesh gage as a parameter | 5-43 |
| 5-17 | Power throughput capability as a function of length for potassium in stainless steel heat pipes with mesh wicks, diameter of 0.5 in. and wall thickness of 0.050 in. at a temperature of 627°C and a temperature drop of 25°C with wick structure as a parameter | 5-44 |
| 5-18 | Power throughput capability as a function of length for potassium in stainless steel heat pipes with mesh wicks, diameter of 1.0 in. and wall thickness of 0.050 in. at a temperature of 627°C and a temperature drop of 25°C with wick structure as a parameter | 5-44 |
| 5-19 | Power throughput capability as a function of length for potassium in stainless steel heat pipes with mesh wicks, diameter of 1.5 in. and wall thickness of 0.050 in. at a temperature of 627°C and a temperature drop of 25°C with wick structure as a parameter | 5-45 |
| 5-20 | Power throughput capability as a function of length for potassium in stainless steel heat pipes with mesh wicks, diameter of 2.0 in. and wall thickness of 0.050 in. at a temperature of 627°C and a temperature drop of 25°C with wick structure as a parameter | 5-45 |
| 5-21 | Power throughput capability as a function of length for sodium heat pipes 1.0 in. in diameter at a temperature of 677°C and a temperature drop of 28°C | 5-46 |
| 5-22 | Power throughput capability as a function of length for sodium heat pipes 1.5 in. in diameter at a temperature of 677°C and a temperature drop of 28°C | 5-47 |
| 5-23 | Power throughput capability as a function of length for sodium heat pipes 2.0 in. in diameter at a temperature of 677°C and a temperature drop of 28°C | 5-47 |
| 5-24 | Power throughput capability as a function of length for potassium heat pipes 1.0 in. in diameter at a temperature of 677°C | 5-48 |
| 5-25 | Power throughput capability as a function of length for potassium heat pipes 1.5 in. in diameter at a temperature of 677°C | 5-48 |
| 5-26 | Power throughput capability as a function of length for potassium heat pipes 2.0 in. in diameter at a temperature of 677°C | 5-49 |
| 5-27 | Power throughput capability as a function of length for sodium in stainless steel heat pipes with a diameter of 0.5 in and a wall thickness of 0.050 in. at a temperature of 943°C | 5-49 |

LIST OF ILLUSTRATIONS (Continued)


| Figure | | Page |
|---|---|---|
| 5-28 | Power throughput capability as a function of length for sodium in stainless steel heat pipes with a diameter of 1.0 in. and a wall thickness of 0.050 in. at a temperature of 943°C | 5-50 |
| 5-29 | Power throughput capability as a function of length for sodium in stainless steel heat pipes with a diameter of 2.0 in. and a wall thickness of 0.050 in. at a temperature of 943°C | 5-50 |
| 5-30 | Power throughput capability as a function of length for lithium in TZM-molybdenum heat pipes operating at an evaporator temperature of 850°C | 5-52 |
| 5-31 | Power throughput capability as a function of length for lithium in TZM-molybdenum heat pipes operating at an evaporator temperature of 960°C | 5-52 |
| 5-32 | Power throughput capability as a function of length with diameter as a parameter for lithium in TZM-molybdenum heat pipes operating at an evaporator temperature of 950°C | 5-53 |
| 5-33 | Power throughput capability as a function of length with diameter as a parameter for lithium in TZM-molybdenum heat pipes operating at an evaporator temperature of 1000°C | 5-53 |
| 5-34 | Product of maximum power throughput and length at zero g and weight-to-length ratio as functions of diameter for lithium in TZM-molybdenum heat pipes operating at an evaporator temperature of 943°C | 5-54 |
| 5-35 | Product of maximum power throughput and length at zero g and weight-to-length ratio as functions of diameter for sodium in stainless steel heat pipes at an evaporator temperature of 943°C | 5-54 |
| 5-36 | Product of maximum power throughput and length and weight-to-length ratio as functions of diameter for sodium in stainless steel heat pipes with 66 mesh wicks operating at an evaporator temperature of 627°C | 5-55 |
| 5-37 | Product of maximum power throughput and length and weight-to-length ratio as functions of diameter for potassium in stainless steel heat pipes with 40 mesh wicks operating at an evaporator temperature of 627°C | 5-55 |
| 5-38 | Heat pipe input and output methods | 5-57 |
| 5-39 | Vapor temperature drops as a function of heat pipe diameter for 12-in. pipes with 350-W throughputs | 5-57 |
| 5-40 | Thermal flux characteristics of sodium | 5-62 |

LIST OF ILLUSTRATIONS (Continued)


| Figure | | Page |
|---|---|---|
| 5-41 | Total temperature drop as a function of diameter for a 12-in-long sodium in stainless steel heat pipe and a copper rod | 5-63 |
| 5-42 | Total temperature drop as a function of diameter for a 12-in-long sodium in nickel heat pipe and a copper rod | 5-63 |
| 5-43 | Total temperature drop as a function of diameter for a 12-in-long in molybdenum heat pipe and a copper rod | 5-64 |
| 5-44 | Total temperature drop as a function of diameter as a parameter for a 12-in-long lithium in molybdenum heat pipe and a copper rod | 5-64 |
| 5-45 | Total temperature drop as a function of diameter for a 12-in-long sodium in stainless steel heat pipe and a copper rod | 5-65 |
| 5-46 | Total temperature drop as a function of diameter for a 12-in-long sodium in nickel heat pipe and a copper rod | 5-65 |
| 5-47 | Total temperature drop as a function of diameter for a 12-in-long potassium in stainless steel heat pipe and a copper rod | 5-66 |
| 5-48 | Total temperature drop as a function of diameter for a 12-in-long potassium in nickel heat pipe | 5-66 |
| 5-49 | Total temperature drop as a function of length for heat pipes and a copper rod with a throughput of 350 W | 5-67 |
| 5-50 | Constant-temperature heat pipe system | 5-69 |
| 5-51 | Product of power throughput and length and weight-to-length ratio as functions of inside diameter for an ammonia heat pipe at a temperature of 30°C | 5-72 |
| 5-52 | Temperature drop as a function of diameter for solid aluminum and for ammonia in aluminum heat pipes with a throughput of 190W | 5-74 |
| 5-53 | By-pass heat pipe | 5-76 |
| 5-54 | Heat radiated to space as a function of radiator temperature | 5-79 |
| 5-55 | Solar energy absorbed by radiator as a function of solar absorptivity for a solar constant of 0.93 W/in.$^2$ | 5-80 |
| 5-56 | Honeycomb heat pipe radiator | 5-81 |
| 5-57 | Radiator weight as a function of area for single-sided solid-aluminum and heat-pipe radiators, a heat dissipation of 350W, and a PE of 0.3 | 5-83 |
| 5-58 | Cross-section of heat-pipe radiator | 5-84 |
| 5-59 | Fin effectiveness as a function of profile number with PE as a parameter | 5-86 |
| 5-60 | Radiator weight as a function of area for a single-sided heat-pipe radiator at a heat-pipe temperature of 300°K | 5-88 |

LIST OF ILLUSTRATIONS (Continued)


| Figure | | Page |
|---|---|---|
| 5-61 | Radiator weight as a function of area for a single-sided heat-pipe radiator at a heat-pipe temperature of 325°K | 5-89 |
| 5-62 | Radiator weight as a function of area for a single-sided heat-pipe radiator weight as a function of area for a single-sided heat-pipe radiator at a heat-pipe temperature of 350°K | 5-90 |
| 5-63 | Radiator weight as a function of area for a double-sided heat-pipe radiator at a heat-pipe temperature of 300°K | 5-91 |
| 5-64 | Radiator weight as a function of area for a double-sided heat-pipe radiator at a heat-pipe temperature of 325°K | 5-92 |
| 5-65 | Radiator weight as a function of area for a double-sided heat-pipe radiator at a heat-pipe temperature of 350°K | 5-93 |
| 5-66 | Maximum Q ($Z + Z_a$) product as a function of inner wall radius for an oxygen heat pipe with a homogeneous wick at a temperature of 90°K | 5-97 |
| 5-67 | Maximum Q ($Z + Z_a$) product as a function of inner wall radius for a nitrogen heat pipe with a homogeneous wick at a temperature of 77°K | 5-97 |
| 5-68 | Maximum Q ($Z + Z_a$) product as a function of inner wall radius for a nitrogen heat pipe with a homogeneous wick at a temperature of 90°K | 5-98 |
| 5-69 | Maximum Q ($Z + Z_a$) product as a function of inner wall radius for an oxygen heat pipe with a homogeneous wick at a temperature of 77°K | 5-98 |
| 5-70 | Maximum Q ($Z + Z_a$) product as a function of inner-wall radius for a nitrogen heat pipe with a channel wick at a temperature of 77°K | 5-99 |
| 5-71 | Maximum Q ($Z + Z_a$) product as a function of inner-wall radius for a nitrogen heat pipe with a channel wick at a temperature of 90°K | 5-99 |
| 5-72 | Maximum Q ($Z + Z_a$) product as a function of inner-wall radius for an oxygen heat pipe with a channel wick at a temperature of 77°K | 5-100 |
| 5-73 | Maximum Q ($Z + Z_a$) product as a function of inner-wall radius for an oxygen heat pipe with a channel wick at a temperature of 90°K | 5-100 |
| 5-74 | Maximum Q ($Z + Z_a$) product as a function of inner-wall radius for a zero-g field with $r_c$ optimized and $r_v/r_w = 2/3$ in a heat pipe with a homogeneous wick | 5-101 |

LIST OF ILLUSTRATIONS (Continued)


| Figure | | Page |
|---|---|---|
| 5-75 | Maximum Q (Z + $Z_a$) product as a function of inner-wall radius for g Z sin $\phi$ = 500 $cm^2/s^2$ in a heat pipe with a homogeneous wick | 5-101 |
| 5-76 | Maximum Q (Z + $Z_a$) product as a function of inner-wall radius for g Z sin $\phi$ = 1000 $cm^2/s^2$ in a heat pipe with a homogeneous wick | 5-102 |
| 5-77 | Maximum Q (Z + $Z_a$) product as a function of inner-wall radius for g Z sin $\phi$ = 1520 $cm^2/s^2$ in a heat pipe with a homogeneous wick | 5-102 |
| 5-78 | Maximum Q (Z + $Z_a$) product as a function of inner-wall radius for g Z sin $\phi$ = 3040 $cm^2/s^2$ in a heat pipe with a homogeneous wick | 5-103 |
| 5-79 | Maximum Q (Z + $Z_a$) product as a function of inner-wall radius for g Z sin $\phi$ = 6080 $cm^2/s^2$ in a heat pipe with a homogeneous wick | 5-103 |
| 5-80 | Maximum Q (Z + $Z_a$) product as a function of inner-wall radius for zero-g in a heat pipe with a channel wick | 5-104 |
| 5-81 | Maximum Q ( Z + $Z_a$) product as a function of inner-wall radius for g Z sin $\phi$ = 1520 $cm^2/s^2$ in a heat pipe with channel wick | 5-104 |
| 5-82 | Maximum Q (Z + $Z_a$) product as a function of inner-wall radius for g Z sin $\phi$ = 3040 $cm^2/s^2$ in a heat pipe with a channel wick | 5-105 |
| 5-83 | Maximum Q (Z + $Z_a$) product as a function of inner-wall radius for g Z sin $\phi$ = 6080 $cm^2/s^2$ in a heat pipe with a channel wick | 5-105 |
| 5-84 | Cryogenic liquid thermal conductivity as a function of temperature with working fluid as a parameter | 5-107 |
| 5-85 | Screen-covered channel wick geometry | 5-111 |
| 5-86 | Experimental nucleate and film pool boiling of oxygen at 1 atm compared with predictive correlation | 5-114 |
| 5-87 | Predictive nucleate and film pool boiling correlations for oxygen | 5-115 |
| 5-88 | Experimental nucleate and film pool boiling of nitrogen at 1 atm compared with predictive correlations | 5-115 |
| 5-89 | Predictive nucleate and film pool boiling correlations for nitrogen | 5-115 |
| 5-90 | Temperature drop and heat pipe length as functions of inner-wall radius for oxygen heat pipe at 77 °K with g Z sin $\phi$ = 6080 $cm^2/s^2$ | 5-117 |

LIST OF ILLUSTRATIONS (Continued)


| Figure | | Page |
|---|---|---|
| 5-91 | Temperature drop and maximum heat pipe length as functions of inner-wall radius for oxygen heat pipe at 77°K with g Z sin $\phi$ = 500 $cm^2/s^2$ | 5-118 |
| 5-92 | Temperature drop and maximum heat pipe length as functions of inner-wall radius for oxygen heat pipe at 90°K with g Z sin $\phi$ = 6080 $cm^2/s^2$ | 5-118 |
| 5-93 | Temperature drop and heat pipe length as functions of inner-wall radius for oxygen heat pipe at 90°K with g Z sin $\phi$ = 500 $cm^2/s^2$ | 5-119 |
| 5-94 | Temperature drop and heat pipe length as functions of inner-wall radius for oxygen heat pipe at 77°K with g Z sin $\phi$ = 680 $cm^2/s^2$ | 5-119 |
| 5-95 | Temperature drop and heat-pipe length as functions of inner-wall radius for nitrogen heat pipe at 77°K with g Z sin $\phi$ = 500 $cm^2/s^2$ | 5-120 |
| 5-96 | Temperature drop and heat-pipe length as functions of inner-wall radius for nitrogen heat pipe at 90°K with g Z sin $\phi$ = 6080 $cm^2/s^2$ | 5-120 |
| 5-97 | Temperature drop and heat-pipe length as functions of inner-wall radius for nitrogen heat pipe at 90°K with g Z sin $\phi$ = 500 $cm^2/s^2$ | 5-121 |
| 5-98 | Temperature drop and heat-pipe length as functions of inner-wall radius for oxygen heat pipe at 77°K with g Z sin $\phi$ = 1520 $cm^2/s^2$ | 5-122 |
| 5-99 | Channel wick heat transfer model | 5-124 |
| 5-100 | Temperature drop as a function of inner-wall radius for oxygen heat pipes at 77°K with g Z sin $\phi$ = 500 $cm^2/s^2$ contrasted with solid aluminum rods of fixed lengths | 5-125 |
| 6-1 | Heat leak into heat pipes as a function of pipe length with pipe diameter as a parameter | 6-2 |
| 6-2 | Relatively simple insulating schemes | 6-3 |
| 6-3 | 40-layer Mo-$ThO_2$ insulation samples - mixture 115 $ThO_2$ powder | 6-4 |
| 6-4 | 40-layer Mo-$ThO_2$ insulation samples - mixture 116 $ThO_2$ powder | 6-4 |
| 6-5 | Heat flux vs. source temperature - planar W-$ThO_2$ insulation | 6-5 |
| 6-6 | Insulation performance as a function of the applied compressive load | 6-7 |

LIST OF ILLUSTRATIONS (Continued)


| Figure | | Page |
|---|---|---|
| 6-7 | Cylindrical-planar corner configurations around a radioisotope heat source | 6-8 |
| 6-8 | Various corner configurations | 6-9 |
| 6-9 | Corner configuration performance comparison | 6-10 |
| 6-10 | Package being qualified for transit | 6-11 |
| 6-11 | Heat loss from isitipe container (basic container has 6 in diameter and is 7.5 in long) | 6-11 |
| 6-12 | Heat loss per foot of hot heat pipe length ($T_h$ = 950°C) | 6-12 |
| 7-1 | Thermal control schematics | 7-5 |
| 7-2 | Schematic of electromechanical thermal actuator | 7-10 |
| 7-3 | Schematic of fluid expansion thermal actuator | 7-11 |
| 7-4 | Schematic of bimetal thermal actuator | 7-13 |
| 8-1 | Hot heat pipe condenser section | 8-2 |
| 8-2 | Interface thermal conductance vs. noncondensible gas thickness (helium) | 8-3 |
| 8-3 | VM hot cylinder | 8-3 |
| 8-4 | VM hot heat pipe thermal coupling | 8-4 |
| 8-5 | Radiation coupler | 8-6 |
| 8-6 | Hot heat pipe temperature vs. VM hot cylinder temperature as a function of black body ($\epsilon$ = 1.0) | 8-8 |
| 8-7 | Hot heat pipe to VM coupling height vs. total net heat transfer to net heat transfer flux ratio for various surface finish emissivities | 8-9 |
| 8-8 | Thermodynamics of the crankcase | 8-10 |
| 8-9 | Contact conductance vs. contact pressure for bare metal joints | 8-11 |
| 8-10 | Thermal resistances of metallic interface with various filler materials | 8-12 |
| 8-11 | Method for interfacing heat pipes with VM cold finger | 8-14 |
| 9-1 | ITOS spacecraft | 9-5 |
| 9-2 | Heat source assembly | 9-11 |
| 9-3 | Normalized net refrigeration vs. crankcase temperature | 9-12 |

## LIST OF TABLES


| Table | | Page |
|---|---|---|
| 2-1 | Satellite Observations which Require Cryogenic Cooling | 2-4 |
| 2-2 | Relative Performance Characteristics of Earth Looking and Space Looking Receivers | 2-6 |
| 2-3 | 3-Axis Rigid Thermal Isolation Mount Characteristics | 2-10 |
| 2-4 | 2-Axis Rigid Thermal Isolation Mount Characteristics | 2-10 |
| 2-5 | VHRR Heat Loads | 2-30 |
| 2-6 | Estimated Cooling Loads | 2-31 |
| 2-7 | Cooling Loads for A 10.6 Micron Laser Receiver | 2-31 |
| 2-8 | Candidate for ICICLE Application Systems | 2-32 |
| 4-1 | Radioisotope Fuel Characteristics | 4-6 |
| 4-2 | Typical Material Application | 4-7 |
| 4-3 | Survey of Nuclear Fuel Capsules and Development Status - Aerospace Application | 4-9/4-10 |
| 5-1 | Vapor Pressure Drops | 5-17 |
| 5-2 | Sonic Axial Heat-Flux Limits | 5-24 |
| 5-3 | Vapor Pressure - Temperature Data of Candidate Materials | 5-38 |
| 5-4 | Temperature Drops for Various Heat Pipe Input and Output Methods and Materials | 5-58 |
| 6-1 | Isotope Container Heat Losses | 6-13 |
| 7-1 | Evaluation of Thermal Switch Configuration | 7-15/7-16 |
| 8-1 | Conductance Test Results | 8-5 |
| 9-1 | Weight Tabulation | 9-6 |
| 9-2 | Cooling Load Tabulation | 9-7 |

Section 1

# INTRODUCTION

As meteorological and communication spacecraft continue to require more sophisticated infrared scanning radiometers, infrared laser systems and microwave systems, the need for cooled detectors will continue to increase. An example of the benefit of cryogenic cooling for sensors is evident from Fig. 2-1 which shows the temperature dependence of the specific detectivity of Hg-Cd-Te photoconductors, which are the most commonly used detectors for very high resolution radiometers. Full exploitation of this technology is limited by life, size and complexity of systems required to provide cryogenic refrigeration.

An Integrated Cryogenic Isotope Cooling Engine System (ICICLE) is an attractive concept for providing long life (2 years or more) cryogenic cooling in space. The ICICLE is a central spacecraft system for cooling to cryogenic temperatures. A miniature Vuilleumier (VM) cycle cryogenic engine is the central cooling refrigerator.

The Vuilleumier refrigerator is based on a heat driven thermodynamic cycle patented by Rudolph Vuilleumier in 1918. Successful development and application of the cycle has awaited recent advances in regenerator technology. Displacers are used to circulate helium gas back and forth through regenerators to the high temperature power cylinder, the cryogenic temperature refrigeration cylinder and an ambient temperature crankcase. Displacers and regenerators coordinate to assure that a sufficient amount of gas is in both the power cylinder at high temperature and in the refrigeration cylinder at cryogenic temperature to allow for heat transfer into the engine during the expansion phase of the cycle. They also assure that a maximum amount of gas is in the crankcase to allow for heat rejection during the compression phase of the cycle.

Two key aspects of the VM refrigerator make it attractive for long life satellite application: 1) the fact that the primary driving energy in the cycle is heat that can be supplied from a high energy density source, such as an isotope; and 2) the engine has long life potential due to low bearing loads, low cycling speeds and low pressure differentials across the displacer seals.

The engine has three distinct temperature regions: a hot volume (900°K), an ambient temperature volume (310°K) and a cold volume (75°K). The VM engine operates on thermal power, which is provided by a radioisotope. Because safety considerations dictate the location of the isotope and because experiment requirements

dictate the location of the detectors which must be cooled, the components of the ICICLE system will probably be distributed on a spacecraft. Consequently, heat pipes are used to couple the VM engine to other components of the system.

Thermal power (250 W) is supplied to the hot volume of the engine via a heat pipe (Na at about 1216°K) from a remotely located radioisotope. An ambient temperature heat pipe couples the crankcase of the engine to a space radiator to satisfy the heat rejection process of the cycle. Cryogenic heat pipes (operating at about 77°K and transferring 1 to 5 W) distribute the cryogenic cooling to one or more remotely located cooling platforms. A thermal switch is incorporated into the system so as to shunt the isotope power away from the VM engine when it is not operating. The thermal switch also provides for slow engine startup and maintains the temperature of the isotope within tolerable levels. This report describes the technical considerations involved with the design of the ICICLE system.

A three-fold approach was used to design the system. First, the requirements in future spacecraft for this type of system were reviewed; second, the feasibility of the required components was investigated and presented in parametric form to allow selection and sizing of a feasible system; third, a preferred feasible system was integrated into a specific spacecraft to explore the system-spacecraft interface and to confirm ICICLE feasibility.

## Section 2

# ICICLE COOLING REQUIREMENTS STUDY


*Summary*

*Future spacecraft missions will have an increasing requirement for cryogenic refrigeration. The experiments which will constitute the major part of this requirement will include systems for detection of infrared signals for radiometric or communications applications. The cooling of the varactor diode used in a parametric amplifier will reduce the signal required for accurate information transmission and will reduce transmitter power for interspacecraft communication.*

*The preferred temperature range for infrared detector operation is 80–110°K, depending on detected wavelength. Varactor diodes should be cooled to as low a temperature as possible although temperatures in the range of 70°K offer a good compromise between improved performance and system complexity to reach the required temperature.*

*The refrigeration capacity represented by an infrared detector consists of the active power dissipated, heat leak through leads, heat leak through a mounting platform, heat leak to cold finger and thermal link, and extraneous radiant heat leak from the optical system. The capacity to meet these requirements will be in the range of 0.30 to 1.00 W, with 0.50 W a good design value.*

*The thermal capacity required by a cooled parametric amplifier is more difficult to specify accurately since its major component is the heat leak down the coaxial connections. The requirements on the coax for high electrical and thermal performance conflict, but a design which leads to a total thermal load of 0.75 W appears to offer a good tradeoff. This is consistent with other designs reported in which the cooling requirements are approximately 1.00 W.*

*A projection of future spacecraft missions indicates that the cryogenic cooling requirements will be in the 3.0 to 5.5 W range, possibly reaching 7.0 W.*

*The progress in radiometer and low noise communications systems is limited by the lack of high capacity, long life refrigeration systems which are insensitive to orientation and orbit parameters. Development of ICICLE will fill this technology gap.*


## A. TYPES OF SYSTEMS REQUIRING CRYOGENIC COOLING

### 1. Meteorological

Infrared scanning radiometers have been used to remotely observe cloud cover, determine cloud height, identify soil moisture content, and measure surface

temperature. As the requirements for better resolution and sensitivity have increased, the necessity for using cooled detectors has increased and will continue to increase until room temperature detectors, such as metal-to-metal point contact diodes, are developed.

The HgCdTe photoconductors are the most commonly used detectors for Very High Resolution Radiometers (VHRR). Figure 2-1 shows the temperature dependence of Hg-Cd-Te photoconductors. The curves in Fig. 2-1 show that, in order to obtain maximum specific detectivity in the 8.0 $\mu$m region, an operating temperature of approximately 110°K is required and in the 13.0 $\mu$m region an operating temperature of approximately 90°K would be required.

Although Fig. 2-1 is typical, these curves will vary in both optimum operating temperature and flatness of the curves, due to the present state of the art in detector manufacturing. If the peak detectivity should occur some distance above or below the normal operating temperature of the VM, the detector could be operating at the edge of the crest, whereupon a change of temperature in the wrong direction would result in a large decrease in detectivity. For example, at a wavelength of 13 $\mu$m and at 100°K the detectivity could be approximately 4.5 inches by 10 inches, at 105°K it would be approximately 3.4 inches by 10 inches, and at 110°K it would be approximately 2.25 by 10 inches. This means a detectivity decrease of 25 percent for a 5°K change in temperature and a 50 percent decrease for 10°K change in temperature. This indicates a need for some type of detector temperature control, either by VM control or heater control at the detector mount. Heater control will be effective provided the VM is operated far enough below the desired detector temperature to allow for VM degradation.

Development of detectors which operate in the 120°K to 140°K region is being attempted, but such detectors are not available at this time. For the purposes of determining ICICLE cooling requirements, the temperature requirements as shown in Fig. 2-1 will be used.

The resolution obtainable with a single detector at 600-750 nautical miles (nmi) altitude (normal altitude for meteorological and earth resources spacecraft) is approximately 0.2 nmi. At synchronous altitude (22,000 nmi) the resolution is on the order of 5.0 nmi. The resolution obtainable is not fixed but depends on such things as the temperature measurement accuracy requirement. In order to obtain higher resolutions and/or greater temperature accuracy it is necessary to use multiple detectors or detector arrays. Arrays of over 100 elements have been built. At present most VHRR syetems employ single detectors, but radiometers with detector arrays with a small number of elements (5 to 20) are being developed, and larger arrays will probably be developed in the 1970s.

Table 2-1 lists most of the types of observations desirable for nephanalysis and meteorology, which would require cryogenic cooling. There are many other types of observations which are or could be made, but they do not require cryogenic cooling.

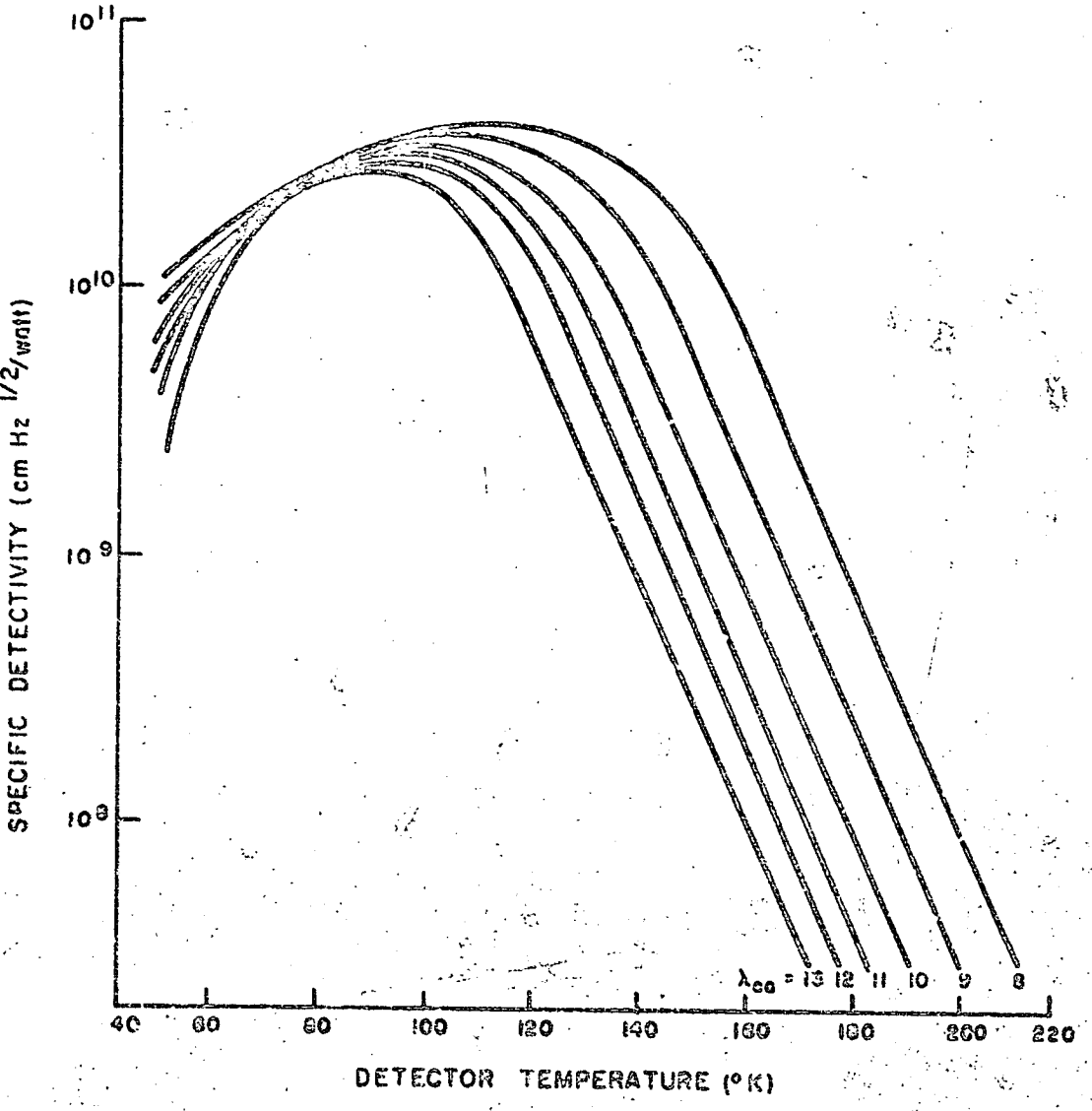



Fig. 2-1. Temperature dependence of HgCdTe photoconductor.

## 2. Communications

There are two types of communication systems which could benefit from cryogenic cooling: 1) microwave systems employing cooled parametric amplifiers and 2) IR laser systems.

## TABLE 2-1. SATELLITE OBSERVATIONS WHICH REQUIRE CRYOGENIC COOLING

| Application | Observation | Operating Wavelength (μm) | Resolution (nmi) | Number of Detectors | Operating Temperature (°K) | Observation Frequency (Times Per Day) | Estimated Cooling Load (W) | |
|---|---|---|---|---|---|---|---|---|
| | | | | | | | Minimum | Maximum |
| Nephanalysis | Cloud Type & Dist. | 10.5-12.5 | 0.1 1.0 | 1-10 | 80 - 110 | 4 | 0.204 | 0.746 |
| | Cloud Top Temp. & Ht. | 10.5-12.5 | 0.1 1.0 | 1-10 | 80 - 110 | 4 | 0.204 | 0.746 |
| | Snow Cover | 10.5-12.5 | 0.5 1.0 | 1 | 80 - 110 | .1 - 1 | 0.204 | 0.531 |
| Meteorology | Cloud Type & Dist. | 10.5-12.5 | 0.2 0.5 | 1-2 | 80 - 110 | 4 - 12 | 0.204 | 0.555 |
| | Cloud Top Ht. & Temp. | 10.5-12.5 | 0.1 0.5 | 1 | 80 - 110 | 4 - 12 | 0.204 | 0.531 |
| | Vertical Temp. Dist. | 14-16 | 1-10 | 1 | 70 - 90 | 4 - 12 | 0.204 | 0.531 |
| Aviation Weather | Cloud Types & Dist. | 10.5-12.5 | 1 | 1 | 80 - 110 | 12 | 0.204 | 0.531 |
| | Cloud Top Temp. & Ht. | 10.5 12.5 | 0.1 0.5 | 1-10 | 80 - 110 | 4 - 12 | 0.204 | 0.746 |
| Oceanography | Surface Temp. | 10.5 12.5 | .04 1.0 | 1-20 | 80 - 110 | 1 - 4 | 0.204 | 0.982 |
| | Sea Ice | 10.5 12.5 | 1-10 | 1 | 80 - 110 | 0.1 - 1 | 0.204 | 0.531 |
| | Icebergs | 10.5 12.5 | 10 ft | 200 | 80 - 110 | 4 | 0.532 | 2.660* |
| Hydrology & Hydrography | Surface Temp. | 10.5 12.5 | 0.1 0.5 | 1-10 | 80 - 110 | 2 | 0.204 | 0.746 |
| | Snow Cover | 10.5 12.5 | 0.5 1.0 | 1 | 80 - 110 | 0.1 - 1 | 0.204 | 0.531 |
| | Sea Ice | 10.5 12.5 | 1-10 | 1 | 80 - 110 | 0.1 - 1 | 0.204 | 0.531 |
| | Surface Temp. | 10.5 12.5 | 0.1 - 0.5 | 1-40 | 80 - 110 | 1 | 0.204 | 1.450 |
| Forestry, Air & Stream Pollution, Geology | Surface Temp. | 10.5 12.5 | 0.1 - 0.5 | 1 - 10 | 80 - 110 | 1 - 4 | 0.204 | 0.746 |
| | Surface Temp. | 10.5 12.5 | 0.1 - 0.5 | 1 - 10 | 80 - 110 | 0.1 - 1 | 0.204 | 0.746 |
| | Surface Comp. | 7-12.5 | 0.1 - 1.0 | 2 - 40 | 80 - 120 | 0.1 - 4 | 0.206 | 1.450 |
| Wildlife Management | Surface Temp. | 10.5 12.5 | 0.01 - 1 | 1 - 49 | 80 - 110 | 0.1 - 12 | 0.204 | 1.450 |
| | Snow Cover | 10.5 12.5 | 0.5 - 1.0 | 1 | 80 - 110 | 0.1 - 1 | 0.204 | 0.531 |
| Marine Experiments | $CO_2$ Measurements | 14-16 | 1-10 | 1 | 70 - 90 | | 0.204 | 0.531 |
| | Water Mapping | 5-7 | 1-10 | 1 | 100 - 140 | | 0.204 | 0.531 |

*The Maximum Value based on the original assumptions used in Table 2-5 is unreasonably high. Therefore, a more reasonable value of five times the minimum is used.

The cooled paramp systems would be used only for spacecraft-to-spacecraft data links since the ground receivers and transmitters are not power limited and also since little is to be gained by cooling earth looking receivers. Table 2-2 shows the relative performance characteristics of earth looking and space looking (spacecraft-to-spacecraft) receivers. The data link capability of a 77°K paramp at X-band is 3 times that of the uncooled paramp, and at S-band it is 2.67 times that of the uncooled paramp. At 20°K the increases are 7.5 and 5.33 to one, respectively. This means that the data handling capability can be increased by these factors or the transmitter power can be reduced by these factors.

There has been little, if any, consideration given to use of cryogenic temperature paramps for satellite communications due to the lack of practical long life cooling equipment (such as passive radiation coolers) which can provide the high heat handling capability required (on the order of 1.0 W per paramp).

The availability of a system such as ICICLE would make the use of cooled paramps feasible and would greatly increase the data handling capability or would decrease the power requirements of spacecraft such as the Data Relay Satellites.

The Data Relay Satellite System consists of three or four spacecraft equally spaced in synchronous orbit. The spacecraft could serve as data collection or relay centers for information gathered by low-altitude satellites or could provide a world-wide communications network by means of satellite-to-satellite relay.

The IR laser communications system would employ a $CO_2$ laser operating at 10.6 $\mu$m. The receiver will probably employ HgCdTe detectors cooled to approximately 95°K. There is a 10.6 $\mu$m laser communications experiment proposed for the ATS-F and ATS-G spacecraft and an advanced 10.6 $\mu$m laser communication experiment proposed for a satellite available in 1975. The advanced experiment differs from the ATS-F and G experiment in that it will communicate with a low-altitude satellite such as ERTS or Tiros in addition to communication between synchronous satellites as proposed in the ATS-F and G experiment.

The IR laser receiver will employ five detectors. Four of the detectors will be used for error sensing and fine beam pointing, and the fifth will be used for signal information detection. Future systems could possibly employ error sensing detector arrays of 36 by 36 elements which could eliminate the acquisition scanning system. This would be an array of 1296 elements which would greatly increase the cooling requirements of the system.

Detailed information concerning the IR laser experiments can be found in Goddard Space Flight Center documents X-524-68-206, 10.6-Micron Laser Communications System Experiment for ATS-F and ATS-G, dated May 1968, and X-524-68-478, An Advanced 10.6-Micron Laser Communication Experiment, dated November 1968.

TABLE 2-2. RELATIVE PERFORMANCE CHARACTERISTICS OF EARTH LOOKING AND SPACE LOOKING RECEIVERS

| EARTH LOOKING GEOSTATIONARY ANTENNA (Earth Temperature Contribution = 300°K) | | | | | | |
|---|---|---|---|---|---|---|
| Device | S-Band | | | X-Band | | |
| | Receiver Noise Temp. (°K) | Total Temp. (°K) | Link Capability Increase | Receiver Noise Temp. (°K) | Total Temp. (°K) | Link Capability Increase |
| Uncooled Paramp | 150 | 450 | 1.0 | 300 | 600 | 1.0 |
| Paramp at 77°K | 50 | 350 | 1.29 | 100 | 400 | 1.5 |
| Paramp at 20°K | 20 | 320 | 1.41 | 40 | 340 | 1.77 |

| SPACE LOOKING GEOSTATIONARY ANTENNA | | | | | | |
|---|---|---|---|---|---|---|
| Device | S-Band | | | | X-Band | |
| | Galactic Noise Temp. (°K) | Receiver Temp. (°K) | Total Temp. (°K) | Link Capability Increase | Receiver Temp. (°K) | Link Capability Increase |
| Uncooled Paramp | 10 | 150 | 160 | 1 | 300 | 1 |
| Paramp at 77°K | 10 | 50 | 60 | 2.67 | 100 | 3 |
| Paramp at 20°K | 10 | 20 | 30 | 5.33 | 40 | 7.5 |
| Maser | 10 | 8 | 18 | 8.9 | 12 | 25 |

### 3. Earth Resources

The cooling requirements for earth resources equipment are similar to or the same as for meteorology. The primary devices which require cooling are the VHRR subsystems. There is little difference between earth resources IR radiometers and meteorological IR radiometers. The major difference is that for earth resources the primary point of interest is the surface of the earth whereas for meteorology the primary point of interest is the atmosphere. Table 2-1 lists most of the types of observations desirable for earth resources studies which require cryogenic cooling.

## B. CONCEPTUAL DESIGN OF DETECTOR CRYOGENIC PLATFORM

### 1. Focus Sensitive Detector System

A focus sensitive detector system is one whose IR energy beam is focused at a plane which is fixed with respect to the collector optical system. For this type of VHRR system the detector and therefore the cryogenic platform must be fixed in all three axes with respect to the optical system.

Figure 2-2 shows a design concept which will fix the detector position in all three axes as well as fix the rotational position. The detector is mounted on a rigid 3-axis thermal isolation support which is mechanically tied into the radiometer housing. This will permit optical alignment and focus of the sensor at room temperature and pressure and will maintain this alignment and focus as the detector is cooled to cryogenic temperatures in a vacuum. The detector is thermally connected to the cryogenic heat pipe by means of a flexible thermal conductor such as a piece of braided or twisted flexible copper wire. The platform end of the cryogenic heat pipe is supported by means of a 2-axis thermal insulation support which permits axial movement of the cryogenic heat pipe due to the change in physical dimensions during cooldown from ambient to cryogenic temperatures.

Figure 2-3 shows the design concept of a 3-axis rigid thermal isolation mount which can meet the thermal and mechanical requirements of most sensor systems. Table 2-3 lists the important characteristics of the 3-axis rigid thermal isolation mount.

Figure 2-4 shows the design concept of a 2-axis rigid thermal isolation mount and Table 2-3 lists its important characteristics.

Figure 2-5 shows the required cross-sectional area of braided copper wire per inch of length versus heat transferred for various thermal gradients in the flexible conductor. The braided copper wire will have a thermal conductivity of about 2.0 W/in-°C.

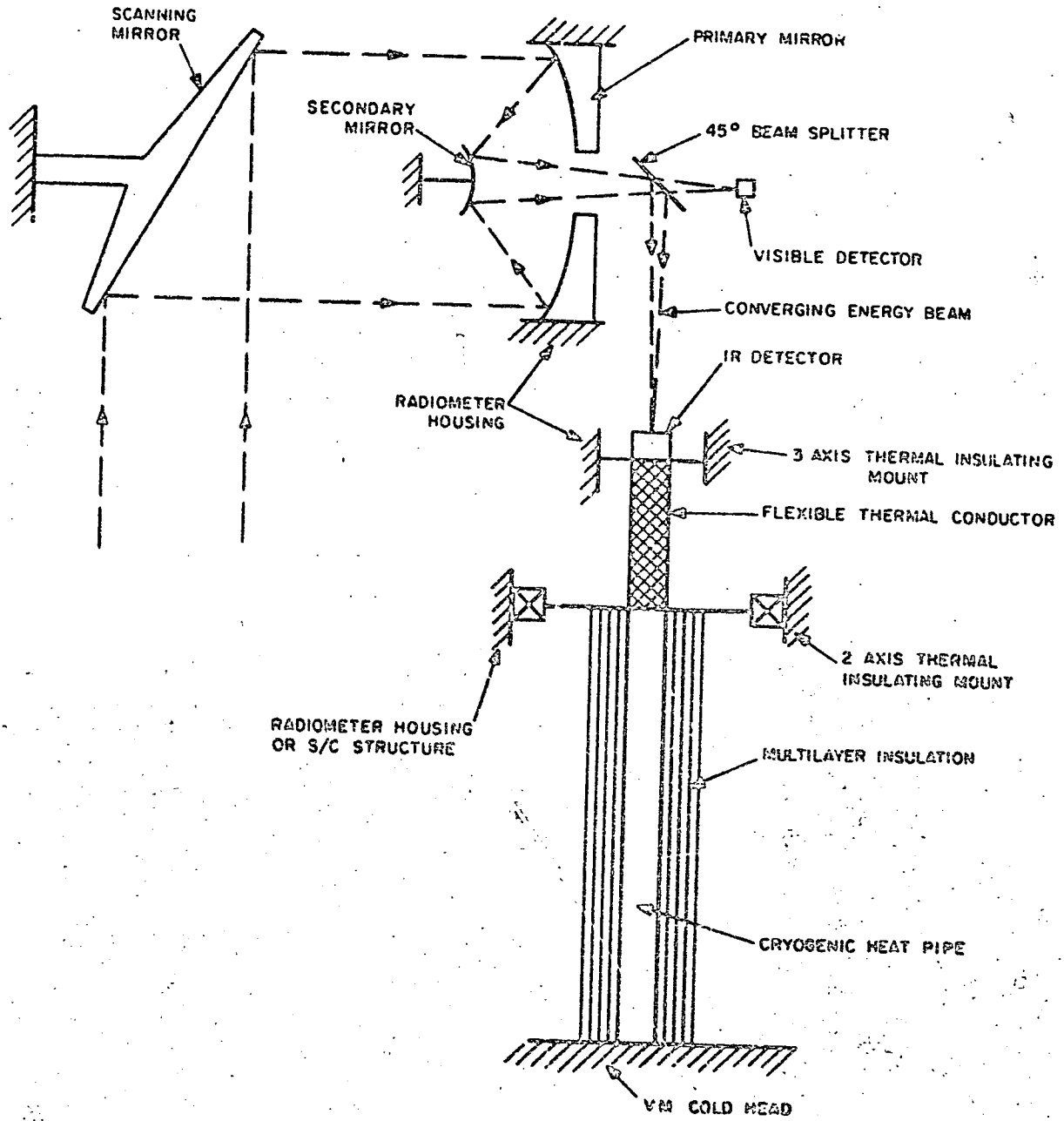



Fig. 2-2. 3-axis detector mounting scheme.

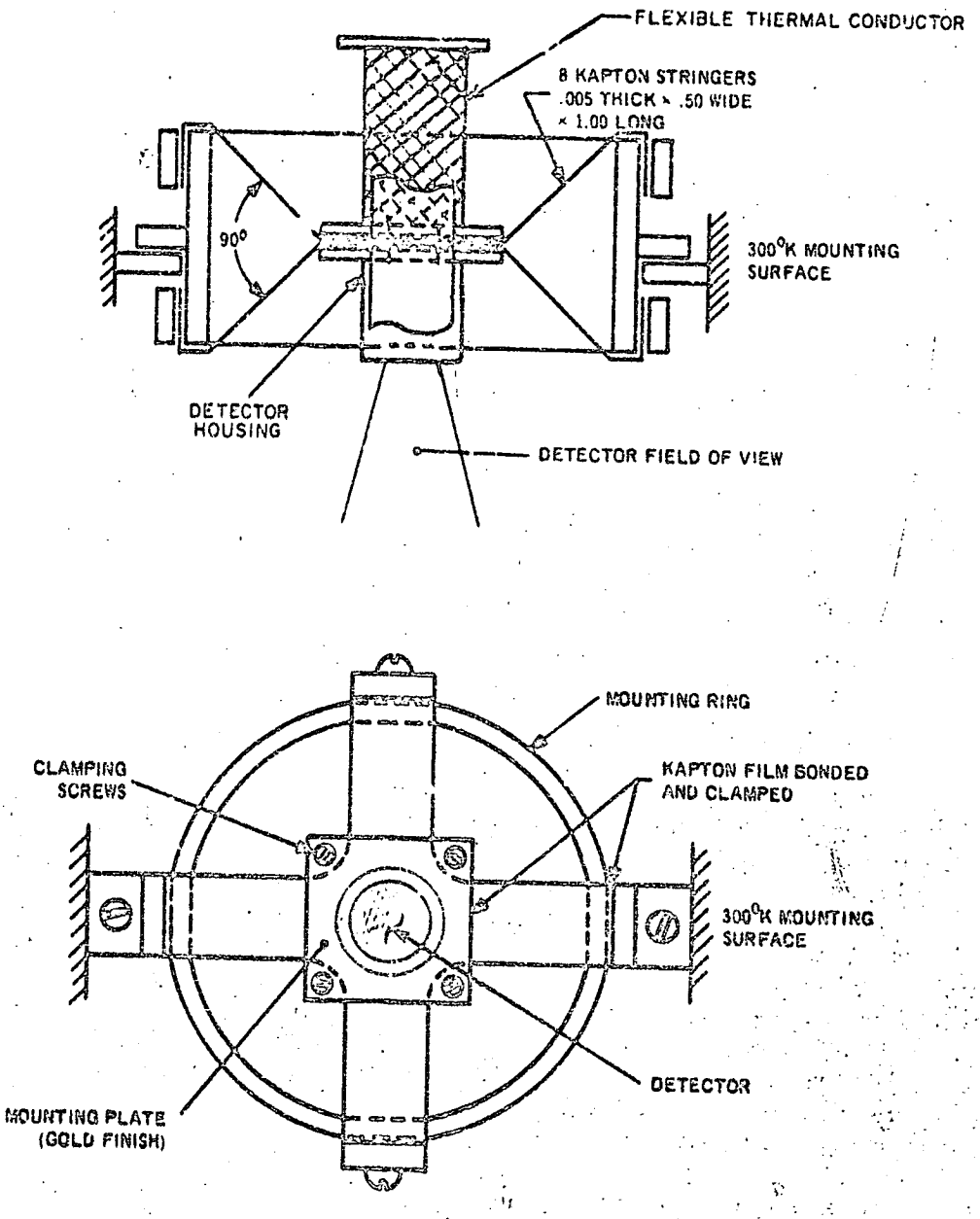



Fig. 2-3. 3-axis thermal isolation mount.

TABLE 2-3. 3-AXIS RIGID THERMAL ISOLATION MOUNT CHARACTERISTICS

| | |
|---|---|
| Max. Service Temperature | 500° K |
| Min. Service Temperature | 5° K |
| Thrust Strength | 35 lb |
| Lateral Strength | 18 lb |
| Thermal Heat Leak | 0.054 W |
| Mounting and Surrounds Temperature | 300° K |
| Mounting Plate Temperature | 77° K |

TABLE 2-4. 2-AXIS RIGID THERMAL ISOLATION MOUNT CHARACTERISTICS

| | |
|---|---|
| Max. Service Temperature | 500° K |
| Min. Service Temperature | 5° K |
| Allowable Axial Movement | 0.10 inch |
| Lateral Strength | 25 lb |
| Thermal Heat Leak | 0.058 W |
| Mounting and Surrounds Temperature | 300° K |
| Mounting Plate Temperature | 77° K |

2. Focus Insensitive Detector System

A focus insensitive detector system is one whose optical system is such that the location in the axial direction of the detector with respect to the collector optics is not critical. This is accomplished by collimating the energy beam at some point in the optical path and then refocusing near the detector. As long as the refocusing lenses are fixed in location with respect to the detector, the detector and lens assembly can be moved along the optical axis (within limits imposed by the degree of collimation) with no change in performance. Figure 2-6 shows a design concept which can meet the requirements of a focus insensitive detector system.

This type of system is less complex mechanically and will have less heat leak since only a single thermal isolation support is required as opposed to two supports for the focus sensitive system.

Figure 2-7 shows a design concept for a VHRR system which would require two or more separately cooled detectors. This design uses only one heat pipe to cool more than one detector. The schematic shows only two cooling stations, but as many cooling stations as necessary could be provided. If reliability requirements indicate the need for independent cryogenic platforms, the multiple station single heat pipe concept would not be used.

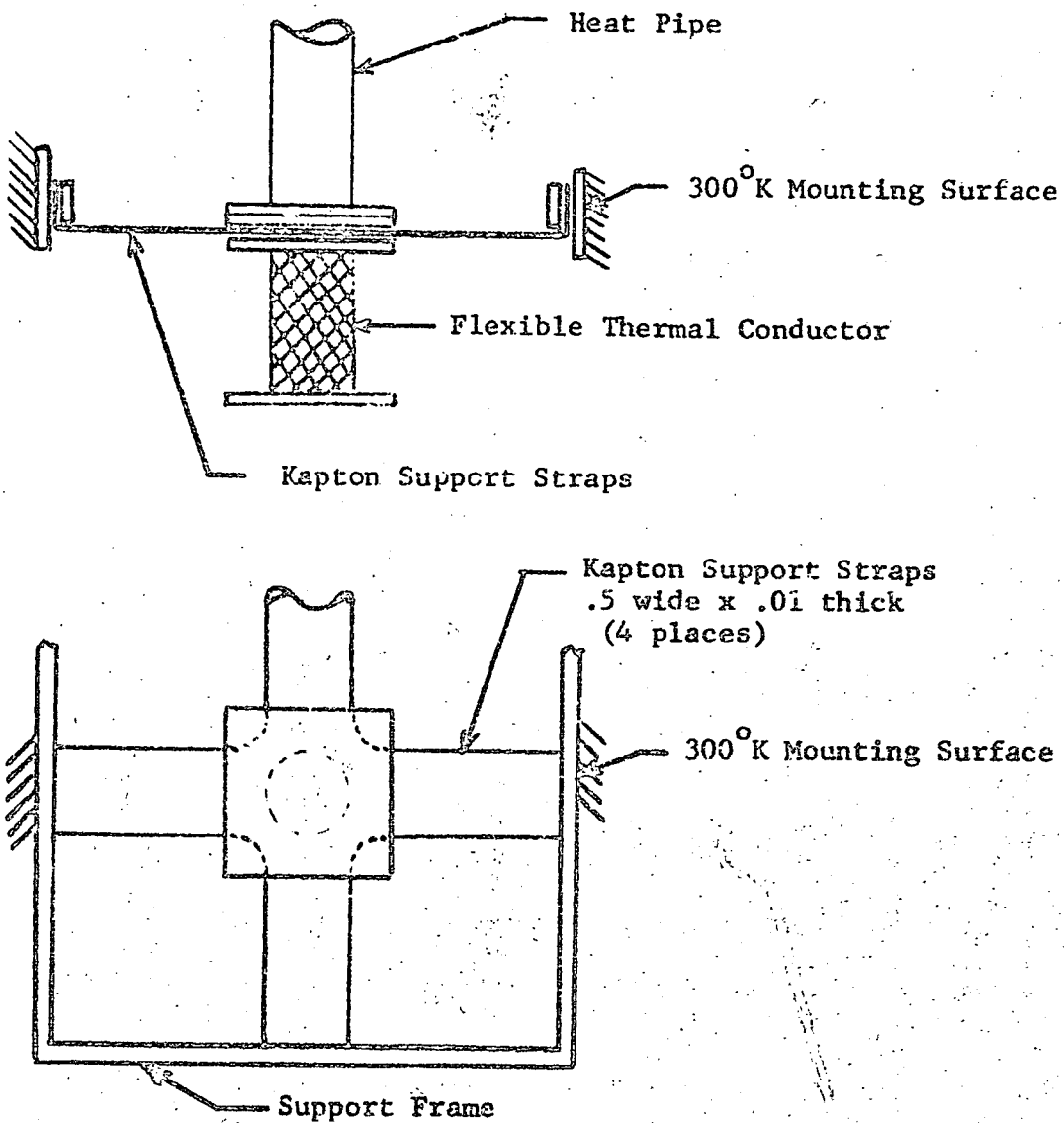



Fig. 2-4. 2-axis rigid thermal isolation mount.

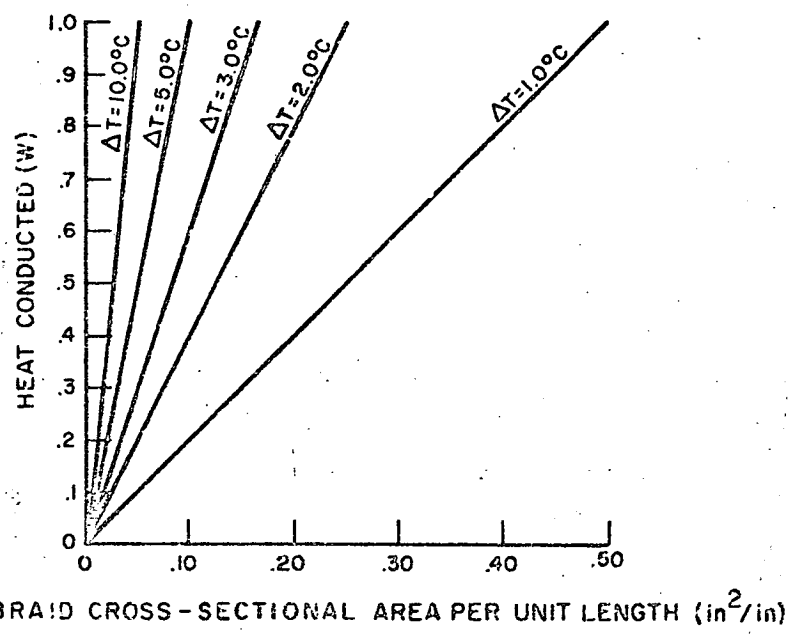



Fig. 2-5. Heat conducted in flexible copper braid vs. cross-sectional area per unit length for various thermal gradients.

3. Structural Requirements of Thermal Isolation Mounts

The thermal isolation mounts must be able to withstand the spacecraft launch environment. A design which will withstand 50 g's should be satisfactory for most launch conditions. Detector subassemblies will probably not exceed 0.05 lb and could be considerably lighter. The 3-axis rigid thermal isolation mount shown in Fig. 2-3 is designed to withstand 100 g's with a detector weight of 0.05 lb.

The thickness of the Kapton stringers can be adjusted up or down to accommodate heavier or lighter detector subassemblies, with a resultant increase or decrease in heat leak. The mechanical characteristics are shown in Table 2-3.

The 2-axis rigid thermal isolation mount shown in Fig. 2-4 is designed to support a 0.05 lb sensor subassembly plus one-half of a 0.36 lb cryogenic heat pipe or conductor rod at 50 g's and will permit a movement of ±0.1 in with only 0.5 percent elongation.

Both the 3-axis and 2-axis rigid thermal isolation mount stringers are prestressed so that they do not go slack (stress=0) during maximum loading. This is done to prevent snapping or impact loading during vibration.

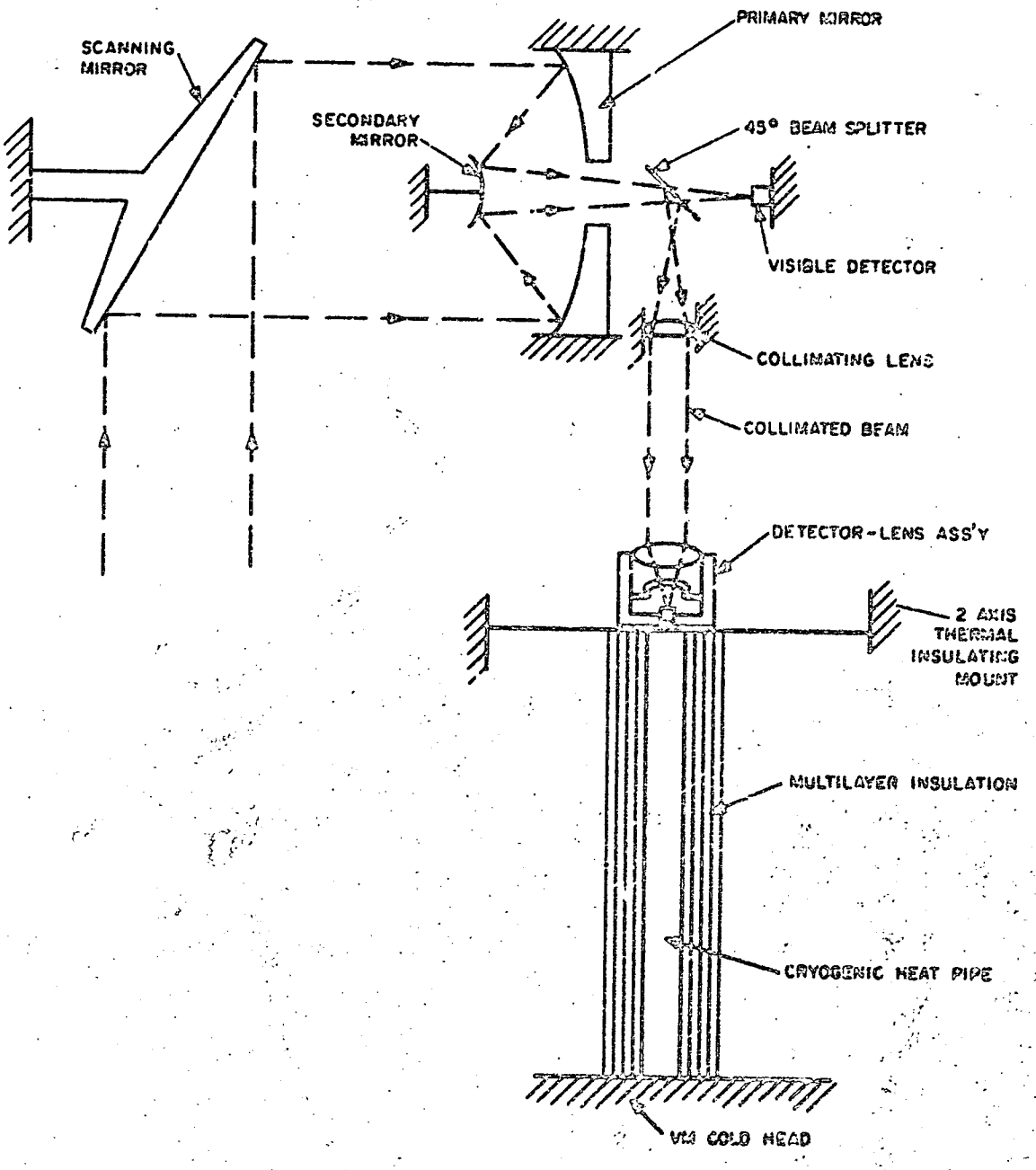



Fig. 2-6. Design concept of focus insensitive detector system.

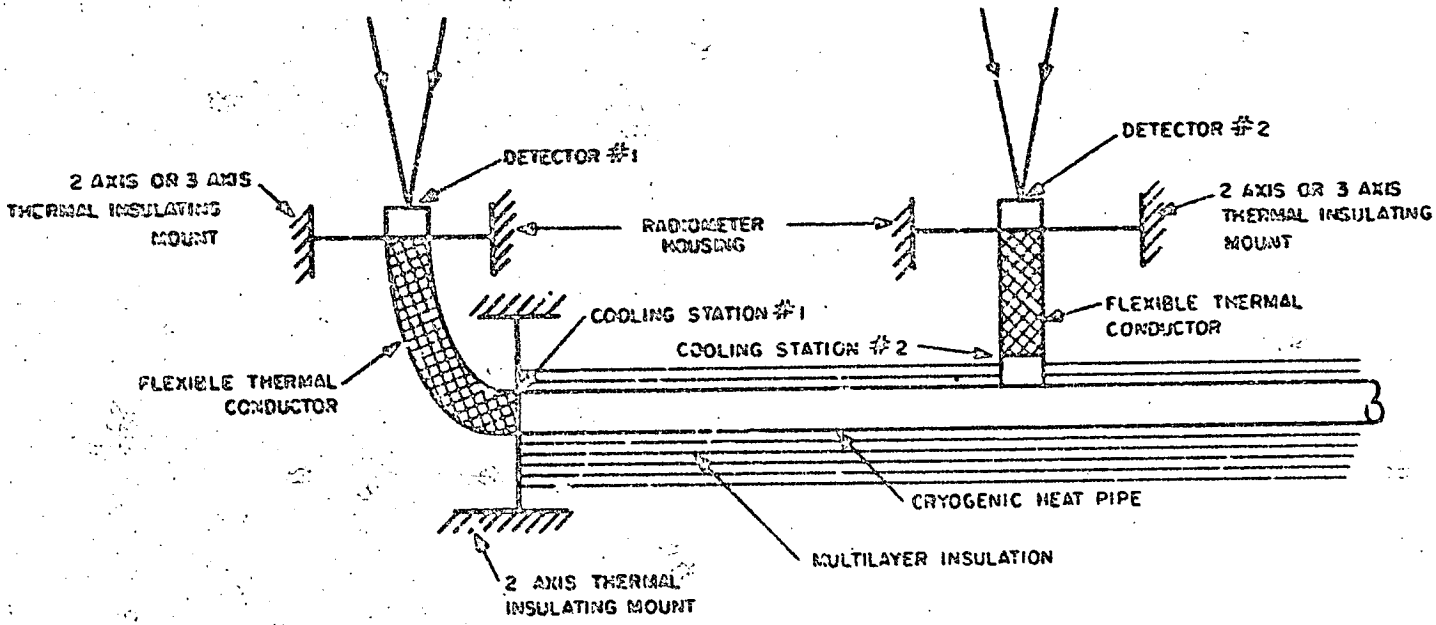



Fig. 2-7. Design concept for a VHRR system.

The thermal isolation mounts are designed with a mechanical safety factor of two.

## C. HEAT LOADS

### 1. Electrical

The HgCdTe detectors normally dissipate a maximum of 5 mW each in VHRR systems and they will probably be operated at a level of 1 to 2 mW.

A maximum electrical dissipation value of 2 mW per element for detector arrays is a reasonable value for first generation arrays of 20 elements or less. Later arrays with as many as 200 elements or more will probably not dissipate more than 1 mW per element, or a total of 200 mW.

### 2. Detector Subassembly Heat Leak

Detector subassemblies designed for use with focus insensitive VHRR systems will have the largest heat leak since the subassembly contains a focusing lens which is large enough to accept the collimated energy beam. These subassemblies should not exceed 1 in. in diameter and 1 in. in length. The opening at the front of the subassembly is approximately 0.75 in. in diameter, with an effective thermal radiation absorptivity of approximately 0.5. The rest of the subassembly will be gold plated or covered with multilayer insulation. The gold plating will have an undegraded emissivity of the order of 0.03. Multilayer insulation can provide effective emissivities of less than 0.01.

The detector subassembly surrounds will be at approximately 300°K maximum (normal spacecraft maximum temperature). With the surrounds having an effective emissivity of 1.0 (black body), the radiation heat leak will be as follows:

a. Heat Absorbed by Lens Opening ($Q_L$)

$$Q_L = A_L \epsilon_L F_{L-S} (\sigma T_S^4 - \sigma T_L^4)$$

where:

$A_L$ = Area of lens opening ($in^2$)

$\epsilon_L$ = Emissivity of lens opening: 0.5

$F_{L-S}$ = View factor from lens to surrounds: 1.0

$\sigma$ = Stephan-Boltzmann constant ($3.6572 \times 10^{-11}$ W/$in^2$ °K)

$T_s$ = Surrounds temperature: 300°K

$T_L$ = Lens temperature: 80°K

$Q_L$ = Radiation heat leak to lens opening

$$Q_L = \frac{\pi (0.75)^2}{4} \times 0.5 \times 1.0 \; (0.29623 - 0.00150)$$

$$Q_L = 0.065 \text{ W}$$

b) Heat Absorbed by Housing

$$Q_H = A_H \, \epsilon_H \, F_{H-S} \, (\sigma T_s^4 - \sigma T_H^4)$$

where:

$A_H$ = Area of housing ($in^2$)

$\epsilon_H$ = Emissivity of housing: 0.05 max.

$F_{H-S}$ = View factor from housing to surrounds: 1.0

$T_H$ = Housing temperature: 80°K

$Q_H$ = Radiation heat leak to detector subassembly housing (W)

$$Q_H = \left[\pi \times 1.0 \times 1.0 + \left(\frac{\pi (1.0)^2}{4} - \frac{\pi (0.75)^2}{4}\right)\right] \times 0.05 \times 1.0 \; (0.29623 - 0.00150)$$

$$Q_H = 0.041 \text{ W}$$

Total radiation heat leak $Q_H + Q_L = 0.106$ W

The heat leak through electrical leads will be as follows:

$$Q_{EL} = \frac{K A}{L} \; (T_s - T_H)$$

where:

$T_H$ = Temperature of housing (°K)

K = Thermal conductivity of wire material (W/in °K)

A = Cross-sectional area of wire ($in^2$)

L = Length of wire (in)

$Q_{EL}$ = Conduction heat leak through electrical leads (W)

Figure 2-8 shows the heat leak per wire for various sizes and various lengths from a 300°K terminal to an 80°K detector subassembly. The curves are for copper wire. Included on the graph are correction factors ($F_L$) for some selected wire materials.

The heat leak, although based on bare wire, will be approximately the same for insulated wire since the conduction through normal insulation materials is a small fraction of that of the metal wire.

For example, the thermal conductivities of Teflon, nylon, polydimide, and rubber are all on the order of 0.005 W/in °K, whereas copper is 10, aluminum is 5.6, iron is 1.9, nickel is 1.7 constantan is 0.6, and stainless steel is 0.5 W/in °K. This shows that the insulation material has a thermal conductivity which is 1 percent that of stainless steel and 0.05 percent that of copper. Therefore, the insulation can be neglected in computing conduction heat leaks in the wires.

A single element detector will require a minimum of four electrical leads (two for the detector and two for temperature sensing and/or temperature control). Assuming 40 gauge copper wire 5 in. long, and heat leak will be 3.5 mW per wire.

3. 3-Axis Rigid Thermal Isolation Mount Heat Leak

The 3-axis rigid thermal isolation mount shown in Fig. 2-3 will have heat leaks as follows:

a. Conduction Heat Leak Through Stringers

$$Q_{SC} = \frac{K_K A_S}{L_S} (T_S - T_D)\, N$$

where:

$Q_{SC}$ = Conduction heat leak in 3-axis mount (W)

$K_K$ = Thermal conductivity of Kapton (W/in °K)

$A_S$ = Cross-sectional area of stringer ($in^2$)

$L_S$ = Length of stringer (in)

$T_S$ = Temperature of surrounds (°K)

$T_D$ = Temperature of detector subassembly (°K)

N = Number of stringers: 8

$$Q_{SC} = \frac{0.005 \times 0.001}{0.5} (300-80)\ 8$$

$$Q_{SC} = 0.0176\ W$$

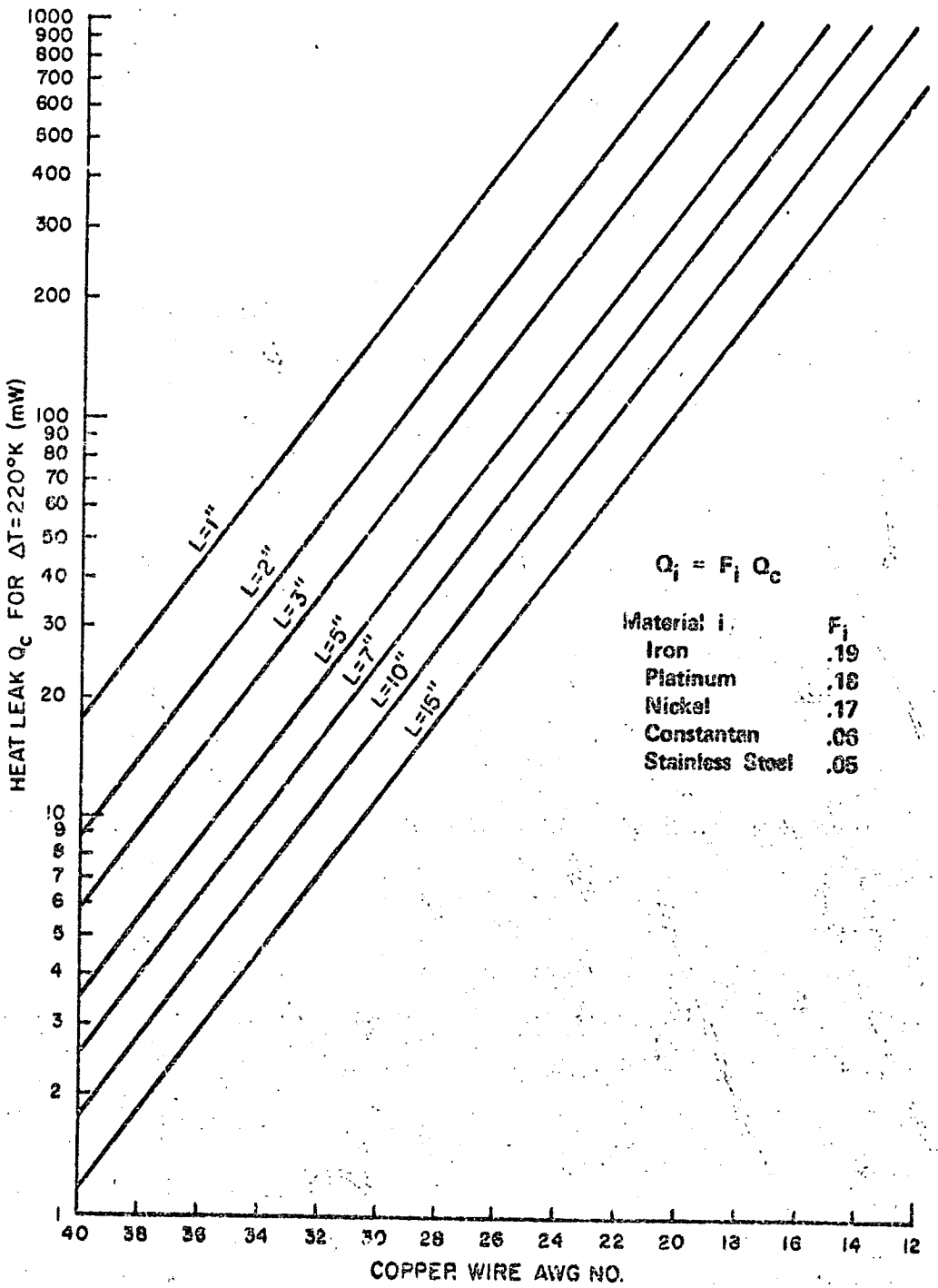



Fig. 2-8. Heat leak vs. AWG wire size for copper wire of various lengths.

b. Radiation Heat Leak to Stringers

The radiation heat leak to stringers is held to a minimum by vapor depositing gold on the surface of the stringers. The order of magnitude of this heat leak can be determined by assuming the stringers to have a linear thermal gradient from 300°K to 80°K and then computing the radiation input to the stringer:

$$Q_{SR} = A_{SS}\, \epsilon_S\, F_{S-S}\, (\sigma T_S^4 - \sigma T_{ave}^4)\, N$$

where:

$Q_{SR}$ = Radiation heat leak to stringer (W)

$A_{SS}$ = Surface area of stringer ($in^2$)

$\epsilon_S$ = Emissivity of stringers: 0.05 max.

$F_{S-S}$ = View factor from stringers to surrounds: 1.0 max.

$\sigma T_{ave}^4$ = Average $\sigma T^4$ of stringers

$$\sigma T_{ave}^4 = \frac{\sigma \int_{T_1}^{T_2} T^4\, dT}{T_2 - T_1} = \frac{\sigma(T_2^5 - T_1^5)}{5(T_2 - T_1)}$$

where:

$T_1$ = Temperature at cold end of stringer: 80°K

$T_2$ = Temperature at hot end of stringer: 300°K

$$\sigma T_{ave}^4 = \frac{\sigma\left[(300)^5 - (80)^5\right]}{5(300-80)}$$

$$\sigma T_{ave}^4 = 0.08110$$

$$Q_{SR} = 0.25 \times 0.05 \times 1.0\ (0.29623 - 0.08110)\ 8$$

$$Q_{SR} = 0.021\ W$$

Since the maximum heat leak due to stringers will not exceed the sum of the superimposed heat leaks, the maximum heat leak will not exceed 0.039 W. The mounting platform for the detector subassembly is finished with vapor deposited gold, and the only heat leak is by radiation coupling.

The mounting plate heat leak is as follows:

$$Q_{MP} = A_{MP} \epsilon F_{MP} (\sigma T_S^4 - \sigma T_{MP}^4)$$

where:

$A_{MP}$ = Exposed area of mounting plate ($in^2$)

$\epsilon$ = Emissivity of gold: 0.05 max.

$T_{MP}$ = Temperature of mounting plate: 80° K

$F_{MP}$ = View factor from mounting plate to surrounds: 1.0 max.

$$Q_{MP} = 1 \times 0.05 \times 1 (0.29623 - 0.00150) = 0.015 \text{ W}$$

The maximum total heat leak for the 3-axis rigid thermal isolation mount will be 0.054 W.

4. 2-Axis Rigid Thermal Isolation Mount Heat Leak

The maximum conduction heat leak is 0.022 W and the maximum radiation heat leak is 0.021 W via the stringers and 0.015 W via the mounting plate, for a total maximum heat leak of 0.058 W.

5. Flexible Conductor Heat Leak

The heat leak per inch of length for the flexible conductor is shown in Fig. 2-9.

The flexible conductor will probably be less than 1.0 in long. Therefore, the heat leak should not exceed 0.037 W.

6. Heat Pipe Heat Leak

Heat pipe heat leaks are due to radiation coupling to the surrounds and leaks due to necessary mechanical supports such as the 2-axis rigid thermal isolation mount.

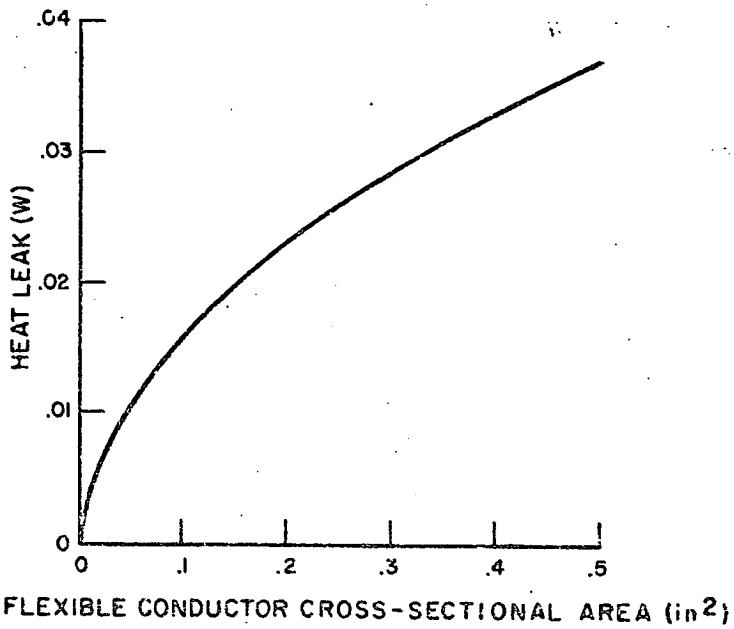



Fig. 2-9. Flexible conductor heat leak vs. cross-sectional area.

The heat leaks due to mounts or supports are treated separately. The radiation coupling heat leaks can be minimized by use of multilayer insulation.

Since the cryogenic heat pipe is a cylinder, the heat transfer equation for pipe insulation will apply by assuming the outer layer of the multilayer insulation to be at ambient temperature (300° K). This can be achieved in practice by finishing the outer layer with a high emissivity finish (such as black paint).

The heat leak can be calculated as follows:

$$Q/L = F2\pi K \Delta T / \ln\left(\frac{r_o}{r_i}\right)$$

where:

K = Apparent thermal conductance of the multilayer insulation (Btu/h/ft/° F)

F = Conversion factor: 0.293 W per Btu/h

$\Delta T$ = Thermal gradient across insulation (° F)

$r_o$ = Outer radius of insulation

$r_i$ = Inner radius of insulation

Q/L= Heat loss per foot of length (W/ft)

Figure 2-10 is a plot of cryogenic heat pipe heat leak per foot of length as a function of the insulation outer radius to inner radius ratio ($r_o/r_i$) for various values

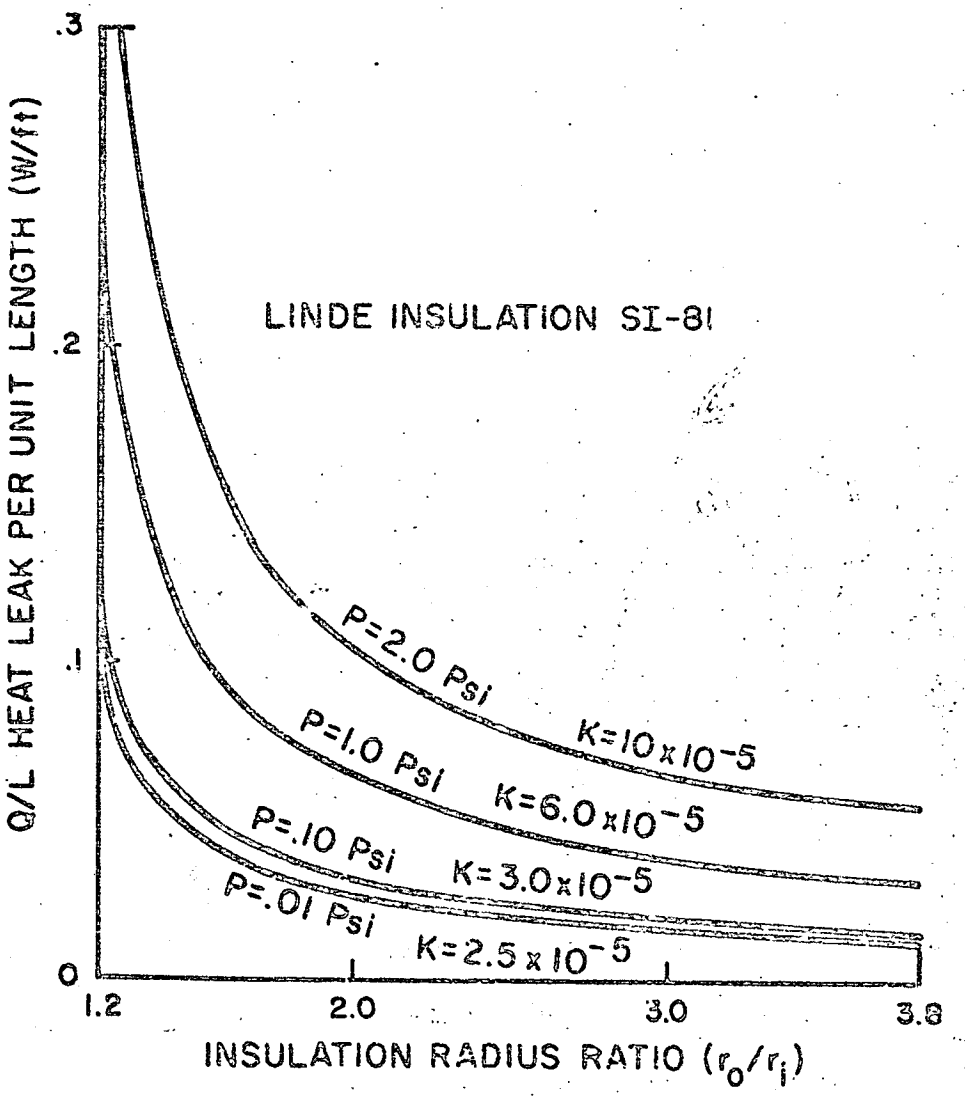



Fig. 2-10. Heat leak vs. insulation outer to inner radius ratio.

of compressive load on the insulation. The apparent thermal conductivities used for the calculations are the values reported by Linde for their SI-81 insulation. This is one of their better insulations and the values reported are similar to values reported for other similar insulations. SI-81 has approximately 400 layers per inch at a compressive load of 2 psi and approximately 150 layers per inch at a compressive load of 0.1 psi.

It should be noted that the apparent thermal conductivity (K) for any multilayer insulation is not a constant but is a function of the absolute values of the inner layer and outer layer temperatures. The values used in the calculations for SI-81 are for boundary conditions of 78° K and 295° K in a vacuum of less than $1 \times 10^{-4}$ torr. This variable apparent conductivity is due to the fact that the heat transfer mode is a combination of conduction and radiation. Therefore, in order to determine the apparent conductivity of any insulation system, it must be tested with the temperature conditions and physical configuration as close as possible to actual.

The lowest heat leak will be achieved with multilayer insulation on a straight heat pipe. Any bends in the heat pipe will increase the heat leak since the insulation will have to be cut or crushed in order to accommodate such bends. It is not possible to predict accurately the effects of bends, but an indication of the effect due to crushing can be obtained by comparing the insulation heat leak at low compressive load on the insulation with the insulation heat leak at high compressive load on the insulation. That is, at a radius ratio of 2.0 and a compressive load of 0.01 psi, the heat leak is 0.023 W/ft, and at a compressive load at 2.0 psi it is 0.103 W/ft, which is greater than a 4 to 1 increase.

Figure 2-10 shows that little is to be gained by using insulation which is thicker than the heat pipe radius.

The heat leaks shown in Fig. 2-10 do not include edge or joint effects. The exposed edge of the multilayer insulation will absorb energy like a black body. In order to minimize this heat leak, the cut edge of the multilayer insulation can be shielded with a radiation barrier which is attached to the heat pipe. Figure 2-11 is one possible concept which can achieve the desired results.

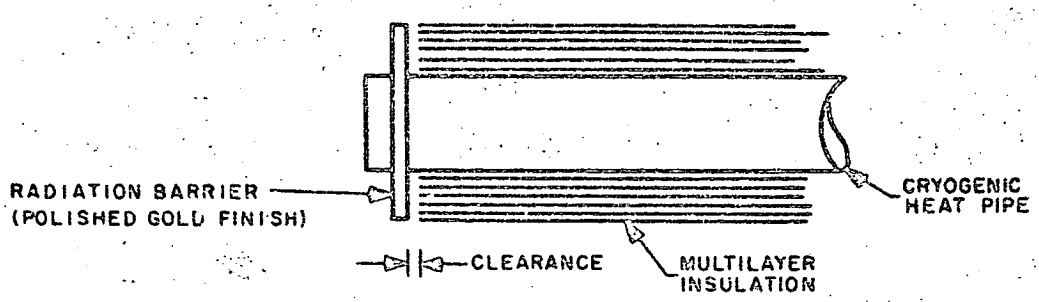



Fig. 2-11. Thermal radiation barrier for multilayer insulation edge.

The heat leak for this configuration is as follows:

$$Q_L = Q_{RB} + Q_C$$

where:

$Q_L$ = Total heat leak

$Q_{RB}$ = Heat leak into radiation barrier

$Q_C$ = Heat leak due to clearance

$$Q_{RB} = A_{RB} \epsilon_{RB} (\sigma T_s^4 - \sigma T_{RB}^4)$$

$$Q_C = A_c \epsilon_c (\sigma T_s^4 - \sigma T_{HP}^4)$$

where:

$A_{RB}$ = Exposed area of radiation barrier ($in^2$)

$A_C$ = Clearance area ($in^2$)

$\epsilon_{RB}$ = Emissivity of radiation barrier: 0.05 max. (gold)

$\epsilon_C$ = Emissivity of clearance area: 1.0 (black body)

$T_{RB}$ = Temperature of radiation barrier: 80° K

$T_{HP}$ = Temperature of heat pipe: 80° K

The radiation barrier will be at the same temperature as the heat pipe ($T_{RB} = T_{HP}$).

Therefore:

$$Q_L = (A_{RB} \epsilon_{RB} + A_C \epsilon_C) (\sigma T_s^4 - \sigma T_{HP}^4)$$

For a 0.25 in diameter heat pipe and a $r_o/r_i$ of 2.0 and a clearance of 0.025 between the radiation barrier and insulation, the heat leak is as follows:

$$Q_L = [\pi(0.25^2 - 0.125^2) \times 0.05 + \pi\, 0.5 \times 0.025]\,(0.29623 - 0.00150)$$

$$Q_L = 0.014\ \text{W}$$

Figure 2-12 is a plot of insulation edge heat leaks for various heat pipe diameters, with insulation having a $r_o/r_i = 2.0$ and a clearance of 0.025 in between the radiation barrier and the insulation.

## D. CONCEPTUAL DESIGN FOR A COOLED PARAMETRIC AMPLIFIER

### 1. Parametric Amplifiers Configuration

Cooled parametric amplifiers for space use will probably be of the integrated type as shown in Fig. 2-13. The paramp would be enclosed in a box of approximately 1.2 x 1.2 x 1.5 in. in order to provide RF shielding.

### 2. Cooling

Due to the small size of the integrated paramp, the most feasible method of cooling would be to cool the entire assembly. Figure 2-14 shows one concept for

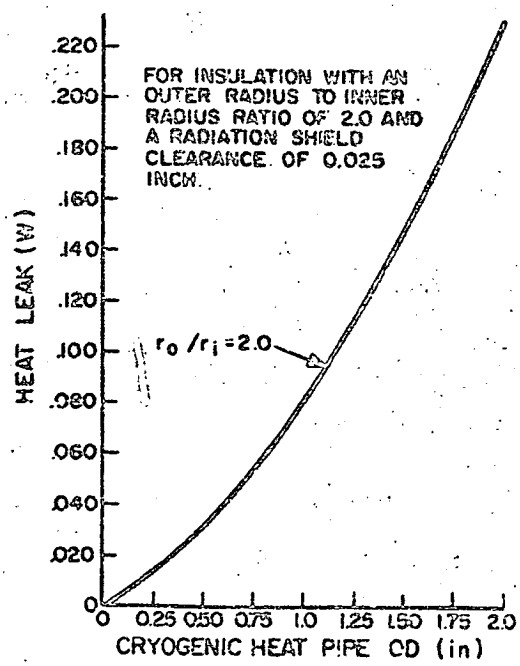



Fig. 2-12. Insulation edge heat leak vs. heat pipe OD.

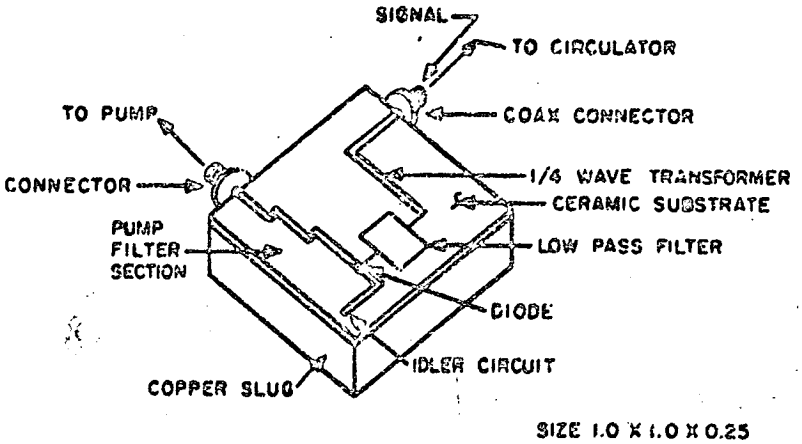



Fig. 2-13. Integrated parametric amplifier.

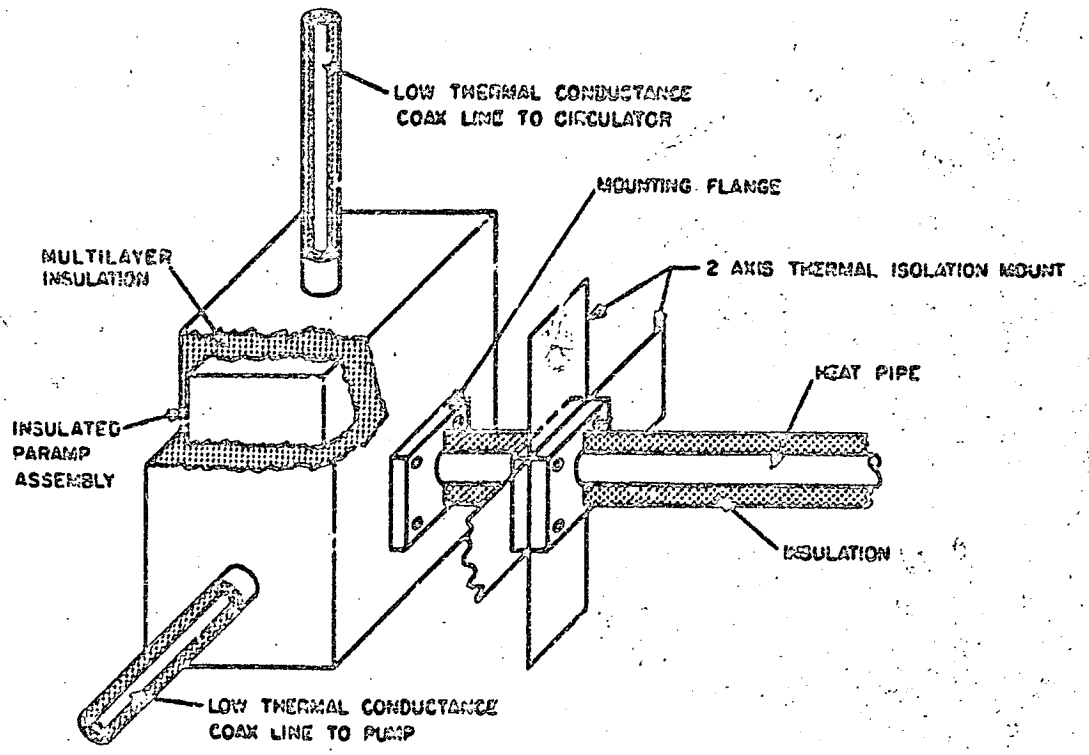



Fig. 2-14. Parametric amplifier mounting concept.

mounting the paramp to the heat pipe in order to obtain minimal heat leak. For this concept the paramp is mounted directly on the cryogenic platform, with no other mechanical support. This is possible due to the small size and low mass of this type of paramp (on the order of 1 to 2 oz).

The electrical heat load is essentially the required pump power, which will be on the order of 50 to 100 mW. The thermal heat leak will consist of the conduction leak through the two coax lines and the 2-axis thermal isolation mount and the radiation heat leaks through the insulation.

The insulation heat leak will be approximately 30 mW, based on a box surface area of 10 $in^2$ and an effective emissivity of 0.01. By assuming that the low thermal conductance coaxes are 6 in long and are constructed of thin wall (.005 in) stainless steel tubing with 0.5 mil of gold on the electrical conducting surfaces, the conduction heat leak can be calculated. Assuming a coax OD of 0.25 in and an ID of 0.07 in, the heat leak will be approximately 250 mW per line, or a total of 500 mW for the two lines. The 2-axis thermal isolator will have a heat leak of approximately 60 mW. The heat pipe will have a heat leak of approximately 50 mW.

This gives a total cooling requirement of 0.690 to 0.740 W, which is a good agreement with the cooling requirements estimated by various developers (estimated to be approximately 1 W or less).

These heat leaks are based on a paramp temperature of 80° K. For colder paramp temperatures the heat leaks would increase.

### 3. Number of Cooled Parametric Amplifiers Required in a Spacecraft

In order to determine the number of cooled parametric amplifiers required in a spacecraft, it is necessary to identify a typical communications system. Figure 2-15 is one concept of a data relay satellite system using three geostationary satellites. For this configuration, each of the geostationary satellites would have two cooled paramps each since they each have two space-looking receivers. Each low altitude satellite would have one cooled paramp each.

The system as shown can be used to perform the following functions:

a. Full-time communication link between low altitude satellites (such as ERTS, ES$^3$, and Tiros) and any ground station. This will permit data and telemetry transmission from the low altitude satellite to any ground station at any time. This can be real time or stored data and will eliminate the problem of limited data storage capacity of tape recorders.

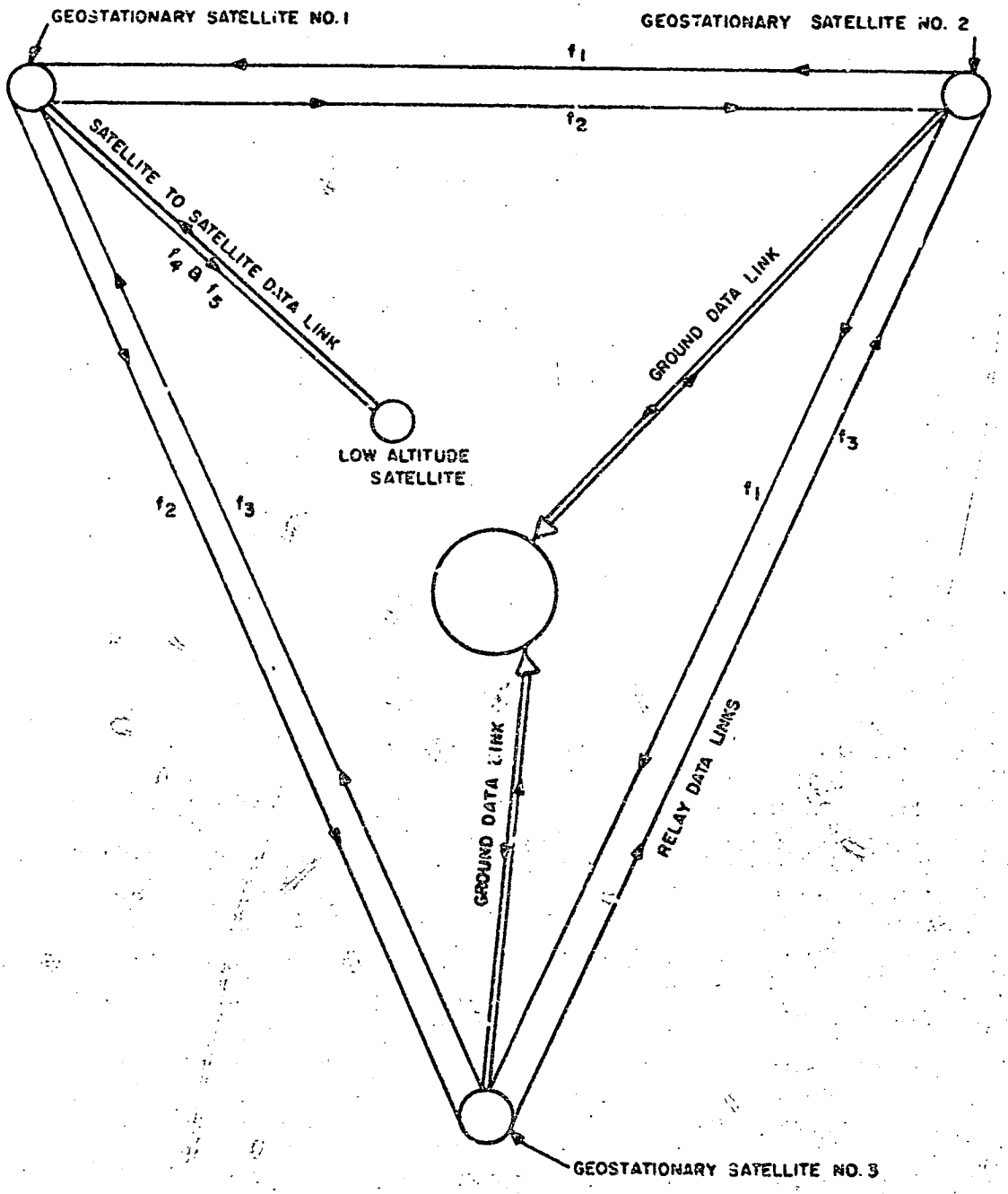



Fig. 2-15. Satellite communications system concept.

b. World-wide ground-to-ground communication links can provide world-wide telephone communications, world-wide radio communications, world-wide TV transmission, world-wide data links for computers, and any other application which can use a world-wide communication link. It is conceivable that the usage of such a system could grow to the point where the system would be saturated and it would be necessary to double the number of frequency bands. This would double the number of cooled paramps in each geostation satellite or would require two full satellite systems. If redundancy is required, the number of paramps will double.

4. Temperature Requirements

The signal-to-noise ratio for a paramp is inversely proportional to its temperature. Therefore, although there is no optimum temperature, the temperature should be as low as possible for best performance.

## E. LASER COMMUNICATION

The 10.6 $\mu$m laser communication system will employ the same type of detectors which are used on the VHRR's (HgCdTe). The only difference between the radiometer detectors and the 10.6 $\mu$m laser detectors is the manner in which they are used. The mounting techniques used in the radiometer are directly applicable to 10.6 $\mu$m laser detectors. The operating temperature will be approximately 90° K, and the heat loads will be the same as for a five detector radiometer array.

## F. DETERMINATION OF ICICLE SYSTEM HEAT LOADS

Table 2-5 lists the maximum and minimum heat loads for the various items associated with a VHRR system. If the VHRR characteristics are known (number of detector elements and type of system — focus sensitive or focus insensitive), the probable maximum and minimum heat load can be computed.

The estimated cooling loads shown in Table 2-6 are computed from Table 2-5 data, using the minimum number of detectors and assuming a focus insensitive system for the minimum cooling load and the maximum number of detectors coupled with a focus sensitive system for the maximum cooling load.

The cooling loads for a 10.6 $\mu$m laser receiver are shown in Table 2-7.

The cooling load for parametric amplifiers can only be estimated at this time, but it appears that a maximum of 1 W and a minimum of 0.5 W are reasonable.

TABLE 2-5. VHRR HEAT LOADS

| Item | Heat Load (mW) |
|---|---|
| Detector Electrical | $N^{(1)}$ Min. — $N^{(1)}$ Max. |
| Detector Subassembly | 106 |
| Wire Leads | $0.3(2N^{(1)}+2)$ Min.[2] — $9(2N^{(1)}+2)$ Max.[2] |
| 2-Axis Mount | 58 |
| 3-Axis Mount (Focus Sensitive Units Only) | 54 |
| Flexible Conductor (1 inch long) (Focus Sensitive Units Only) | Determine from Figs. 2-5 and 3-2 using Items 1, 2, 3 and 5 Heat Loads - Use $\Delta T$ = 1.0°C for Max. and $\Delta T$ = 5.0°C for Min. |
| Heat Pipe Insulation ($r_o/r_i$ = 2) | 26 Min.[4] — 192 Max.[5] |
| Heat Pipe Insulation Termination (Qty. 2) | 12 Min.[6] — 64 Max.[7] |

(1) N = Number of detector elements.

(2) 40 gauge Ni wire 10 in long.

(3) 36 gauge Cu wire 5 in long.

(4) P = 0.01 psi - 1 ft long.

(5) P = 1.0 psi - 3 ft long.

(6) 0.12 in OD heat pipe.

(7) 0.50 in OD heat pipe.

The total cooling load requirement for an ICICLE system will vary, depending upon the number and type of items on a spacecraft which must be cooled.

Based on a study of cooling requirements, it appears that the operational satellites such as Tiros, ERTS (earth resources) and DRS (data relay satellite) would be by far the biggest users of an ICICLE system. The experimental satellites such as Nimbus and ATS would require less cooling capacity since they normally fly experimental systems with no redundancy. Table 2-6 lists the equipment which will result in the

TABLE 2.6. ESTIMATED COOLING LOADS

| Item | Maximum Heat Load (mW) | Minimum Heat Load (mW) |
|---|---|---|
| Detector Electrical | 100 | 20 |
| Detector Subassembly | 106 | 106 |
| Wire Leads | 378 | 13 |
| 3-Axis Mount | 54 | 54 |
| Flexible Thermal Conductor | 30 | 6 |
| 2-Axis Mount | 58 | 58 |
| Heat Pipe Insulation | 192 | 26 |
| Heat Pipe Insulation Termination | 64 | 12 |
| TOTAL | 982 | 295 |

TABLE 2-7. COOLING LOADS FOR A 10.6 MICRON LASER RECEIVER

| Item | Maximum Heat Load (mW) | Minimum Heat Load (mW) |
|---|---|---|
| Detector Electrical | 25 | 5 |
| Detector Subassembly | 106 | 106 |
| Wire Leads | 108 | 4 |
| 3-Axis Mount | 58 | 58 |
| Flexible Thermal Conductor | 20 | 6 |
| 2-Axis Mount | 58 | 58 |
| Heat Pipe Insulation | 192 | 26 |
| Heat Pipe Insulation Termination | 64 | 12 |
| TOTALS | 631 | 275 |

## TABLE 2-8. CANDIDATE FOR ICICLE APPLICATION SYSTEMS

| Spacecraft | Minimum Equipment | | | Maximum Equipment | | |
|---|---|---|---|---|---|---|
| | Quantity | Item | Min. Cooling Load (W) | Quantity | Item | Max. Cooling Load (W) |
| Tiros | 2 | Single Detector Radiometer | 0.41 W<br>Total 0.41 W | 2<br>2<br>2<br>2 | Cooled Paramps<br>10 Element Radiometer<br>2 Element Radiometer<br>Single Detector Radiometer<br>Total | 2.0<br>1.5<br>1.1<br>1.1<br>5.7 W |
| ERTS | 2 | Single Detector Radiometer | 0.41 W<br>Total 0.41 W | 2<br>2<br>2<br>2 | Cooled Paramps<br>40 Element Radiometer<br>2 Element Radiometer<br>Single Element Radiometer<br>Total | 2.0<br>2.9<br>1.1<br>1.1<br>7.1 W |
| DRS | 1 | Experimental IR Laser Receiver | 0.28 W<br>Total 0.28 W | 4<br>1 | Cooled Paramps<br>Experimental IR Laser Receiver<br>Total | 4.0<br>.6<br>4.6 W |
| Nimbus | 1 | Single Detector Radiometer | 0.41 W<br>Total 0.41 W | 1<br>1<br>1 | Experimental IR Laser Receiver<br>40 Element Radiometer<br>20 Element Radiometer<br>Total | 0.6<br>1.5<br>1.0<br>3.1 W |
| ATS | 1 | Single Detector Radiometer | 0.41 W<br>Total 0.41 W | 1<br>1<br>1 | Experimental IR Laser Receiver<br>40 Element Radiometer<br>Cooled Paramp<br>Total | 0.6<br>1.5<br>1.0<br>3.1 W |

maximum and minimum cooling load requirements for five satellite systems which will most likely have need of an ICICLE system. The 200 element VHRR required for iceberg detection is not shown since the development of such a VHRR is of secondary importance and will probably not occur in the near future.

## C. CONCLUSIONS TO SECTION 2

The cooling load requirements of an ICICLE system appear to be on the order of 5.0 W in the 1970-1980 period but will probably increase as the state of the art in radiometers, IR lasers, communicating systems, etc. advances. There are systems presently being developed which could make use of an ICICLE system as early as 1970, and many more are being studied and developed for use in the period 1973 and beyond.

The progress in VHRR radiometers and communication systems is presently limited by the lack of a high capacity long life cryogenic cooling system which is insensitive to spacecraft orientation and orbit parameters. The development of an ICICLE system will open the way for future advances in the state of the art.

## Section 3

# VUILLEUMIER THEORY AND PRACTICE


*Summary*

*Cryogenic refrigeration can be provided from a central refrigeration plant operating on a Vuilleumier thermodynamic cycle. This type of machine is unique in that a power cycle and refrigeration cycle are integrated into a single device and share the components required for implementation. As a result, the primary form of energy required to power the cycle is thermal. This can be supplied efficiently for long periods from a radioisotope.*

*A second unique feature of a Vuilleumier cycle machine is that all parts of the machine are nearly isobaric. This means that hard seals and heavily loaded bearings can be eliminated from a mechanical implementation of the cycle. Bearing and seal wear can thus be minimized and the major limitations to machine life greatly eased.*

*Rigorous analytical description of a Vuilleumier cycle machine is difficult, as are such descriptions of any regenerative heat engine. Performance descriptions can be made by assuming that ideal thermodynamic performance and losses do not interact and can be calculated independently. When this is done, performance descriptions can be developed which are verified by experimental data on existing prototype hardware.*

*On the basis of calculations and experimental testing, the feasibility of meeting ICICLE refrigeration requirements can be established. A realistic goal for a VM refrigerator specification would call for a capacity of 5 W at 77°K and thermal input of 250 W at 900°K. The electrical power input can be 15 W and a refrigerator weight of 7 lb. The life and reliability of such a machine will be limited by working fluid containment and bearing wear problems. Two years of unmaintained life should be achievable with VM engines presently being developed.*

*A VM refrigeration machine is a feasible approach to achieving central refrigeration in a spacecraft. It is the most promising choice for this application by virtue of its operation on thermal energy and its potential for long life.*


## A. INTRODUCTION

The background and state of the art of VM refrigeration are fairly limited. This section presents a more comprehensive, more rigorous, analysis of idealized VM performance than can be found in the literature. This analysis is summarized by Eqs. 3-14a and 3-14b. Loss mechanisms operative in a real VM are described.

A basic assumption underlying actual VM performance analysis is separability – that is, that the various loss mechanisms do not interact with each other so that the total loss is the sum of the separate losses. The other separability assumption is that the ideal refrigeration is produced and that the summed losses can be subtracted to determine the net refrigeration available. Using this assumption, the technique is used to predict performance versus temperature for a given VM design. This approach permits the prediction of performance variation of a VM engine as its design is varied at a given temperature.

## B. IDEALIZED VM PERFORMANCE

### 1. Derivation of Performance Equations for Ideal VM Cycle

Rudolph Vuilleumier patented (U.S. Patent 1,275,507) a unique heat-driven refrigerator in 1918. Similar concepts were later patented by Vannevar Bush in 1938 (U.S. Patent 2,127,286), and K.W. Taconis in 1951 (U.S. Patent 2,567,474). These patents describe different physical apparatus to achieve refrigeration but are thermodynamically similar. The ideal cycle produces refrigeration due to gas compression and expansion brought about by a high-temperature heat source and an ambient-temperature heat sink. The idealized cycle has perfect mechanisms, perfect heat transfer, and no gas friction, thus operating without mechanical energy input. The history of VM refrigeration is available in the literature.[1-6*]

Since ideal VM refrigerator has no irreversible processes, it has a single value of coefficient of performance (COP) for a given set of: refrigeration temperature ($T_c$), heat rejection temperature ($T_a$), and heat source temperature ($T_h$). The coefficient of performance is the ratio of heat absorbed ($Q_c$) at $T_c$ to the heat supplied ($Q_h$) at $T_h$. The value of COP is that obtained by a Carnot engine (efficiency $P/Q_h$) driving a Carnot refrigerator (coefficient of performance $Q_c/P$). These relationships are shown in Fig. 3-1.

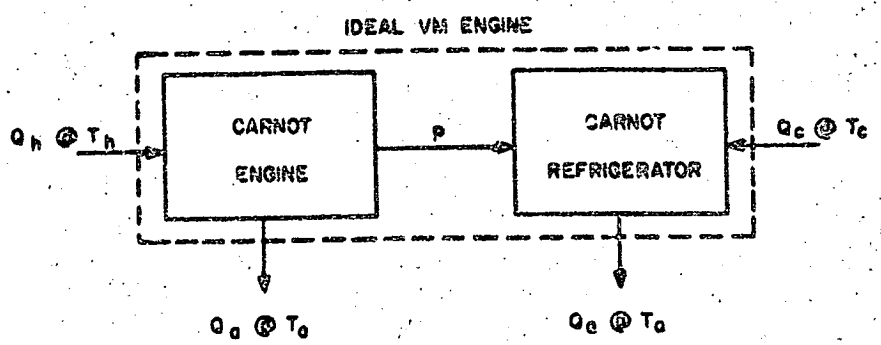



Fig. 3-1. Ideal VM-cycle engine, block diagram.

*References cited in Sec. 3 appear at end of Sec. 3.

$$COP = \frac{Q_c}{Q_h} = \left(\frac{Q_c}{P}\right)\left(\frac{P}{Q_h}\right) = \left(\frac{T_c}{T_a - T_c} \times \frac{T_h - T_a}{T_h}\right) \tag{3-1}$$

This section will discuss the parameters that affect the magnitude of $Q_c$ but do not affect the ratio $Q_c/Q_h$. A cranked configuration of a VM engine is shown in Fig. 3-2. The hot and cold displacer regenerators (HDR and CDR) are not constrained to have the same stroke length. Also, it is not necessary that the connecting rods to the HDR and CDR originate from a common crank pivot, but can be separated by some angle $\alpha$. In addition, the angle between the hot and cold cylinders may be some angle $\beta$. The net effect of these two angles is to establish some phase angle $\phi$ by which the HDR leads the CDR:

$$\phi = \beta - \alpha \tag{3-2}$$

If the kinematic complications of the connecting rod are neglected, the movements of the HDR and CDR are assumed sinusoidal. Therefore, the instantaneous value of hot volume ($V_h$) and cold volume ($V_c$) is related to the hot swept volume ($V_{ho}$), the cold swept volume ($V_{co}$), any clearance or void volumes ($V_{vc}$ and $V_{vh}$) at top dead center, and the pertinent angles:

$$\begin{aligned} V_c &= \frac{V_{co}}{2}(1 - \sin\theta) + V_{vc} \\ V_h &= \frac{V_{ho}}{2}\left[1 - \sin(\theta + \phi)\right] + V_{vh} \end{aligned} \tag{3-3}$$

Likewise, the instantaneous ambient volume $V_a$ which must have a swept volume of $V_{co} + V_{ho}$:

$$V_a = \frac{V_{co}}{2}(1 + \sin\theta) + \frac{V_{ho}}{2}\left[1 + \sin(\theta + \phi)\right] + V_{va} \tag{3-4}$$

Three control volumes and the manner in which they vary with $\theta$ or time have now been defined. The following specific attributes which make this an ideal VM-cycle engine must be clarified:

1) No thermal conduction exists along cylinder walls, regenerator walls, or in the axial direction through the regenerator matrix.

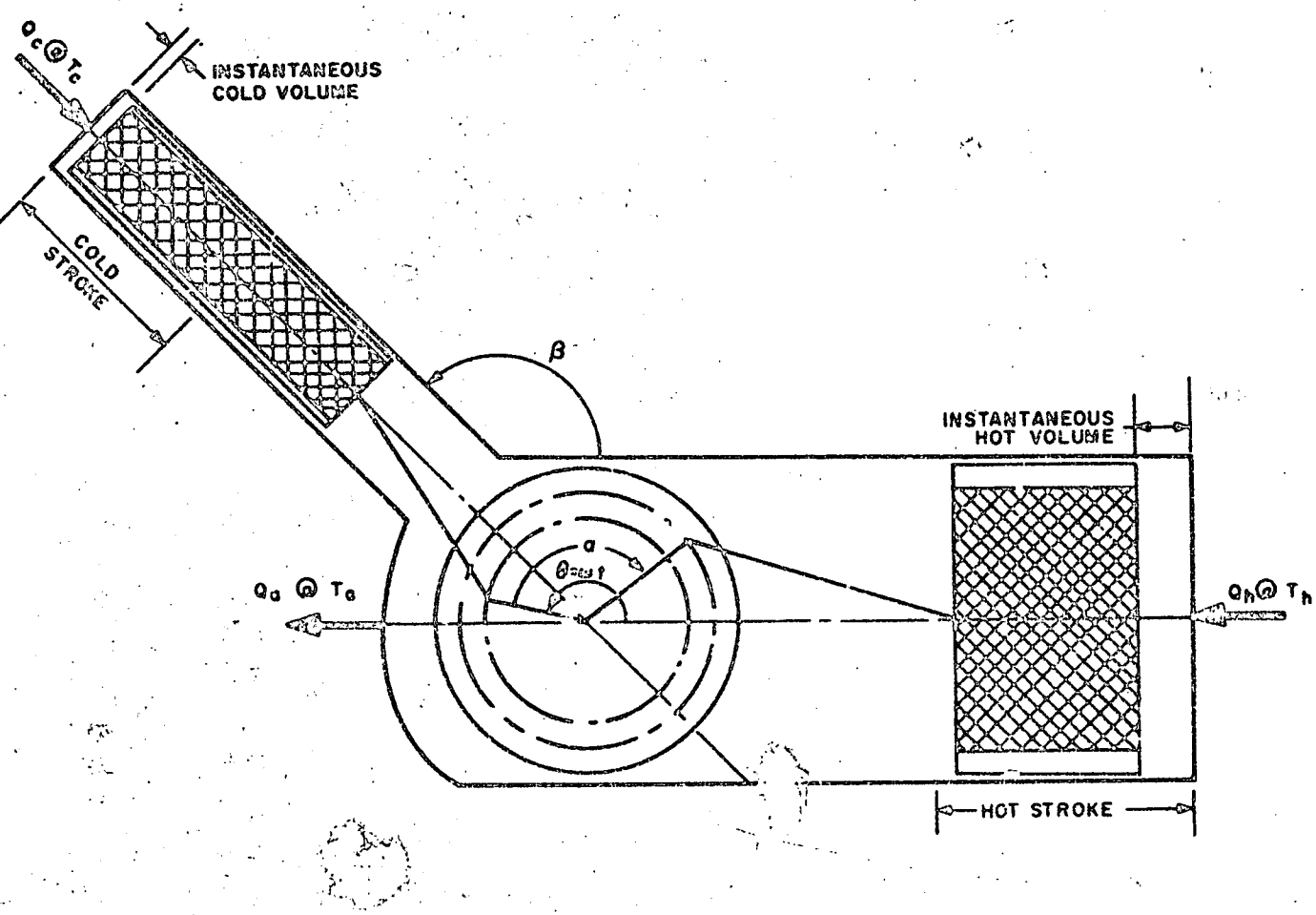



Fig. 3-2. Schematic diagram of Vuilleumier-cycle refrigerator.

2) Perfect thermal communication exists between all gas molecules and the walls in each of the central volumes.

3) Temperatures are time steady, and cyclic equilibrium exists.

4) No leakage exists around CDR and HDR.

5) Regenerator action is perfect.

6) No mechanical or gas friction exists (e.g., isobaric conditions obtained).

Under the above assumptions, the first law of thermodynamics for a non-steady, quasi-static, open system is applied:

$$dU = dQ - Pd\,V + h_e dM \tag{3-5}$$

If each of the energy terms is integrated around a complete cycle (see Fig. 3-3), the total internal energy must return to the original values: $\oint dU = 0$. The assumption of constant gas temperatures allows $\oint h_e dM$ to be $h_e \oint dM$, and obviously there can be no mass accumulation, so that $h_e \oint d\,M = 0$. The term $\oint dQ$ becomes the net heat interchange Q per cycle:

$$Q_{h,\,c,\,a} = \oint P\,dV_{h,\,c,\,a} \tag{3-6}$$

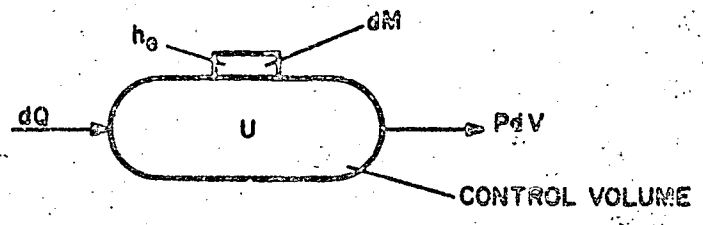



Fig. 3-3. Open cycle energy balance.

The method of obtaining $\oint PdV$ is to find system pressure, P, as a function of $\theta$ so that the closed path integral will be from $\theta = 0$ to $\theta = 2\pi$. Using the perfect gas law to sum the mass (M) as it is distributed around the refrigerator,

$$M = \frac{P}{R}\left[\frac{V_c}{T_c} + \frac{V_h}{T_h} + \frac{V_a}{T_a} + \frac{V_{vRc}}{T_{Rc}} + \frac{V_{vRh}}{T_{Rh}}\right] \tag{3-7}$$

where $V_{vRc}/T_{Rc}$ and $V_{vRh}/T_{Rh}$ are the contribution to the mass that exists in the voids in the hot and cold perfect regenerators. For a uniformly distributed void volume in a regenerator with a linear temperature distribution, it can be shown that the effective hot and cold regenerator temperatures $T_{Rc}$, $T_{Rh}$ should be calculated by:

$$T_{Rc} = \frac{T_c - T_a}{\ln\left(\frac{T_c}{T_a}\right)}$$

$$T_{Rh} = \frac{T_h - T_a}{\ln\left(\frac{T_h}{T_a}\right)} \qquad (3\text{-}8)$$

When Eqs. 3-3 and 3-4 are placed in Eq. 3-7, we will obtain a group of terms that represent the effect of void volume distributed around the VM:

$$\frac{V_v}{T_v} = \frac{V_{vRc}}{T_{Rc}} + \frac{V_{vRh}}{T_{Rh}} + \frac{V_{va}}{T_a} + \frac{V_{vc}}{T_c} + \frac{V_{vh}}{T_h} \qquad (3\text{-}9)$$

After substituting Eqs. 3-3 and 3-4 into Eq. 3-7 and multiplying numerator and denominator by $T_a$ and solving for P:

$$P = \frac{2MRT_a}{\left[V_{co}\left(1+\frac{T_a}{T_c}\right)+V_{ho}\left(1+\frac{T_a}{T_h}\right)+2\frac{V_v}{T_v}\cdot T_a + V_{co}\left(1-\frac{T_a}{T_h}\right)\sin(\theta+\phi) + V_{co}\left(1-\frac{T_a}{T_c}\right)\sin\theta\right]} \qquad (3\text{-}10)$$

Where

$$a = V_{co}\left(1+\frac{T_a}{T_c}\right) + V_{ho}\left(1+\frac{T_a}{T_h}\right) + 2\frac{V_v}{T_v}\cdot T_a$$

$$b = V_{ho}\left(1-\frac{T_a}{T_h}\right)$$

$$c = V_{co}\left(1-\frac{T_a}{T_c}\right)$$

$$P = \frac{2MRT_a}{a + b\sin(\theta+\phi) + c\sin\theta} \qquad (3\text{-}11)$$

The value of $Q_c$ is found by integration:

$$Q_c = \int_0^{2\pi} \left[P(\theta)\right]\left[\frac{d\left[V_c(\theta)\right]}{d\theta}\right] d\theta \qquad (3\text{-}12)$$

For Eq. 3-12 the rigorous integral is

$$Q_c = -\frac{MRT_a V_{co} 2\pi b \sin\phi}{b^2+c^2+2cb\cos\phi}\left[1-\frac{a}{(a^2-b^2-c^2-2cb\cos\phi)^{1/2}}\right]$$

$$Q_h = \frac{MRT_a 2\pi c \sin\phi}{b^2+c^2+2cb\cos\phi}\left[1-\frac{a}{(a^2-b^2-c^2-2cb\cos\phi)^{1/2}}\right] \qquad (3\text{-}13)$$

For the condition where $a^2 > b^2 + c^2$ (which is true for $T_h > T_a$ and $T_c < T_a$).

It is interesting to note that F.N. Magee and R.D. Doering[5] present the solution of the integral incorrectly. Their integral is for the case for $\phi = \pi/2$ and leaves only the term in front of the bracket, which results in the incorrect sign for $Q_c$ and far too large a magnitude of $Q_c$.

F.F. Chellis and W.H. Hogan's solution[2] is limited to $\phi = \pi/2$ but appears to approximate the rigorous case, but not within the 5 percent error they indicate. T.T. Rule and F.B. Qvale[6] derived a rigorous expression for $Q_c$ and a variable phase angle $\phi$, but the expression is considerably more complex than Eq. 3-12.

If Eq. 3-13 were used to obtain an understanding of idealized VM performance characteristics, a temperature set $T_c$, $T_a$, $T_h$ would first have to be assumed. Then, within this assumption, values for the charge factor $MRT_a$, hot swept volume $V_{ho}$, void volume $V_v/T_v$ and phase angle $\phi$ must all be simultaneously assumed to allow $Q_c$ to be plotted versus cold swept volume $V_{co}$, for example. Then all of the independent variables $MRT_a$, $V_{ho}$, $V_v/T_v$, and $\phi$ would have to be separately iterated to investigate all design possibilities within the assumed temperature set $T_c$, $T_a$, $T_h$. A large number of graphs would be generated that would defy interpretation and understanding. However, nearly all of this complexity can be obviated by redefining all variables into a dimensionless form. The following definitions are used, with the horizontal slash indicating a dimensionless variable:

$$\not{V}_c = V_c/V_{ho}$$

$$\not{V}_h = V_h/V_{ho}$$

$$\not{V}_a = V_a/V_{ho}$$

$$\not{P} = \frac{P}{MRT_a/V_{ho}}$$

$$\not{V}_{co} = V_{co}/V_{ho}$$

$$\not{Q}_c = \frac{Q_c}{MRT_a}$$

and groupings:

$$c = \psi_{co}\left(1 + \frac{T_a}{T_c}\right) + \left(1 + \frac{T_a}{T_h}\right) + 2\psi_v$$

$$b = 1 - \frac{T_a}{T_h}$$

$$a = \psi_{co}\left(1 - \frac{T_a}{T_c}\right)$$

Therefore

$$Q_c = -\frac{\psi_{co}\, 2\pi\, b \sin\phi}{b^2 + c^2 + 2cb\cos\phi}\left[1 - \frac{a}{(c^2 - b^2 - c^2 - 2ab\cos\phi)^{1/2}}\right] \qquad (3\text{-}14a)$$

$$Q_h = \frac{2\pi\, c \sin\phi}{b^2 + c^2 + 2cb\cos\phi}\left[1 - \frac{a}{(c^2 - b^2 - c^2 - 2ab\cos\phi)^{1/2}}\right] \qquad (3\text{-}14b)$$

$$P = \frac{2}{a + b\sin(\theta + \phi) + c\sin\theta} \qquad (3\text{-}15)$$

Note that when $Q_c$ is divided by $Q_h$, the bracket term and front denominator divide out, leaving

$$\frac{Q_c}{Q_h} = -\frac{\psi_{co}\, 2\pi\, b \sin\phi}{2\pi\, c \sin\phi} = -\frac{\psi_{co}\left(1 - \frac{T_a}{T_h}\right)}{\psi_{co}\left(1 - \frac{T_a}{T_c}\right)} = \left(\frac{T_h - T_a}{T_h}\right)\left(\frac{T_a - T_c}{T_c}\right) \qquad (3\text{-}16)$$

Equation 3-16 indicates that the ideal VM engine will produce the Carnot refrigerator times the Carnot Engine-COP irrespective of the choice of $\phi$ or $\psi_{co}$. Therefore, after a temperature set has been chosen, heat absorption per cycle, $Q_h$, becomes a function of the two independent variables: swept volume ratio $\psi_{co}$ ($V_{co}/V_{hc}$) and phase angle $\phi$. In principle, some analytical technique, such as LaGrange's method of undetermined multipliers, could be used to find the values of $\psi_{co}$ and $\phi$ which simultaneously make a maximum. Unfortunately, exceedingly complex expressions result. As an alternative, RCA has employed a computer to calculate a parametric display to determine this maximum.

## 2. Heat Pumping Versus Phase Angle and Volume Ratio

For this analysis, RCA has chosen three refrigeration temperatures of interest to ICICLE, 25°K, 77°K, and 125°K. The ambient temperature was fixed at 300°K. The heat source temperature of 900°K was chosen on the basis of successful laboratory experience:

$$A\begin{cases} T_c = 25°K \\ T_a = 300°K \\ T_h = 900°K \end{cases} \qquad B\begin{cases} T_c = 77°K \\ T_a = 300°K \\ T_h = 900°K \end{cases} \qquad C\begin{cases} T_c = 125°K \\ T_a = 300°K \\ T_h = 900°K \end{cases}$$

Figures 3-4, 3-5 and 3-6 show $\Phi_c$ versus phase angle for various constant values of $\Psi_{co}$ with $\Psi_v = 0$ in all cases. The optimum phase angle goes from approximately 100° at 25°K to 95° at 125°K. In all cases, values of $\Psi_{co}$ close to the optimum value were plotted. The value of $\Psi_{co}$ optimum at $\varphi$ optimum increases from about 0.1 at 25°K to 0.4 at 125°K. However, the gain in $\Phi_c$ at $\Psi_{co}$ optimum and $\varphi$ optimum over $\Phi_c$ at $\Psi_{co}$ opt and $\varphi$ = 90 degrees is 2.5 percent at 25°K and less than 1 percent at 77°K and 125°K. There would be substantial practical difficulty in implementing a VM engine with values of $\varphi$ from 95° to 100°. Therefore, it is concluded that a gain in $\Phi_c$ of less than 2.5 percent at all design temperatures above 25°K is not worth the cost in complexity. It should be noted that at temperatures much less than 25°K, a phase angle other than 90° might be worth the investment.

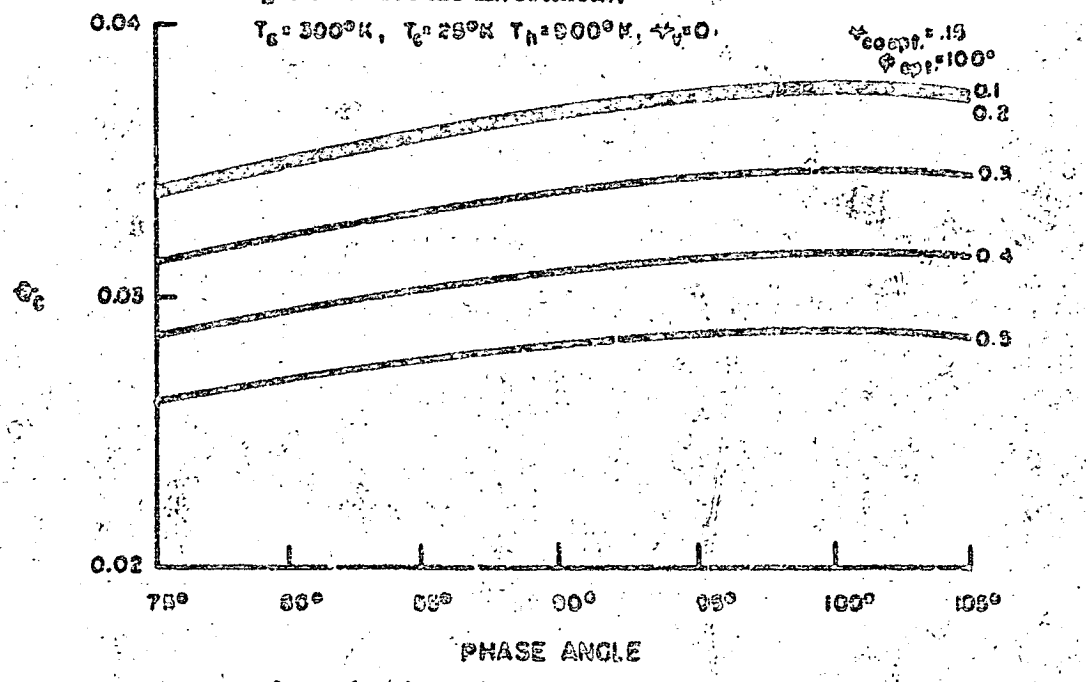



Fig. 3-4. Dimensionless ideal heat absorption per cycle as a function of phase angle with swept volume ratio as a parameter for a $T_c$ of 25°K.

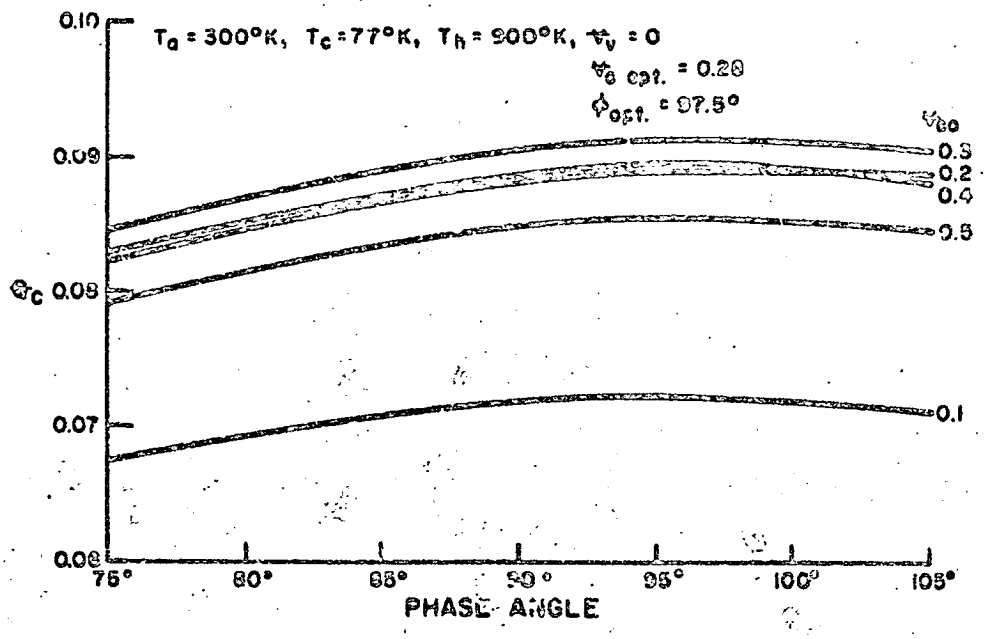



Fig. 3-5. Dimensionless ideal heat absorption per cycle as a function of phase angle with swept volume ratio as a parameter for a $T_c$ of 77°K.

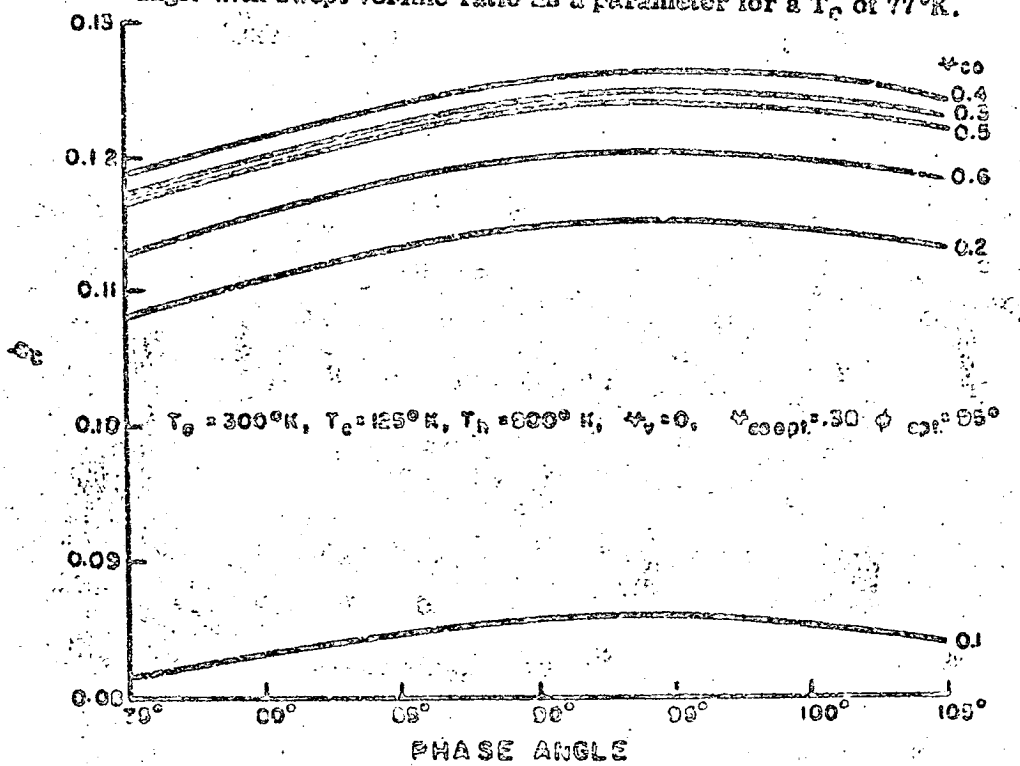



Fig. 3-6. Dimensionless ideal heat absorption per cycle as a function of phase angle with swept volume ratio as a parameter for a $T_c$ of 125°K.

### 3. Heat Pumping Versus Volume Ratio and Void Volume at Phase Angle of 90°

After fixing $\varphi$ at 90°, the effects of swept volume ratio $V_{co}$ ($V_{co}/V_{ho}$) and void volume are explored. The effect of void volume and its distribution can be found by modifying Eq. 9:

$$\frac{V_v}{T_v} = \frac{V_{vRc}}{T_{Rc}} + \frac{V_{vRh}}{T_{Rh}} + \frac{V_{va}}{T_a} + \frac{V_{vc}}{T_c} + \frac{V_{vh}}{T_h}$$

$$\frac{V_v}{V_{ho}}\frac{1}{T_v} = \frac{V_{vRc}}{V_{ho}}\frac{1}{T_{Rc}} + \frac{V_{vRh}}{V_{ho}}\frac{1}{T_{Rh}} + \frac{V_{va}}{V_{ho}}\frac{1}{T_a} + \frac{V_{vc}}{V_{ho}}\frac{1}{T_c} + \frac{V_{vh}}{V_{ho}}\frac{1}{T_h} \qquad (3\text{-}17)$$

$$\tau_v \equiv \frac{V_v}{V_{ho}}\frac{T_a}{T_v} = \frac{V_{vRc}}{V_{ho}}\frac{T_a}{T_{Rc}} + \frac{V_{vRh}}{V_{ho}}\frac{T_a}{T_{Rh}} + \frac{V_{vo}}{V_{ho}}\frac{T_a}{T_a} + \frac{V_{vc}}{V_{ho}}\frac{T_a}{T_c} + \frac{V_{vh}}{V_{ho}}\frac{T_a}{T_h}$$

Hence, $\tau_v$ reflects the effect of the temperature of the various void volumes as well as the magnitude relative to $V_{ho}$. In effect, any void volume at $T_c$ is much more important than an equal void volume at $T_h$.

Figures 3-7, 3-8 and 3-9 display $\phi_c$ versus $\tau_{co}$ for various fixed values of $\tau_v$ for the A, B and C temperature set. The value of $\tau_{co}$ that maximizes $\phi_c$ increases with increasing values of $\tau_v$ at all temperature sets. Clearly void volume is very costly in $\phi_c$ at all temperature sets. A value of $\tau_v$ equal to approximately 0.3 represents the void volume in current VM laboratory models. Obviously, $\tau_v$ should approach zero in a real design. The percentage loss in $\phi_c$ for given $\tau_v$ is about the same at all temperature sets.

By far the most interesting point displayed by Figs. 3-7, 3-8 and 3-9 is the flatness in $\phi_c$ near the optimum value. This means that a VM engine optimized for 77°K will not be very far from optimum at 25°K or 125°K. For example, at 77°K, an optimized design produces a value of $\tau_{co}$ of 0.38 at $\tau_v = 0.20$. At 25°K, this engine would produce a $\phi_c$ only 12 percent less than a 25°K optimized engine could produce. If the 77°K engine is operated at 125°K, the $\phi_c$ it can produce is only 2 percent less than the $\phi_c$ an optimized 125°K VM could produce. The characteristic of being able to operate near optimum over a large temperature range indicates that a VM engine is inherently flexible and adaptable to a large range of requirements.

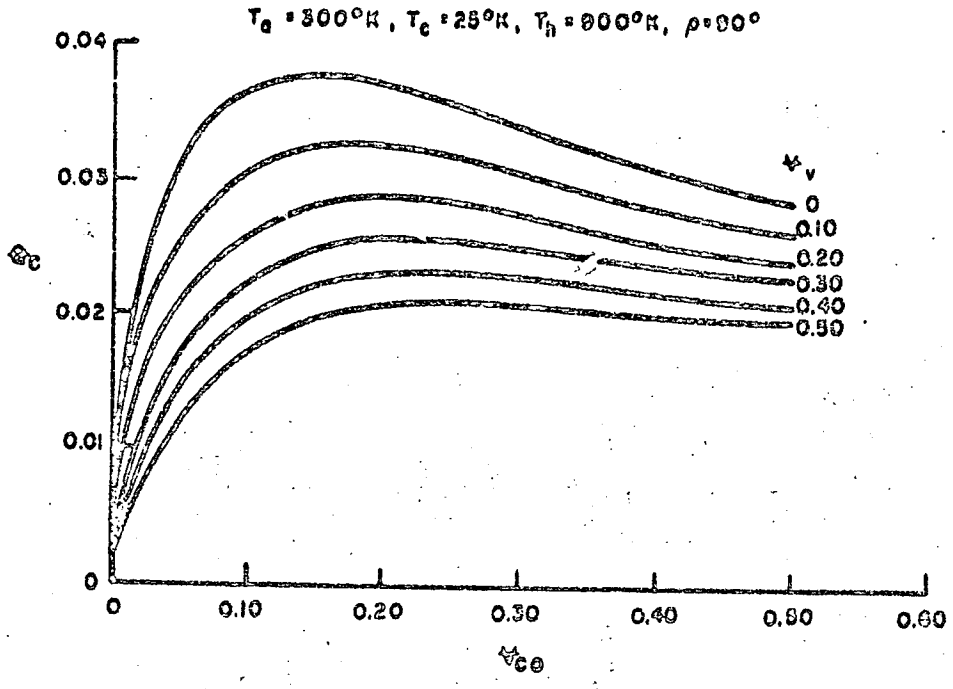



Fig. 3-7. Dimensionless ideal heat absorption per cycle as a function of swept volume ratio with temperature-weighted dimensionless void volume as a parameter for a $T_c$ of 25°K.

## 4. Off Design Operation of VM Engines

This section will evaluate the off design performance of a VM engine for separately changing $T_c$, $T_a$ and $T_h$. On each of Figs. 3-10, 3-11 and 3-12, there are six curves representing the off design performance from optimized engines designed to the criteria listed below:

A Set - $T_h$ = 900 °K, $T_a$ = 300 °K, $T_c$ = 25 °K

for $\Phi_v$ = 0 and $\Phi_v$ = 0.5

B Set - $T_h$ = 900 °K, $T_a$ = 300 °K, $T_c$ = 77°K

for $\Phi_v$ = 0 and $\Phi_v$ = 0.5

C Set - $T_h$ = 900 °K, $T_a$ = 300 °K, $T_c$ = 125°K

for $\Phi_v$ = 0 and $\Phi_v$ = 0.5

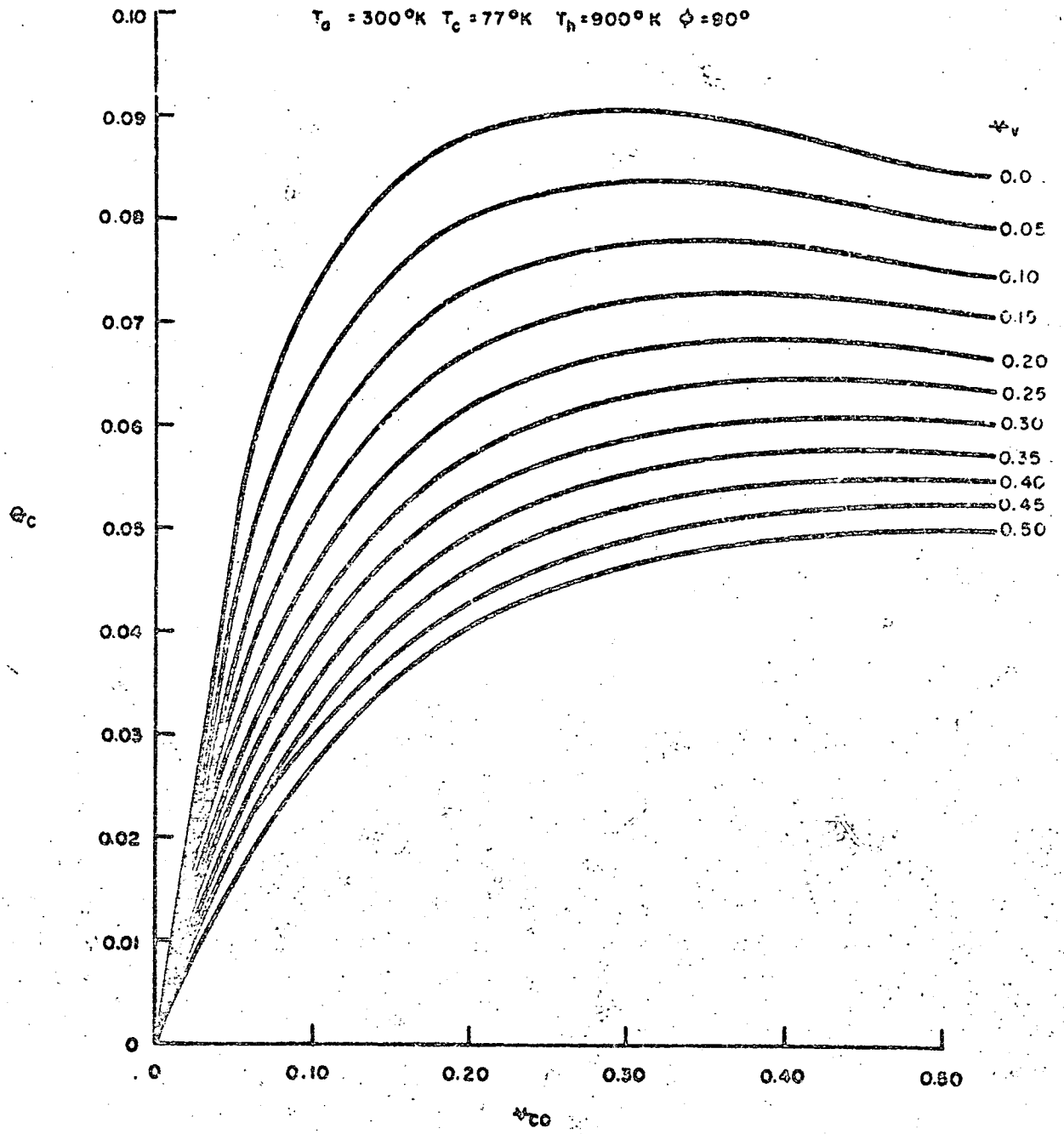



Fig. 3-8. Dimensionless ideal heat absorption per cycle as a function of swept volume ratio with temperature-weighted dimensionless void volume as a parameter for a $T_c$ of 77°K.

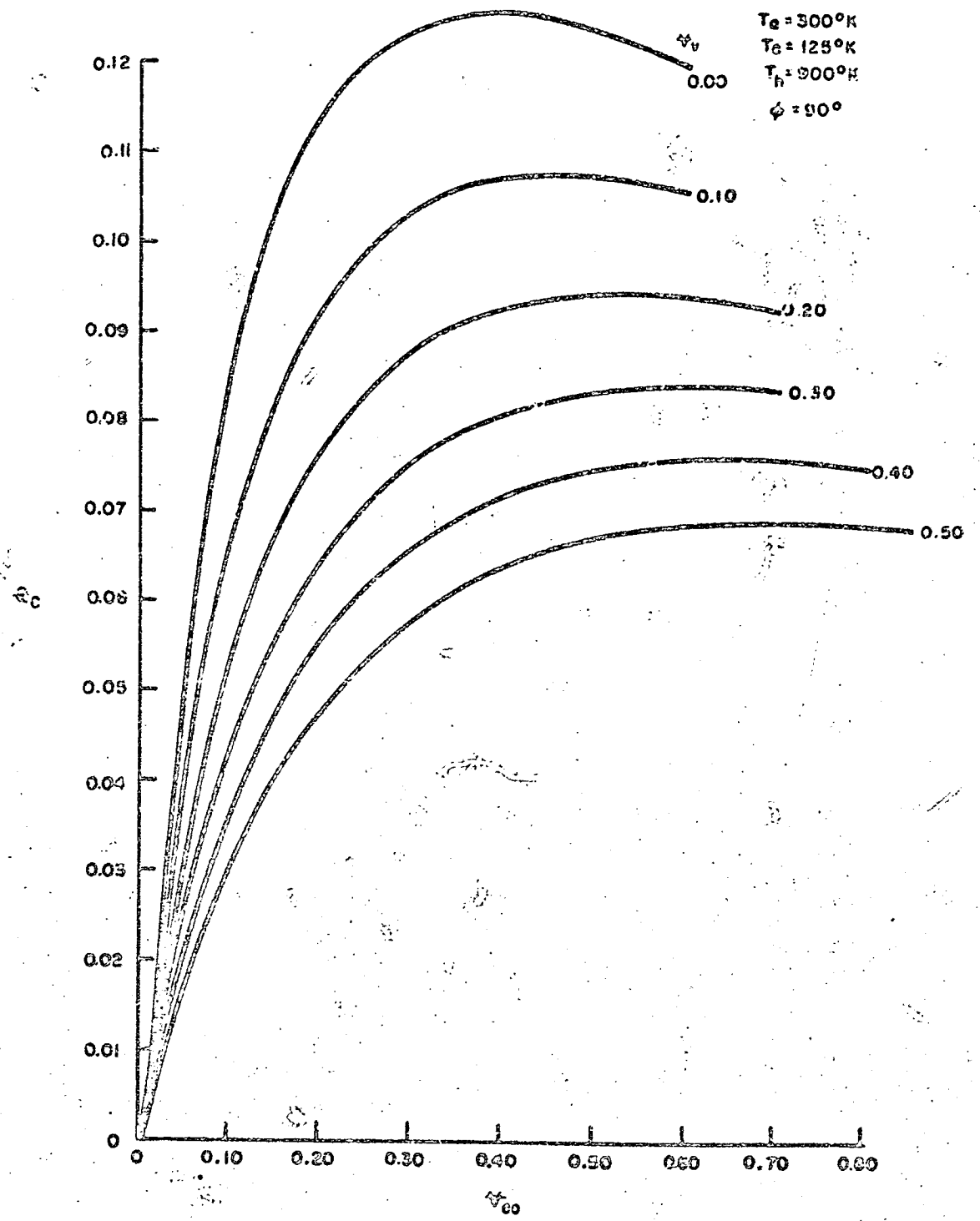



Fig. 3-9. Dimensionless ideal heat absorption per cycle as a function of swept volume ratio with temperature-weighted dimensionless void volume as a parameter for a $T_c$ of 125°K.

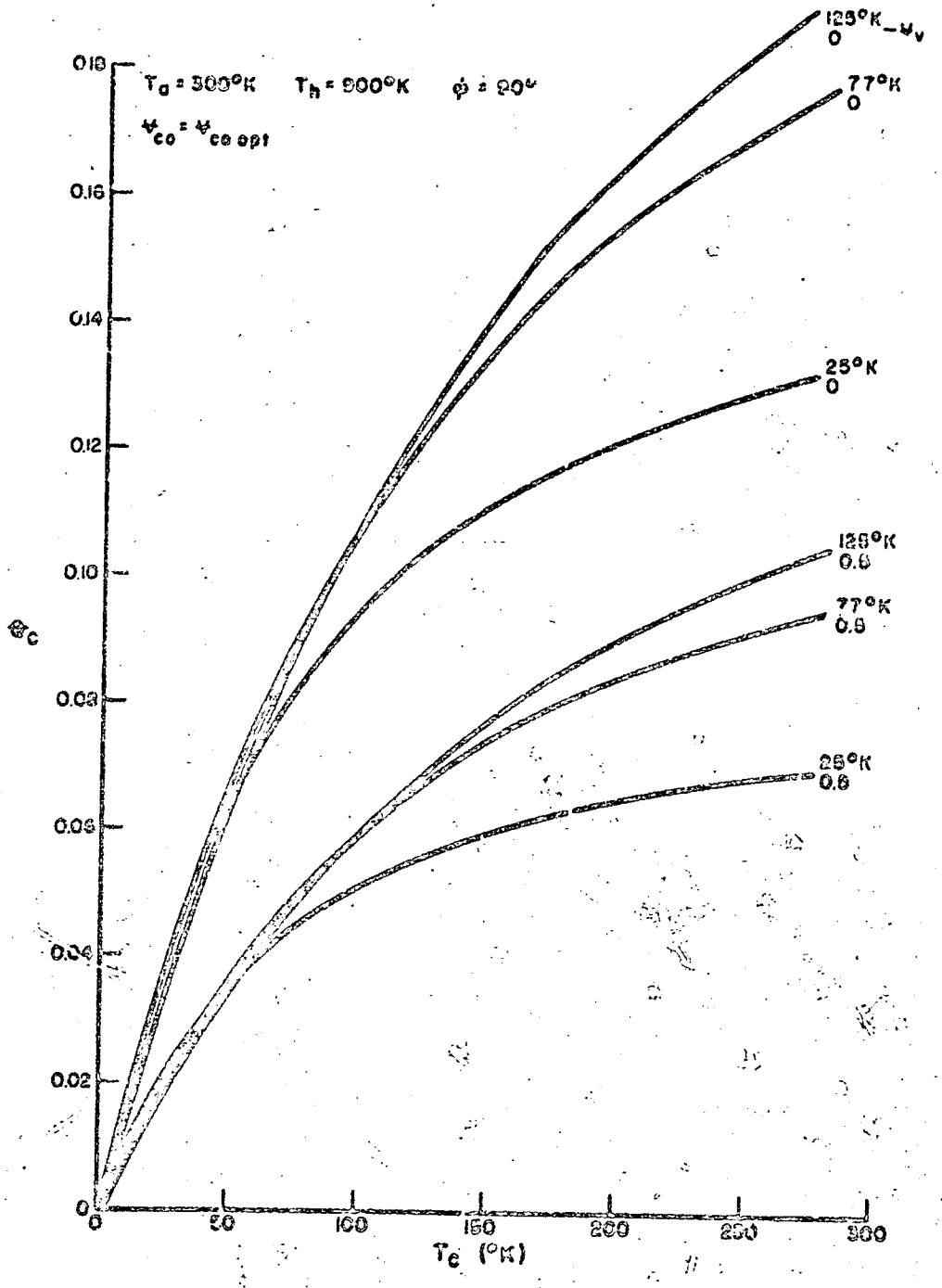



Fig. 3-10. Dimensionless ideal heat absorption per cycle as a function refrigeration temperature for various optimized refrigerators.

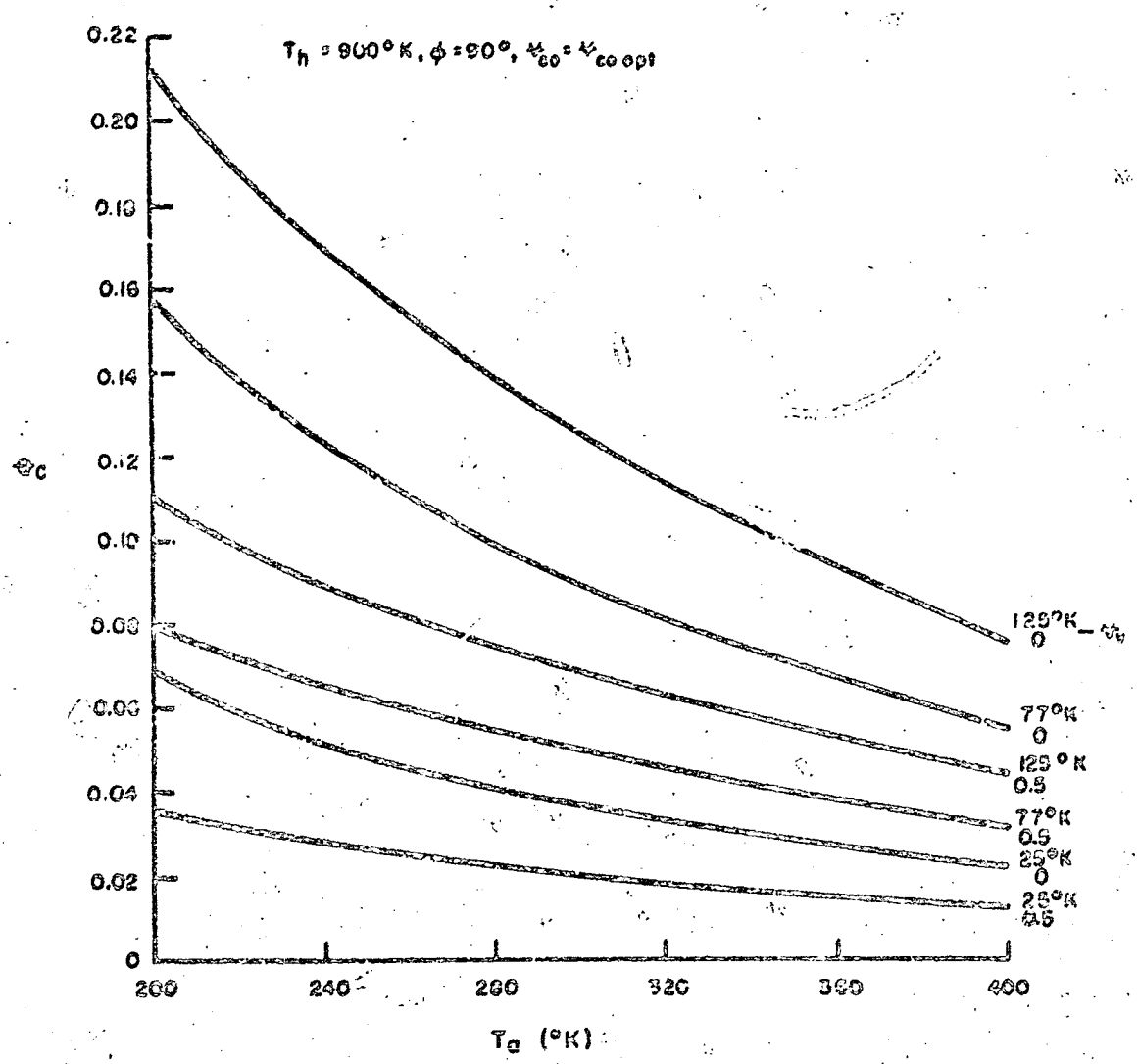



Fig. 3-11. Dimensionless ideal heat absorption per cycle as a function of ambient temperature for various optimized refrigerators.

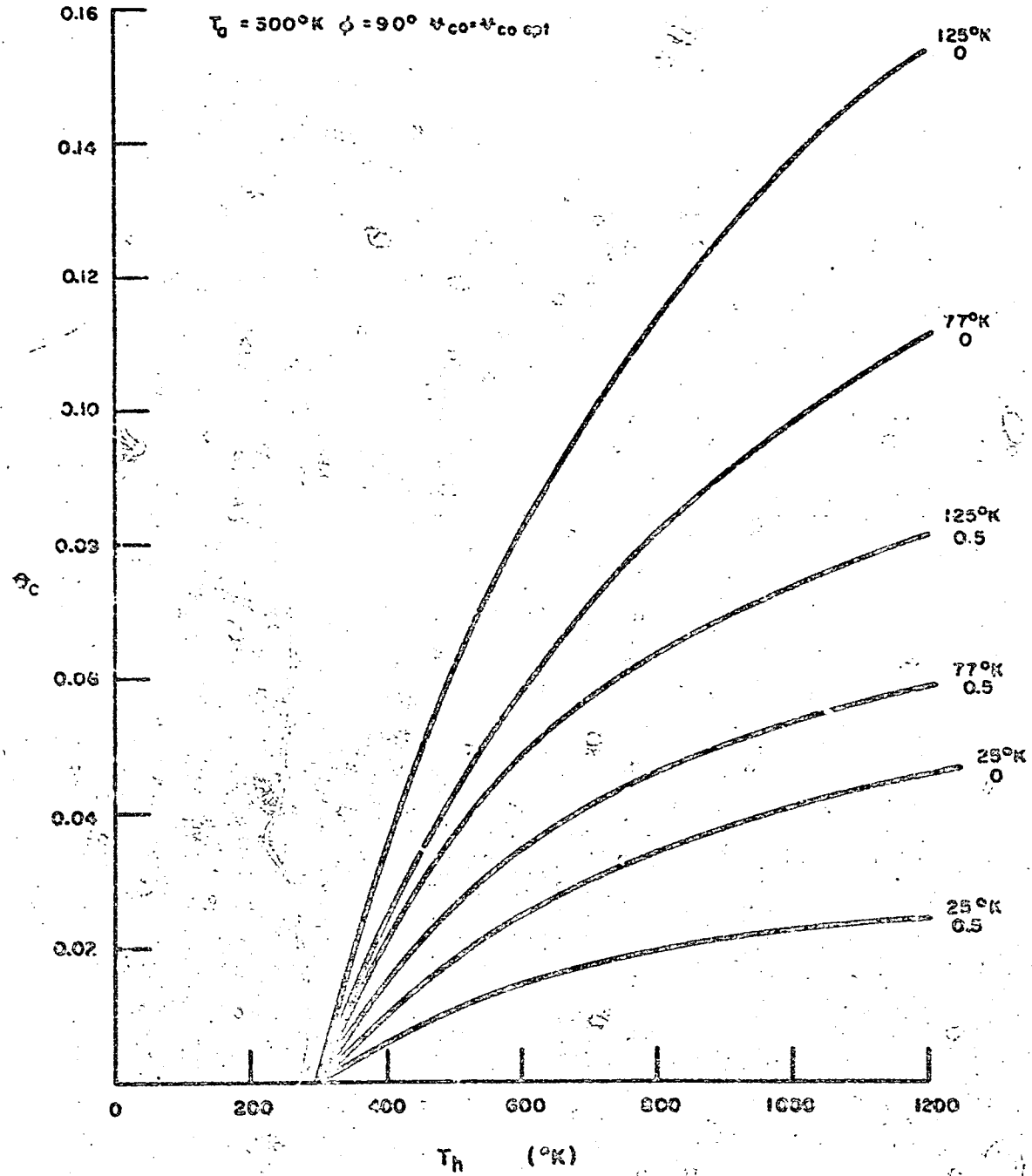



Fig. 3-12. Dimensionless ideal heat absorption per cycle as a function of heat source temperature for various optimized refrigerators.

Figure 3-10 shows how $\eta_c$ would vary from 0°K to 300°K. Note that the inherent flexibility to operate over broad temperature ranges is also displayed in this illustration. It is seen that the optimized 77°K and 25°K engines only slightly exceed the 125°K optimized output at the 77°K and 25°K temperature range.

Figure 3-11 displays $\eta_c$ versus $T_a$ from 200°K to 400°K. In general, it can be seen that $\eta_c$ is not overly sensitive to $T_a$. This is a desirable characteristic since space radiator weight can be traded off against VM performance to optimize the ICICLE System.

Figure 3-12 displays $\eta_c$ versus $T_h$ from 300°K to 1200°K. Theoretically, $\eta_c$ will continue to rise until $T_h = \infty$. However, as higher temperatures are used, the improved performance is achieved at the expense of increasing problems with materials, life, and reliability.

## C. VM SIZING PARAMETERS STUDY

### 1. Introduction

The ICICLE System concept can be applied to a variety of thermal loads and temperatures in various spacecraft systems. From a spacecraft system viewpoint, an ICICLE is a convenient purveyor of refrigeration to various components. In order to obtain this refrigeration, a price must be paid in size, weight and other factors to put an ICICLE on board a spacecraft. The question being answered here is the rather more limited one of the cost for the VM engine itself — specifically, the relationship between the purchase of net refrigeration and 1) net thermal power, 2) weight, 3) size, 4) mechanical actuation power, and 5) thermal efficiency.

It will be immediately clear to anyone who has considered the analysis of VM engines in some detail, that there is no optimum relationship between the various VM parameters. Therefore, a method of predicting VM parameters that is definitely achievable in the real world was required. In fact, it will be clear that the performance curves subsequently developed can undoubtedly be surpassed. Therefore, the parameters developed can be considered as conservative.

The method of approach used was to take the experimental results of an IR&D VM development program as the basis for developing the parameters. RCA's VM engine delivers 2.5 W at 77°K, 500 rpm, and 400 psig helium charge pressure. A reference design was established by removing the present water cooled crankcase and adding heat input/output flanges as described in Sec. 5. Therefore, this reference design is identical within the thermodynamic working space to the 2.5 W model in existence. Analytical methods based on the characteristics of the real engine were developed that predict the net refrigeration at 77°K and the net heat input at 900°K to within 9 percent and 16 percent, respectively. With confidence thus established in the analytical predictions, the preference design is scaled up and down by a scale factor $S_f$. Therefore, all VM parameters developed are relative to this independent variable scale factor $S_f$.

### 2. Description of Reference Design

The VM engine developed by RCA is shown in Fig. 3-13. A full size cross sectional view of the engine and cylinder covers is shown in Fig. 3-14. The displacer-regenerator drive shown in Fig. 3-14 is a crank drive. The engine currently has a Scotch yoke drive for crankcase void volume reduction. This Scotch yoke drive is shown in Fig. 3-15, which is full size, two view reference design. Figure 3-15 is representative of a 6-W VM engine for ICICLE when multiplied by a scale factor of $S_f = 1.14$. The general design of interface flanges is as shown, without all the details.

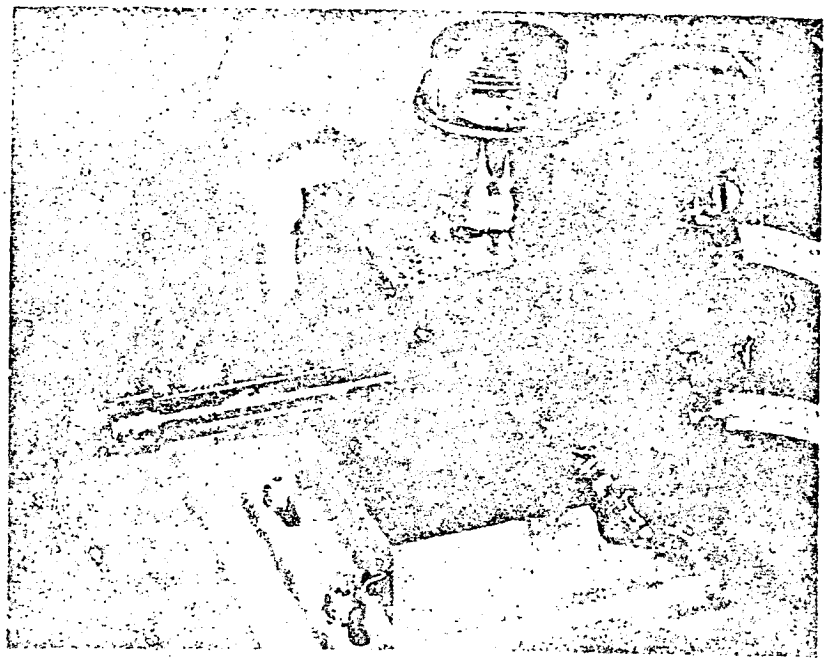


Fig. 3-13. RCA VM engine.

A summary of the pertinent characteristics of the VM model is presented below.

a. Physical Description

$T_h$ = 900°K - hot cylinder temperature

$T_a$ = 300°K - crankcase temperature

$V_{ho}$ = 11.01 $cm^3$ - hot swept volume

$V_{co}$ = 1.92 $cm^3$ - cold swept volume

$Y_p$ = 0.946 cm - stroke

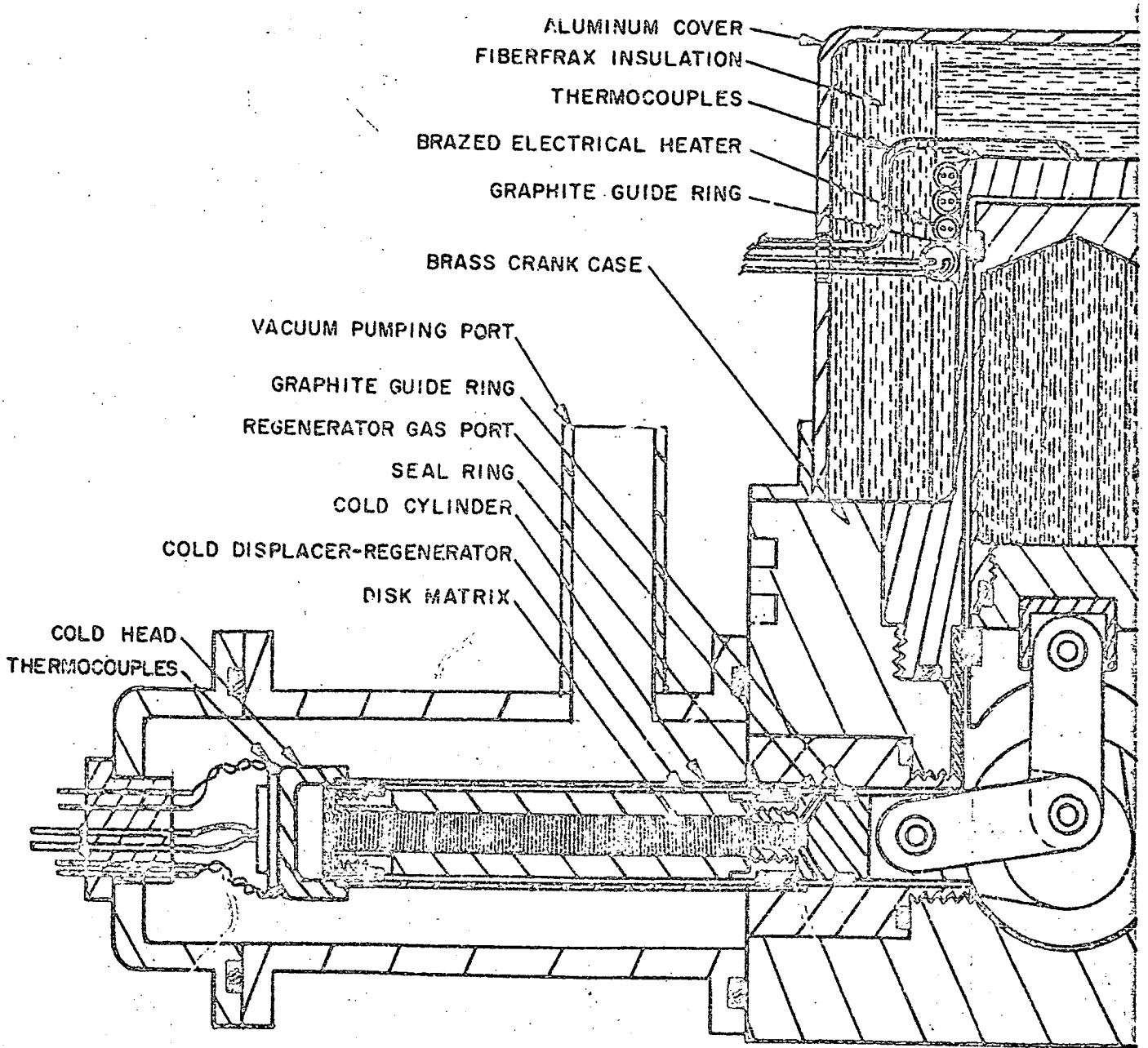
$V_t$ = 20.1 $cm^3$ - total gas volume

$\bar{V}_{vrh}$ = 0.0773 - void regenerator hot dimensionless, temperature weighted

$\bar{V}_{vrc}$ = 0.701 - void regenerator cold

$\bar{V}_{va}$ = 0.145 - void ambient (crankcase)

$\bar{V}_v$ = 0.923 - total void




Fig

FOLDOUT FRAME 7

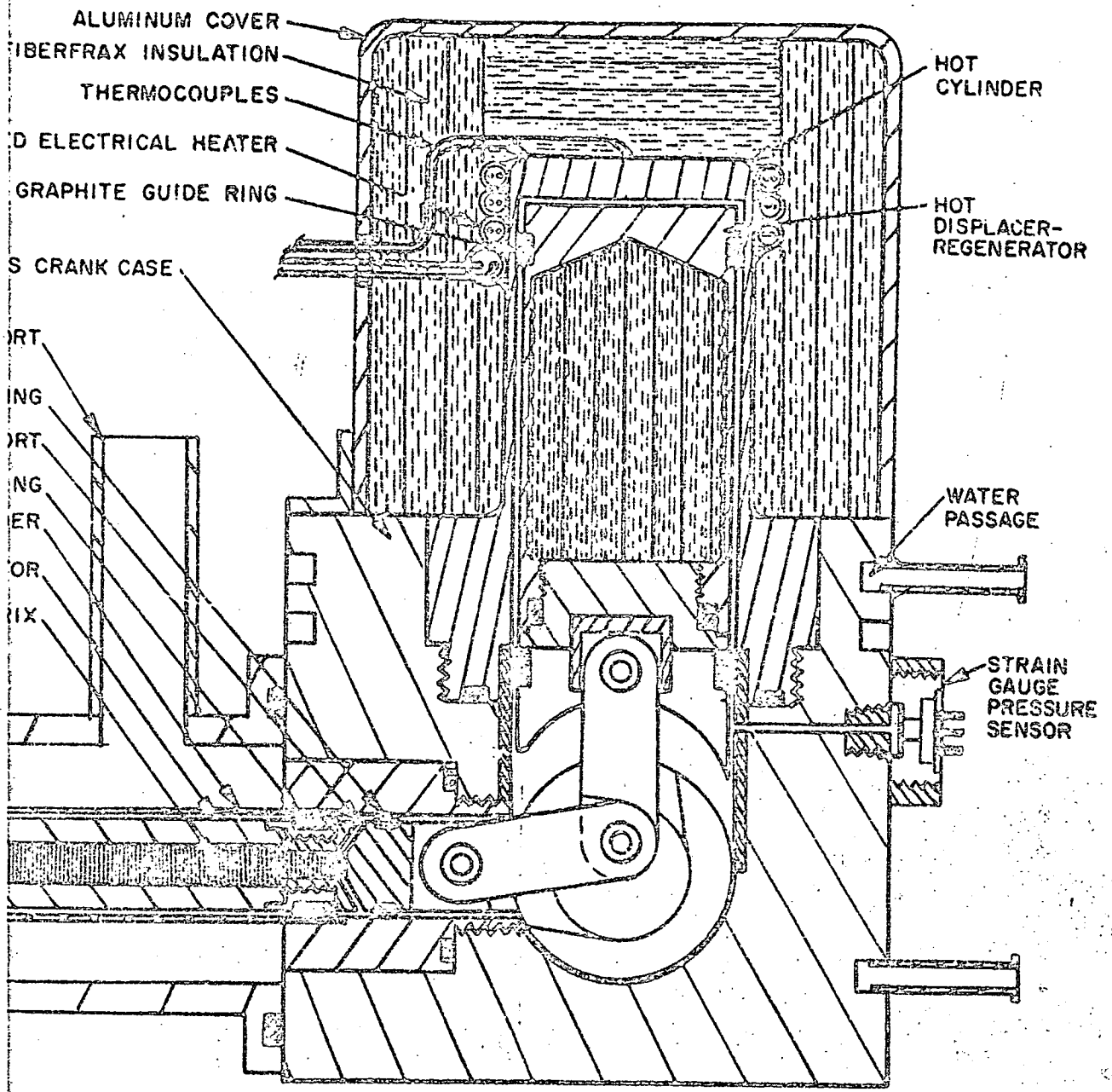
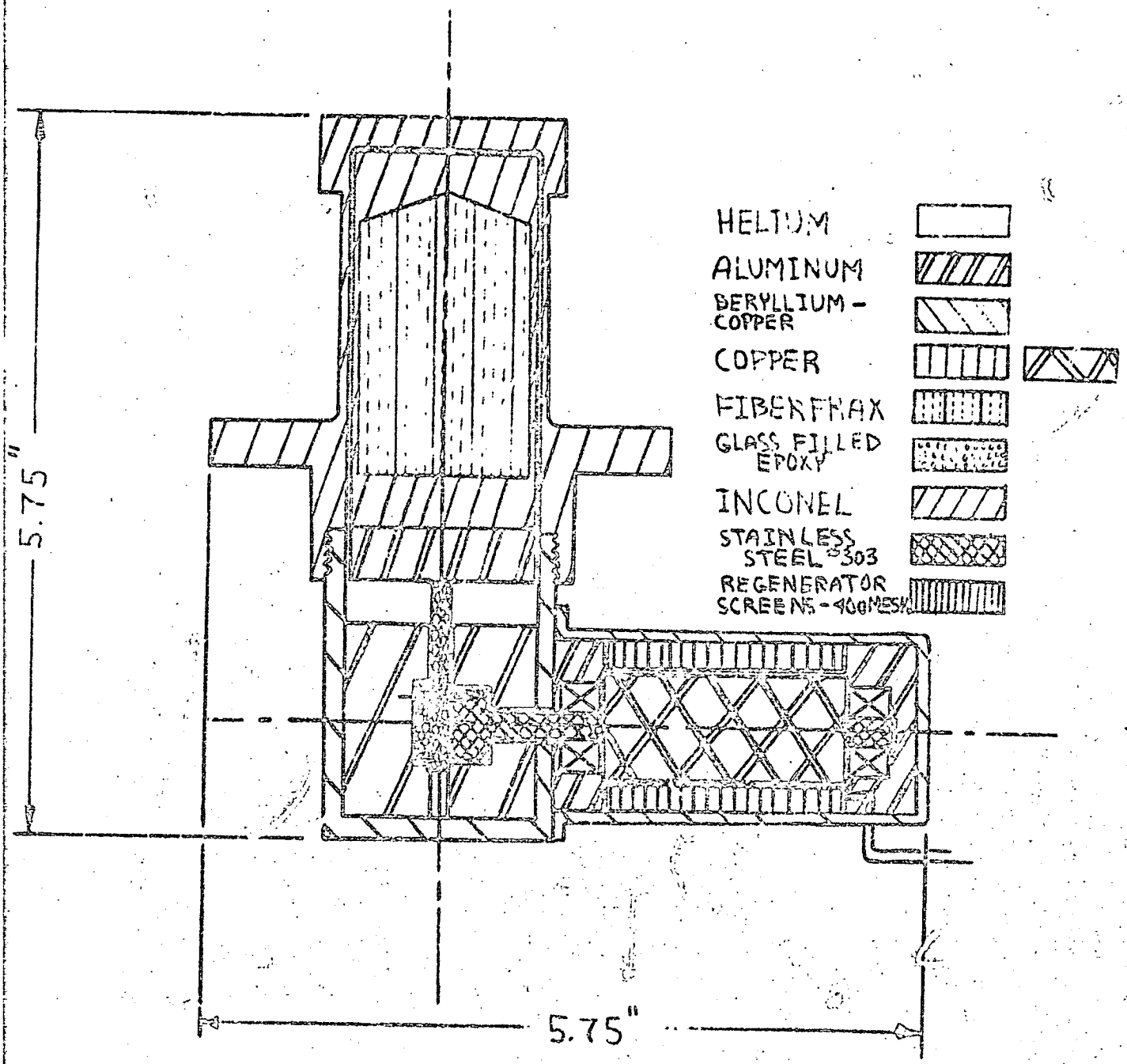



Fig. 3-14. RCA VM engine, full size cross-sectional view.

FOLDOUT FRAME 2




FOLDOUT FRAME 1

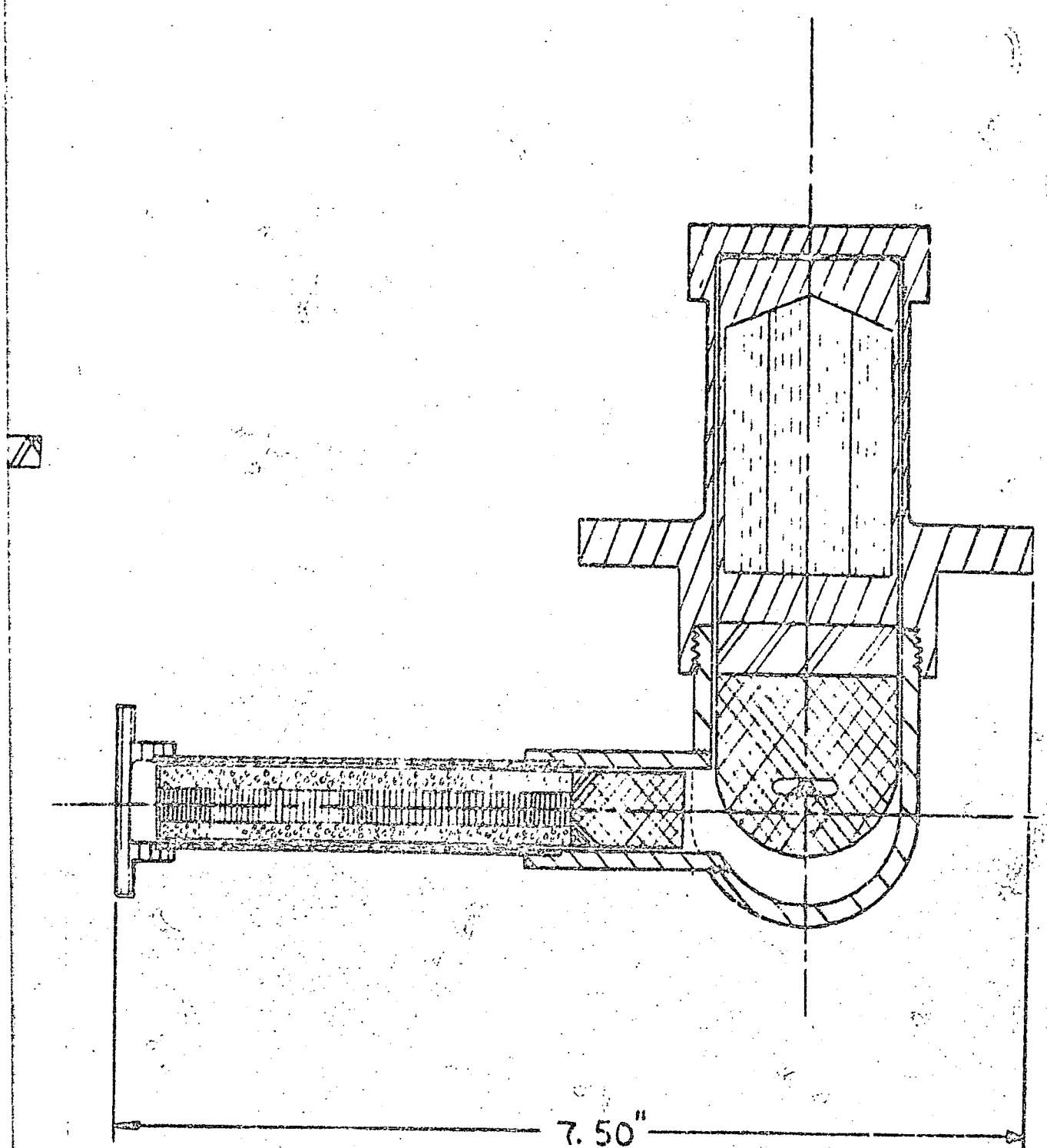



Fig. 3-15. Full size, two view reference design.



FOLDOUT FRAME 2

b. Performance Description

$N$ = 500 rpm - speed

$P_c$ = 400 psig - charge pressure

$\dot{Q}_{cnet}$ = 2.6 W - net refrigeration at 77° K

$\dot{Q}_{hnet}$ = 190 W - heat input at 900° K

Therefore, it is the intention of this study to describe how a physically linear scaling of this model at constant speed (500 rpm) and constant charge pressure (400 psig) will perform.

3. Mass Distribution in Reference Design

In order to perform the loss analysis detailed in Para. 4 below, it is necessary to know the gas charge mass distribution within the reference design as a function of crank position. As derived in Sec. 3.B, the pressure is related to crank position $\theta$ in Eq. 3-15. Then, the mass of gas in any volume can be found by the perfect gas law. The mass of gas in the cold swept volume is,

$$M_c = \frac{P V_c}{R T_c}$$

$$V_c = \frac{V_{co}}{2}(1 - \sin\theta) \qquad (3\text{-}18)$$

$$P = \frac{2 M_t R T_a}{a + b \sin\theta + c \sin\theta}$$

$$M_t = \frac{P_c V_t}{R T_a}$$

Where the charge pressure $P_c$, is measured with the entire engine held at the design temperature of the crankcase $T_a$.

These equations can be manipulated to form dimensionless quantities everywhere. Note that throughout Sec. III a horizontal bar through a variable denotes a dimensionless quantity.

$$\frac{M_c}{M_t} = \bar{M}_c = \frac{\bar{V}_{co}(1-\sin\theta) \cdot \dfrac{T_a}{T_c}}{\bar{a} + \bar{b}\cos\theta + \bar{c}\sin\theta} \qquad (3\text{-}19)$$

Where all quantities (except $M_c$) are as previously defined in Sec. 3.B. Note that $M_c$ is simply the fraction of the total mass that is in the cold space at that value of $\theta$.

By a similar derivation, the mass in the hot space is found to be

$$\frac{M_h}{M_t} = \mathcal{M}_h = \frac{(1-\cos\theta)\frac{T_a}{T_h}}{\mathcal{A} + \mathcal{B}\cos\theta + \mathcal{C}\sin\theta} \tag{3-20}$$

Likewise, the mass fraction in the crankcase or ambient space is

$$\frac{M_a}{M_t} = \mathcal{M}_a = \frac{2\mathcal{V}_{va} + 1 + \cos\theta + \mathcal{V}_{co}(1+\sin\theta)}{\mathcal{A} + \mathcal{B}\cos\theta + \mathcal{C}\sin\theta} \tag{3-21}$$

The mass fraction within the cold regenerator is

$$\frac{M_{rc}}{M_t} = \mathcal{M}_{rc} = \frac{2\mathcal{V}_{vrc}}{\mathcal{A} + \mathcal{B}\cos\theta + \mathcal{C}\sin\theta} \tag{3-22}$$

The mass fraction within the hot regenerator is

$$\frac{M_{rh}}{M_t} = \mathcal{M}_{rh} = \frac{2\mathcal{V}_{vrh}}{\mathcal{A} + \mathcal{B}\cos\theta + \mathcal{C}\sin\theta} \tag{3-23}$$

These mass fractions are plotted in Fig. 3-16 versus $\theta$ for the dimensionless volume distribution as it exists in the RCA VM engine and the reference design. Note that if all the dimensions of the reference design are scaled up or down, the relative volume distribution (that is, $\mathcal{V}_{co}$, $\mathcal{V}_{vrc}$, $\mathcal{V}_{vrh}$, $\mathcal{V}_{va}$ and $\mathcal{V}_v$) remain unchanged. Therefore, the mass fraction distribution versus crank angle is good for any scale factor $S_f$.

Now mass flow rate can be determined by simply taking the derivative with respect to $\theta$ of Eqs. 3-19 through 3-23. The flow rate versus crank angle is shown in Fig. 3-17. The symbol $\dot{\mathcal{M}}_c$, for example, means differentiation with respect to $\theta$:

$$\dot{\mathcal{M}}_c = \frac{d\mathcal{M}_c}{d\theta} \tag{3-24}$$

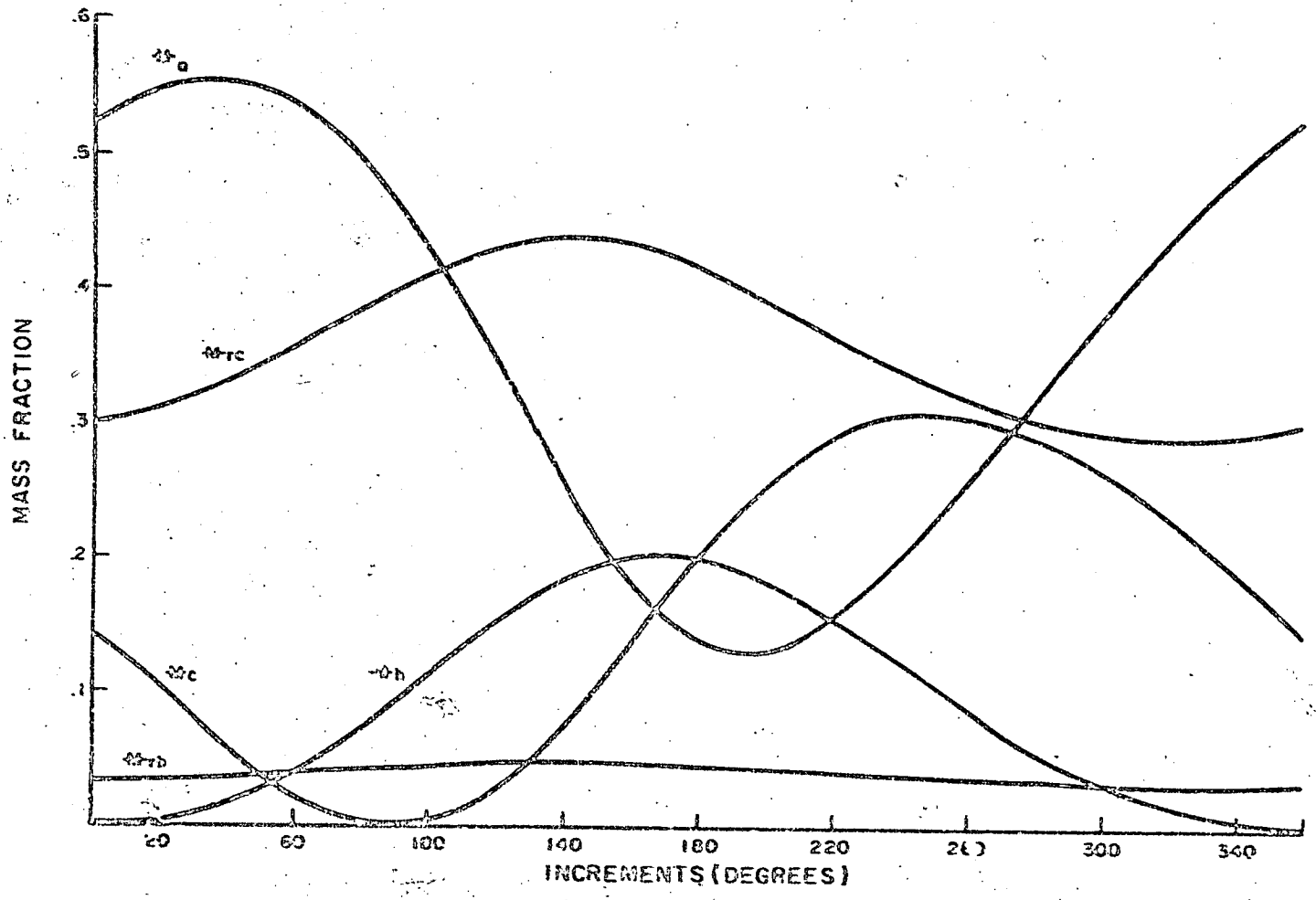



Fig. 3-16. Mass fraction distribution in reference design vs. crank angle.

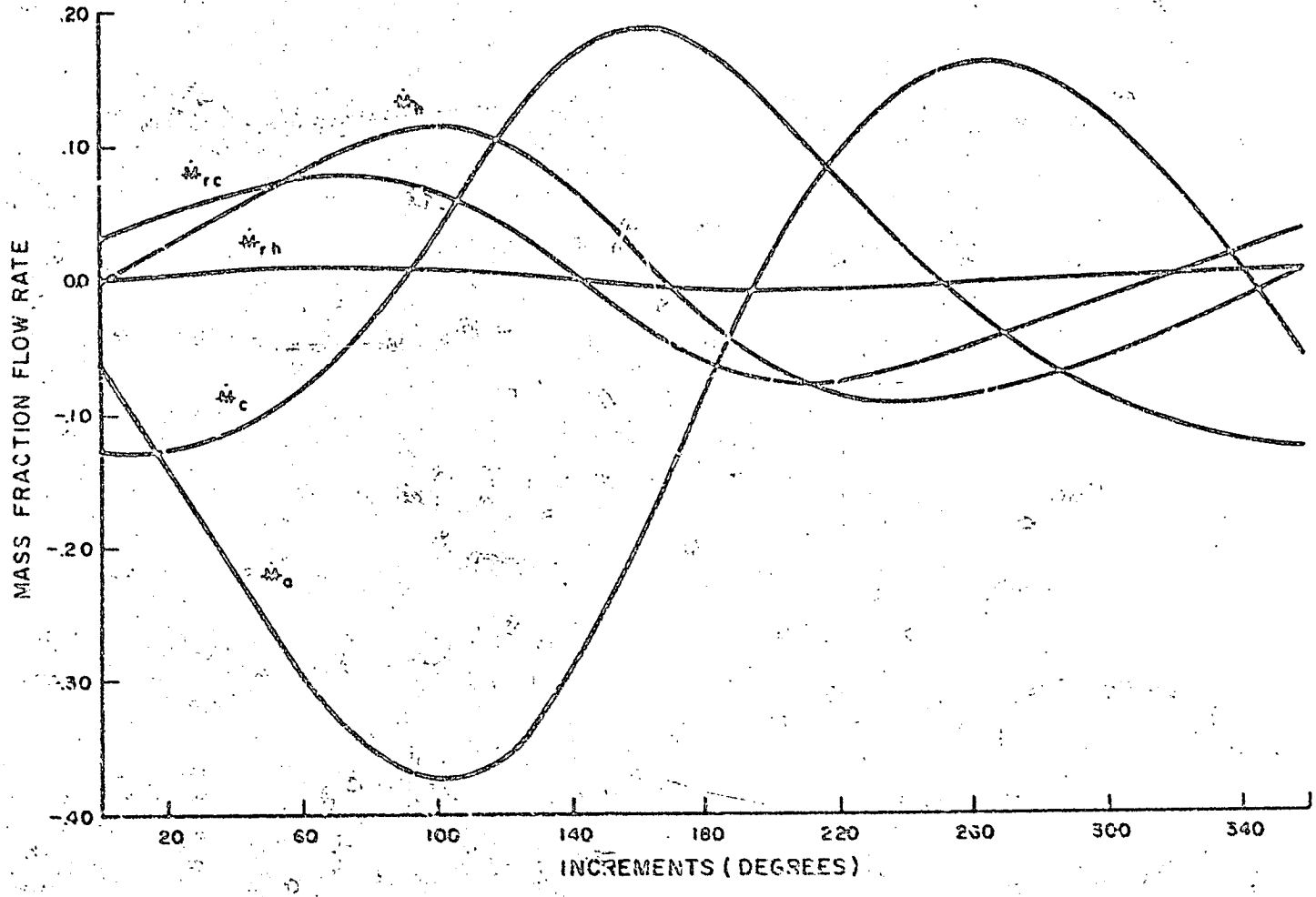



Fig. 3-17. Mass fraction flow rate in reference design vs. crank angle.

The conversion from dimensionless to dimensional quantities is, for example,

$$M_c = \frac{P_c V_t}{R T_a} \mathcal{M}_c \tag{3-25}$$

$$\frac{dM_c}{dt} = 2\pi N \frac{P_c V_t}{R T_a} \dot{\mathcal{M}}_c \tag{3-26}$$

Several important aspects of regenerator mass flow can now be deduced. Note the increasing mass in cold space must be the rate out of the regenerator cold (end) rcc:

$$\dot{\mathcal{M}}_{rcc} = \dot{\mathcal{M}}_c \tag{3-27}$$

Note also that the mass flow rate into the regenerator cold ambient (end) rca is the sum of the accumulation rate in the cold regenerator and the cold space:

$$\dot{\mathcal{M}}_{rca} = \dot{\mathcal{M}}_{rc} + \dot{\mathcal{M}}_c \tag{3-28}$$

where plus values are flow towards lower temperature and negative valves are mass flow along an increasing temperature gradient. The result plotted in Fig. 3-18 shows that from 62° to 80° flow is going into both ends of the regenerator simultaneously. Also, from 218° to 248° flow is going out from both ends of the regenerator simultaneously.

A similar analysis was conducted on the low void annular hot regenerator. Here $\dot{\mathcal{M}}_{rha}$ and $\dot{\mathcal{M}}_{rhh}$ are regenerator hot ambient end and regenerator hot end mass flows with plus flow going toward $T_h$. Due to the comparatively small void, the accumulation and flow lags are much smaller; this is shown in Fig. 3-19.

The pressure versus crank angle will be common for all scale factored reference designs. The dimensionless pressure versus crank angle is shown in Fig. 3-20. Note that dimensionless pressure was defined as:

$$\mathcal{P} = \frac{P}{\frac{M_o R T_a}{V_{ho}}} \tag{3-29}$$

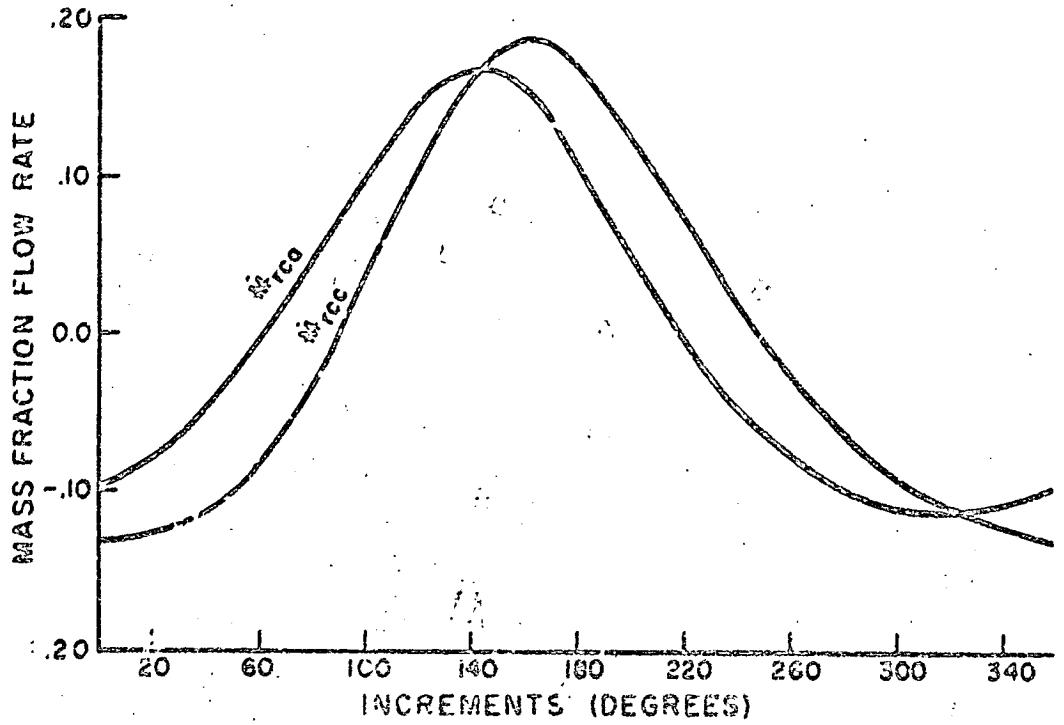



Fig. 3-18. Cold regenerator dimensionless flow rate at ambient ($\dot{m}_{rca}$) and cold ($\dot{m}_{rcc}$) ends.

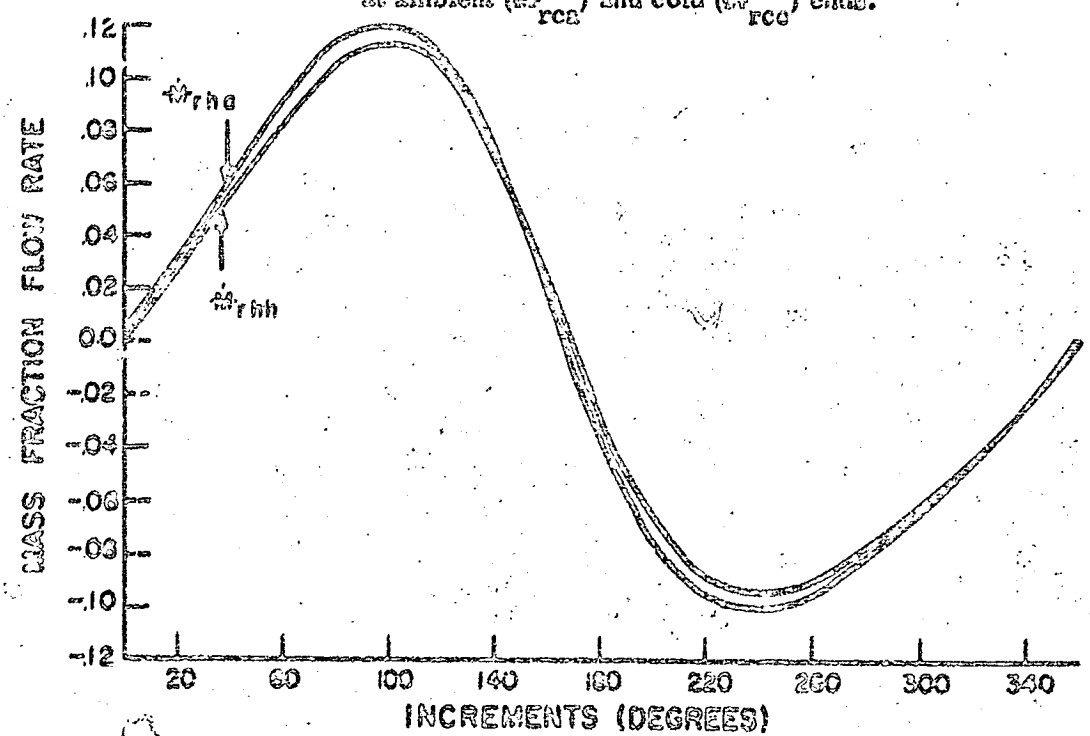



Fig. 3-19. Hot regenerator dimensionless flow rate at ambient ($\dot{m}_{rha}$) and hot ($\dot{m}_{rhh}$) ends.

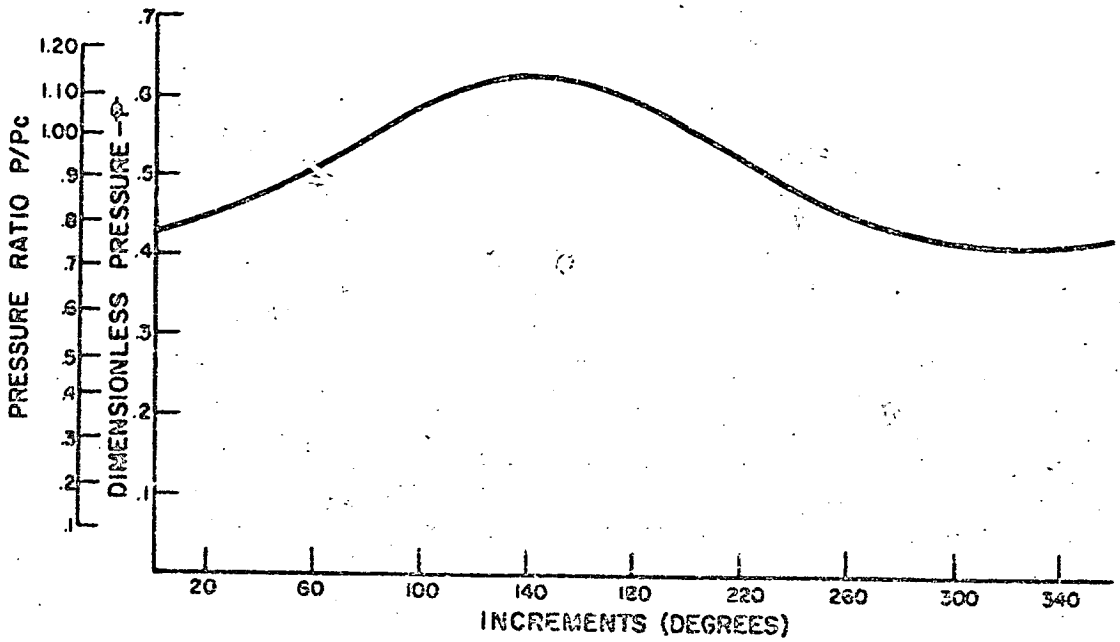



Fig. 3-20. Dimensionless pressure and pressure ratio vs. crank angle.

Manipulating this way

$$\Phi = \frac{P}{\frac{M_t R T_a}{V_{ho}}} = \frac{P}{\frac{P_c V_t}{V_{ho}}} = \frac{P}{P_c}\left(\frac{V_{ho}}{V_t}\right) \qquad (3\text{-}30)$$

$$\frac{P}{P_c} = \Phi\left(\frac{V_t}{V_{ho}}\right)$$

A quantity that relates instantaneous pressure P to charge pressure $P_c$ is more useful. Using the stated volume distribution and fixed temperatures (900, 300, 77°K) the ratio of $V_T/V_{ho}$ can be determined as $V_T/V_{ho} = 2.84$. Therefore, a second ordinate can be formed that is the pressure relative to charge pressure.

Therefore, Figs. 3-16 through 3-20 define mass, mass flow, and pressure for all scaled Reference Designs. The only factor neglected that makes this depart from a rigorous condition is flow pressure drop. However, the shaft power requirements (5.56 W) indicate flow pressure drop is very small compared to the pressure pulse ($P_{max} - P_{min}$).

## 4. Loss Equations for Hot and Cold Cylinder

In order to make the analysis of a VM engine tractable within the resources available, some simplifying assumption has to be made. If the results predicted by the simplification are consistent within experimentation, then confidence can be placed in it. The assumption is that ideal refrigeration is produced and that all loss mechanisms are mutually independent and cumulative. The error between predicted net refrigeration at 77° K and observed was only 9 percent. On the hot cylinder, the error is 16 percent. Therefore, within the context of most complex thermal systems, this agreement is quite good. The following subsections describe the relationships used.

### a. Regenerator Heat Transfer Loss

Assume that the cold regenerator matrix has a linear temperature profile from $T_a$ to $T_c$ which remains constant during a flow cycle. From heat exchanger theory, the heat added to the cold space $dQ_{rch}$ due to regenerator cold heat transfer limitations for a $dM_c$ can be shown to be

$$dQ_{rch} = I_{ec}\, C_p\, (T_a - T_c)\, dM_c \tag{3-31}$$

Where the regenerator inefficiency coid $I_{ec}$ is a function of the net transfer units of the regenerator.

$$I_{ec} = \frac{1}{\frac{NTU}{2} + 1} \tag{3-32}$$

$$NTU >> 1$$

$$I_{ec} = \frac{2}{NTU} \tag{3-33}$$

Now the NTU (and $I_{ec}$) is in turn a function of mass rate $M_c$ and flux $G_c$.

$$I_{ec} = \frac{2\dot{M}_c\, C_p}{hA} \tag{3-34}$$

where h is the gas-surface film heat transfer coefficient and A is the total matrix surface area. Kays and London[11] give an experimental relation between Stanton Number ($N_{st}$) and Reynolds Number ($N_{re}$) for crossed screen matrices. An analytical representation of this experimental curve is

$$(N_{st})\,(N_{pr})^{2/3} = 0.68\,(N_{re})^{-0.407} \tag{3-35}$$

For a constant Prandtl number for helium of 0.70, the relationship between h and $G_c$ can be found:

$$h = .864\ G_c\ C_p \left(\frac{4\,G_c\,r_h}{\mu}\right)^{-0.407} \tag{3-36}$$

Now if Eq. 3-36 is substituted in Eq. 3-34 and the known relationships between porosity $P_o$, hydraulic radius $r_h$, and surface/volume ratio $\alpha$ is used, one obtains

$$l_{ec} = \frac{2.32\ r_h \left(\frac{4\,G_c\,r_h}{\mu}\right)^{+0.407}}{L_{rc}} \tag{3-37}$$

where $L_{rc}$ is regenerator matrix length.

This dynamic relationship for $l_{ec}$ is placed in Eq. 3-31, along with the mass flow relationships from Para. 3 above. The following relationships result:

$$\dot{Q}_{rch} = \frac{Q_{rch}}{\frac{2.32\ r_h}{L_{rc}}\left(\frac{4\ r_h}{\mu}\right)^{0.407} C_p\,(T_a - T_c)\left(\frac{2N}{P_o r^2}\right)^{0.407}\left(\frac{P_c\,V_t}{RT_a}\right)^{1.407}} \tag{3-38}$$

$$d\dot{Q}_{rcc} = \dot{M}_c^{\,1.407}\,d\theta \tag{3-39}$$

The simplification of using $\dot{M}_{rcc}$ for the regenerator through flow was used. Integrating over the crank angles during which mass enters the cold space,

$$\dot{Q}_{rch} = \int_{\theta=90^\circ}^{\theta=247^\circ} \dot{M}_{rcc}\,d\theta = 0.1374 \tag{3-40}$$

Therefore, the regenerator cold heat transfer loss rate is

$$\dot{Q}_{rch} = \frac{2.32\ r_h \left(\frac{4r_h}{\mu}\right)^{0.407} C_p\,(T_a - T_c)}{L_{rc}}\left(\frac{2}{P_o r^2}\right)\left(\frac{N P_c V_t}{R\,T_a}\right)^{1.407} \dot{Q}_{rch} \tag{3-41}$$

The hot regenerator heat transfer loss $Q_{rhh}$ is a similar derivation except with fully developed laminar flow along essentially the whole annular regenerator length. Under this condition, the film coefficient is not a function of $G_h$ but is constant at a fixed Nusselt Number of Nu = 8.23.

Going through a similar derivation results in

$$\dot{Q}_{rhh} = \frac{\dot{Q}_{rhh}}{\dfrac{0.486\, C_p^{\,2}\,(D_o - D_i)\,(T_h - T_a)}{k(D_o + D_i)\,L_{rh}} \quad \dfrac{P_c V_t^{\,2}}{RT_a}} \tag{3-42}$$

$$\dot{Q}_{rhh} = \int_{\theta=0°}^{\theta=168°} \dot{M}_{rhh}\, d\theta = 0.0177 \tag{3-43}$$

Note that $D_o$ and $D_i$ are the outer and inner annulus diameters.

b. Regenerator Temperature Swing Loss

Now the effects of regenerator temperature swing will be considered, independently of regenerator heat transfer.

Figure 3-21 shows the matrix and gas temperature during heating and cooling and the swing. This presumes that all gas entering matrix at the ambient does so at $T_a$; likewise all entering the regenerator at the cold end does so at $T_c$. Note that $\Delta T_s$ is the temperature swing at the cold end of the matrix during a cycle. Therefore, effectively all the gas ($M_c$ max) during one cycle enters the cold space at the temperature excess of $\Delta T_s/2$.

The heat added to the matrix must equal that removed from the gas:

$$M_{cmax}\, C_p\, (T_a - T_c) = M_{matrix}\, C_p\, \Delta T_s$$

$$\Delta T_s = \frac{M_{cmax}\, C_p}{M_{matrix}\, C_p} (T_a - T_c) \tag{3-44}$$

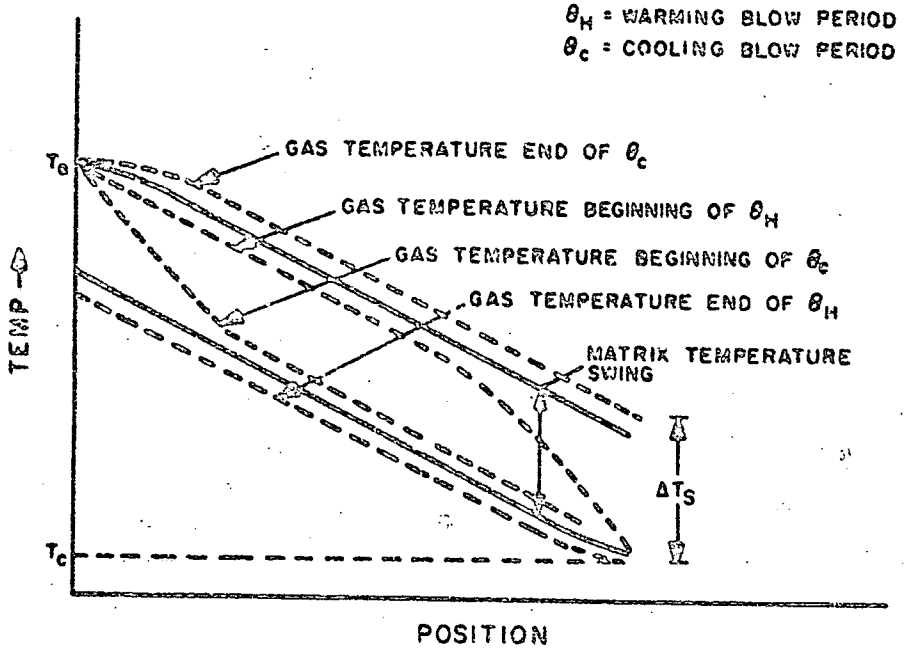



Fig. 3-21. Regenerator gas and matrix temperature profile at various times during a cycle.

This represents an amount of heat added to the cold space per cycle of

$$Q_{rcs} = M_{cmax}\, C_p\, \Delta T_s/2 \qquad (3\text{-}45)$$

Using Eq. 3-44 for $\Delta T_s$ and the speed N, the rate of heat added $\dot{Q}_{rcs}$ (due to regenerator cold swing) is:

$$\dot{Q}_{rcs} = N\, M_{cmax}\, C_p \left( \frac{M_{cmax}\, C_p}{M_{matrix}\, C_p} \right) (T_a - T_c) \qquad (3\text{-}46)$$

For the hot case, the problem is more complicated. A regenerative cycle cannot couple in the entire annular regenerator mass. In the cold regenerator, the 1 mil wire diameter allows the entire regenerator mass to participate in the temperature swing. By using Carslaw and Yaeger's analysis[12] of a sinusoidial heat flux applied to a semi-infinite solid, a solution can be found. For the thermal properties of a Inconel ($\rho$, Cp, k), the following relationship can be found for temperature swing of the regenerator surface:

$$\frac{\Delta T_s}{2} = \frac{0.10?\, C_p\, (T_h - T_a) \left( \frac{P_c\, V_t}{R T_a} \right)}{\pi\, (D_o + D_i)\, L_{rh}} \left( \frac{2\, \pi\, N}{\rho\, C_p\, k} \right)^{1/2} \qquad (3\text{-}47)$$

Therefore, the heat loss rate due to regenerator hot swing $\dot{Q}_{rhs}$ is

$$\dot{Q}_{rhs} = \frac{N\, M_{hmax}\, (0.102)\, C_p^{\,2}\, (T_h - T_a)}{\pi\, (D_o + D_i)\, L_{rh}} \left(\frac{P_c V_t}{R T_a}\right)\left(\frac{2\pi N}{\rho C_p k}\right)^{1/2} \qquad (3\text{-}48)$$

c. Shuttle Heat Transfer Loss

Heat is caused to deposit in the cold region by the oscillation of the cold displacer regenerator CDR or hot displacer regenerator within its respective cylinder (see Fig. 3-22).

As the illustration depicts, when the CDR is at BDC or any point to the right of midstroke, there is heat flow from the warmer cylinder wall to the CDR through the gas films. When the CDR is to the left of midstroke, the heat flow direction reverses and heat is deposited in the vicinity of the load. If the heat flow across the gas annulus is integrated around a complete cycle, the following expression results:

$$\dot{Q}_s = 0.585\; Y_p^{\,2}\; \frac{D k_g}{s}\; \frac{(T_a - T_c)}{L_c} \qquad (3\text{-}49)$$

d. Cylinder Wall Conduction Losses

The most pervasive loss is a wall conduction loss $Q_w$ in the pressure-carrying hot and cold cylinders and in the walls of the hot and cold displacer regenerators:

$$\dot{Q}_w = \frac{k_w A_w}{L_w} (T_a - T_c) \qquad (3\text{-}50)$$

The wall area $A_w$ is related to the pressure for the hot and cold cylinders:

$$A_w = 2\pi r \left(\frac{P_{max}\, r}{\sigma}\right) \qquad (3\text{-}51)$$

When this is placed in Equation 50

$$\dot{Q}_w = \frac{2\pi r^2 P_{max}}{\sigma}\; \frac{k_w}{Lw}\; (T_a - T_c) \qquad (3\text{-}52)$$

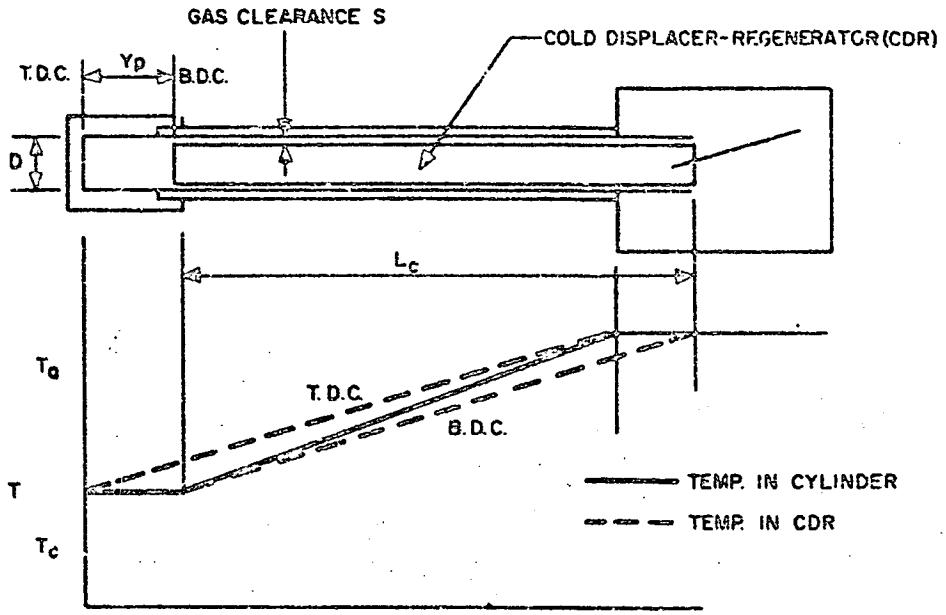



Fig. 3-22. Shuttle loss mechanism.

Equation 3-50 represents the reduction in useful heat pumping in the cold end and the increase in heat required of the hot end if the temperature $T_h$ and $T_a$ are substituted for $T_a$ and $T_c$ respectively.

e. Pumping Loss

The pumping loss occurs because of the alternate compression and decompression of the annular gas region between the CDR and cylinder wall. Assume that a perfect gas seal exists between the CDR skirt and cylinder and that the regenerator is a matrix in the center of the CDR. The mass (M) of gas in annular volume ($V_a$) is $V_a\rho$. The time rate of mass to or from the annulus (dM/dt) is $V_a$ $d\rho/dt$ or $V_a$ $(d\rho/dP)$ $(dP/dt)$. The average value of dM/dt may be approximated by:

$$\dot{M} = \frac{V_a (P_{max} - P_{min})\, N}{R\overline{T}} = \frac{D\pi\, L_c S (P_{max} - P_{min})\, N}{R\left(\frac{T_a + T_c}{2}\right)} \qquad (3\text{-}53)$$

The two walls of the annulus act as regenerators of efficiency ($n_r$) and inefficiency ($1-n_r$) so that the net pumping loss $\dot{Q}_p$ is:

$$\dot{Q}_p = \dot{\bar{M}}\ C_p\ (T_a - T_c)\ (1-n_r)$$

$$\dot{Q}_p = \frac{D\pi\ L_c S\ (P_{max} - P_{min})\ N\ C_p\ (T_a - T_c)\ (1-n_r)}{R\left(\frac{T_a - T_c}{2}\right)} \qquad (3\text{-}54)$$

The equations for shuttle loss and pumping loss are from Magee and Doering.[5] The regenerator heat transfer and matrix swing equations were developed for this study. The pumping loss could be analyzed by use of the same techniques developed for the regenerators. However, time did not permit its inclusion. In any case, the pumping loss exists only in the cold cylinder and is quite small.

Other loss mechanisms such as heat transfer $\Delta T$'s, and flow pressure drops should be considered eventually. At present, these are neglected.

## 5. VM Parameter Calculations

The following paragraphs describe how the relationships presented thus far are used to generate a specific figure.

### a. Net Refrigeration at 77°K vs. Scale Factor

Using the relationships derived for an ideal VM refrigerator with the parameters of the reference design laboratory model,

$\gamma_{co} = 0.1745$ $\qquad$ $T_h = 300°K$

$\gamma_v = 0.923$ $\qquad$ $T_a = 300°K$

$T_c = 77°K$

Obtains:

$\phi_c = 0.0232$

So at N = 500 rpm, $P_c$ = 400 psig

$$\dot{Q}_c = NP_cV_t\Theta_c = 11.11 \text{ W}$$

All the losses are computed as

$\dot{Q}_{cylinder}$ = 0.84 W - pressure cylinder

$\dot{Q}_{shuttle}$ = 2.02 W

$\dot{Q}_{pumping}$ = 0.20 W

$\dot{Q}_{rch}$ = 0.68 W - regenerator cold heat transfer

$\dot{Q}_{rcs}$ = 4.13 W

$\dot{Q}_{back}$ = 0.51 W - back conduction epoxy holder and screen matrix

$\dot{Q}_L$ = 8.38 W

The computed net is:

$$\dot{Q}_{cnet} = \dot{Q}_c - Q_L = 11.11 - 8.38 = 2.73 \text{ W}$$

The measured net was 2.49 W; therefore, the deviation is:

$$\text{Percent D} = \frac{2.73 - 2.49}{2.49} \times 100 = 8.9 \text{ percent}$$

Now all dimensions except regenerator specifics are considered to be variable, formed by multiplying a scale factor $S_f$ times the existing dimensions. The net exponent of $S_f$ for each loss is thus determined to be:

$$\dot{Q}_{cylinder} = 0.84\, S_f$$

$$\dot{Q}_{shuttle} = 2.02\, S_f$$

$$\dot{Q}_{pumping} = 0.20\, S_f^{4.2}$$

$$\dot{Q}_{rch} = 0.68\, S_f^{2.46}$$

$$\dot{Q}_{rcs} = 4.13\, S_f^{3}$$

$$\dot{Q}_{back} = 0.51\, S_f$$

Likewise the gross $\dot{Q}_c$ will be given by:

$$\dot{Q}_c = 11.11\, S_f^{\,3}$$

Carrying out this computation over a range of $S_f$ from 0 to 2 results in Fig. 3-23. Note that below $S_f = 0.72$, $Q_c$ net goes negative.

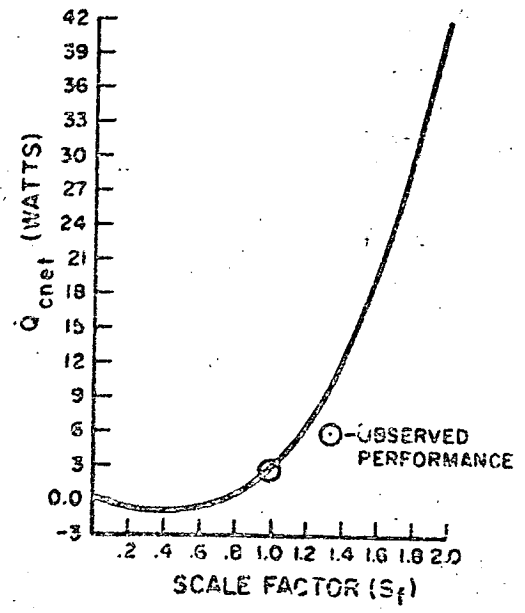



Fig. 3-23. $\dot{Q}_{c\ net}$ vs. scale factor.

b. Net Heat Input at 900° K vs. Scale Factor

Using all the loss relationships already discussed for the hot cylinder results in:

$\dot{Q}_{cylinder}$ = 14.9 W - hot cylinder wall

$\dot{Q}_{reg\ w}$ = 15.9 W - regenerator wall

$\dot{Q}_{rins}$ = 10.1 W - regenerator fiberfrax insulation

$\dot{Q}_{shuttle}$ = 21.6 W - shuttle loss

$\dot{Q}_{rhi}$ = 33.4 W - regenerator hot heat transfer

$\dot{Q}_{rhs}$ = 0.6 W - regenerator hot swing

$\dot{Q}_{h}$ = 48.4 W - ideal cycle input

$\dot{Q}_{L}$ = 144.9 W - total calculated applicable losses

$\dot{Q}_{oins}$ = 22.3 - outward air insulation loss

167.2 W

Note the $Q_{oins}$ is the computed outward insulation loss due to operation with air filled fiberfrax. In space with multifoil insulation, this loss is reducible to less than 1 W.

The measured electrical power input was 190 W. Subtracting the outward insulation loss, the deviation is

$$\text{Percent D} = \frac{190-22.3-144.9}{144.9} \times 100 = 16 \text{ percent}$$

The relationships as functions of scale factors are:

$\dot{Q}_{cylinder} = 14.9\ S_f$

$\dot{Q}_{reg\ w} = 15.9\ S_f$

$\dot{Q}_{rins} = 10.1\ S_f$

$\dot{Q}_{shuttle} = 21.6\ S_f$

$$\dot{Q}_{rhh} = 33\, S_f^{\,5}$$

$$\dot{Q}_{rhs} = 0.6\, S_f^{\,4}$$

$$\dot{Q}_{h} = 48.4\, S_f^{\,3}$$

Carrying out this computation over a range of $S_f$ from 0-2 results in Fig. 3-24.

c. Weight vs. Scale Factor

Using the material and size as shown in the two-view reference design, the weight is computed to be 5 lb. The torque demand by the VM is expected to go up with $S_f^3$, and the torque supply by the motor will go up as $S_f^3$. Therefore, the total weight of the VM and drive motor will go up as $S_f^3$. This results in Fig. 3-25.

d. Mechanical Power vs. Scale Factor

The torque demand vs. speed was measured on the laboratory model VM engine. A straight line of torque vs. N resulted with a zero speed intercept of 7.6 in-lb$_f$ and 13.6 in-lb$_f$ at 500 rpm. The slope is indicative of flow pressure drops, and the intercept is indicative of running friction.

It can easily be shown that running friction and flow pressure drops in a scaled design will all go as the cube of the scale factor. The shaft power of the laboratory model is $P_s = 5.56$ W. Using a typical motor efficiency of 50 percent gives motor electrical input. This relationship is shown in Fig. 3-26.

e. Thermal Efficiency vs. Scale Factor

By dividing the net heat input $Q_h$ net by the net refrigeration $Q_c$ net, the efficiency versus scale factor is determined. This is shown in Fig. 3-27.

f. Conclusion

All parameters displayed were related to existing RCA VM engine performance. Many methods of improvement are obvious with sufficient effort. The parameters are judged to be attainable and conservative.

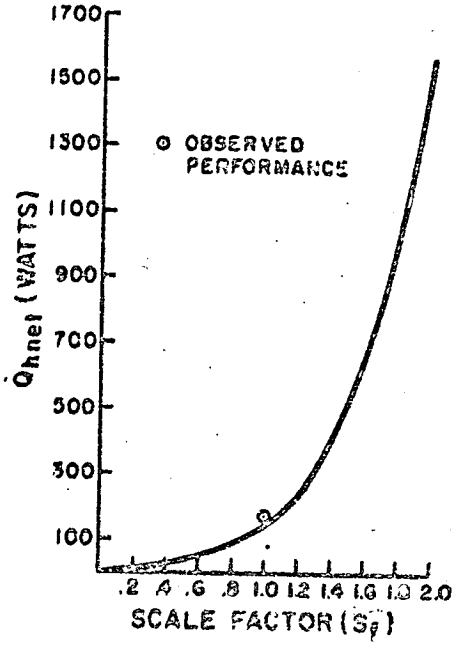



Fig. 3-24. $\dot{Q}_{h\ net}$ vs. scale factor.

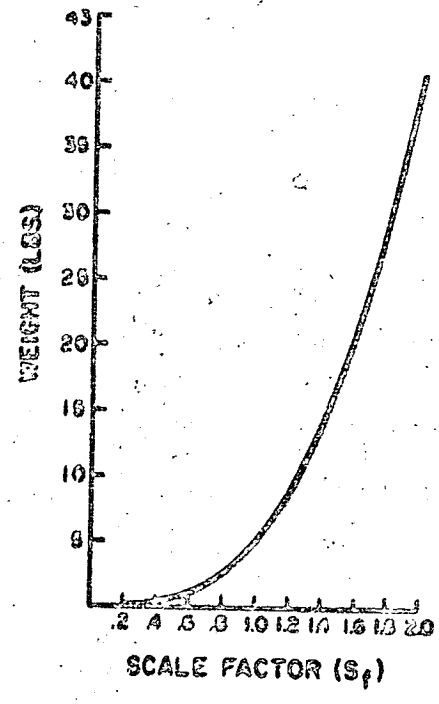



Fig. 3-25. Weight vs. scale factor for VM.

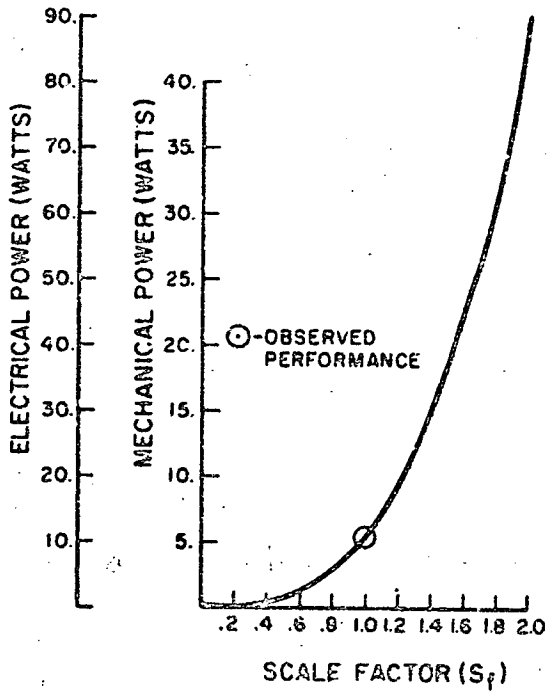



Fig. 3-26. Power vs. scale factor.

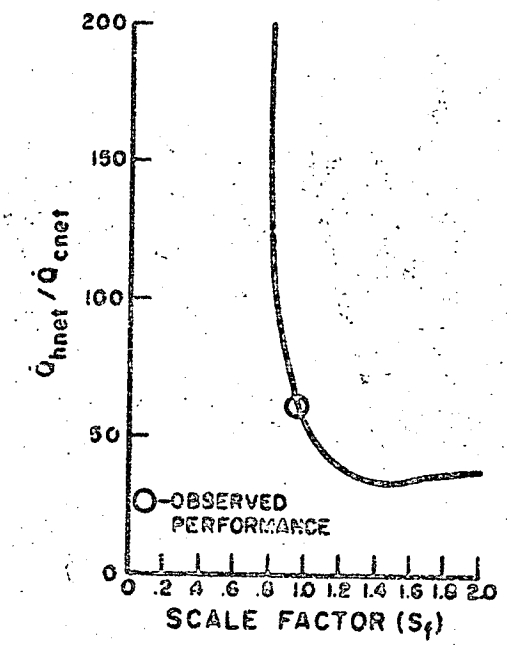



Fig. 3-27. $\dot{Q}_{h\ net}/\dot{Q}_{c\ net}$ vs. scale factor.

## D. SYMBOL GLOSSARY

$A_w$ - Area of the wall normal to heat flow

CDR - Cold displacer regenerator

BDC - Bottom dead center

COP - Coefficient of performance

$D_h D_c$ - Internal diameter of hot or cold cylinder

$D_r$ - Regenerator ID

$F_f$ - Friction force

HDR - Hot displacer regenerator

$g_c$ - Conversion factor in Newton's law of motion; equals 32.2 ft x (lb matter)/(s) (s) (lb force)

$h$ - Film heat transfer coefficient, heat rate per unit area, per unit temperature difference

$\overline{h}$ - Position and time average film heat transfer coefficient in some defined region

$h_e$ - Enthalpy of convected mass per unit mass

$h_x$ - Average film heat transfer coefficient in the region X

$I_e$ - Regenerator inefficiency

$K$ - Overall conductance, heat rate per unit temperature difference

$k_g$ - Thermal conductivity of the gas

$L_c$ - Length of the cylinder

$k_w$ - Thermal conductivity of the wall

$L_w$ - Length of the wall

$L_r$ - Regenerator length

$L_s$ - Length of seal, regenerator to cylinder

$M$ - Mass

$\dot{M}_a$ - Annulus mass flow rate

$\dot{M}_r$ - Regenerator mass flow rate

$N$ - Revolutions per unit time of the VM engine

$\bar{P}$ - Dimensionless pressure

$P_c$ - Charge pressure with all of VM engine at $T_a$

$P$ - Pressure

$P_{max}$ - Maximum pressure in one cycle of a VM engine

$P_{min}$ - Minimum pressure in one cycle of a VM engine

$P_r$ - Prandtl number

$\Delta P$ - Total pressure drop through the regenerator

$\bar{Q}_a$ - Dimensionless, ideal, heat rejection per cycle at $T_a$

$Q_a$ - Ideal heat rejection, per cycle at $T_a$

$\dot{Q}_a$ - Ideal heat rejection rate, at $T_a$

$\dot{Q}_{a\ net}$ - Net heat rejection rate of a real VM engine at $T_a$

$\bar{Q}_c$ - Dimensionless, ideal, heat absorption per cycle at $T_c$

$Q_c$ - Ideal heat absorption, per cycle at $T_c$

$\dot{Q}_c$ - Ideal heat absorption rate, at $T_c$

| | |
|---|---|
| $\dot{Q}_{c\ net}$ | - Net refrigeration rate of a real VM engine at $T_c$ |
| $\dot{Q}_f$ | - Frictional heat generation rate |
| $\dot{Q}_{HT}$ | - Equivalent loss rate due heat transfer $\Delta T$ from working fluid to the VM engine walls |
| $\bar{Q}_h$ | - Dimensionless, ideal, heat absorption per cycle at $T_h$ |
| $Q_h$ | - Ideal heat absorption, per cycle at $T_h$ |
| $\dot{Q}_h$ | - Ideal heat absorption rate, at $T_h$ |
| $\dot{Q}_{h\ net}$ | - Net heat absorption rate of real VM engine at $T_h$ |
| $\dot{Q}_L$ | - Loss heat rate, sum of all losses to cold or hot cylinder for a given VM configuration and temperature |
| $\dot{Q}_p$ | - Pumping heat transfer loss rate |
| $\dot{Q}_r$ | - Regenerator heat loss rate |
| $\dot{Q}_s$ | - Shuttle heat transfer rate |
| $\dot{Q}_w$ | - Wall heat conduction rate |
| R | - Universal gas constant |
| r | - Internal radius of a thin walled pressure carrying cylinder |
| S | - Radial gas clearance of CDR or HDR to cylinder |
| t | - Time |
| $T_a$ | - Ambient, crank case heat rejection temperature |
| $T_c$ | - Cold cylinder, refrigeration temperature |
| TDC | - Top dead center |
| $T_h$ | - Hot cylinder, heat source temperature |
| $T_{Rc}$ | - Effective cold regenerator temperature |

$T_{Rh}$ - Effective hot regenerator temperature

$U_s$ - Gas stream velocity

$U$ - Total energy contained within a control volume

$\forall_a$ - Dimensionless, instantaneous ambient volume

$V_a$ - Instantaneous total ambient volume

$\dot{V}$ - Average gas velocity

$\dot{V}_a$ - Average gas velocity in the annulus

$\dot{V}_r$ - Average gas velocity in the regenerator

$\forall_c$ - Dimensionless instantaneous cold volume

$V_c$ - Instantaneous total cold volume

$\forall_{co}$ - Cold swept volume to hot swept volume ratio

$V_{co}$ - Total cold swept volume

$\forall_h$ - Dimensionless instantaneous hot volume

$V_h$ - Instantaneous total hot volume

$V_{ho}$ - Total hot swept volume

$V_t$ - Total volume in a VM engine

$V_v$ - Total void volume in engine

$\forall_v$ - Temperature weighted, dimensionless void volume

$V_{vc}$ - Clearance or void volume at TDC for CDR

$V_{vh}$ - Clearance or void volume at TDC for HDR

$V_v/T_v$ - The summation of all void elements divided by the temperature of that void element

$V_{vRc}$ - Total void volume in cold regenerator

$V_{vRh}$ - Total void volume in hot regenerator

$W$ - Number of regenerator screens per unit length

$Y_p$ - HDR or CDR stroke length

$Z$ - Clearance, regenerator to cold head for improved heat transfer

$Z_1$ - Clearance, regenerator seal to cylinder ID

$\alpha$ - Crankshaft angle from CDR pivot to HDR pivot

$\beta$ - Angle from hot cylinder to cold cylinder

$\theta$ - Instantaneous angle from hot cylinder center line to CDR crankshaft pivot

$\mu$ - Dynamic viscosity of the working fluid

$\eta_r$ - Regenerator efficiency

$\rho$ - Gas mass density

$\sigma$ - Design stress

$\gamma$ - Kinematic viscosity of the working fluid

$\phi$ - Net phase angle by which the HDR leads the CDR

## E. REFERENCES FOR SECTION 3


1. E. F. Yendall, "A novel refrigerating machine," Advances in Cryogenic Engineering, vol. 2, pp. 188-196, 1960.

2. F. F. Chellis and W. H. Hogan, "A liquid-nitrogen-operated refrigerator for temperatures below 77° K," Advances in Cryogenic Engineering, vol. 9, pp. 545-551, 1964.

3. R. White and W. J. Uhl, Jr., "Vuilleumier Heat Driven Cryogenic Refrigerator," Air Force Flight Dynamics Laboratory, January 1967.

4. F. T. Turner and W. H. Hogan, "Small cryopump with integral refrigerator," The Journal of Vacuum Science and Technology, vol. 3, no. 5, pp. 252-257.

5. F. N. Magee and R. D. Doering, "Vuilleumier Cycle Cryogenic Refrigerator Development," Technical Report AFFDL-TR-68-67, August 1968.

6. T. T. Rule and F. B. Quale, "Steady state operation of the idealized vuilleumier refrigerator," 1966 Cryogenic Engineering Conference, Case Western Reserve University, Paper J-2, August 1966.

7. William E. Gifford, "Basic Investigation of Cryogenic Refrigeration Methods," Technical Report AFFDL-TR-66-23, May 1966.

8. William E. Gifford, "Basic Investigation of Cryogenic Refrigeration Methods," Technical Report AFFDL-TR-67-41, July 1967.

9. R. B. Flemming, "Regenerators in Cryogenic Refrigerators," Technical Report AFFDL-TR-66-143, September 1966.

10. W. L. Rogers and L. H. McClintock, "Plasma needle arc delves into tomorrow," Linde Distributor Progress, vol. 3, no. 3.

11. W. M. Kays and A. L. London, Compact Heat Exchangers, 2nd ed. New York: McGraw-Hill, 1964.

12. H. Carslaw and J. Yaeger, Conduction of Heat in Solids, Oxford Press, 1959.

Section 4

# RADIOISOTOPE FEASIBILITY


*Summary*

*The selection of a heat source for the ICICLE reduces to isotope or a solar collector for long life applications. From purely technical considerations the isotope is the preferred method for providing heat. Size, weight, complexity, reliability and life are much more attractive with the isotope source. The safety and nontechnical criteria which impact on the feasibility of isotope use are being addressed in such programs as the SNAP series, Transit spacecraft, and Pioneer spacecraft. It appears that satisfactory solutions are being achieved and that feasibility will not be limited by these factors.*

*Projected mission length will limit the choice of fuels to $Pu^{238}$ or $Pm^{147}$ for space applications. The physical characteristics of $Pu^{238}$ make it the most attractive choice for use as an ICICLE heat source. Its half life is 82 years so that its power input can be considered constant for the two to five year ICICLE lifetime. Since $Pu^{238}$ is an alpha emitter with a high power density, it can be packaged into a compact, lightweight heat source. Heat sources using this fuel and a refractory shell design are currently undergoing test for launch approval for the Transit and Pioneer programs. $Pu^{238}$ is the only material with which such testing and development have been done, and $Pu^{238}$ is the only material which is presently being developed in the power range required for an ICICLE application.*

*A radioisotope heat source using $Pu^{238}$ fuel appears to be feasible for the ICICLE application on the basis of performance, size, weight and life. This feasibility is supplemented by the existence of a body of developmental and test data for use of a similar capsule in a space application.*


An important aspect of the feasibility of the ICICLE involves the feasibility of the radioisotope heat source. Generally, there are three questions which must be answered when one is considering the use of an isotope. First, the feasibility of meeting the technical requirements of the system must be satisfied. Such factors as thermal output, operating temperature, size, weight and life must be met to establish feasibility. Secondly, a study of availability and cost of the preferred isotope must be made to determine whether the mission has sufficient priority to merit the use of the limited supply of certain isotopes. In addition, more available fuel forms must be evaluated to determine whether the penalty of poorer technical characteristics compromises mission performance unacceptably. Thirdly, a specific mission analysis must

be completed to establish suitable safety requirements and test procedures. Feasibility is established if adequate containment and shielding technology exists to meet the requirements of a mission.

The technical feasibility of using an isotope for the ICICLE system is, in our opinion, an established fact. Many isotope sources have been developed for use in space. Typical examples are given by Gerwin.[1*] Of the systems listed by Gerwin, the STEP II built by Sanders Nuclear Corporation would almost exactly meet the requirements of ICICLE. STEP II is a thermoelectric converter which has an electrical output of 10 W when driven by a plutonium 238 heat source which generates 250 W. The heat source is in the form of plutonium oxide and is contained in a 4-in diameter spherical vessel and weighs 4 lb. The maximum operating temperature for this source is 1800°F, with current development being done to raise this to 2000°F. The curve shown in Fig. 4-1 gives the fuel capsule temperature required to transfer 250 W to the receiver at the temperature indicated on the abscissa. Both source and receiver are assumed to have an emissivity of 0.9. The conclusion from this data is that the size and temperature of existing isotope capsules can easily meet the technical requirements of the ICICLE program.

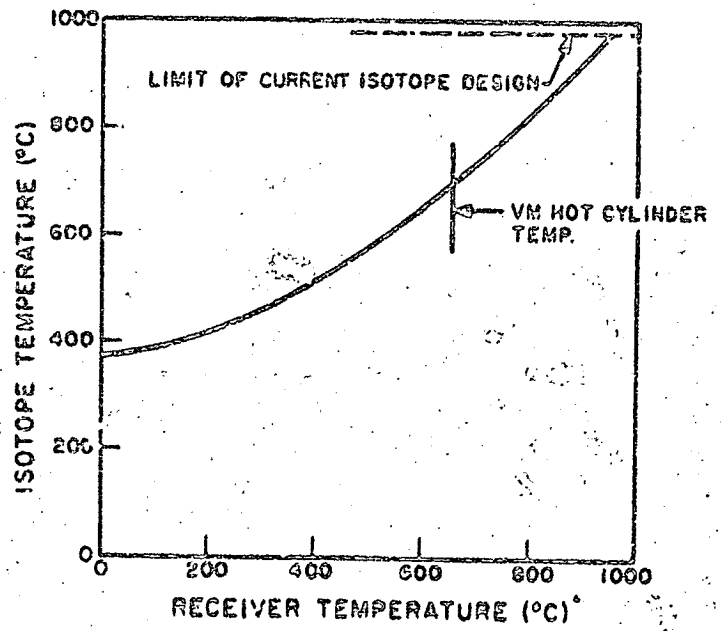



Fig. 4-1. Fuel capsule temperature required to transfer 250 W to the receiver.

*References for this section are at the end of this section.

If one accepts the conclusions that the effect of isotope selection is binary on the feasibility of ICICLE (i.e., if an alpha emitter is available, the isotope will not bar feasibility; if such an emitter cannot be used, then ICICLE will not be feasible because of excessive shielding weight), then the process of fuel selection can be separated from system feasibility. In this study, fuel selection is not made, but a general description of candidate fuels is presented.

The source of heat in a radioisotope is the continuous decay of the material from an excited energy state to a lower energy state. This decay follows an exponential relationship with time in accordance with

$$P = P_o e^{-\lambda t}$$

P = Power

$\lambda$ = Decay Constant = $\frac{0.693}{\text{Half Life}}$

t = Time

This relationship is shown in Fig. 4-2 for several materials. Clearly, the preferred isotope for two to five year life is plutonium 238. Its output degrades about 1 percent in two years and 4 percent in five years. $Tm^{170}$ and $Po^{210}$ are unacceptable for long missions because of their short decay time. Promethium 147 ($Pm^{147}$) has a decay characteristic intermediate between these two. In two years, it decays to 80 percent of its original capability and in five years to just over 25 percent. A two year mission using $Pm^{147}$ would require an initial charge of 250/0.80 = 415 W, and a five year mission would require 1000 W initial charge.

Decay of radioactive materials is accompanied by the emission of particles such as alpha ($\alpha$), beta ($\beta$) and neutron ($\eta$), as well as electromagnetic radiation called gamma ($\gamma$) rays. These decay products interact with matter to generate the heat generated in isotopes. Alpha emissions can be contained by very light enclosures so that all the thermal energy is available at the isotope capsule. Beta and gamma emissions require more massive enclosures for capture. Table 4-1 shows the properties of various candidate isotopes categorized by type of primary radiation emission.[2] Strontium 90 ($Sr^{90}$), which looks like a good possibility in Fig. 4-2, is eliminated by the shielding requirement indicated in Table 4-1. An example of the extent of the weight penalty because of shielding is the SNAP 21B, which has approximately the same thermal output as the Step II but weighs 840 lb. While it can be argued that the SNAP 21B, which is designed for undersea use, might not be representative of a space source, the difficulty of using $\gamma$ sources would make them impractical.

The question of fuel selection would thus probably reduce to a choice between $Pu^{238}$ and $Pm^{147}$. Since curium 244 is still an experimental material, it would not be available for consideration in the 1972 time frame. There is adequate $Pu^{238}$ available to satisfy the ICICLE requirement, which is for approximately 650 g. The latest

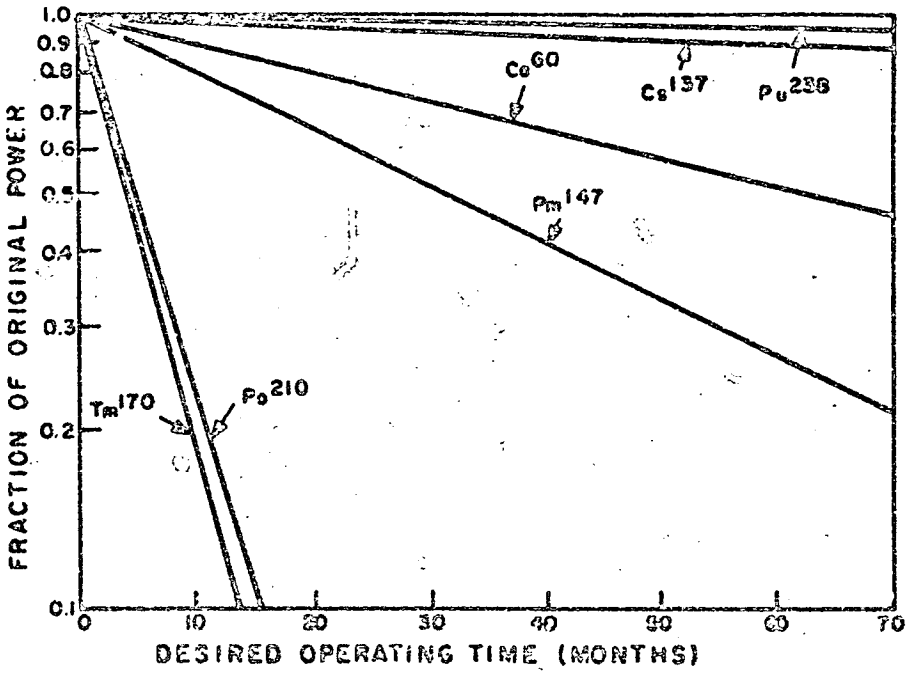



Fig. 4-2. Power decay with time for various isotopes.

cost estimates are $700/thermal watt,[3] so that fuel costs would be $280,000. Because ICICLE probably could command adequate priority, it appears that $Pu^{238}$ would be the recommended fuel.

The third, and most difficult, requirement in showing isotope feasibility is safety. This aspect of safety is less a matter of physiological injury in handling the fuel capsule (since this is an absolute requirement in the technical considerations) than it is protection against incident during reentry and short duration. Three requirements generally are considered during isotope capsule evaluations. First is survivability in a launchpad failure, which is obviously different for a Scout propulsion system than it is for a Saturn. Secondly, survivability during reentry ranging from random orbital decay to superorbital must be demonstrated. Thirdly, the capsule must survive earth impact and burial. The real difficulty with this aspect of isotope feasibility is that the goal in all missions is for "absolute" safety, which is difficult to describe or test.

Extensive testing has been done on a variety of fuel capsules. High temperature soak at 2200°F for 1 h or burial in a burner block of rocket fuel has been used to demonstrate survivability to launch pad failure.

Reentry has been dealt with extensively by Brunner et al.[4] They summarize the problems for intact reentry from a mission abort as follows:

1) Off the pad. Booster explosions, fireballs and after-fire.

2) Power flight. Difficulty of ejecting fuel assemblies against high dynamic pressure and danger of booster explosion or damage from other debris.

3) Suborbital. Inability of reentry system to separate and orient properly so that aerodynamic heating at nondesign angles of attack causes capsule burnout.

4) Parking orbit (100 nmi). Reentry system must be designed to withstand reentry environments, ground impact and postimpact thermal loads. This trajectory is usually the design case.

5) Long-life orbit. Reentry systems must survive long-time space-thermal-radiative environments prior to reentry and impact.

6) Superorbital return. Extremely high thermal fluxes, inertial loads, and dynamic pressures can occur through a wide range of values.

Heat protective systems and materials as listed in Table 4-2 have been developed to meet most requirements. Using these materials and techniques, as well as preferred vehicle shapes, adequate reentry protection can be provided. Various isotope capsules have been successfully tested in a 6-in diameter plasma arc to simulate reentry.

Another aspect of reentry was demonstrated by the recovery of an aborted SNAP 19. The technology which allowed adequate vehicle tracking and trajectory calculation to permit recovery of the capsule plays an important part in establishing isotope feasibility. It also justifies the use of expensive but long lived $Pu^{238}$ since a source with a half life of 86 years can be reused many times.

The impact requirements call for impacting onto solid granite at the terminal velocity of the specific capsule configuration. Survival after this test has been demonstrated with several fuel configurations.

While these considerations must certainly be made to assure isotope feasibility, a fourth practical but possibly overriding consideration is the availability of an acceptable developed capsule. It would be naive to suppose that some already developed capsule could be simply used as is in the ICICLE System since each space flight has its own special requirements. ICICLE would be a substantially more sound concept economically if developed technology could be used. Table 4-3 is a summary of isotope development capsules as reported by Hittman Associates.[5] As pointed out by

# TABLE 4-1. RADIOISOTOPE FUEL CHARACTERISTICS

| Characteristic | Gamma | Beta | | | | | | Alpha | | | |
|---|---|---|---|---|---|---|---|---|---|---|---|
| Isotope | $Co^{60}$ | $Kr^{85}$ | $Sr^{90}$ | $Cs^{137}$ | $Ce^{144}$ | $Pm^{147}$ | $Tm^{170}$ | $Po^{210}$ | $Pu^{238}$ | $Cm^{242}$ | $Cm^{244}$ |
| Half-life (years) | 5.3 | 10.7 | 1.9 | 30 | 0.78 | 2.6 | 0.35 | 0.38 | 85 | 0.45 | 18 |
| Principal Energy (Mev) | | | | | | | | | | | |
| $\alpha$ | - | - | - | - | - | - | - | 5.3 | 5.49 | 6.11 | 5.80 |
| $\beta$ | 0.31 | 0.68 | 0.55 | 0.510 | 0.303 | 0.223 | 0.96 | | | | |
| $\gamma$ | 1.33 | 0.514 | - | 0.66 | 0.13 | 0.121 | 0.084 | 0.8 | 0.044 | 0.04 | 0.1 |
| Fuel Form | Metal | $SrTiO_3$ | Metal | CsCl | $CeO_2$ | $Pm_2O_3$ | $Tm_2O_3$ | GdFe | $PuO_2$ | $Cm_2O_3$ | $Cm_2O_3$ |
| Watts/Curie Compound | 0.3 | 0.22 | 1.1 | 0.32 | 0.8 | 0.225 | 1.07 | 1.34 | 0.39 | 99 | 2.27 |
| Density of Compound g/cm³ metal or pwr lb | 8.7 | 2.3 | 22.2 | 3.6 | 6.6 | 7.43 | 9.5 | 9.3 | 10 | 9 | 9 |
| Power Density w/cm³ compound | 15.3 | 0.51 | 13.6 | 0.42 | 2.3 | 2.13 | 9.1 | 2210 | 3.9 | 882 | 20.4 |
| Shielding Required | Heavy | Heavy | Heavy | Heavy | Heavy | Minor | Moderate | Minor | Minor | Minor | Moderate |
| Curies/Watt | 65 | 340 | 100 | 230 | 125 | 2780 | 560 | 32 | 30 | 28 | 29 |
| Melting Point (°C) | 1480 | 1500 | 2430 | 645 | 1200 | 1280 | 2300 | 1675 | 2280 | 1950 | 1950 |
| MPC in Air (Ci/cm³) | $3 \times 10^{-9}$ | $10^{-12}$ | $3 \times 10^{-9}$ | $5 \times 10^{-9}$ | $3 \times 10^{-8}$ | $2 \times 10^{-8}$ | $10^{-8}$ | $7 \times 10^{-11}$ | $7 \times 10^{-13}$ | $4 \times 10^{-11}$ | $3 \times 10^{-12}$ |
| Present Cost ($/watt) (projected) | 225 | 115 | | | | 600 | 75 | 100 | 1010 | | |

TABLE 4-2. TYPICAL MATERIAL APPLICATION

| Heat-Protective System | Material |
|---|---|
| Ablation | Graphite,[a] special graphites,[b] 3DGFM[c] and ESM[d] |
| Transpiration Cooling | Matrix: graphite, metals, ceramics and 3DGFM<br>Coolants:<br>Active - He, $H_2O$, $N_2$ and $NH_3$<br>Passive - Be, Ni, LiF, BaF, B and BN, Cu |
| Film Cooling | He, $H_2O$, $N_2$ and $NH_3$ |
| Liquid-metal Cooling | Li, Na and Mg |
| Heat Sink | Cu, Be and graphites |
| Reradiation | Graphites, René 41, TZM, Hf-Ta |

NOTES:

a. ATJ graphite, pyrolytic graphite, and POCO graphite.

b. Reinforced pyrolytic graphite felt (RPGF), reinforced pyrolized plastic (RPP), Pyrocarb, and Carbitex.

c. Three-dimensional graphite fibrous material.

d. Typical elastomeric shield material for lower operational temperature environment: T = 600° F.

Hitman, items 19 and 20 are entirely relevent to the ICICLE program. Capsule number 20 has a thermal power of 850 W and will be flown in an RTG in a Transit spacecraft in early 1971. This capsule is currently undergoing launch approval testing. The Transit capsule is an outgrowth of the LRHS program (item number 10) in which the technology was developed during fabrication of 16 devices. Containment of the fuel is with a platinum clad tantalum capsule, which is then enclosed with a graphite reentry cap. The extension of the thermal power of from 204 W to 850 W was in a straightforward fashion, which leads us to conclude that within the framework of the

development program required to use any isotope in ICICLE, specification of the required output would not represent an important complication. The necessity of the relatively large reentry can make the total source size and weight relatively insensitive to thermal output. The LRHS capsule, for instance, weighs approximately 9 lb compared to 14 lb for the Transit capsule. Ten pounds seems like a good estimate for potential ICICLE capsule weight.

A competing capsule configuration also undergoing launch approval testing is a modified SNAP 19 configuration (item number 19), which is scheduled for flight on Pioneer F and Pioneer G. This capsule, an outgrowth of the original SNAP 19 program (item number 9), is slightly lighter than the Transit capsule and uses TZM containment. It is scheduled for flight late in 1971.

ICICLE can and should utilize a modification of the Transit or SNAP 19 capsules as a heat source. The feasibility of using an isotope as a heat source for an ICICLE System requires similar considerations as are required in the study of an TRG. Since these have been shown to be feasible by study and experiment, there is good reason to expect that the isotope will not be a critical item relative to ICICLE feasibility.

References for Section 4


1. H. J. Gerwin, "Selected Thermoelectric, Thermionic, and Electron-Voltaic Energy Conversion Device Characteristics," SC-ARPIC-1011.

2. J. K. Evert and R. Y. Parkinson, "Radioisotope heaters for thermal control," Fifth Space Congress, Cocoa Beach, Florida, March 11-14, 1968.

3. Private communication, J. Jacobs, Sandia Corporation.

4. M. J. Brunner et al., "Re-entry of radioactive power sources," J. of Spacecraft and Rockets, vol. 5, April 1968.

5. Preliminary Investigation - ICICLE System Nuclear Heat Source: HIT - 4 and 6, Hitman Associates, Inc., Sept. 1969.

## TABLE 4-3. SURVEY OF NUCLEAR FUEL CAPSULES AND DEVELOP STATUS - AEROSPACE APPLICATION

| Item No. | Year of Fuel Capsule Availability For First Application | Designation | Thermal Power (Watts) | Application | Agency/ Responsibility | Fuel | Fuel Form | Fuel Capsule Size | Fuel Capsule Technology |
|---|---|---|---|---|---|---|---|---|---|
| 1 | 1961 | SNAP-3B | 52.8 | Transit 4A Transit 4B | USAEC/Martin Marietta Corp. | Pu-238 | Metal | 0.55 $in^3$ (Capsule Volume) | Superalloy, Burn-up Design, Non-Vented |
| 2 | 1963 | SNAP-9A | 460 | Navigational Satellites | USAEC/Martin Marietta Corp. | Pu-238 | Metal | 4.82 $in^3$ (Capsule Volume) | Superalloy Burn-up Design, Non-Vented |
| 3 | 1965 | SNAP-19C-2 | 105 | Nimbus-3<br>Swim Suit Heater (1967) | USAEC/Martin Marietta Corp. | Pu-238 | Metal $PuO_2$ (Microspheres) | 0.981" Dia. x 5.732" Long, (Right Circular Cylinder) | Superalloy, Burn-up Design, Non-Vented |
| 4 | 1966 | POODLE | 1670 | $H_2$ - Thruster | USAEC-USAF/ TRW Systems | Po-210 | Polonium Compound | 1.950" Dia. x 4.703" Long (Right Circular Cylinder) | Refractory, Non-Vented, Non-Intact Impact Design |
| 5 | 1967 | SNAP-19 (Reference Design) | 570 | Nimbus-B | USAEC/Martin Marietta Corp. | Pu-238 | $PuO_2$ (Microspheres) | 2.980" Dia. x 6.125" Long (Right Circular Cylinder) | Superalloy, Burn-up Design, Non-Vented |
| 6 | 1967 | Radioisotope (RIJ) | 60 | $NH_3$ - Thruster | USAEC/NASA-GSFC | Pm 147 | $Pm_2O_3$ | 1" Dia. x 2.5" Long (Hemispherically ended cylinder | Superalloy, Non-Vented |
| 7 | 1967 | DART | 155 | Attitude Control Thruster | USAEC/TRW Systems | Pu 238 | $PuO_2$ (Microspheres) | 1.563" Dia. x 4.109" Long (Right Circular Cylinder) | Refractory, Non-Vented, Non-Intact Impact Design |
| 8 | 1968 | AMSA | 65 | Component Heater | USAEC/Sandia Labs. | Pm-147 | $Pm_2O_3$ | 2" Dia. x 2" Long (Right Circular Cylinder) | Refractory, Non-Vented |
| (9) | 1968 | SNAP-19 (IRHS) | 570 | Nimbus-B | USAEC/Isotopes, Inc. | Pu-238 | $PuO_2$ (Microspheres) | 2.125" Dia. x 5.5" Long (Hemispherically Ended Cylinder) | Superalloy Vented (Non-Selective), Intact Design |
| (10) | 1969 | AI Capsule | 204 | Technology Program and LRHS | USAEC/Atomics International | Pu-238 | $PuO_2$ | 1.725" Dia. x 7.371" Long | Refractory, Non-Vented Intact-Impact Design |
| 11 | 1969 | SNAP-27 | 1480 | Lunar Gravimeter | USAEC/General Electric Co. | Pu-238 | $PuO_2$ (Microspheres) | 2.519" Dia. x 15.60" Long (Right Circular Cylinder) | Superalloy, Vented (Non Selective), Special Cask Designed for Aerospace Nuclear Safety |
| 12 | 1969 | SNAP-29 | 1050 | No application assigned | USAEC/Isotopes, Inc. | Po-210 | Polonium Compound | 0.0975" Dia. x 13.594" Long (Hemispherically Ended Cylinder | Refractory, Non-Vented |
| 13 | 1969 | ALRH | 15 | Lunar Seismometer Heater | USAEC/NASA-MSC | Pu-238 | $PuO_2$ (Microspheres) | 3" Dia. x 3" Long (Right Circular Cylinder) | Refractory, Non-Vented, Intact Impact Design |

FOLDOUT FRAME 1

# /EY OF NUCLEAR FUEL CAPSULES AND DEVELOPMENT
# ITATUS - AEROSPACE APPLICATION

| ency/ nsibility | Fuel | Fuel Form | Fuel Capsule Size | Fuel Capsule Technology | Launch Approval* | Remarks |
|---|---|---|---|---|---|---|
| :/Martin ta Corp. | Pu-238 | Metal | 0.55 $in^3$ (Capsule Volume) | Superalloy, Burn-up Design, Non-Vented | Yes | This fuel capsule would not satisfy current aerospace nuclear safety criteria. |
| :/Martin ta Corp. | Pu-238 | Metal | 4.82 $in^3$ (Capsule Volume) | Superalloy Burn-up Design, Non-Vented | Yes | This fuel capsule would not satisfy current aerospace nuclear safety criteria. |
| :/Martin ta Corp. | Pu-238 | Metal $PuO_2$ (Microspheres) | 0.981" Dia. x 5.732" Long, (Right Circular Cylinder) | Superalloy, Burn-up Design, Non-Vented | No | This fuel capsule was not used for Nimbus-B. The fuel capsule (slightly modified) was fueled for the Swim Suit Heater application. |
| :-USAF/ ystems | Po-210 | Polonium Compound | 1.950" Dia. x 4.703" Long (Right Circular Cylinder) | Refractory, Non-Vented, Non-Intact Impact Design | Ground Test Only | This fuel capsule was fueled and used in a ground system test. Three capsules make up one assembly. For the ground test, each capsule was fueled to 300 watts only. The capsule was partially qualified, i.e., thermal and impact testing was performed. |
| :/Martin ta Corp. | Pu-238 | $PuO_2$ (Microspheres) | 2.980" Dia. x 6.125" Long (Right Circular Cylinder) | Superalloy, Burn-up Design, Non-Vented | No | This fuel capsule was not used for Nimbus-B. |
| :/NASA | Pm-147 | $Pm_2O_3$ | 1" Dia. x 2.5" Long (Hemispherically ended cylinder | Superalloy Non-Vented | Ground Test Only | This fuel capsule was fueled and used in the RIJ system ground test that was performed at Mound Laboratories. |
| :/TRW s | Pu-238 | $PuO_2$ (Microspheres) | 1.563" Dia. x 4.103" Long (Right Circular Cylinder) | Refractory, Non-Vented, Non-Intact Impact Design | Ground Test Only | This fuel capsule was fueled and used in a ground system test. The capsule was partially qualified, i.e. thermal and impact testing was performed. |
| :/Sandia | Pm-147 | $Pm_2O_3$ | 2" Dia. x 2" Long (Right Circular Cylinder) | Refractory Non-Vented | Ground Test Only | Advanced Manned Strategic Aircraft. This fuel capsule was fueled and used in a ground system test. The capsule was not designed for aerospace applications. |
| :/Isotopes, | Pu-238 | $PuO_2$ (Microspheres) | 2.125" Dia. x 5.5" Long (Hemispherically Ended Cylinder) | Superalloy Vented (Non-Selective), Intact Design | Yes | This fuel capsule was fueled and launched into earth orbit on April 14, 1969 as a part of the SNAP-19/Nimbus-B satellite program. |
| :/Atomics ational | Pu-238 | $PuO_2$ | 1.726"Dia. x 7.371" Long | Refractory, Non-Vented, Intact-Impact Design | No | A modified design of this fuel capsule has been tentatively selected for use on the Transit program. Extensive development testing has been performed for this capsule. Four capsules will be fueled in the near future. One will most likely include a vent. This fuel capsule will most likely be used for the Large Reentry Heat Source Program in conjunction with a Brayton Cycle System. |
| :/General ic Co. | Pu-238 | $PuO_2$ (Microspheres) | 2.519" Dia. x 15.60" Long (Right Circular Cylinder) | Superalloy, Vented (Non Selective), Special Cask Designed for Aerospace Nuclear Safety | Yes (For capsule contained in Reentry Cask) | This fuel capsule has been fueled and flight qualified for launch in a special reentry protection cask. The SNAP-27 generator is planned to be flown on the Apollo-12 Mission this year. |
| :/Isotopes, | Po-210 | Polonium Compound | 0.0995" Dia. x 13.984" Long (Hemispherically Ended Cylinder | Refractory Non-Vented | No | Program terminated. Fuel capsule was only partially development tested. |
| :/NASA | Pu-238 | $PuO_2$ (Microspheres) | 3" Dia. x 3" Long (Right Circular Cylinder) | Refractory, Non-Vented, Intact Impact Design | Yes | Apollo Lunar Radioisotope Heater. Completely flight qualified. Two heaters used per solenoid motor assembly. Flown on Apollo-11 in July 1969. |

FOLDOUT FRAME 2

4-9/4-10

## TABLE 4-3. SURVEY OF NUCLEAR FUEL CAPSULES AND D
## STATUS - AEROSPACE APPLICATION (Cont'd)

| Item No. | Year of Fuel Capsule Availability For First Application | Designation | Thermal Power (Watts) | Application | Agency/ Responsibility | Fuel | Fuel Form | Fuel Capsule Size | Fuel Capsule Technology |
|---|---|---|---|---|---|---|---|---|---|
| 14 | 1969 | ——— | to 50 | Spacecraft Component Heater | NASA-Houston (MSC)/McDonnell-Douglas | Unknown | Unknown | Unknown | Unknown |
| 15 | 1969 | Hittman Associates Spherical Capsule Program | 870 | Technology Program | USAEC/Hittman Associates, Inc. | Pu-238 | $PuO_2$ (Microspheres) | 8.10" Dia. (Sphere) | Superalloy, Non-Vented, Intact-Impact Design |
| 16 | 1969 | Sandors Assoc. Spherical Capsule Program | 600 | Technology Program | USAEC/Sandors Associates, Inc. | Pu-238 | $PuO_2$ (Microspheres) | 4.06" Dia. (Sphere) | Ceramic, Vented, Intact-Impact Design |
| 17 | 1969 | GGA Spherical Capsule Program | 700 | Technology Program | USAEC/Gulf General Atomics | Pu-238 | $PuO_2$ (Microspheres) | 8" Dia. (Sphere) | Refractory, either Vented or Non-Vented, Intact-Impact Design |
| 18 | 1969 | TRW Capsule Program | 900 | Technology Program | TRW Systems (In-House) | Pu-238 | $PuO_2$ (Microspheres) | 2.09" Dia. x 6.06" Long (Hemispherically Ended Cylinder) | Refractory, Vented Intact-Impact Design |
| (19) | 1969 | SNAP-19 (Modified IRHS) | 675 | Technology Program | Isotopes, Inc. (Primarily on In-House Program, Some USAEC Funding) | Pu-238 | $PuO_2$ (Microspheres) | Reentry Shape is Hexagonal 3.5" Across Flats x 6.75" Long | Refractory, Vented Intact-Impact Design |
| (20) | Future | Transit Heat Source | ~850 | Transit Spacecraft | USAEC/TRW Systems | Pu-238 | Solid Solution Cermet | 2.46" Dia. x 6.70" Long (Hemispherically Ended Cylinder). Reentry can is a right circular cylinder; 5.04" Dia. x 8.04" Long | Refractory, Vented Intact-Impact Design |
| 21 | Future | LSS Heat Source | ~400 | Future Life Support System Program | USAEC-NASA-WPAF/General Electric Co. | Unknown | Unknown | Unknown | Unknown |
| (22) | Future | Multi-Hundred Watt (Electrical) Heat Source(s) | Unknown | Future Space Missions | USAEC/General Electric Co. | Unknown | Unknown | Unknown | Unknown |

Notes:

* Launch approval is granted for the Heat Source System, integrated into a specific launch vehicle and specified for specific mission parameters.

Numbers enclosed in ◯ and △ indicate specific Heat Sources that are discussed within report Section II.B.

N/A means not applicable.

FOLDOUT FRAME 1

## URVEY OF NUCLEAR FUEL CAPSULES AND DEVELOPMENT STATUS - AEROSPACE APPLICATION (Cont'd)

| y/ hility | Fuel | Fuel Form | Fuel Capsule Size | Fuel Capsule Technology | Launch Approval* | Remarks |
|---|---|---|---|---|---|---|
| uston Donnell- | Unknown | Unknown | Unknown | Unknown | No | This is a study contract to evolve a family of fuel capsule designs which are suitable for S/C component heaters in the range of 0-50 watts. The final report is due to be released in the near future. |
| ttman Inc. | Pu-238 | $PuO_2$ (Microspheres) | 8.10" Dia. (Sphere) | Superalloy, Non Vented, Intact-Impact Design | No | This is a technology program only. Extensive development testing was performed. Final reports will be released in the near future. |
| nders Inc. | Pu-238 | $PuO_2$ (Microspheres) | 4.06" Dia. (Sphere) | Ceramic, Vented, Intact-Impact Design | No | This is a technology program only. Limited development testing was performed. Program still in progress. |
| IF tomics | Pu-238 | $PuO_2$ (Microspheres) | 8" Dia. (Sphere) | Refractory, either Vented or Non-Vented, Intact-Impact Design | No | This is a technology program only. Limited development testing was performed. Many technology problems exist. Program completed. Final report will be released in the near future. |
| es | Pu-238 | $PuO_2$ (Microspheres) | 2.09" Dia. x 6.06" Long (Hemispherically Ended Cylinder) | Refractory, Vented, Intact-Impact Design | No | This is a technology program only. Limited development testing was performed. Program completed. |
| ce. on rogram, C | Pu-238 | $PuO_2$ (Microspheres) | Reentry Shape is Hexagonal 3.5" Across Flats x 6.75" Long | Refractory, Vented, Intact-Impact Design | No | This is a technology program only. Some development testing was performed. Program status is unknown. |
| W | Pu-238 | Solid Solution Cermet | 2.46" Dia. x 6.70" Long (Hemispherically Ended Cylinder). Reentry can is a right circular cylinder, 5.04" Dia. x 8.04" Long | Refractory, Vented, Intact-Impact Design | N/A | The contract to develop a heat source that is suitable for the Transit Spacecraft mission was let recently. Program is in early stage. A modified Item 10 fuel capsule is the basis for this design. |
| ISA- ter | Unknown | Unknown | Unknown | Unknown | Presently being Designed for a Ground System Test | This program was awarded to G. E. in June 1969. Initially an electrically heated unit will be used for ground testing. Subsequently a fueled unit will be used for ground testing (~two years in the future). No flight system requirements have been specified. |
| neral | Unknown | Unknown | Unknown | Unknown | N/A | This is a study program that was awarded to G. E. in August 1969. Program is just getting under way. |

ted into a specific launch

hat are discussed within

FOLDOUT FRAME 2

## Section 5

# HEAT PIPES


*Summary*

*The most efficient means of transferring heat in an ICICLE system in terms of low weight and low temperature gradients is to employ heat pipes at high, ambient, and cryogenic temperatures.*

*High-temperature (943°C) heat (350 W) transfer from the radioisotope to the VM hot cylinder can best be achieved by the heat pipe combination of sodium working fluid, molybdenum wick, and TZM-molybdenum wall material. A 0.5-in diameter heat pipe would exhibit a total temperature drop of about 10°C. If pre-launch testing is done in air, nickel wall and wick material should be used with sodium, which would result in a total heat pipe temperature drop of about 13°C. The weight of a 0.5-in. OD heat pipe is approximately 0.25 pound per foot of length.*

*If a short half-life radioisotope is employed, a constant-temperature bypass heat pipe can be used to transfer excess isotope heat to space. A 1-in-diameter, 12-in-long sodium heat pipe with a helium reservoir will transfer 350 W while maintaining a temperature of from 935°C to 965°C and would weight about 0.75 lb.*

*Ambient-temperature heat rejection from VM crankcase to space is best handled by a heat pipe-honeycomb radiator linked to the VM by a primary heat pipe. A heat pipe-honeycomb radiator configuration is recommended because of its low weight and low temperature gradients. Ammonia is recommended for the working fluid in both the primary heat pipe and the radiator or secondary heat pipes. A 1-in-diameter primary heat pipe with aluminum wall and wick will transfer 190 W at 30°C with a temperature drop of 7°C and will weigh about 1 lb/ft. Aluminum wall and wick is also recommended for the secondary heat pipes which are 0.25 in. in diameter, and will exhibit an 11°C temperature drop and weigh about .05 pounds per foot.*

*In the cryogenic heat pipes, minimum temperature drops can be achieved by using screen-covered channel wicks. The pore radius and the wick thickness ratio should be optimized to permit ground testing at the full design heat load. The fluid flow and heat transfer characteristics of oxygen are superior to nitrogen in the temperature range 77°K to 90°K, but a complete lack of experimental data for oxygen heat pipes precludes its recommendation. An optimized nitrogen heat pipe operating at 77°K with an aluminum channel wick with an OD of 0.3 in and a length of 4 ft will weigh 0.05 lb and exhibit a temperature drop of less than 1°C for a heat transfer rate of 1 W.*


## A. GENERAL HEAT PIPE THEORY

### 1. Introduction

The necessary heat pipe technology for an ICICLE system requires a synthesis of existing heat pipe theory and the expansion of that theory to permit a more complete understanding of heat pipe fluid flow and heat transfer processes. The

operating temperature range for ICICLE heat pipes encompasses virtually all areas of heat pipe investigation to this date. In this section a thorough treatment of heat pipe theory will be presented, which will include analysis of fluid flow dynamics, heat transfer mechanisms, operational limits and optimization techniques.

## 2. Liquid and Vapor Flow Dynamics

The fluid driving force in a heat pipe is due to the surface tension forces in the wick. These forces depend upon the liquid-vapor surface tension, the radius of curvature of the evaporator and condenser menisci and the liquid-solid wetting angle. This capillary pumping force is resisted by viscous shear forces in the liquid and vapor, by momentum changes in the liquid and vapor, and, depending on the orientation, by gravitational forces acting on the liquid. The effect of gravity on the vapor flow is always assumed to be negligible. These forces may be combined in the following pressure-balance equation for steady-state heat pipe operation:

$$\Delta P_c = \Delta P_{\ell f} + \Delta P_v + \Delta P_{\ell g} \qquad (5\text{-}1)$$

Where

$\Delta P_c$ is the capillary pumping pressure

$\Delta P_{\ell f}$ is the liquid pressure drop caused by viscous drag in the wick

$\Delta P_v$ is the vapor pressure drop

$\Delta P_{\ell g}$ is the gravitational liquid pressure drop

### a. Capillary Pumping Pressure

The pressure difference across a curved liquid-vapor interface is given by the Laplace-Young equation,

$$\Delta P_c = \frac{2\gamma \cos\theta}{r_c} \qquad (5\text{-}2)$$

where:

$\gamma$ is the liquid surface tension

$\theta$ is the liquid-solid contact angle.

$r_c$ is the capillary pore radius.

The surface tension of common heat pipe working fluids is generally well defined and the contact angle is usually taken to be 0°, which can lead to large errors in calculating $\Delta P_c$. However, for fluids such as liquid sodium, ammonia, and nitrogen in contact with metallic wicks, the assumption of zero contact angle is valid.

Good heat pipe design dictates that the characteristic capillary pore radius, $r_c$, be experimentally determined. Commercial powdered metal or fiber metal wicks contain a distribution of pore sizes with the largest pore being typically five times larger than the smallest pore. Two standard experimental techniques for determination of the characteristic pore size in a wick are the equilibrium capillary rise test and the maximum pressure test. The capillary rise test consists of measuring the maximum height, z, to which a wetting liquid of density $\rho_\ell$ will rise in a vertical wick. The equilibrium condition requires that the capillary pumping pressure be balanced by the hydrostatic pressure of the liquid:

$$\Delta P_c = \Delta P_{\ell g} \tag{5-3}$$

or

$$\frac{2\gamma}{r_c} = \rho_\ell g z \tag{5-4}$$

where:

$\rho_\ell$ is the density of the liquid

g is the local acceleration of gravity.

The maximum pressure test involves pressurizing a saturated wick until the air pressure exceeds the capillary pressure as evidenced by air bubbles escaping through the wick. This technique is much simpler and faster than the capillary rise test. It has been shown that both techniques yield similar results.[1]

b. Liquid Pressure Drops

The pressure drop in the liquid caused by gravity is simply

$$\Delta P_{\ell g} = \rho_\ell g Z \sin\phi \tag{5-5}$$

where:

Z is the length of the heat pipe.

$\phi$ is the heat pipe angle of tilt measured from the horizontal.

For derivation of the liquid pressure drop due to viscous shear, incompressible, one dimensional, fully developed, laminar flow with constant properties is assumed. The Reynolds number, $R_e$, for liquid flow in a pore is usually below 10.

The following Reynolds number calculation is typical for a high temperature sodium heat pipe:

$$R_e = \frac{\dot{m}_\ell \, 2 r_c}{A_c \eta_\ell} \tag{5-6}$$

where:

$\dot{m}_\ell$ is the liquid mass flow rate $\dot{m}_\ell = \frac{Q}{h}$ (5-7)

$A_c$ is the cross sectional area, $A = \pi (r_w^2 - r_v^2)\, e$ (5-8)

Q is the heat pipe throughput

$\eta_\ell$ is the liquid viscosity

h is the latent heat of vaporization

$r_w$ is the heat pipe inner wall radius

$r_v$ is the vapor radius

e is the wick porosity.

Assuming values of 1000 W for Q, $1.82 \times 10^{-3}$ gm/cm/s for $\eta_\ell$ 3870 W·s/g for h, 0.01 cm for $r_c$, 1.27 cm for $r_w$, 1.00 cm for $r_v$, and 0.8 for e, $R_e$ is calculated to be 1.11. The well-known momentum equation of the boundary layer is derived in cylindrical coordinates[3]

$$\rho_\ell u \frac{\partial u}{\partial x} + \rho_\ell v_r \frac{\partial u}{\partial r} + g \frac{dP}{dx} = \frac{1}{r} \frac{\partial}{\partial r} \left( r \eta_\ell \frac{\partial u}{\partial r} \right) \tag{5-9}$$

where:

u is the local axial velocity

x is the distance along the flow direction as illustrated in Fig. 5-1.

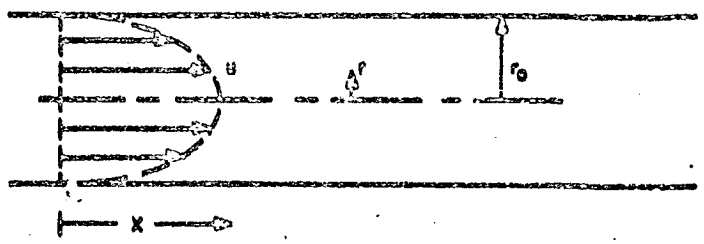



Fig. 5-1. One-dimensional fluid flow model.

For a fully developed velocity profile, $v_r = 0$ and $\frac{\partial u}{\partial x} = 0$, Eq. 5-9 then becomes,

$$g \frac{\partial P}{\partial x} = \frac{1}{r} \frac{\partial}{\partial r} \left( r \eta_\ell \frac{\partial u}{\partial r} \right) \tag{5-10}$$

Applying the boundary conditions,

$$\left. \frac{\partial u}{\partial r} \right|_{r=0} = 0 \tag{5-11}$$

$$\left. u \right|_{r=r_o} = 0 \tag{5-12}$$

Integrating Eq. 5-10 twice with respect to r,

$$\frac{\partial}{\partial r} \left( r \frac{\partial u}{\partial r} \right) = \left( \frac{g}{\eta_\ell} \frac{dP}{dx} \right) r$$

$$r \frac{\partial u}{\partial r} = \left( \frac{g}{\eta_\ell} \frac{dP}{dx} \right) \left( \frac{r^2}{2} + C_1 \right)$$

$$\frac{\partial u}{\partial r} = \left( \frac{g}{\eta_\ell} \frac{dP}{dx} \right) \left[ \frac{r}{2} + \frac{C_1}{r} \right] \tag{5-13}$$

$$u = \left(\frac{g}{\eta_\ell}\ \frac{dP}{dx}\right)\left[\frac{r^2}{4} + C_1 \ln r + C_2\right] \qquad (5\text{-}14)$$

The first boundary condition, Eq. 5-11, yields $C_1 = 0$; the second boundary condition Eq. 5-12, yields

$$0 = \left(\frac{g}{\eta_\ell}\ \frac{dP}{dx}\right)\left[\frac{r_o^2}{4} + C_2\right]$$

or

$$C_2 = \frac{-r_o^2}{4}$$

Equation 5-14 becomes

$$u = \left(\frac{g}{\eta_\ell}\ \frac{dP}{dx}\right)\left[\frac{r^2}{4} - \frac{r_o^2}{4}\right] \qquad (5\text{-}15)$$

or

$$u = \frac{g}{4\eta_\ell}\ r_o^2\ \left(\frac{-dP}{dx}\right)\left[1 - \frac{r^2}{r_o^2}\right] \qquad (5\text{-}16)$$

Equation 5-16 yields the local axial velocity, u , in terms of the axial pressure gradient $\frac{dP}{dx}$. The local velocity can be expressed in terms of a mean velocity, V, by determining V such that

$$\dot{m} = \rho_\ell V A_c \qquad (5\text{-}17)$$

The total mass flow rate ($\dot{m}$) can also be found by integrating u over the cross-sectional flow area,

$$\dot{m} = \int_{A_c} u\, \rho_\ell\, dA_c \qquad (5\text{-}18)$$

Therefore,

$$V = \frac{\dot{m}}{\rho_\ell A_c} = \frac{1}{\rho_\ell A_c} \int_{A_c} u\ \rho_\ell\, dA_c \qquad (5\text{-}19)$$

Since $\rho_\ell$ is a constant over the cross section,

$$V = \frac{1}{A_c} \int_{A_c} u dA_c \qquad (5\text{-}20)$$

For a circular tube,

$$A_c = \pi r_o^2$$
$$dA_c = 2\pi\, r dr$$

Equation 5-20 now becomes,

$$V = \frac{1}{\pi r_o^2} \int_o^{r_o} 2\pi\, u\, r\, dr$$

$$V = \frac{2}{r_o^2} \int_o^{r_o} u\, r dr \qquad (5\text{-}21)$$

Substituting Eq. 5-16 into Eq. 5-21,

$$V = \frac{2}{r_o^2} \int_o^{r_o} \frac{g\, r_o^2}{4\eta_\ell} \left(-\frac{dP}{dx}\right) \left[1 - \frac{r^2}{r_o^2}\right] r dr \qquad (5\text{-}22)$$

$$V = \frac{g}{2\eta_\ell} \left(-\frac{dP}{dx}\right) \int_o^{r_o} \left[r - \frac{r^3}{r_o^2}\right] dr$$

$$V = \frac{g}{2\eta_\ell} \left(-\frac{dP}{dx}\right) \left[\frac{r^2}{2} - \frac{r^4}{4r_o^2}\right]_o^{r_o}$$

$$V = \frac{g}{\eta_\ell} \left(-\frac{dP}{dx}\right) \left(\frac{r_o^2}{8}\right) \qquad (5\text{-}23)$$

$$\frac{dP}{dx} = -\left[\frac{8\eta_\ell}{g\, r_o^2}\right] V \qquad (5\text{-}24)$$

In a heat pipe the total Q is transferred by mass transport or $Q = \dot{m}h$.

For steady-state flow, $\dot{m}_\ell = -\dot{m}_v$

or

$$\dot{m}_\ell = \frac{Q}{h} = \rho_\ell V_\ell A$$

and

$$V_\ell = \frac{\dot{m}_\ell}{\rho_\ell A}$$

Equation 5-24 becomes (with "x" replaced by "z", the distance along the axis of the heat pipe)

$$\frac{dP}{dz} = -\frac{8\eta_\ell}{g\, r_o^2}\left(\frac{\dot{m}_\ell}{\rho_\ell A}\right) \qquad (5\text{-}25)$$

where A is the total liquid flow area, $A = \pi\left[r_w^2 - r_v^2\right]$.

$$\frac{dP}{dz} = -\frac{8\eta_\ell \dot{m}_\ell}{\rho_\ell \pi\left(r_w^2 - r_v^2\right) g r_o^2} \qquad (5\text{-}26)$$

The liquid mass flow rate, $\dot{m}_\ell$, in each section of the heat pipe, shown in Fig. 5-2, is,

$$\dot{m}_\ell = \frac{Q}{h}\frac{z}{Z_e} \qquad 0 \le z \le Z_e$$

$$\dot{m}_\ell = \frac{Q}{h} \qquad Z_e \le z \le Z_o$$

$$\dot{m}_\ell = \frac{Q(Z-z)}{h Z_o} \qquad Z_o \le z \le Z$$

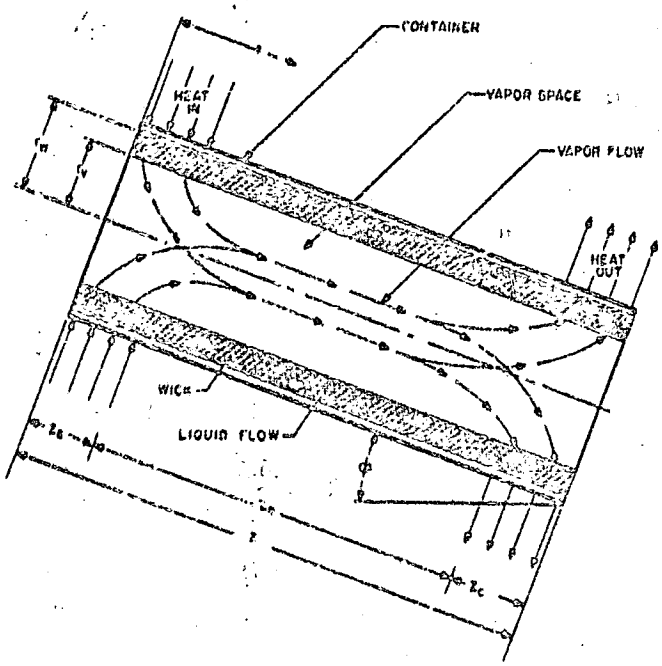



Fig. 5-2. Heat pipe geometry.

The liquid pressure drop in all three sections of the heat pipe can be found by integrating Eq. 5-26. Thus:

$$\int_{P(o)}^{P(Z)} dP = -\frac{8\eta_\ell}{\rho_\ell \pi (r_w^2 - r_v^2) or_c^2}\left(\frac{Q}{h}\right)\left[\frac{1}{Z_e}\int_o^{Z_e} z\,dz + \int_{Z_e}^{Z_c} dz + \frac{1}{Z_c}\int_{Z_c}^{Z} (Z-z)\,dz\right] \quad (5\text{-}27)$$

$$\int_{P(o)}^{P(Z)} dP = \frac{-8\eta_\ell}{\rho_\ell \pi (r_w^2 - r_v^2) or_c^2}\left(\frac{Q}{h}\right)\left[\frac{1}{Z_e}\left(\frac{Z_e^2}{2}\right) + \left(Z_c - Z_e\right) + \frac{1}{Z_c}\left[Zz - \frac{z^2}{2}\right]_{Z_c}^{Z}\right]$$

$$P(o) - P(z) = \frac{8\eta_\ell}{\rho_\ell \pi (r_w^2 - r_v^2) or_c^2}\left(\frac{Q}{h}\right)\left[\frac{Z_e}{3} + Z_a + \frac{Z_c}{2}\right]$$

$$\Delta P_\ell = \frac{8\eta_\ell Q}{2\rho_\ell \pi (r_w^2 - r_v^2) or_c^2 h}\left[Z + Z_a\right] \quad (5\text{-}28)$$

The constant 8 in Eq. 5-28 comes from the assumption that all the pores in the wick may be represented by straight, parallel, capillary tubes of radii $r_c$. The true liquid pressure drop in a wick structure will be somewhat higher, depending on how the actual liquid flow path deviates from that of the straight capillary tube. To account for this deviation, the constant 8 in Eq. 5-28 is replaced by a tortuousity constant, b which may vary upwards from 8. The b factor is commonly assumed to vary from 10 to 20, but this implies that b may vary independently of $\epsilon$, and $r_c^2$, which is not correct.

Just as the characteristic $r_c$ should be determined experimentally, the grouping

$$\frac{b}{\epsilon r_c^2}$$

should also be found by experiment. This is commonly done by either the forced flow permeability test or the gravity flow permeability test. The latter is used for very thin wicks where the flow resistance is a function of the meniscus radius of the liquid-vapor interface. This subject is covered thoroughly in the literature.[1]

Equation 5-28 with b in place of the 8 is valid for wicks of the sintered powdered metal, screen mesh and fiber-metal types. These three types are commonly referred to as homogeneous wicks. Another common wick structure is the channel wick, consisting of many longitudinal groves or channels in the heat pipe wall, which provides a low-resistance flow path for liquid return. The liquid flow in rectangular channel is very similar to the model which was just developed for flow in long, narrow capillary tubes. The analysis of the $\Delta P_\ell$ for channel flow results in the following equation:[3]

$$\Delta P_\ell = \frac{(2 + t/r)\,\beta\,\eta_\ell\,Q(Z + Z_g)}{2\pi\rho_\ell\,h\,r_v(r_w - r_v)\,r^2} \qquad (5\text{-}29)$$

c. Pressure Drop in Vapor

In addition to the effects of viscous shear, vapor flow pressure drop analysis must also take into account the effects of momentum and, in a few cases, turbulent vapor flow. Whether viscous shear or momentum changes is the dominant contributor to the pressure drop depends on the magnitude of a radial flow Reynolds number (based on the radius, rather than the usual diameter). The radial Reynolds number, $R_{e_r}$, is defined by

$$R_{e_r} = \frac{\rho_v\,r_v\,v_r}{\eta_v} = \frac{1}{2\pi\eta_v}\,\frac{d\dot{m}_v}{dZ} \qquad (5\text{-}30)$$

For very small rates of evaporation and condensation, $|R_{e_r}| << 1$ indicating the dominance of viscous shear. The vapor pressure drop for this case may be found by a perturbation expansion of Eq. 5-26 in powers of the $R_{e_r}$.

$$\frac{dP_v}{dZ} = -\frac{8\eta_v \dot{m}_v}{\rho_v(\pi r_v^2) r_v^2}\left[1 + \frac{3}{4} R_{e_r} - \frac{11}{27} R_{e_r}^2 + \ldots\right] \qquad (5\text{-}31)$$

The expanded terms account for the effect of momentum changes, which cause the pressure drop in the evaporator to be higher than for viscous shear and the pressure drop in the condenser to be lower than for viscous shear due to a pressure rise in the decelerating flow in the condenser section.

For high rates of evaporation, the axial velocity profile is no longer parabolic, but proportional to $\cos\left[\pi/2\,(r/r_v)^2\right]$. A perturbation expansion can be made in powers of $R_{e_r}$ to obtain the $dP_v/dz$ in the evaporator. For high condensation rates, the velocity profile is similar to that of turbulent flow in which the profile is very flat across most of the radius, dropping off sharply to zero in a thin layer near the pipe wall. In this case, the pressure increases in the flow direction due to partial dynamic recovery in the decelerating flow. In the limit, as $R_{e_r} \to \infty$, the $\Delta P_v$ in the evaporator is given[4] by

$$\frac{dP_v}{dz} = -\frac{s\,\dot{m}_v}{4\rho_v r_v^4}\frac{d\dot{m}_v}{dz} \qquad (5\text{-}32)$$

Where s, a constant, is 1 for evaporation and $4/\pi^2$ for condensation. This expression is conservative since it does not account for compressibility. The pressure recovery for high axial heat fluxes may exceed 50%[5] when compressibility is considered.

In the adiabatic section of a heat pipe, there is essentially no mass addition or subtraction, hence $R_{e_r} = 0$. The $\Delta P_v$ in this section depends on the axial flow Reynolds number (based on the radius, $r_v$)

$$R_{e_z} = \frac{\dot{m}_v r_v}{\eta_v A_c} = \frac{\dot{m}_v}{\pi \eta_v r_v} \qquad (5\text{-}33)$$

For laminar vapor flow in the adiabatic section ($R_{e_z} < 1000$), the pressure gradient may be found using the same analysis which resulted in Eq. 20, for the laminar flow $\Delta P_\ell$. The density is assumed constant.

The result is

$$\frac{dP_v}{dz} = \frac{-8\eta_v \dot{m}_v}{\pi \rho_v r_v^4} \qquad Z_e < z < Z_c \qquad (5\text{-}34)$$

For fully developed turbulent flow in the adiabatic section ($Re_z > 1500$, $Z >> r_v$), the Blasius equation which is based on direct pipe pressure drop measurements is commonly used [4]

$$\frac{dP_v}{dZ} = \frac{-0.0655\ \eta_v^2}{\rho_v r_v^3} (R_{e_z})^{7/4} \qquad Z_e \leq z \leq Z_c \qquad (5\text{-}35)$$

Before integrating these pressure gradients, some typical Reynolds numbers will be calculated.

d. Radial Reynolds Number

In a typical ICICLE system, the lowest radial Reynolds number would occur in the cryogenic heat pipe due to the small heat load it must transport.

For a nitrogen heat pipe, with $Q = 2W$, $T = 77°K$, $h = 200$ W.s/gm, $\eta_v = 0.55 \times 10^{-4}$ gm/cm/s, and $Z_e = 5$ cm, $\dot{m}$ would be 0.01 gm/s and $R_{e_r}$ would be 5.8.

In comparison, for a typical sodium heat pipe with $Q = 350$ W, $T = 900°C$, $h = 3870$ W.s/gm, $\eta_v = 2.32 \times 10^{-4}$ gm/cm/s, $R_{e_r}$ would be 12.4.

Under these same respective conditions, the axial Reynolds number $R_{e_z}$, for the $N_2$ and Na heat pipes with $r_v$ of 0.7 cm would be 176 and 83, respectively.

The usual conditions for vapor flow in a typical ICICLE system is, then, a high radial Reynolds number in the evaporator and condenser section, and laminar flow in the adiabatic region.

The vapor pressure gradients are integrated as follows for three commonly encountered flow regimes.

For $R_{e_r} << 1$ and $R_{e_z} < 1000$, Eq. 5-31 applies in the evaporator and condenser section.

Neglecting terms of $R_e^2$ and higher order, Eq. 5-31 can be integrated for the evaporator section.

$$\int_0^{Z_e} dP_v = \frac{-8\eta_v}{\pi \rho_v r_v^4} \int_0^{Z_e} \left( \dot{m}_v + \frac{3}{4} \frac{\dot{m}_v \, d\dot{m}_v}{2\pi \eta_v dz} \right) dz$$

where

$$\dot{m}_v = \frac{Qz}{hZ_c} \quad (0 \le z \le Z_e)$$

$$\int_c^{Z_e} dP_v = \frac{-8\eta_v}{\pi \rho_v r_v^4} \left[ \frac{Qz^2}{hZ_e^2} + \frac{3Q^2 z^2}{16 \pi \eta_v h^2 Z_o^2} \right]_0^{Z_e}$$

$$P_v(o) - P_v(Z_e) = \Delta P_e = \frac{4\eta_v Q Z_e}{\pi \rho_v h r_v^4} + \frac{3Q^2}{2\pi^2 \rho_v r_v^4 h^2} \qquad (5\text{-}36)$$

In the adiabatic section, Eq. 5-34 is used.

$$\frac{dP_v}{dZ} = \frac{-8\eta_v \dot{m}_v}{\pi \rho_v r_v^4} \quad \text{where } \dot{m}_v = Q/h$$

$$\int_{Z_e}^{Z_c} dP_v = \frac{-8\eta_v Q}{\pi \rho_v r_v^4 h} \int_{Z_e}^{Z_c} dz$$

$$P_v(Z_e) - P_v(Z_c) = \Delta P_a = \frac{8\eta_v Q Z_a}{\pi \rho_v r_v^4 h}. \qquad (5\text{-}37)$$

For the condenser section, Eq. 5-31 is again integrated

$$\int_{Z_c}^{Z} dP_v = \frac{-8\eta_v}{\pi \rho_v r_v^4} \int_{Z_c}^{Z} \left( \dot{m}_v + \frac{3}{8\pi \eta_v} \dot{m}_v \frac{d\dot{m}_v}{dz} \right) dz$$

where

$$\dot{m}_v = \frac{Q(Z - z)}{h Z_c} \qquad \frac{d\dot{m}_v}{dZ} = \frac{-Q}{hZ_c}$$

$$\int_{Z_c}^{Z} dP_v = \frac{-8\eta_v}{\pi \rho_v r_v^4} \int_{Z_c}^{Z} \left( \frac{Q\,(Z-z)}{hZ_c} - \frac{3\,Q^2\,(Z-z)}{8\pi\eta_v h^2 Z_c^2} \right) dz$$

$$\int_{Z_c}^{Z} dP_v = \frac{-8\eta_v Q}{\pi \rho_v r_v^4 h Z_e} \int_{Z_c}^{Z} \left[ (Z-z) - \frac{3Q\,(Z-z)}{8\pi\eta_v h Z_c} \right] dz$$

$$P_v(Z_c) - P_v(Z) = \Delta P_{v_c} = \frac{8\pi\eta_v hQZ_c - 3Q^2}{2\pi^2 \rho_v r_v^4 h^2} \qquad (5\text{-}38)$$

The total vapor pressure drop for the conditions $R_{e_r} << 1$ and $R_{e_z} < 1000$ is, then,

$$\Delta P_v = \Delta P_{v_e} + \Delta P_{v_a} + \Delta P_{v_c}$$

$$= \frac{4\eta_v Q Z_e}{\pi \rho_v h r_v^4} + \frac{3Q^2}{2\pi^2 \rho_v r_v^4 h^2} + \frac{8\eta_v Q Z_a}{\pi \rho_v r_v} + \frac{4\eta_v Q Z_c}{\pi \rho_v r_v^4 h} - \frac{3Q^2}{2\pi^2 \rho_v r_v^4 h^2}$$

$$\Delta P_v = \frac{4\eta_v Q (Z + Z_a)}{\pi \rho_v h r_v^4} \qquad R_{e_r} << 1,\ R_{e_z} < 1000 \qquad (5\text{-}39)$$

For $R_{e_r} >> 1$ and $R_{e_z} > 1500$, in the evaporator section

$$\int_0^{Z_e} \frac{dP_v}{dz} = -\frac{1}{\pi \rho_v r_v^4} \int_0^{Z_e} \dot{m}_v \frac{d\dot{m}_v}{dz} \qquad (5\text{-}32)$$

$$\int_0^{Z_e} dP_v = -\frac{1}{\pi \rho_v r_v^4} \int_0^{Z_e} \frac{Q^2 z}{h^4 Z_e^2}$$

$$\Delta P_{v_c} = \frac{1}{\pi \rho_v r_v^4} \frac{Q^2}{h^2 Z_e^2} \left( \frac{Z_e^2}{2} \right) = \frac{Q^2}{\pi \rho_v r_v^4 h^2} \qquad (5\text{-}40)$$

In the adiabatic section, the Blasius equation (5-35) yields

$$\frac{dP_v}{dz} = -\frac{0.0655\,\eta_v^{2}}{\rho_v r_v^{3}}\left(\frac{\dot{m}_v}{\pi r_v \eta_v}\right)^{7/4} \tag{5-41}$$

$$\int_{Z_e}^{Z_c} dP_v = \frac{0.0655\,\eta_v^{2}}{\rho_v r_v^{3}}\left(\frac{Q}{h\pi r_v \eta_v}\right)^{7/4} \int_{Z_e}^{Z_c} dz$$

$$\Delta P_{v_a} = \frac{0.0655\,\eta_v^{0.25}}{\rho_v r_v^{4.75}}\, Z_a \left(\frac{Q}{h\pi}\right)^{1.75} \tag{5-42}$$

In the condenser section, $s = 4/\pi^2$

$$\int_{Z_c}^{Z} dP_v = \frac{\frac{4}{\pi^2}}{4\rho_v r_v^{4}} \int_{z_c}^{z} \frac{Q^2}{h^2 Z_c^2}\,(Z - z)\,dz$$

$$\Delta P_{v_c} = \frac{-\frac{4Q^2}{\pi^2}}{8\rho_v r_v^{4} h^2} \tag{5-43}$$

The total vapor pressure drop for the conditions $R_{e_r} >> 1$ and $R_{e_z} > 1500$ is

$$\Delta P_v = \frac{\left(1 - \frac{4}{\pi^2}\right) Q^2}{8\rho r_v^{4} h^2} + \frac{0.0655\,\eta_v^{0.25}\, Z_a}{\rho_v r_v^{4.75}}\left(\frac{Q}{h\pi}\right)^{1.75} \tag{5-44}$$

For the conditions $R_{e_r} >> 1$ and $R_{e_z} < 1000$, from the preceding analysis

$$\Delta P_{v_e} = \frac{Q^2}{8\rho_v r_v^{4} h^2}$$

$$\Delta P_{v_a} = \frac{8\eta_v Q Z_a}{\pi \rho_v r_v^4 h}$$

$$\Delta P_{v_c} = \frac{-4Q^2/\pi^2}{8\rho_v r_v^4 h^2}$$

$$\Delta P_v = \frac{\left(1 - \frac{4}{\pi^2}\right) Q^2}{8\rho_v r_v^4 h^2} + \frac{8\eta_v Q Z_a}{\pi \rho_v r_v^4 h} \qquad (5\text{-}45)$$

e. Vapor Pressure Drop-Order of Magnitude

The pressure drop equations for vapor flow in the adiabatic section are well developed for both the laminar and turbulent conditions. Vapor flow in the evaporator and condenser regions, however, is decidedly more complex, due to the radial velocity component and the presence of inertial forces. The present theory describes evaporator and condenser pressure gradients only for radial Reynolds numbers that are either very small or approaching infinity. At these two extremes, the vapor pressure change is considered to be entirely due to viscous shear ($R_{e_r} \ll 1$) or inertia ($R_{e_r} \to \infty$).

Since the radial Reynolds numbers encountered in typical ICICLE heat pipe are between 1 and 100, it is important to examine the magnitude of the vapor pressure drops in the evaporator and condenser as determined for both low and high $R_{e_r}$ and to compare these pressure drops to the adiabatic section and also to the liquid pressure drops.

To compare the high and low $R_{e_r}$ pressure drops, the sum of Eqs. 5-36 and 5-38 is divided by the sum of Eqs. 5-40 and 5-43.

$$\frac{\Delta P_{v_{e+c}}\left(R_{e_r} << 1\right)}{\Delta P_{v_{e+c}}\left(R_{e_r} >> 1\right)} = \left(\frac{4\eta_v Q(Z_e + Z_c)}{\pi \rho_v r_v^4 h}\right) \frac{8\rho_v r_v^4 h^2}{1 - \frac{4}{\pi^2} Q^2}$$

$$\text{Pressure Ratio (P.R.)} = [17(Z_e + Z_c)\eta_v]/\dot{m}$$

To calculate this pressure ratio, the following values are assumed:

$N_2$: $Q = 2W$, $T = 77°K$, $Z_e = Z_c = 5$ cm, $r_v = 0.4$ cm

Na: $Q = 350W$, $T = 1200°K$, $Z_e = Z_c = 5$ cm, $r_v = 0.4$ cm

At these typical conditions the P.R. for $N_2$ at $T = 77°K$ is 0.935 and the P.R. for Na at $T = 1200°K$ is 0.435.

The magnitude of the $\Delta P_{v_{e+c}}$ for these examples is shown in Table 5-1. The $\Delta P_a$ shown is for the laminar flow condition with $Z_a = 30$ cm.

TABLE 5-1. VAPOR PRESSURE DROPS

| Heat-Pipe Fluid | Pressure Drop ($dynes/cm^2$) | | |
|---|---|---|---|
| | $\Delta P_a$ | $\Delta P_{e+c}$ | |
| | | $R_{e_r} \ll 1$ | $R_{e_r} \gg 1$ |
| $N_2$ | 0.35 | 0.060 | 0.064 |
| Na | 2.50 | 37 | 85 |

For this example, the $\Delta P_{e+c}$ for $R_{e_r} \gg 1$ is calculated based on a 40% pressure recovery in the condenser. As stated earlier in this report, the condenser pressure recovery could approach 80% when compressibility effects are considered. This would mean a 6:1 reduction in the $\Delta P_{e+c}$ and cause the $\Delta P_{e+c}$ for small $R_{e_r}$ to be the larger of the two for the conditions assumed in the example. As will be seen in later in this report, the magnitude of the total vapor pressure drop in the optimized heat pipe operating in a gravity field is only a few percent of the combined liquid and vapor pressure drops. Of the total vapor pressure drop, the contribution of the $\Delta P_{e+c}$ is about 20% for the two examples shown in Table 5-1, thus making the $\Delta P_{e+c}$ typically less than 1% of the total liquid and vapor pressure drops for a gravity field optimized heat pipe.

f. Summary of Fluid-Flow Equations

The expressions for heat pipe fluid flow are now substituted into the pressure-balance equation for a homogeneous wick:

$$\frac{2\gamma\cos\theta}{r_c} = \frac{b\eta_\ell Q(Z+Z_a)}{2\rho_\ell \pi(r_w^2 - r_v^2)her_c^2} + \rho_{\ell g} g Z \sin\phi$$

$$+ \begin{cases} \dfrac{4\eta_v Q(Z+Z_a)}{\pi\rho_v h r_v^4} & \begin{cases} Re_z < 1000 \\ Re_r << 1 \end{cases} \\ \dfrac{(1-\frac{4}{\pi^2})Q^2}{8\rho_v r_v^4 h^2} + \dfrac{.0655\eta_v^{.25} Z_a}{\rho_v r_v^{4.75}} \left(\dfrac{Q}{b\pi}\right)^{1.75} & \begin{cases} Re_z > 1000 \\ Re_r >> 1 \end{cases} \end{cases} \qquad (5\text{-}46)$$

For channel wick the $\Delta P_\ell$ term is replaced with .

$$\Delta P_\ell = \frac{(2 + t/r)\,\beta\eta_\ell Q(Z+Z_a)}{2\pi\rho_\ell h r_v (r_w - r_v) r^2}$$

This pressure balance equation is strictly correct only when the radius of curvature of the liquid-vapor interface is equal to the capillary pore radius, $r_c$, which occurs at the maximum heat transfer rate, $Q_{max}$.

3. Optimization Techniques

For a homogeneous wick, Eq. 5-46 shows the capillary pumping pressure, $\Delta P_c$, is inversely proportional to the pore radius, $r_c$, and the liquid frictional pressure drop is inversely proportional to $r_c^2$. Since it is desired to obtain a high $\Delta P_c$, and a low $\Delta P_{\ell f}$, the pore size can be varied, until the difference between $\Delta P_c$ and $\Delta P_{\ell f}$ is a maximum. At this optimum pore radius, $r_{co}$, the throughput will be a maximum for a given fluid, and a given $r_w$, $r_v$, and acceleration field. Similarly, when the $r_{co}$ is determined and substituted into the original pressure balance equation, the vapor-space radius, $r_v$ can also be optimized to yield a maximum Q for a given fluid, $R_w$, and gravity field.

The same procedure can be followed for a screen-covered channel wick where the capillary pumping pore radius is proportional to the channel half-width.

The procedure is as follows for homogeneous wicks:

Equation 5-46 may be written for $R_{e_r} << 1$ and $R_{e_z} < 1000$ as:

$$\frac{2\gamma \cos\theta}{r_c} = \frac{AQ}{r_c^2} + BQ + C \qquad (5\text{-}47)$$

where

$$A = \frac{b\eta_\ell (Z + Z_a)}{2\pi (r_w^2 - r_v^2)\rho_\ell h e}$$

$$B = \frac{4\eta_v (Z + Z_a)}{\pi \rho_v r_v^4 h}$$

$$C = \rho_\ell g Z$$

Rearranging terms,

$$Q = \frac{2\gamma r_c - C r_c^2}{A + B r_c^2} \qquad (5\text{-}48)$$

to find the $r_c$ which maximizes Q, $\partial Q/\partial r_c$ is set to zero.

$$\frac{\partial Q}{\partial R_c} = \frac{(A + r_c^2 B)(2\gamma - 2r_c C) - (2\gamma r_c - r_c^2 C)(2r_e B)}{[A + B r_c^2]^2} = 0$$

collecting terms,

$$(\gamma B) r_c^2 + (AC) r_c - \gamma A = 0$$

Solving for $r_{c_o}$,

$$r_{c_o} = \frac{-AC + \sqrt{(AC)^2 + 4\gamma^2 AB}}{2\gamma B} = 0 \qquad (5\text{-}49)$$

Substituting into Eq. 5-48 the following expression for maximum throughput at $r_c = r_{co}$ and a given $r_v$ is obtained:

$$Q\Big|_{r_{co}} = \frac{2\gamma r_{co} - C r_{co}^2}{A + B r_{co}^2} \tag{5-50}$$

This equation can be differentiated with respect to $r_v$ with $r_w$ held constant and set equal to zero; the resulting expression yields an optimum ratio, $(r_v/r_w)_o$ which can be put into Eq. 5-50 to give the maximum throughput at $r_{co}$ and $(r_v/r_w)_o$ for a given fluid and gravity field. This latter procedure to determine $(r_v/r_w)_o$ becomes very cumbersome if a closed-form solution is attempted; therefore it is best-handled by computer-aided numerical iteration.

In the absence of gravitational forces (C = 0), the optimization procedure is somewhat simplified and results in the following expressions.

$$r_{co} = \frac{\sqrt{4\gamma^2 AB}}{2\gamma B} = \frac{2\gamma\sqrt{AB}}{2\gamma B} = \sqrt{\frac{A}{B}} \tag{5-51}$$

Substituting this Expression into Eq. 5-50 yields:

$$Q\Big|_{r_{co}} = \frac{2\gamma\sqrt{\frac{A}{B}}}{A + B\left(\frac{A}{B}\right)} = \frac{2\gamma\sqrt{\frac{A}{B}}}{2A}$$

$$Q\Big|_{r_{co}} = \frac{\gamma}{\sqrt{AB}} = \left[\frac{\gamma}{\frac{2b\eta_A \eta_V (Z+Z_a)^2}{\pi^2 \rho_V \rho_\ell h^2 c r_v^4 (r_w^2 - r_v^2)}}\right]^{1/2} \tag{5-52}$$

In terms of $r_v$ and $r_w$, $Q|_{r_{co}}$ is a maximum when $\sqrt{r_v^4 (r_w^2 - r_v^2)}$ is a minimum.

Setting $\frac{\partial Q|_{r_{co}}}{\partial r_v} = 0$ yields the optimum $r_v / r_w$ for zero-g operation ($r_w$ is fixed).

$$\left.\frac{\partial Q}{\partial r_v}\right|_{r_{co}} = -r_v^3 (1/2)(r_w^2 - r_v^2)^{-1/2} + (r_w^2 - r_v^2) 2 r_v = 0$$

$$r_v^2 = 2(r_w^2 - r_v^2)$$

$$\frac{r_v^2}{r_w^2} = \frac{2}{3}; \quad (r_v/r_w) = \sqrt{\frac{2}{3}} \tag{5-53}$$

Substituting Eq. 5-53 into Eq. 5-52 yields

$$\left.Q\right|_{\substack{r_{co} \\ (r_v/r_w)_o}} = Q_{max} = \left[\frac{\gamma r_w^3}{\frac{13.5\, b\, \eta_\ell \eta_v (Z + Z_a)^2}{\rho_v \rho_\ell h^2 e}}\right]^{1/2} \tag{5-54}$$

Or, in more general terms, the product of maximum throughput and length becomes

$$Q(Z + Z_a)_{max} = \left[\frac{\gamma r_w^3}{\frac{13.5\, b \eta_\ell \eta_v}{\rho_\ell \rho_v h^2 e}}\right]^{1/2} \begin{cases} r_c = r_{co} & R_{e_r} << 1 \\ (r_v/r_w) = (r_v/r_w)_o & R_{e_z} < 1000 \\ C = 0 \end{cases} \tag{5-55}$$

The fluid parameters in this equation can be grouped as heat-pipe fluid figure of merit, thus

$$\text{F.O.M.} = \gamma h \left[\frac{\rho_\ell \rho_v}{\eta_\ell \eta_v}\right]^{1/2} \tag{5-56}$$

This working-fluid figure of merit for zero g is plotted versus temperature for the candidate ICICLE working fluids in Fig. 5-3. A similar figure of merit expression for heat pipes operating in a gravity field cannot be expressed because the fluid properties in Eq. 5-50 cannot be grouped into a single expression. Close examination of Eq. 5-50 shows the maximum throughput to be a complex function of g-fluid, fluid properties

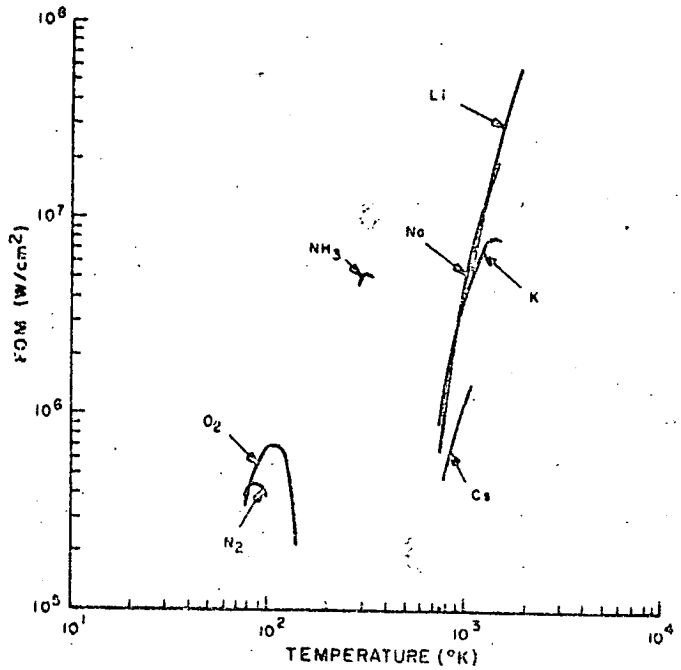



Fig. 5-3. Working-fluid figure of merit as a function of temperature for $N_2$, $O_2$, $NH_3$, Cs, K, Li, and Na at zero g.

and $r_w$. Plots of $Q(Z + Z_a)_{max}$ versus $r_w$ for several g-fields show the strong influence of magnitude of the gravitational field on $Q(Z + Z_a)_{max}$. It should be cautioned here that selection of a heat-pipe working fluid should not be based on the zero-g figure of merit, since the presence of even small g field could result in the selection of a different fluid (see Section 5.F.). Other fluid properties such as liquid thermal conductivity and vapor pressure must be considered in the selection process, but cannot be conveniently grouped with the fluid properties which are germane to the fluid flow expressions. The heat transfer and vapor flow limitations will be examined in later sections. Detailed heat pipe design criteria are discussed in the Sections 5.B, 5.C, and 5.F. dealing with the high, ambient and low temperature heat pipe, respectively.

4. Vapor Flow Operational Limits

In addition to the limits imposed on heat pipe throughput by the wick and pipe geometry (referred to as the capillary pumping limit), there exist three other operational limits on a heat pipe: sonic, entrainment and boiling. The boiling limit is discussed in Section 5.A.5; the sonic and entrainment limits which are both caused by high velocity vapor flow are analyzed below.

a. Sonic Limitation

Heat transfer in a heat pipe is essentially due to the vapor transport of the latent heat or $Q = \dot{m}h$. For steady state operation, $\dot{m}_v = \dot{m}_\ell = \rho_v VA$. Combining these equations for the vapor flow,

$$Q = h\rho_v V_v \pi r_v^2$$

If it is assumed that $h \neq h(T)$, then

$$Q(T) = (h\pi r_v^2) V_v \rho_v(T) \qquad (5\text{-}57)$$

For a given axial heat flux, $Q/\pi r_v^2$, if the operating temperature is reduced by lowering the condenser temperature, the vapor density will decrease and the vapor velocity will increase until sonic velocity is approached. A choking contion will then exist at the evaporator exit, and any increase in heat flux, q, at this temperature will not result in an increase in the vapor velocity; rather, the additional q will cause the heat pipe temperature level to increase. As the heat pipe temperature increases the vapor density increases, which causes a lower vapor velocity. Once the sonic condition exists in a heat pipe, pressure change in the condenser is not transmitted to the evaporator. Hence, large temperature drops along the heat pipe length can develop. The sonic limitation is encountered by all high-temperature heat pipe working fluids which exist in the solid phase at room temperature. Since heat pipes are not normally operated at very low vapor pressures, the sonic limitation will only be encountered during start up and cool down. It is not a catastrophic limitation in the sense that the wicking limitation is, because once the wicking limit is reached, any further increase in q will cause wick dryout and thermal runaway, whereas once the sonic limit is reached, additional heat input will raise the operating temperature and thus lower the vapor velocity which tends to correct the situation.

The heat flux at sonic conditions, $q_s$, can be predicted using the equation developed by Levy:[6]

$$q_s = \frac{\rho_v V_s h}{\sqrt{2(k+1)}}$$

where:

$V_s$ is mean velocity at sonic conditions

$\kappa$ is ratio of specific heat of vapor at constant pressure to specific heat of vapor at constant volume.

Investigators such as Kemme (7) have experimentally verified Levy's equation for several high temperature working fluids. The sonic heat flux limits of candidate ICICLE hot heat pipe fluids is presented in Table 5-2 as a function of temperature.

TABLE 5-2. SONIC AXIAL HEAT-FLUX LIMITS

| Evaporator Exit Temp. (°C) | Heat-Flux Limits ($kW/cm^2$) | | |
|---|---|---|---|
| | Potassium | Sodium | Lithium |
| 400 | 0.5 | — | — |
| 500 | 2.9 | 0.6 | — |
| 600 | 12.1 | 3.5 | — |
| 700 | 36.6 | 13.2 | — |
| 800 | — | 38.9 | 1.0 |
| 900 | — | 94.2 | 3.9 |
| 1000 | — | — | 12.0 |
| 1100 | — | — | 31.1 |
| 1200 | — | — | 71.0 |
| 1300 | — | — | 143.0 |

b. Entrainment Limitation

If there is no physical separation between the liquid and vapor flows in a heat pipe as in one with an open channel wick, the flow of returning condensate is resisted somewhat by the vapor flow, and, at high vapor velocities, the liquid at the wick surface will become entrained, or pushed back toward the condenser. The onset of entrainment in high-temperature heat pipes with open channels has been detected experimentally by the sound of liquid droplets striking the condenser end of the heat pipe. Entrainment begins when the kinetic energy of the vapor exceeds the surface energy of the liquid or

$$\frac{\rho_v V_v^2}{\gamma/d} > 1$$

where $V_v$ is the limiting vapor velocity, d is the characteristic dimension of the vapor-wick interface. This grouping is referred to as the Weber number and is a function of d. For screen mesh wicks, some experimental data has shown that d may be approximated by the wire-to-wire spacing. The quantity d is related to the wavelength of the perturbed liquid surface, and therefore to the dimensions of the wick. The amount of experimental data available, however, is limited and does not clearly establish a method for predicting the value of d for a particular wick-fluid combination.

For the case of unity Weber number the limiting vapor velocity is

$$V_v = \left[\frac{\gamma}{\rho_v d}\right]^{1/2}$$

the corresponding limiting axial heat flux, q, becomes

$$q = \left[\frac{\rho_v \gamma h^2}{d}\right]^{1/2}$$

For a constant dimension d, the quantity $\rho_v \gamma h^2$ may be plotted versus temperature for some high teperature working fluids as shown in Fig. 5-4.

The entrainment limit can be avoided by proper design, i.e., separating the liquids vapor flows with a homogeneous wick. This limitation, like the sonic limitation, is more frequently encountered during the startup of high-temperature heat pipes due to high vapor velocities.

However, the effect of entrainment onset can be burnout since, as some liquid becomes entrained in the condenser a smaller amount of liquid is available to be pumped to the evaporator and if the q is increased the wick would dry out. In an ICICLE system, with radiative coupling from the hot heat pipe to the VM, the entrainment limit will not cause burnout because the heat pipe will be essentially decoupled from its heat sink (VM) during startup. The heat input from the radioisotope during startup will cause a uniform temperature rise in the high-temperature pipe and only when the temperature approaches operating temperature will the pipe begin to transfer a significant amount of heat to the VM hot cylinder. Radiative coupling, therefore, allows the pipe to "warm up" to near the operating temperature before it is required to transfer any heat.

5. Heat Transfer

The primary heat-transfer mechanism for liquid metal heat pipes is ordinary thermal conduction through the liquid-filled wick with surface evaporation at the heat input section, and film condensation with conduction through the filled wick at the condenser section. The liquid-flow velocity is usually very small, and therefore, the contribution of convection to the overall heat transfer is negligible, and the assumption of stationary liquid is a valid one.

Direct observations of boiling in liquid metal pipes have not been made, and most boiling equations indicate a very large superheat is required for incipient boiling. For example, the incipient boiling theory of Hsu[9] predicts the required superheat for saturated potassium at one atmosphere to be 350°C. Experimenters[10] have observed boiling in potassium at a superheat of 190° C. In addition to present theory not supporting the existence of boiling in high-temperature pipes, the very sterile cleaning procedures used to prepare the wick, container, and working fluid, which includes high temperature vacuum bake-out, virtually eliminates

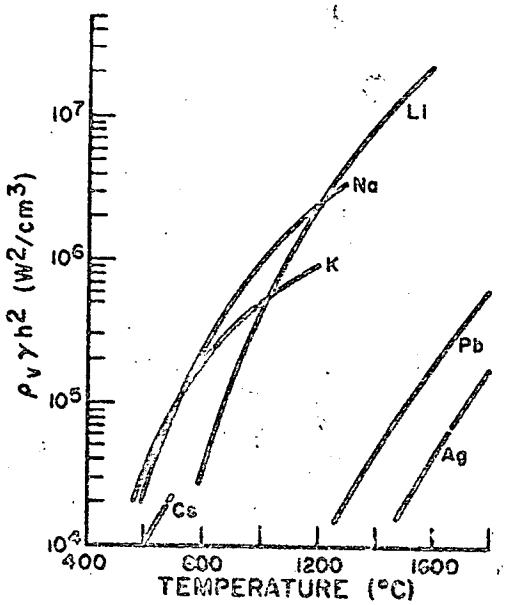



Fig. 5-4. Pertinent fluid properties.

all absorbed gases from the metals and dissolved gases in the fluid. Thus, two possible contributors to the boiling process are removed during the cleaning procedures.

Boiling has been observed in heat pipes with non-metallic working fluids. Experimenters at the U. S. Navy Postgraduate School reported and photographed boiling in a glass-walled water heat pipe with a 100-mesh stainless steel wick[11]. The effect of nucleate boiling in their experiment was to reduce the superheat $\Delta T$ at a given heat flux when compared to ordinary conduction with surface evaporation.

Other experimenters[12] have reported higher $\Delta T$s for water boiling in a more dense wick. The wick density is an important parameter, therefore, in the determination of the method of heat transfer in the heat-pipe evaporator. In general, a densely packed structure such as a sintered array of metallic spheres will inhibit nucleate boiling because it severely restricts the flow of vapor to the wick surface. Such a wick, however, does have a high thermal conductivity due to the dominant role of the metal particles in thermal conduction. The effective thermal conductivity of composites such as a sintered powder metal wick has been expressed by Gorring and Churchill[13] as:

$$\frac{k_c}{k_m} = \left[\frac{r_s}{r_\beta} + \frac{1}{\pi} \ln \frac{2r_s}{r_\beta}\right]^{-1} \qquad (5\text{-}59)$$

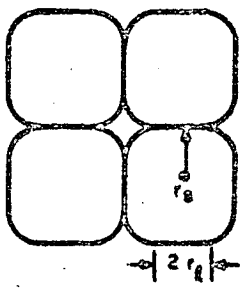



Fig. 5-5. Heterogeneous conduction model.

where

$k_c$ is the thermal conductivity of the composite

$k_m$ is the thermal conductivity of majority carrier, and where the sphere radius, $r_s$ (Fig. 5-5) the contact radius, $r_\ell$, and the porosity, e, are related by

$$e = \frac{\pi}{6\left[1-\left(\frac{r_\ell}{r_s}\right)^2\right]^{2/3}} \left[1-\left(\frac{r_\ell}{r_s}\right)^2\left(2-\sqrt{1-\left(\frac{r_\ell}{r_s}\right)^2}\right)\right] \qquad (5\text{-}60)$$

A typical value for sintered copper powder wick with e = 48% is $k_c$ = 1.265 (W/cm/°C) which is about one-third the thermal conductivity k, of the metal. This formula assumes the liquid to have a zero k and the metal to be the majority carrier in conduction. This is not true, of course, for wicks of the fiber-metal or screen mesh types whose porosities are typically in excess of 80%.

The experience of RCA with ammonia, water, and several freons in contact with high-porosity fiber-metal or screen-mesh wicks has led to the conclusion that a form of nucleate boiling does occur in the wick and the effect of this "irregular" boiling is to improve the heat transfer in an operating heat pipe. Boiling has been observed, at RCA, in glass-walled ammonia heat pipe with a nickel fiber-metal wick. In comparing the measured $\Delta T$ for a 3/8-in-OD ammonia-nickel felt-metal heat pipe to a $\Delta T$ based on ordinary conduction through an ammonia-filled wick, the conduction model predicts a total input-output $\Delta T$ of 14° C which is 2.3 times higher than the measured $\Delta T$ of 6° C. The wick used is only 15% dense with fibers which are randomly oriented. In such a low-density disoriented structure the contribution of the metal to the overall conductivity is negligible. The measured $\Delta T$ of 6° C, therefore, can only be explained by nucleate boiling in the wick which improved the heat transfer.

There is still much investigation to be done with the heat-transfer process in heat pipes with non-metallic working fluids. The bulk of heat-pipe fabrication and

experimentation to date has been in the area of high-temperature liquid-metal heat pipes. However, investigations at RCA into heat pipes in the range to 200° C has resulted in a general agreement with the early work of Allingham and McEntire[14] who concluded that at low heat flux, the presence of a capillary structure improves the heat transfer due to the wick fibers which increase the effective heat-transfer surface area and provide active bubble nucleation sites. At higher heat-flux levels, the wick fibers restrict the turbulent motion of the vapor bubbles and the motion of the vapor to the wick surface interferes with the crossflow of capilary-pumped condensate, which results in lower film coefficients than in fully developed nucleate boiling. Indications are that a form of nucleate boiling does occur in heat pipes with low-density wicks in non-metallic fluids at moderate heat-flux levels and this boiling results in a lower $\Delta T$ than a conduction model would predict. Unfortunately, present theory can only predict wick boiling coefficient for a few of the countless combinations of wicks, fluids, temperatures, and pressures. The model of ordinary thermal conduction through the working fluid with surface evaporation is a conservative starting point for predicting evaporator $\Delta$ Ts.

The heat transfer process in the condenser of a non-liquid-metal pipe is ordinary thermal conduction through a saturated wick. Liquid convection is negligible because of the very low flow velocities. Predicting the heat transfer $\Delta$ Ts in cryogenic heat pipes is a crucial problem because of the poor liquid thermal conductivity and the sharp degradation of the liquid thermal conductivity, $k_\ell$, with increasing temperature. Even if the liquid and metal are assumed to conduct heat in series, the difference in thermal conductivities (over 1000 : 1) and the low wick density causes the liquid to be the major phase with resulting large $\Delta$ Ts. A wick structure based on parallel thermal conduction which significantly reduces the heat transfer $\Delta T$ is described in Section 5.F.

a. Boiling Limitation

In addition to the previously detailed heat pipe limitations of capillary pumping, sonic and entrainment, a fourth limit, related to nucleate boiling may be expressed. In ordinary pool boiling as the heat flux is increased, the bubbles coalesce until a flux is reached where a thin vapor blanket is formed over the heat input surface. At this point, the $\Delta T$ between the wall and the liquid rapidly increases due to the poor thermal conductivity of the vapor. This is the burnout heat flux for pool boiling. For boiling from a bare, flat surface, the limiting, critical value of heat flux $q_c$ has been formulated by Rohsenow and Griffiths[15] as

$$\frac{q_c}{\rho_v h} = 143\, g^{1/4} \left(\frac{\rho_\ell - \rho_v}{\rho_v}\right)^{0.6} \qquad (5\text{-}61)$$

This formula can be used only to compare working fluids; the critical q is also a function of the condition of the boiling surface and in general a roughened surface will result in a higher film coefficient than a smooth surface. The maximum, or burnout heat flux for boiling from a wick has been measured by Pratt and Whitney[16] investigators for a few wick-fluid combinations. Present theory cannot predict a burnout heat

flux due to boiling in a heat pipe but the burnout point is influenced by the ability of the vapor to migrate to the vapor space of the heat pipe. A dense wick would inhibit the vapor flow and result in burnout at a lower heat flux than a less dense wick. The boiling limitation on maximum heat transport for a heat pipe is generally thought to occur at a higher heat flux than the capillary pumping limit. The experience of RCA with heat pipes containing water or ammonia, the low-density (15%-20%) wicks has been that the capillary pumping limitation is the dominant limitation and no observations have been made of those heat pipes becoming boiling-limited at a much lower heat flux than predicted by the wicking limitation. It is quite possible, however, that the wicking and boiling limits could coincide for a particular heat pipe. Both limits are evidenced by thermal runaway and could not be distinguished if they were to occur simultaneously.

b. Material Compatibility

The wick, container, and wicking fluid in a heat pipe must be chemically compatible to insure long and undegrading performance. Because of the fluid circulation in a heat pipe, some dissolution of the wick and wall occurs in the condenser region with subsequent material deposit in the evaporator. Another degrading mechanism in a heat pipe is the chemical reaction of the fluid and the container resulting in the release of a non-condensible gas which collects at the condenser end of the pipe due to vapor momentum and has the effect of shortening the condenser length since no heat is transferred across the pocket of non-condensible gas. This problem of non-condensible-gas generation has been observed by several experimenters including RCA, in water heat pipes with nickel and stainless steel wicks. Since current theories cannot predict the mechanism of mass transfer for particular cases, reference must be made to the expanding data on various heat-pipe life tests. The combination of high temperature heat pipe life data from RCA Lancaster and ambient temperature life data from RCA Camden together with current literature, provides much valuable life data to support a particular fluid-material selection. There is no published life data on cryogenic heat-pipe life, but the depressed temperature level would cause a very slow reaction or dissolution rate. For this reason, the life of a heat pipe could be generally expressed as an inverse function of operating temperature. Specific life test data to support the selection of each ICICLE heat-pipe working fluid is presented later in this report.

## B. HIGH TEMPERATURE HEAT PIPE

The high temperature heat pipe is required to conduct thermal power from the isotope heat source to the input of the VM engine with minimum weight and thermal losses. To accomplish this requirement, design consideration has been given to certain important areas. These are: (1) Fluid flow and thermodynamic design; (2) The selection of the optimal working fluid; (3) The design of the capillary wick structure; and (4) The selection and design of container materials. Each of these design areas is discussed in the following paragraphs.

### 1. Fluid Flow and Thermodynamic Design

RCA has developed a computer program to describe heat pipe performance on the basis of working fluid flow dynamics. This program is based on the expressions developed by Cotter[4] resulting in the basic heat-pipe equation

$$\Delta P_c \geq \Delta P_v + \Delta P_\ell + \Delta P_g$$

where

$\Delta P_c$ is the capillary driving pressure head

$\Delta P_\ell$ is the liquid return pressure drop

$\Delta P_v$ is the vapor pressure drop

$\Delta P_g$ is the pressure drop due to acceleration.

The vapor pressure drop will vary, according to Cotter, depending on whether the flow is laminar (low axial Reynolds number) or turbulent (high axial Reynolds number). For the design of the high temperature ICICLE heat pipe the axial Reynolds number was determined to be less than 1000, hence the following terms were used to describe the laminar flow heat pipe performance in the computer program:

$$\frac{2\gamma \cos\theta}{r_c} \geq \frac{8\eta_v ZQ}{\pi\rho r_v^4 h} + \frac{b\eta_\ell QZ}{\pi\left(r_w^2 - r_v^2\right)\rho_\ell e r_c^2 h} + \rho_\ell g Z \sin\phi$$

where b is wick tortriosity factor.

The fluid properties ($\gamma$, h, $\rho_v$, $\rho_\ell$, $\eta_v$, $\eta_\ell$) all vary with temperature. In order to obtain accurate results, the properties of each of these fluids is stored in the

computer for the entire temperature range of interest. When an operating temperature is selected, a "least squares" fit is made to the data and the properties of the fluid for that temperature are used in the calculations.

The wick properties (b, e, $r_c$) have largely been determined experimentally by separate bench tests. The resulting data has been stored in the computer so that a selection from over 20 different wick structures is available for heat pipe designs.

In using the heat-pipe design program, the heat-pipe dimensions (outside diameter, wall thickness, and length) are chosen along with the heat-pipe working fluid and temperature of operation. A candidate wick structure is selected for evaluation at the operating conditions. The computer will begin at some desired initial heat transfer rate, Q and calculate the resulting heat pipe pressure drops. If the overall drops ($\Delta P_v$, $\Delta P_\ell$, $\Delta P_g$) are less than the capillary pressure head, $\Delta P_c$, the program will automatically increment the heat transfer rate a selected amount and repeat the calculations. The cycle is repeated until the basic heat-pipe expression becomes an equality. At this point, a print out is made of each of the pressure drops and the heat transfer rate capable in that design.

If the liquid pressure drop, $\Delta P_\ell$, is dominant, an enhanced power throughput will result if the wick cross sectional area is increased. The computer will do this automatically in preselected wick-thickness increments, until the vapor space for the chosen dimensions is choked down to where the vapor pressure drop is dominant. The power throughput capability is then a maximum for the particular wick design. A new wick design may be selected from the computer library and the heat-pipe capability re-evaluated. The vapor-pressure drop within the heat pipe results in one of the temperature drops inherent in heat pipe operation. The computer program has been arranged so that a maximum allowable temperature drop down the heat pipe can be selected as a limit. When this value is reached a printout of maximum heat transfer rate is made. The other temperature drops associated with the thermal conductivities and evaporative and condensive drops are calculated by a separate program.

The pressure drop due to gravity, $\Delta P_g$, will add to or detract from the overall heat pipe pressure drops depending on whether the acceleration force on the heat pipe favors or opposes liquid return. The computer will account for this drop by evaluating the heat pipe performance on the basis of the angle of inclination, $\phi$, with the horizontal. For the high temperature heat pipe design calculated for ICICLE, the gravity term was made zero ($\phi = 0$) since zero gravity operation is anticipated. For proper evaluation of these heat pipe designs in a one g environment, they should be operated in a horizontal attitude.

The computer program also has the capability to calculate fluid dynamic performance with composite wick structures. In general, the composite structures consist of wicks with two or more types of porosity. A fine pore structure is used in the evaporator to develop high capillary pumping pressure while a more coarse structure is used in the condenser and adiabatic zones to reduce the liquid pressure drop. The

computer can evaluate heat-pipe performance with both series and parallel composite wicks. In the series structure, a fine wick is used in the evaporator and then connected in series to a coarser wick in the adiabatic and condenser zones. The parallel structure consists of a coarse wick next to the heat-pipe wall for low impedance liquid return and a fine structure facing the vapor space to give high capillary pumping pressure.

The computer program also has a subroutine for calculating the weight of the heat pipe. At the time a printout is made of the pressure drops and thermal power transfer capability, a subroutine is entered which calculates and prints out the weight of the particular heat pipe design. This calculation includes the weight of the container, end plates, wick structure, and working fluid. Using this subroutine a rapid comparison of weights was made for all of the designs calculated for the ICICLE high-temperature heat pipe.

Using the RCA computer heat pipe design program (code HPDP-18), a great many heat-pipe designs were evaluated. These heat pipes contained various working fluids and had a variety of geometries. In general, they were all right circular cylinders, but the length and diameter was allowed to vary. For each geometrical configuration a number of wick structures were evaluated and the most promising selected. The results of these computations were plotted and appear in Section 5.B.5.

## 2. Fluid Selection

The selection of the working fluid for the high temperature heat pipes was based on fluid-flow considerations because the candidate fluids are all liquid metals which have relatively high thermal conductivities; therefore, the heat pipes will have low input and output temperature drops.

For a given temperature, geometry, and wick structure, the maximum power throughput in a heat pipe is proportional to a figure of merit (FOM) which combines the relevent fluid properties. For laminar flow this expression takes the form:

$$\text{FOM} = h\,\gamma \left( \frac{\rho_v \rho_\ell}{\eta_v \eta_\ell} \right)^{1/2} \qquad (5\text{-}61)$$

In selecting working fluids for the high-temperature heat pipe, two operating temperature requirements have been considered. These are (1) 627° C (900° K) for direct coupling of the heat pipe to the VM engine and (2) 943° C (1216° K) for radiation coupling the heat pipe to the VM engine. For these temperatures, four candidate working fluids have been evaluated on the basis of their figures of merit. These are the alkali metals; cesium, potassium, sodium, and lithium. The figure of merit of

each of these fluids was calculated over its normal operating range and is plotted in Fig. 5-6. Cesium is ruled out as a logical candidate because its thermodynamic flow characteristics are relatively poor at the temperatures of interest, as shown in Fig. 5-6.

At temperatures up to 590° C potassium is the superior working fluid. Of temperatures from 590° C to 1170° C sodium is the preferred fluid, and at temperatures above 1170° C lithium has the best power transfer characteristics. Heat pipe power transfer characteristics were calculated using all three of the latter working fluids. The results of these calculations are shown in Section 5.B.5.

In addition to the thermodynamic heat transfer characteristics, the working fluid must have other desirable attributes. The fluids should have a low wetting angle with respect to the capillary surface. In a number of experiments performed on operating heat pipes, it has been determined that the wetting of metal surfaces by potassium, sodium, and lithium is excellent. These highly active metals form a very low wetting angle with the metal containers so that a zero wetting angle was used in all calculations performed.

All three metallic working fluids have high coefficients of thermal conductivity so that thermal drops getting into and out of the heat pipe are minimized. At

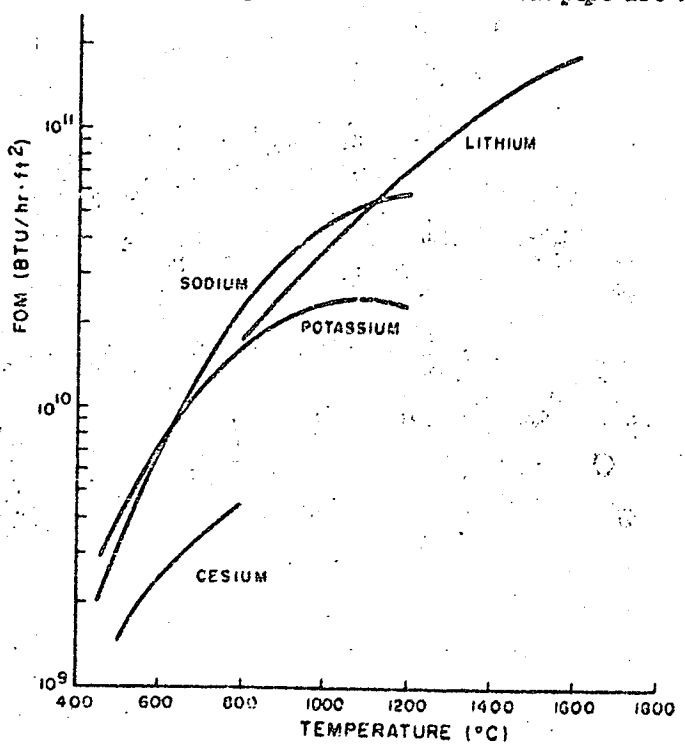



Fig. 5-6. Figure of merit as a function of temperature for potassium, sodium, lithium, and cesium.

the operating temperature of 649° C (1200° F) potassium and sodium have thermal conductivities of 19.5 and 35.5 Btu/h/ft/° F, respectively. At 943° C (1730° F) lithium has a thermal conductivity of 28.7 Btu/h/ft/° F.

The vapor pressure of the working fluid should be sufficiently high at the operating temperature so that heat pipe operation is well below the sonic limit, but not so high as to require an inordinately high wall thickness since this will act to increase the temperature drops getting into and out of the heat pipe as well as to increase the overall weight.

The sonic limit has been defined by Kemme[17] as the ultimate heat transfer rate which can be reached when the average velocity of the vapor leaving the evaporator reaches sonic velocity. Kemme has shown that the rate can be found from the following expression.

$$Q_s = \frac{\rho_v V_s h A}{\sqrt{2 (k + 1)}}. \qquad (5\text{-}62)$$

where

$Q_s$ is the heat transfer rate (cal/sec)

$\rho_v$ is vapor density (gms/cc)

h is latent heat of vapor (cal/gm)

A is cross sectional area of vapor duct ($cm^2$)

k is ratio of specific heats of vapor at constant pressure to vapor at constant volume ($c_p/c_v$)

$V_s$ is velocity of sound in vapor at temperature of interest (cm/sec).

The sonic vapor velocity may be found from:

$$V_s = \sqrt{\frac{k R T}{M}} \qquad (5\text{-}63)$$

where

R is the universal gas constant ($8.3 \times 10^7$ ergs/mol/°

T is temperature (° K)

M is molecular weight of vapor (gms).

Based on the expressions above, the sonic limit, $Q_g/A$, in watts per square cm of vapor space was calculated and plotted for potassium, sodium, and lithium over the temperature ranges of interest as shown in Fig. 5-7.

It can be seen from these data that at an operating temperature of 627° C (900° K) the sonic limit of potassium is 8300 W/cm$^2$ and sodium is 2800 W/cm$^2$ and hence are no limit to any reasonable heat pipe design. At this temperature, lithium would be down to approximately 100 W/cm$^2$ and the sonic limit would be expected to be reached in some heat pipe designs. At the higher temperature of 943° C (1216° K) lithium is well above the sonic limit for most practical pipe designs.

### 3. Wick Design

The basic requirement of the wick is that it must be capable of pumping the condensed working fluid back to the evaporator in the quantities required to sustain heat-pipe operation at the desired power level. The wick design will generally be either a homogeneous or a composite type. Homogeneous wicks have a nearly uniform pore structure so that the pore size must be optimized to give maximum pumping pressure with minimum drag. Composite wicks, as previously described, have small pores to do the pumping and large pores elsewhere to reduce fluid flow resistance. The composite wicks have the disadvantage that when momentary overloads or other non-uniform operating conditions occur, the large pore section will empty

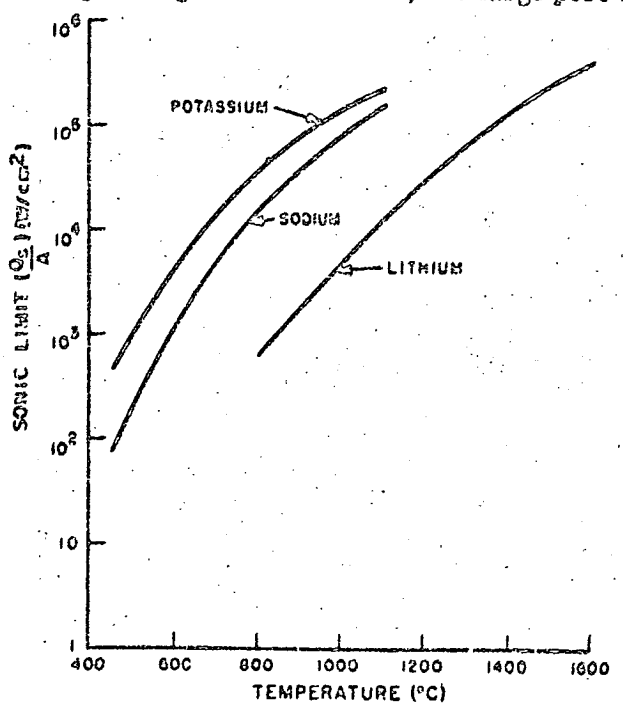



Fig. 5-7. Sonic limit as a function of temperature for potassium, sodium, and lithium.

and cause heat pipe failure. On this basis a self-priming wick structure was indicated for the ICICLE high-temperature heat pipe and consequently a homogeneous wick design was used for all heat pipe calculations. Most of the heat pipes were evaluated with multiple layers of screen wick sintered to the inside of the heat pipe. Wicks of this type have been used extensively in high-temperature heat pipes at RCA. The wick factors b, c, and $r_c$ have been measured and determined empirically so that their characteristics are well known.

4. Containment Material

The material used as the containment vessel of the heat pipe must have several properties which are important for long undegraded performance of the heat pipe. The material should be chemically compatible with the working fluid so that no reaction can occur. It must have sufficient hot strength and long term creep properties to retain the shape for the expected 5 year period of operation. The material should have a low evaporation rate so that the wall thickness does not change appreciably with life. The material should be compatible with the isotope and engine interfaces. The material should lend itself to the cleaning and high temperature outgassing operation required for good heat pipe processing.

At the lower temperature of 627° C (900° K) considered for direct coupling of the heat pipe to the engine, there are a great many materials available for containment. The 300 series stainless steel 304 and 316, pure nickel, and the super alloys such as Inconel and Hastelloy X all have acceptable properties. The chemical compatibility of these materials with sodium and potassium have been proved in life tests at RCA. Heat pipes made from 304, 316 and nickel and using sodium as the working fluid have operated at temperatures above 649° C (1200° F) for periods exceeding 10,000 hours. A Hastelloy X-sodium heat pipe has exceeded 20,000 hours at 715° C and a nickel-potassium heat pipe has exceeded 30,000 hours of undegraded operation at 600° C.

At 649° C (1200° F) potassium and sodium have vapor pressures of 5.0 psia and 0.95 psia respectively. At these internal pressures a wall thickness can be calculated based on published creep strength data according to the hoop stress expression:

$$t = \frac{Pd}{2S} \qquad (5\text{-}64)$$

where

t is the wall thickness (in)

P is the internal pressure (psi)

d is the outside diameter (in)

S is the maximum allowable creep stress (psi)

For 304 stainless steel a stress of 4000 psi is given for a 0.00001 percent per hour creep rate[18] at 649° C (1200° F). Using this limit for potassium at 5.0 psia on the largest diameter pipe considered (2 in), t is calculated to be $1.25 \times 10^{-3}$ in.

Any nominal wall tubing would have acceptable creep stress. All of the computer calculations used a value of 0.050 in. as a standard wall thickness.

The vapor pressures of nickel and the constituents of stainless steels, and super alloys are below $10^{-10}$ torr at 649° C (1200° F). At this low value evaporation of the containment material is not a problem.

These materials are easily formed, welded, and processed into heat-pipe structures. They can be joined to both the isotope capsule or the VM engine by welding, brazing, or mechanical joints.

At the higher temperature of heat-pipe operation required by radiation coupling to the VM engine, the containment problems are more severe. While the lower creep stress of the material and higher internal pressure (26 psia for sodium) dictate a heavier wall thickness, the over-riding factor to be considered is the increased evaporation rate of the wall material at the higher temperature. Excessive evaporation will make it very difficult to retain a high-emissivity surface for coupling the heat from the heat pipe, since it will cause loosening of a high-emissivity coating and thermal polishing of the base metal. In addition, evaporated material could affect the properties of the thermal insulation. It could also affect electronic or other on board equipment.

The amount of material evaporated from a surface may be found from:

$$\mu = \frac{\alpha P}{\sqrt{2\pi MRT}} \qquad (5\text{-}65)$$

where

$\mu$ is the evaporation rate (moles/cm$^2$/s)

P is the vapor pressure of material at temperature, T (dynes/cm$^2$)

$\alpha$ is sticking coefficient

M is molecular weight (gms/mole)

R is universal gas constant (erg/° K/gm/mol)

The evaporation rate $\mu$ for nickel at 1800° F with $\alpha = 1$, $P = 10^{-7}$ mm Hg, M = 58.71 g/mol, and $R = 8.31 \times 10^{-7}$ erg/° K-g-mol, is calculated to be $2.15 \times 10^{11}$ moles/cm$^2$/s.

This rate is equivalent to a total evaporation of 0.010 in. from the surface during a 5-year mission. Comparisons of vapor pressures of nickel, iron, and chromium with the refractory metals are presented in Table 5-3. It can be seen that none of the former metals, which are the main constituents of stainless steels and super alloys, are acceptable for a 943° C (1730° F) heat pipe for a 5-year mission time.

Of the candidate materials, molybdenum, columbium, rhenium, tantalum, and tungsten are the only materials with sufficiently low vapor pressure to be acceptable for the ICICLE high temperature heat pipe if radiation coupling is employed. Rhenium, tantalum, and tungsten can be ruled out from a cost and fabricability standpoint. Consequently, alloys of molybdenum and niobium are recommended for use in the high-temperature heat pipe. RCA has considerable experience with TZM-molybdenum when used as the containment material for lithium and sodium heat pipes. Long life operations results from the good compatibility of these materials. Nobium - 1 Zr can also be used for the heat pipes at 943° C. Pure nobium and molybdenum are not recommended since the small additions of titanium and zirconium in the alloys offer a large measure of protection against oxygen erosion in the heat pipe by reacting with any unwanted residuals of this gas.

TABLE 5-3. VAPOR PRESSURE - TEMPERATURE DATA OF CANDIDATE MATERIALS

| Material | Temperature (°F) | | |
|---|---|---|---|
| | at $10^{-10}$ Torr | at $10^{-8}$ Torr | at $10^{-6}$ Torr |
| Chromium | 1359 | 1539 | 1791 |
| Iron | 1431 | 1638 | 1890 |
| Nickel | 1503 | 1701 | 1952 |
| Molybdenum | 2583 | 3023 | 3312 |
| Columbium | 2682 | 3204 | 3609 |
| Rhenium | 3132 | 3537 | 4023 |
| Tantalum | 3177 | 3555 | 4059 |
| Tungsten | 3411 | 3843 | 4365 |

5. Design Calculations

Using the computer heat pipe design program (code HPDP-16) a large number of potential heat-pipe designs were calculated and evaluated for thermal power transport and weight characteristics. A review of these results are presented in this section.

In the first series of curves, sodium and potassium working fluids were evaluated in stainless steel containers at an operating temperature of 627° C.

Figure 5-8 shows the power throughput capabilities versus length for sodium at 627° C for 1.0-in diameter heat pipe. Each design was calculated for three different wick structures and the optimum number of wraps of mesh is shown. The small numbers beside the data points are the weight in pounds for each design.

Figure 5-9 shows the same data for a 1.5-in OD heat pipe.

Figures 5-10 through 5-15 show cross plots at 627° C of power versus weight for pipe lengths of 6, 12, 24, 48, 72, and 96 in, respectively. In each case the design is evaluated for three different wick structures. The data points are for the optimum wick thickness for maximum heat transfer.

Figure 5-16 is a cross plot showing power versus outside diameter for a 12-in. length of heat pipe with the optimum number of wick wraps.

Figures 5-17 through 5-20 show power versus length for potassium heat pipes operating at 627° C. The illustrations present the data for outside diameters of 0.5, 1.0, 1.5, and 2.0 in. respectively. Each design was calculated for three different wick structures and thickness. The small numbers beside the data points are weights in pounds.

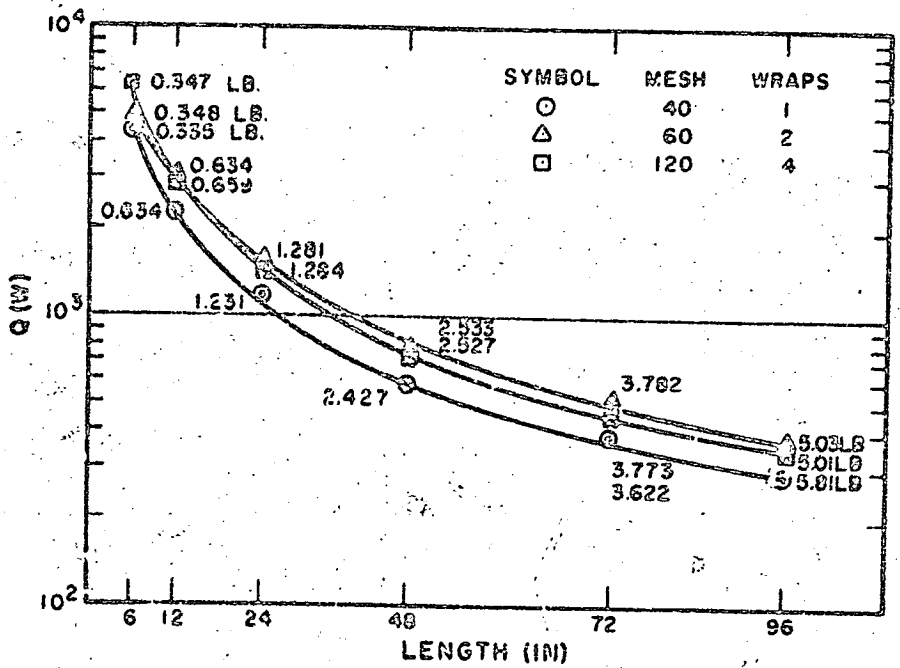



Fig. 5-8. Power throughput capability as a function of length for sodium in stainless steel heat pipes with mesh wicks, diameter of 1.0 in, and wall thickness at 0.05 in. at a temperature of 627° C and a temperature drop of 25° C with wick structure as a parameter.

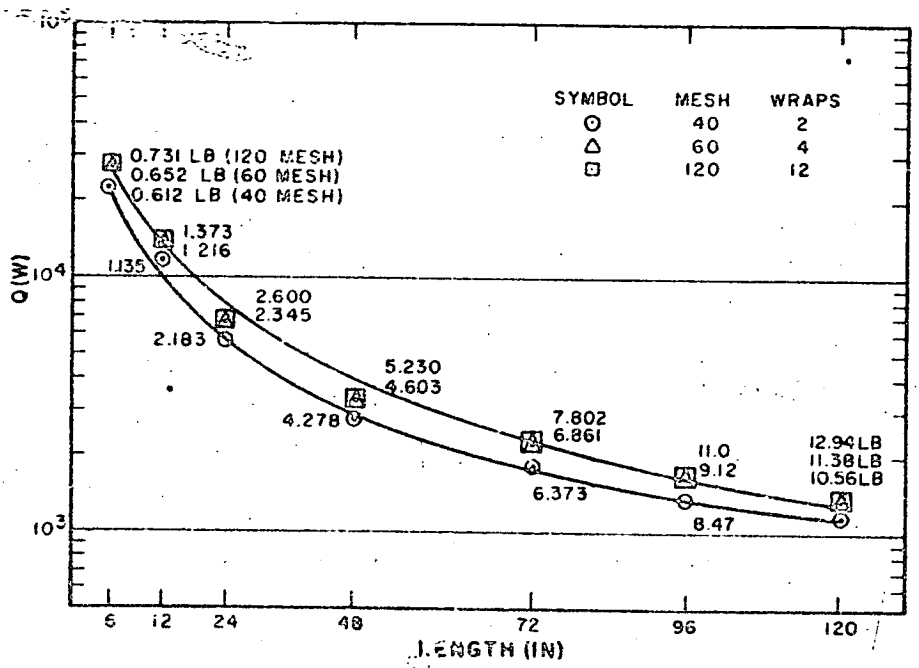



Fig. 5-9. Power throughput capability as a function of length for sodium in stainless steel heat pipes with mesh wicks, diameter of 1.5 in, and wall thickness at 0.05 in. at a temperature of 627° C and a temperature drop of 25° C with wick structure as a parameter.

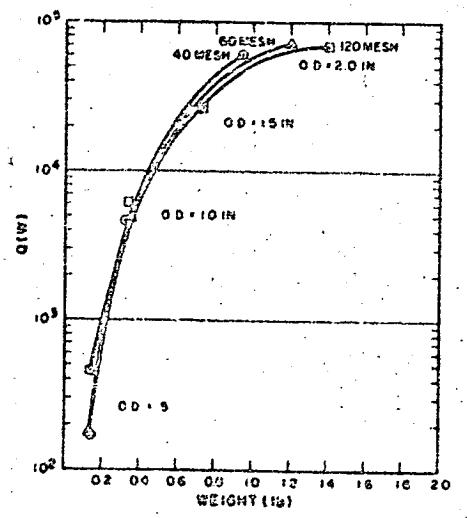



Fig. 5-10. Power throughput capability as a function of weight for 6-in long stainless steel sodium heat pipes with mesh wicks, wall thickness of 0.050 in. at a temperature of 626° C and a temperature drop of 25° C with mesh gage and outside diameter as parameters.

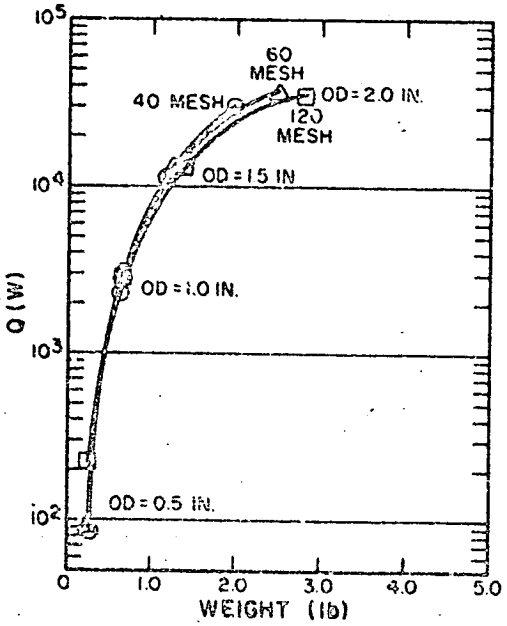



Fig. 5-11. Power throughput capability as a function of weight for 12-in-long sodium in stainless steel heat pipes with mesh wicks, wall thickness of 0.050 in. at a temperature of 627° C with mesh gage and outside diameter as parameters.

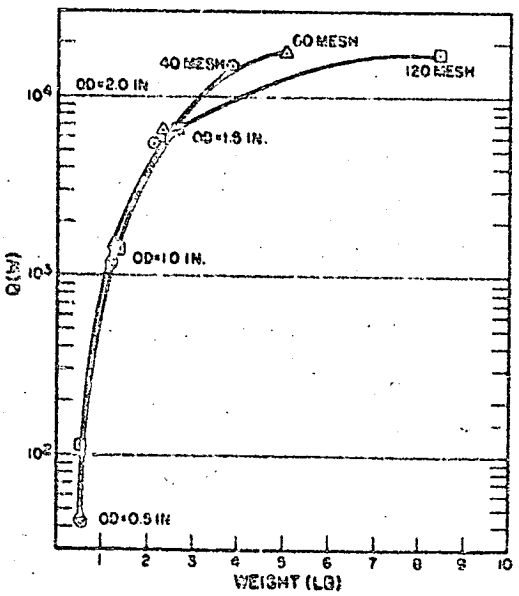



Fig. 5-12. Power throughput capability as a function of weight for 24-in-long sodium in stainless steel heat pipes with mesh wicks, wall thickness of 0.050 in. at a temperature of 627° C with mesh gage and outside diameter as parameters.

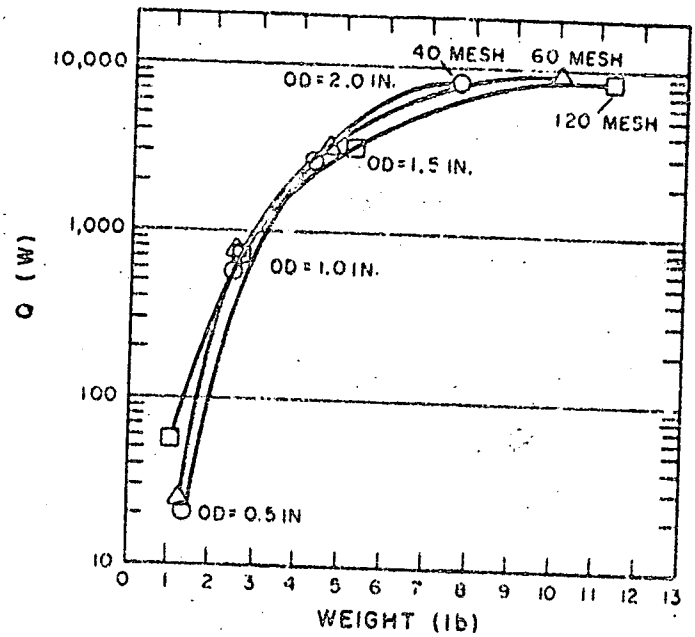



Fig. 5-13. Power throughput capability as a function of weight for 48-in-long sodium in stainless steel heat pipes with mesh wicks, wall thickness of 0.050 in. at a temperature of 627° C with mesh gage and outside diameter as parameters.

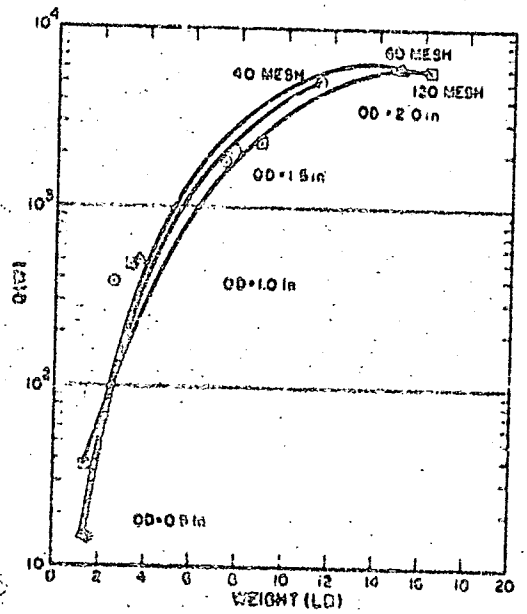



Fig. 5-14. Power throughput capability as a function of weight for 72-in-long sodium in stainless steel heat pipes with mesh wicks, wall thickness of 0.050 in. at a temperature of 627° C with mesh gage and outside diameter as parameters.

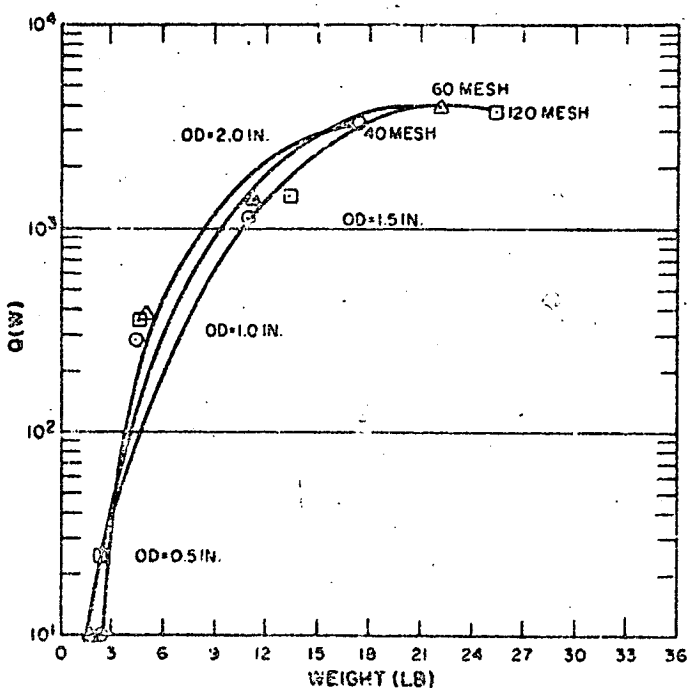



Fig. 5-15. Power throughput capability as a function of weight for 96-in-long sodium in stainless steel heat pipes with mesh wicks, wall thickness of 0.050 in. at a temperature of 627° C with mesh gage and outside diameter as parameters.

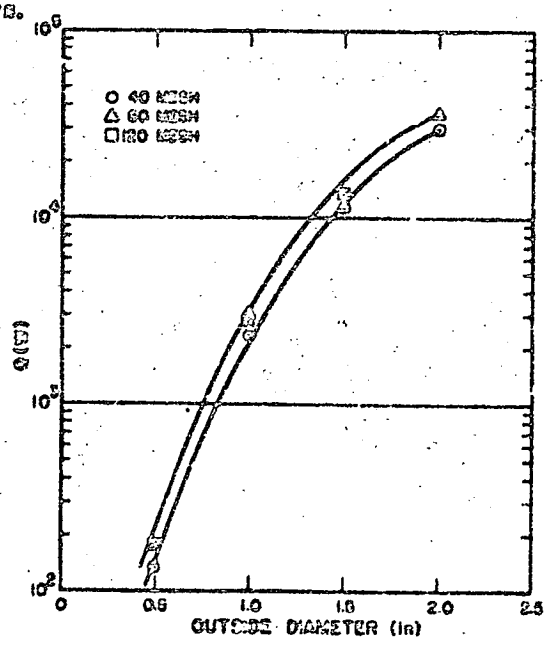



Fig. 5-16. Power throughput capability as a function of outside diameter for 12-in-long sodium in stainless steel heat pipes with mesh wicks at an optimum number of wraps, wall thickness of 0.050 in. at a temperature of 627° C with mesh gage as a parameter.

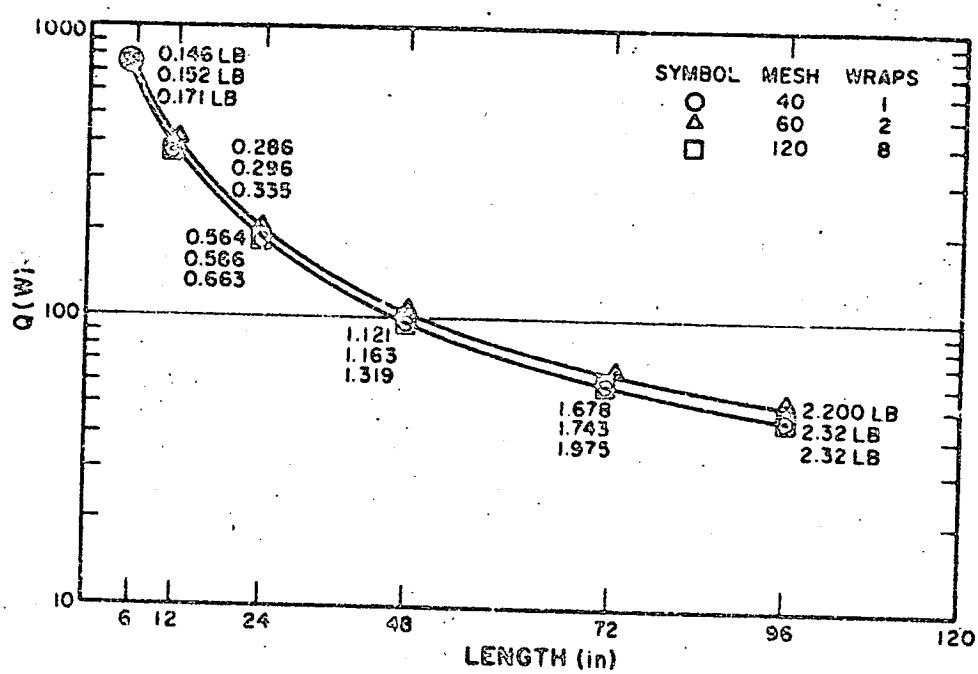



Fig. 5-17. Power throughput capability as a function of length for potassium in stainless steel heat pipes with mesh wicks, diameter of 0.5 in. and wall thickness of 0.050 in. at a temperature of 627° C and a temperature drop of 25° C with wick structure as a parameter.

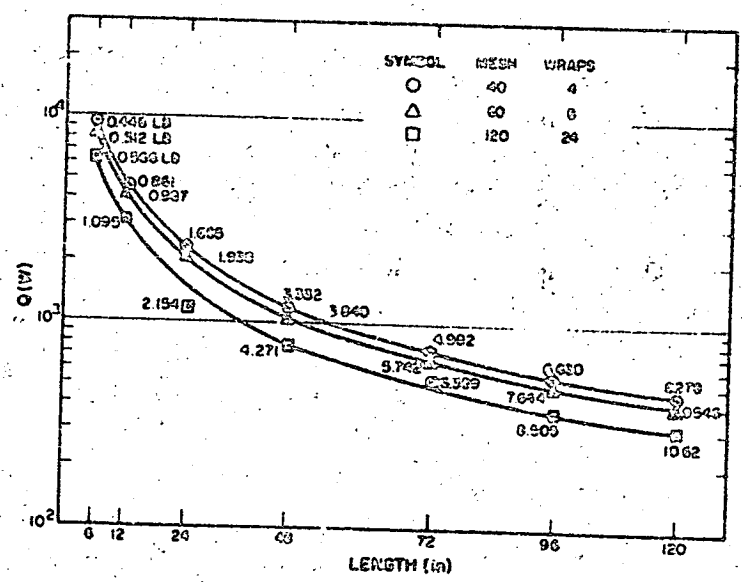



Fig. 5-18. Power throughput capability as a function of length for potassium in stainless steel heat pipes with mesh wicks, diameter of 1.0 in. and wall thickness of 0.050 in. at a temperature of 627° C and a temperature drop of 25° C with wick structure as a parameter.

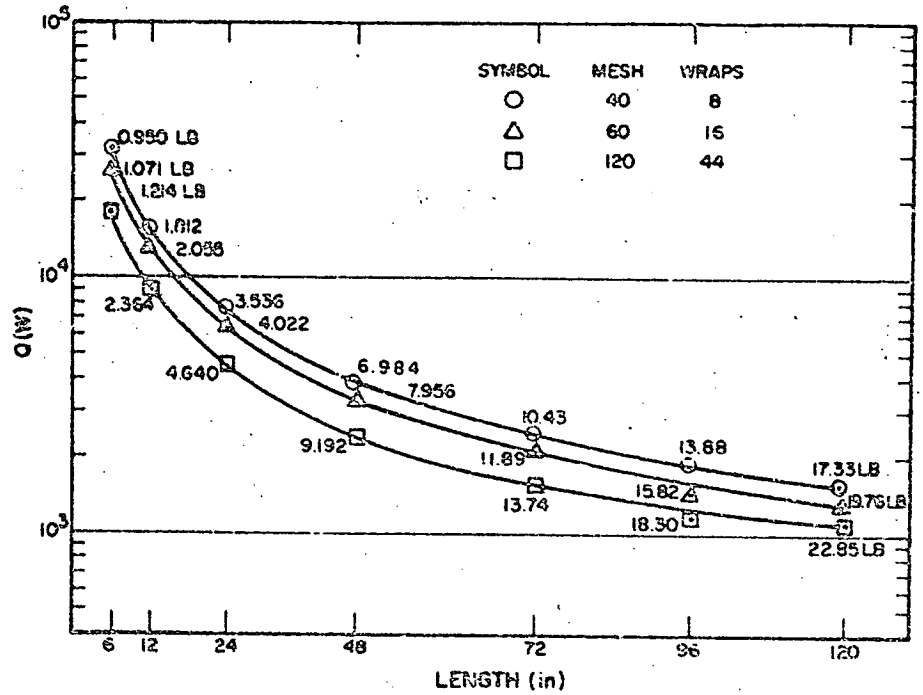



Fig. 5-19. Power throughput capability as a function of length for potassium in stainless steel heat pipes with mesh wicks, diameter of 1.5 in. and wall thickness of 0.050 in. at a temperature of 627° C and a temperature drop of 25° C with wick structure as a parameter.

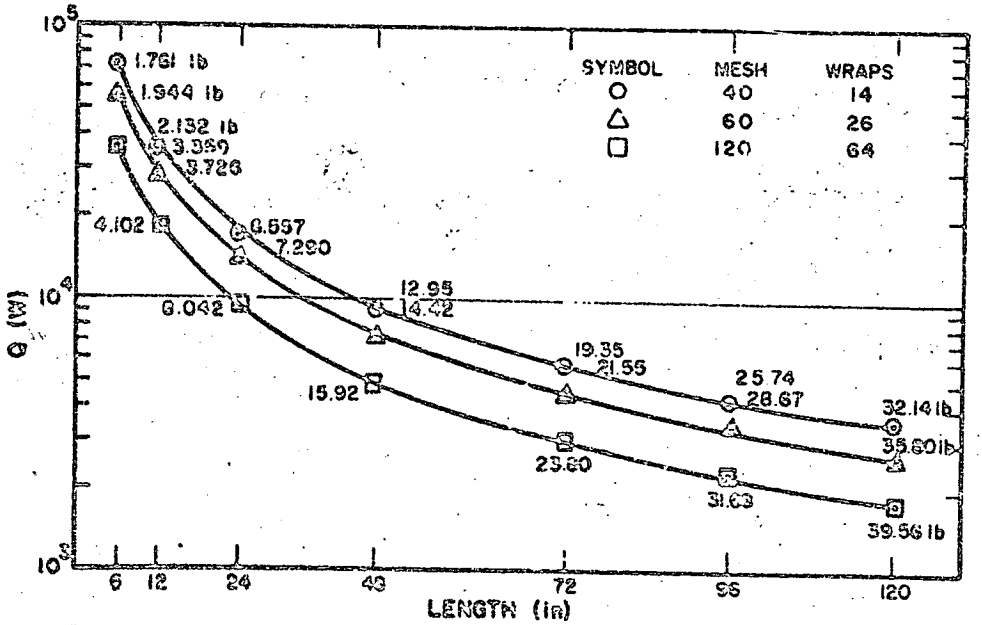



Fig. 5-20. Power throughput capability as a function of length for potassium in stainless steel heat pipes with mesh wicks, diameter of 2.0 in. and wall thickness of 0.050 in. at a temperature of 627° C and a temperature drop of 25° C with wick structure as a parameter.

Figures 5-21, 5-22, and 5-23 show power versus length data for sodium operating at 677° C for heat pipes 1.0, 1.5, and 2.0 in. in diameter, respectively. This temperature assumes 649° C at the VM engine with a 28° C conductive drop between heat pipe and engine. At the higher temperature the power transfer capability has increased primarily because of a higher vapor density.

Figures 5-24, 5-25, and 5-26 show power versus length data for potassium heat pipes operating at 677° C. These data are also for heat pipes having outside diameters of 1.0, 1.5, and 2.0 in. respectively. The weights and capillary mesh sizes are indicated.

Figures 5-27, 5-28, and 5-29 show the characteristics of sodium heat pipes operating at 943° C which is the temperature of operation for radiation coupling the heat pipe to the VM engine. The power transfer capability is considerably increased over the lower temperature heat pipe so that a smaller, lighter-weight heat pipe results. The weights shown are for stainless containers with a 0.050-in wall thickness. The actual heat pipe would use a molybdenum alloy that is approximately 20% heavier than stainless steel. However, the strength-to-weight ratio is higher so that a thinner shell can be used and the weights shown are representative.

Figures 5-30 through 5-33 show the power versus length relationship for lithium-TZM molybdenum heat pipes operating at 850° C, 900° C, 950° C, and 1,000° C,

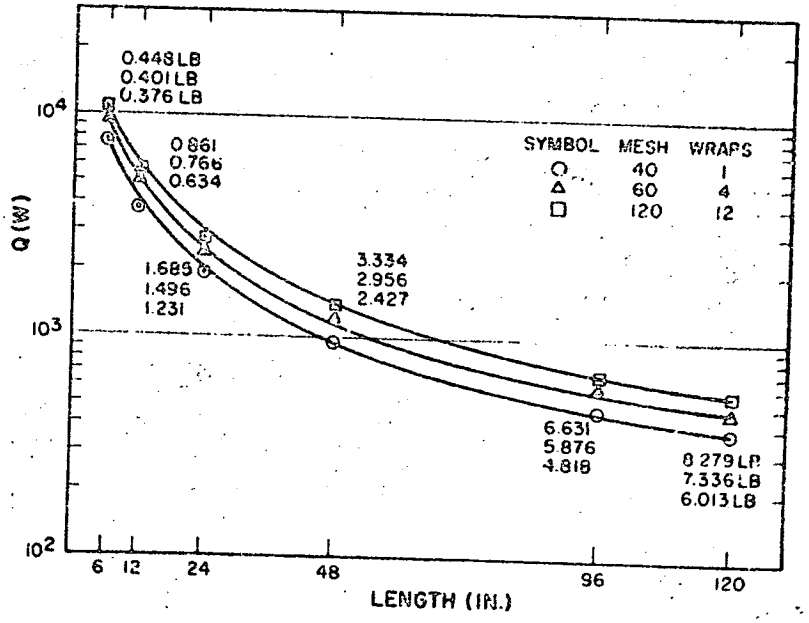



Fig. 5-21. Power throughput capability as a function of length for sodium heat pipes 1.0 in. in diameter at a temperature of 677° C and a temperature drop of 28° C with wick structure as a parameter.

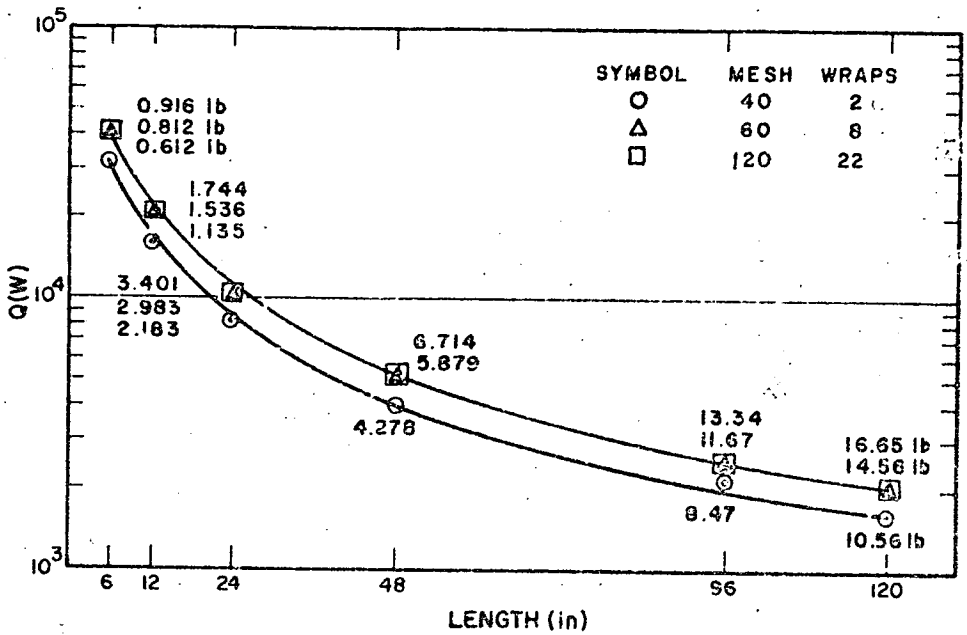



Fig. 5-22. Power throughput capability as a function of length for sodium heat pipes 1.5 in. in diameter at a temperature of 677° C and a temperature drop of 28° C with wick structure as a parameter.

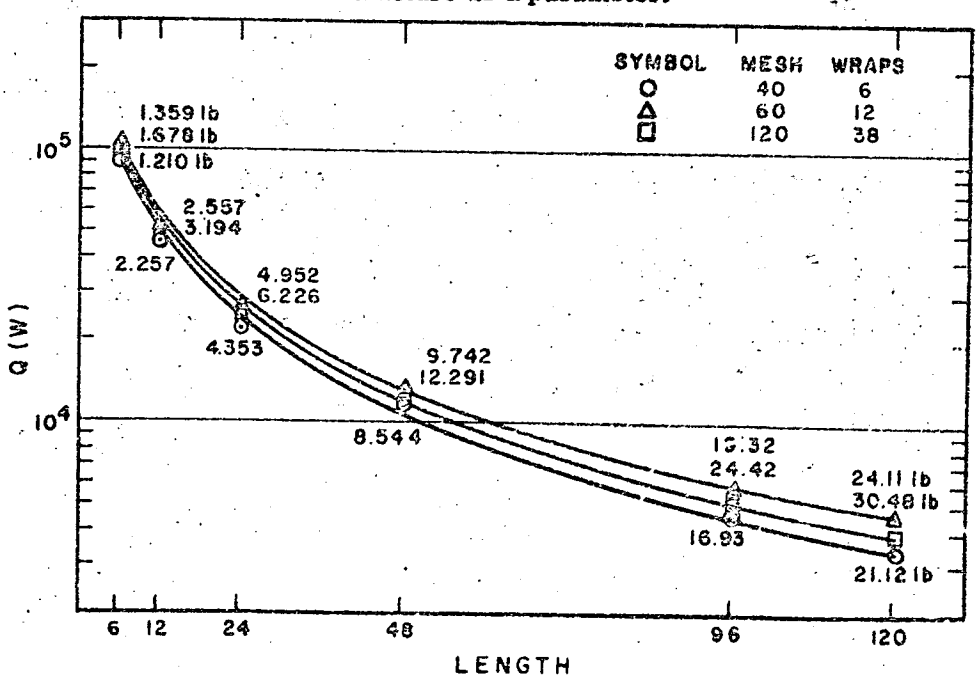



Fig. 5-23. Power throughput capability as a function of length for sodium heat pipes 2.0 in. in diameter at a temperature of 677° C and a temperature drop of 28° C with wick structure as a parameter.

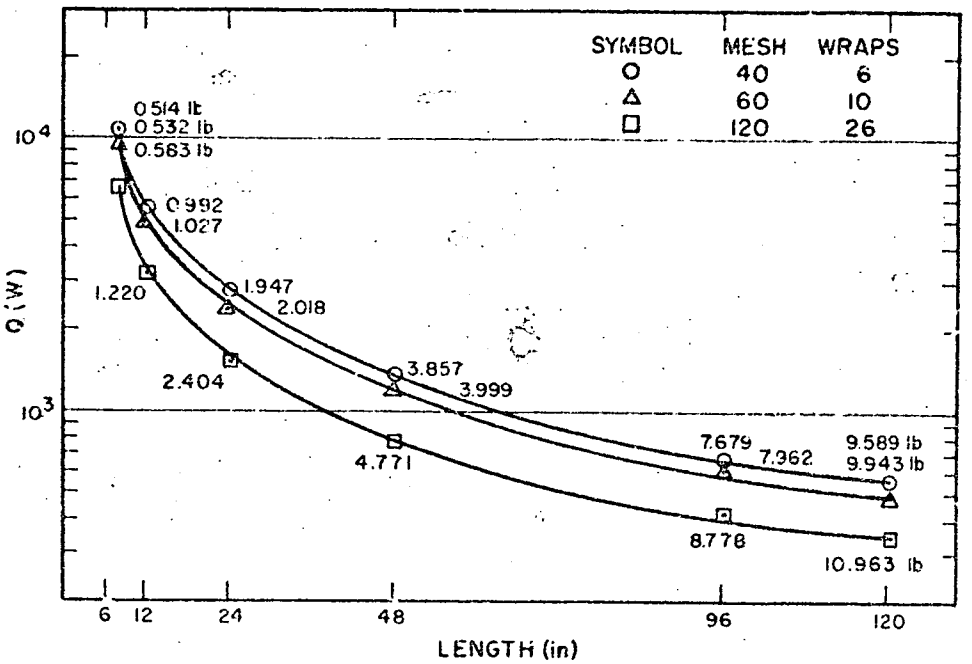
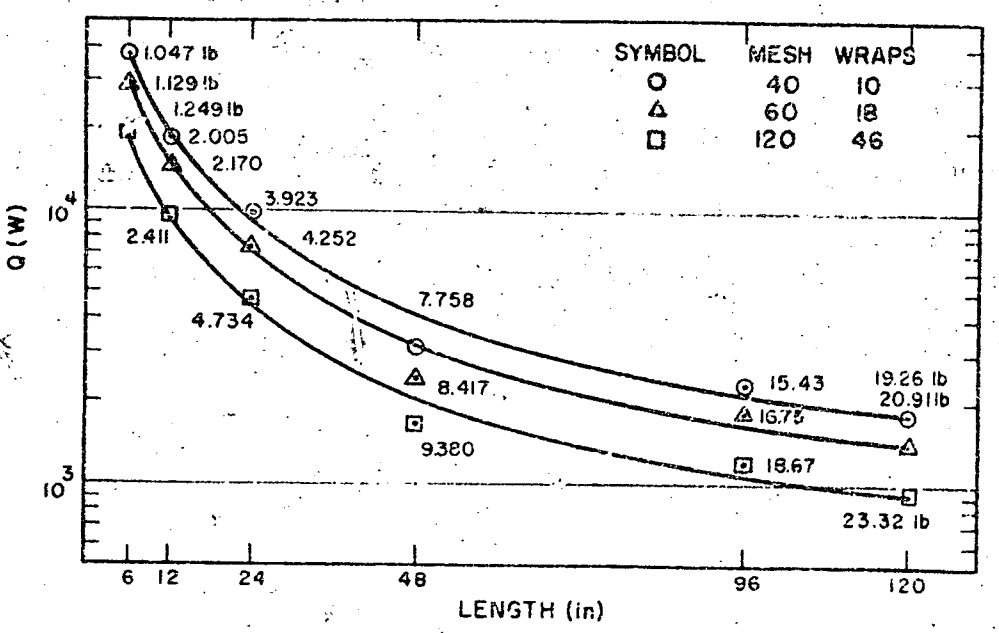



Fig. 5-24. Power throughput capability as a function of length for potassium heat pipes 1.0 in. in diameter at a temperature of 677° C with wick structure as a parameter.




5-25. Power throughput capability as a function of length for potassium heat pipes 1.5 in. in diameter at a temperature of 677° C with wick structure as a parameter.

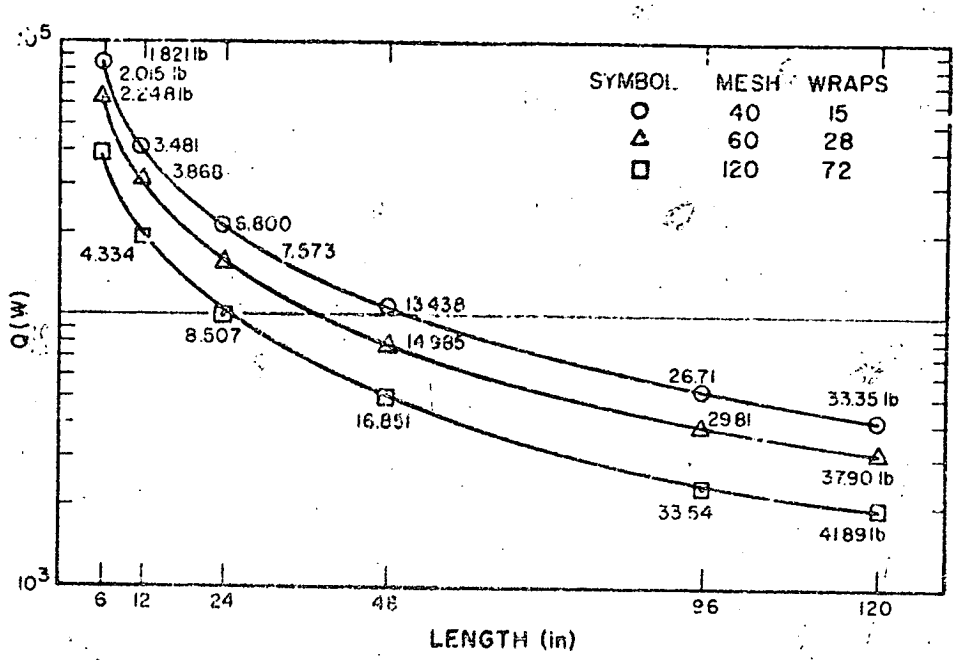



Fig. 5-26. Power throughput capability as a function of length for potassium heat pipes 2.0 in. in diameter at a temperature of 677° C with wick structure as a parameter.

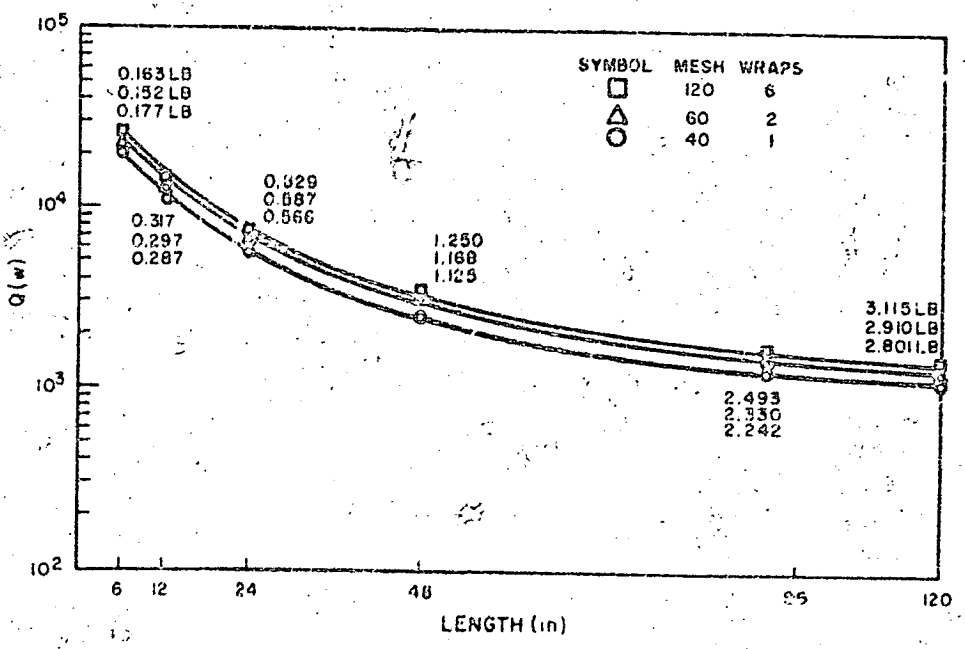



Fig. 5-27. Power throughput capability as a function of length for sodium in stainless steel heat pipes with a diameter of 0.5 in and a wall thickness of 0.050 in. at a temperature of 943° C with wick structure as a parameter.

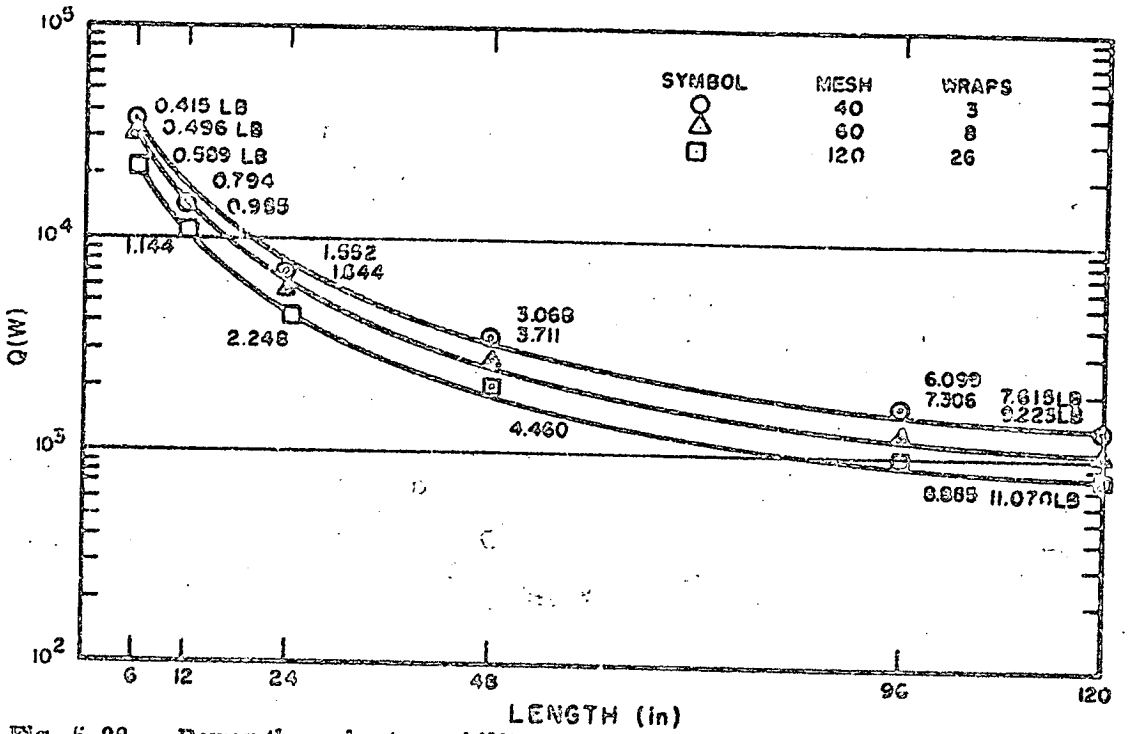
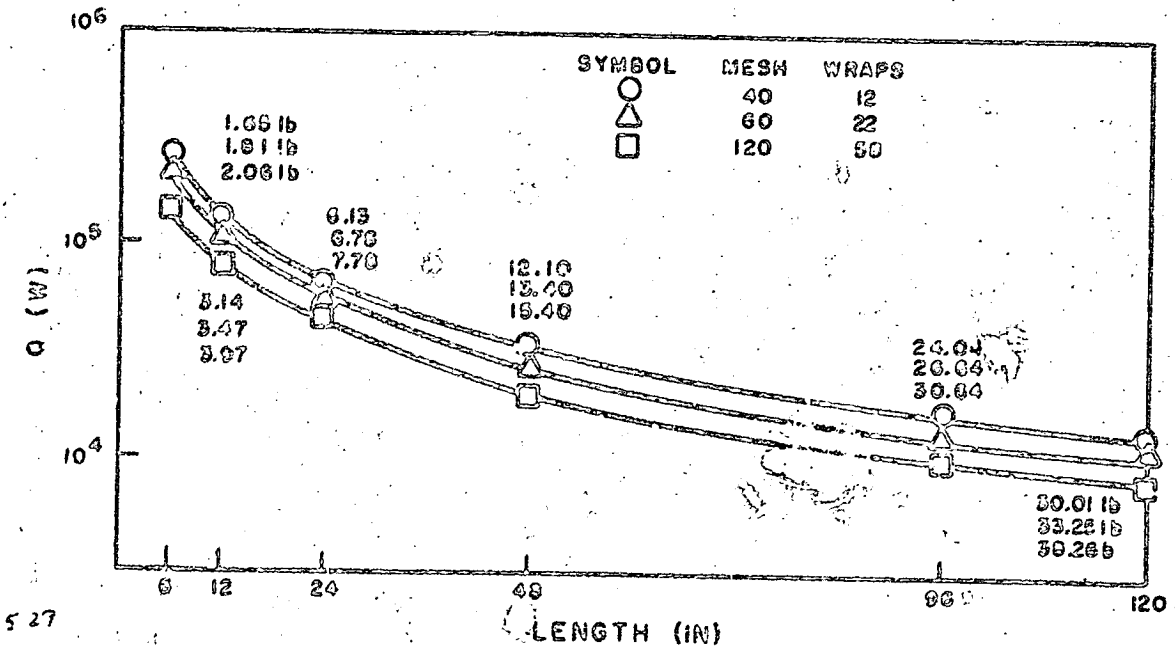



Fig. 5-28. Power throughput capability as a function of length for sodium in stainless steel heat pipes with a diameter of 1.0 in. and a wall thickness of 0.050 in. at a temperature of 843° C with wick structure as a parameter.




5 27

Fig. 5-29. Power throughput capability as a function of length for sodium in stainless steel heat pipes with a diameter of 2.0 in. and a wall thickness of 0.050 in. at a temperature of 843° C with wick structure as a parameter.

respectively. Each illustration shows the data for four heat pipe diameters of 0.5, 1.0, 1.5 and 2.0 in. The wick structure was essentially the same in all the heat pipes because liquid pumping was not the limit on power throughput. Rather, because of the low operating temperatures, the maximum power transfer was limited by the vapor pressure drop and attending temperature drop in the heat pipe. A maximum temperature drop of 50°C was allowed in the calculations and the maximum power transfer is limited by this condition. The sonic limit was tested along each curve and the power at the sonic limit is shown by the triangle. The wall material was 0.05-in-thick TZM-molybdenum so the weights shown are realistic.

## 6. Operational Summary

### a. Thermodynamic Flow

The operating characteristics of the potential heat pipes designs are best depicted by plotting the product of maximum power throughput and length versus the heat pipe diameter. When plotted in this manner the data may be used by multiplying the required power throughput by the desired length of transfer. Entering the curve with this product will yield the minimum heat pipe diameter required. This result will give the diameter required to carry the power, however, a further assessment must be made to determine whether the diameter is acceptable from a temperature drop standpoint. This latter point will be discussed later.

Four heat pipe operational curves have been plotted. Figure 5-34 shows the QZ versus diameter for a lithium-TZM molybdenum heat pipe operating at 943°C (1216°K). Each data point was arrived at by calculating the maximum power throughput, optimum wick size and optimum number of wraps for each diameter. The weight per foot for each design is shown on the lower portion of the curve. Figure 5-35 shows the same type of data for a sodium-stainless steel heat pipe operating at 943°C (1216°K). The weight curve would be increased by approximately 20% if TZM-molybdenum is used as recommended. Figure 5-36 gives the operational data for a sodium in stainless steel heat pipe at 627°C (900°K) and Fig. 5-37 gives the data for a potassium in stainless steel heat pipe at 627°C (900°K). On all curves the optimum number of wraps is shown as the small number beside each data point.

## 7. Temperature Drop

The temperature drop associated with a heat pipe must be considered and accounted for when integrating a high temperature heat pipe into the ICICLE system. The isotope must operate at a high enough temperature to make up for any temperature losses. Consequently, it is necessary to keep the heat pipe temperature drops to a minimum to prevent an excessively high isotope operating temperature.

The overall temperature drop in the heat pipe is:

$$\Delta T_t = \Delta T_l + \Delta T_e + \Delta T_v + \Delta T_c + \Delta T_o \qquad (5\text{-}66)$$

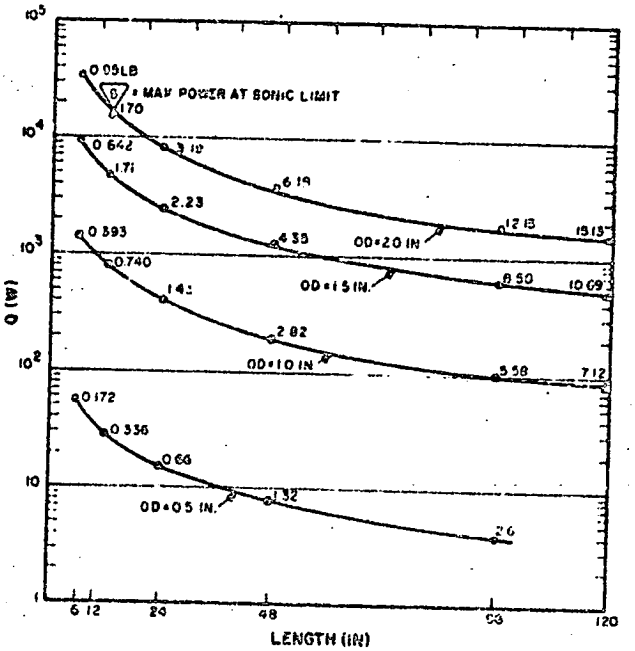



Fig. 5-30. Power throughput capability as a function of length with diameter as a parameter for lithium in TZM-molybdenum heat pipes with 120 mesh wick operating at an evaporator temperature of 850°C and a temperature drop of 50°C.

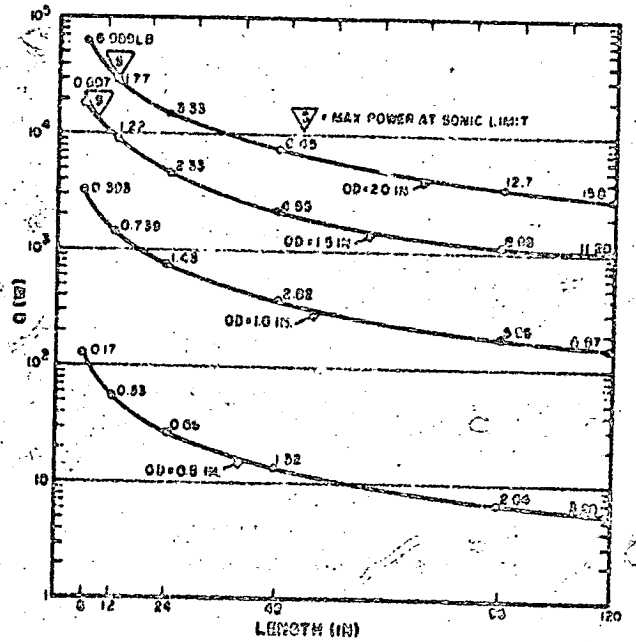



Fig. 5-31. Power throughput capability as a function of length with diameter as a parameter for lithium in TZM-molybdenum heat pipes with 120 mesh wick operating at an evaporator temperature of 900°C and a temperature drop of 50°C.

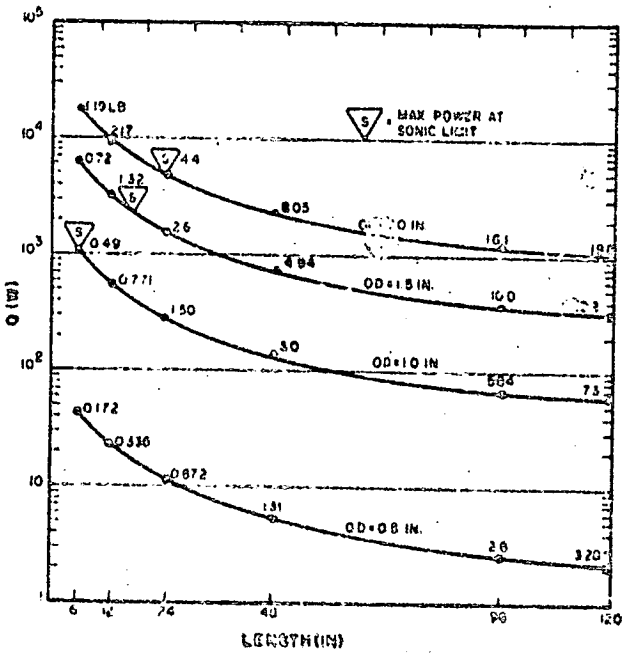



Fig. 6-32. Power throughput capability as a function of length with diameter as a parameter for lithium in TZM-molybdenum heat pipes with 120 mesh wick operating at an evaporator temperature of 850°C and a temperature drop of 50°C.

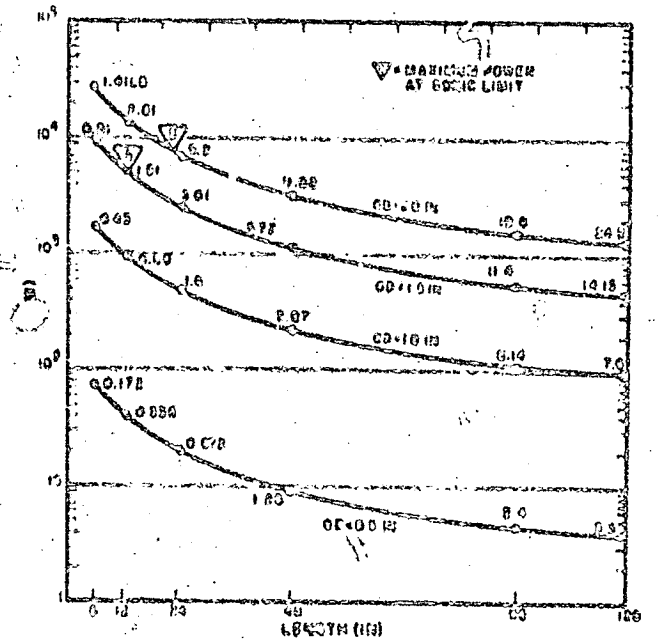



Fig. 6-33. Power throughput capability as a function of length with diameter as a parameter for lithium in TZM-molybdenum heat pipes with 120 mesh wick operating at an evaporator temperature of 1000°C and a temperature drop of 50°C.

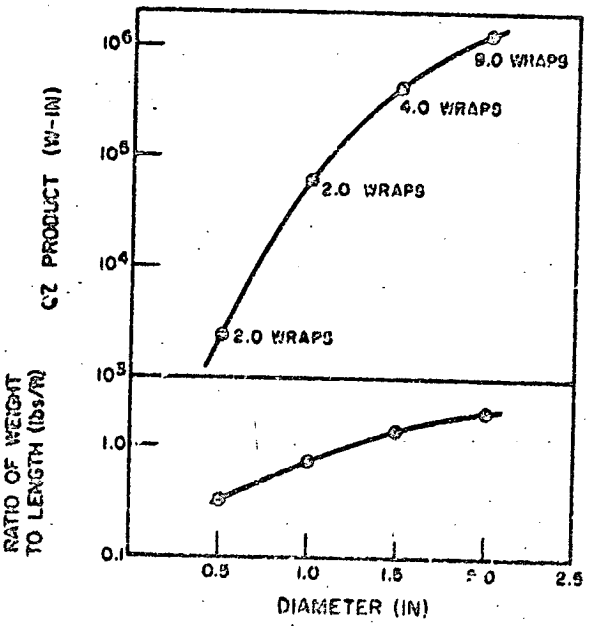



Fig. 5-34. Product of maximum power throughput and length at zero g and weight-to-length ratio as functions of diameter for lithium in TZM-molybdenum heat pipes with 120 mesh wick operating at an evaporator temperature of 943°C.

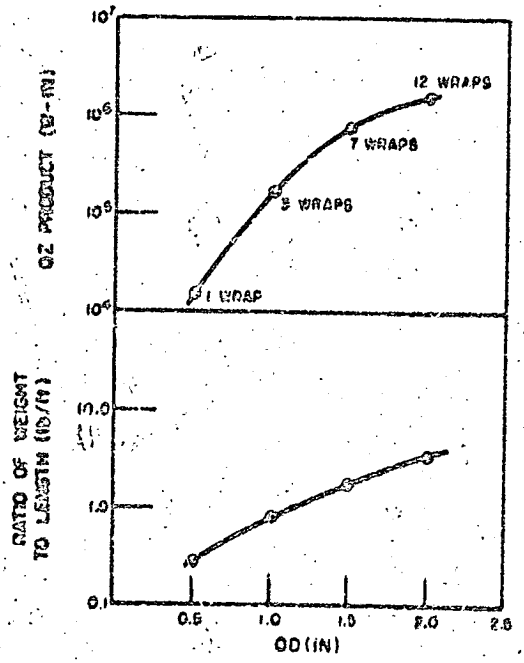



Fig. 5-35. Product of maximum power throughput and length at zero g and weight-to-length ratio as functions of diameter for sodium in stainless steel heat pipes with 40 mesh wicks operating at an evaporator temperature of 943°C.

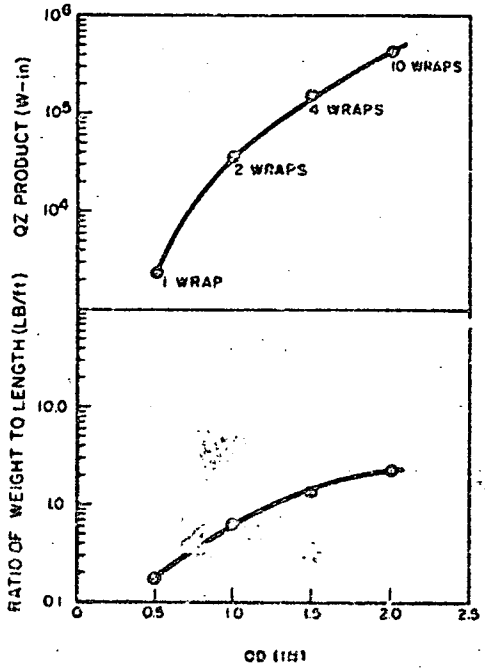



Fig. 5-36. Product of maximum power throughput and length and weight-to-length ratio as functions of diameter for sodium in stainless steel heat pipes with 60 mesh wicks operating at an evaporator temperature of 627 °C.

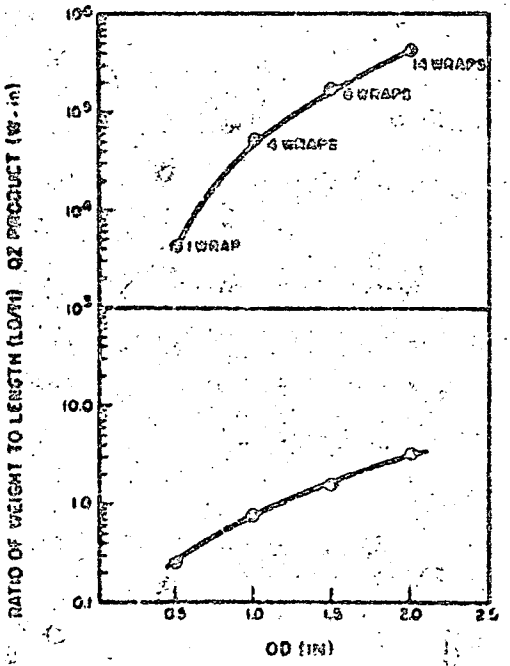



Fig. 5-37. Product of maximum power throughput and length and weight-to-length ratio as functions of diameter for potassium in stainless steel heat pipes with 40 mesh wicks operating at an evaporator temperature of 627 °C.

where:

$\Delta T_t$ is total temperature drop

$\Delta T_i$ is temperature drop in evaporator due to thermal resistance of the wall, wick and working fluid

$\Delta T_e$ is temperature drop due to evaporation

$\Delta T_v$ is temperature drop due to vapor flow down the heat pipe

$\Delta T_c$ is temperature drop due to condensation

$\Delta T_o$ is temperature drop in condenser due to thermal resistance of the wall, wick and working fluid.

Each of these temperature drops is discussed in the following paragraphs.

a. Conduction Temperature Drops

The temperature drops due to thermal resistance in the wall, wick and working fluid were calculated for three different cases as shown in Fig. 5-38. In Case I all the heat enters one flat end of the heat pipe and exits from the other flat end. In Case II, the heat is put in both at the flat end of the heat pipe and over one inch of length of the cylindrical section. This condition can be achieved in practice by using a large copper block to conduct the heat into the heat pipe. The heat exits through a similar device with equal area at the other end. Case III is similar as Case II except that the heat input area is increased by putting the heat in over a 2-in. length of the cylinder section. The heat exits through a similar area. The temperature drops due to the thermal resistances of the heat pipe wall, wick and working fluid are usually the major drops in heat pipe operation. Data were calculated for a power throughput of 350 W for a great many operational cases. The results are shown in Table 5-4.

b. Vapor Temperature Drops

The temperature drop, $\Delta T_v$, due to vapor pressure drop down the heat pipe was calculated as part of the heat pipe computer design program. The vapor temperature drops per foot of length have been plotted versus diameter of the heat pipe for a 350 W throughput in Fig. 5-39. Working fluids and temperature are parameters on these curves. It can be seen from these curves that when the working fluid is operating at substantial vapor pressures, the vapor temperature drop, $\Delta T_v$, is low, as shown for sodium at 943°C, where the temperature drops are so low as to be insignificant. On the other hand when the working fluids are operating near the low end of their range and the heat pipe diameter is small, the vapor temperature drop can be substantial. This is the case with lithium at 943°C and sodium at 627°C. Neither of these combinations should be employed with heat pipe diameters smaller than 1.0 in. Potassium at 627°C lies intermediate between the other working fluids and would be acceptable in heat pipes with diameters as small as 0.70 in.

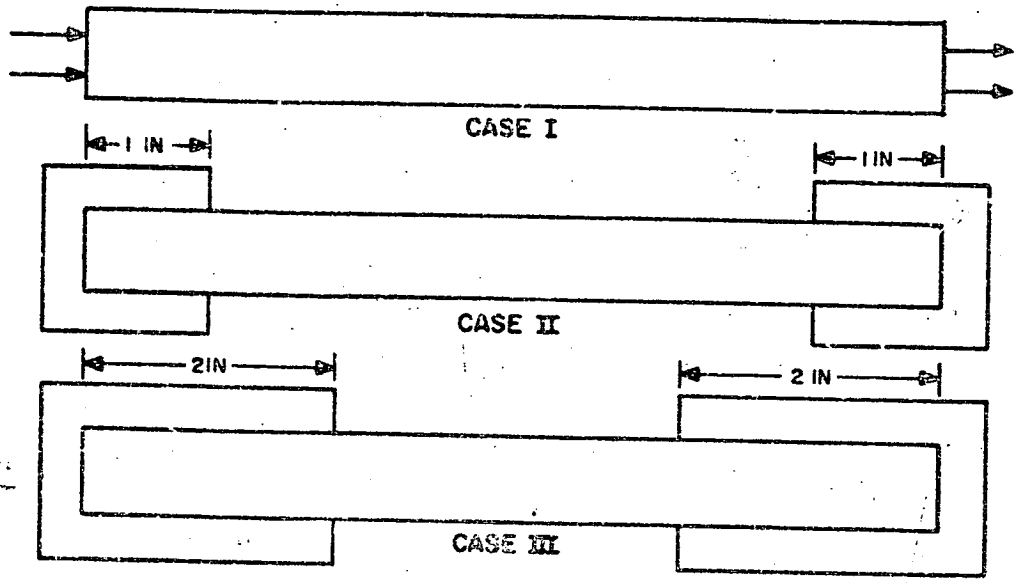



Fig. 5-38. Heat pipe input and output methods.

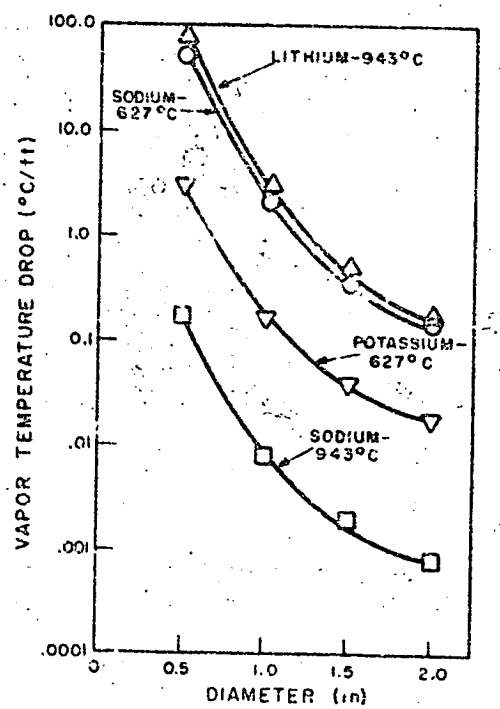



Fig. 5-39. Vapor temperature drops as a function of heat pipe diameter for 12-in. pipes with 350-W throughputs.

TABLE 5-4. TEMPERATURE DROPS FOR VARIOUS HEAT PIPE INPUT AND OUTPUT METHODS AND MATERIALS

| Working Fluid | Temperature (°C) | Wall Material | Diameter (in.) | Case No. | $\Delta T_i + \Delta T_o$ (°C) |
|---|---|---|---|---|---|
| Sodium | 943 | Stainless Steel | 0.5 | I | 383.8 |
| | | | 1.0 | | 128.0 |
| | | | 1.5 | | 85.3 |
| | | | 2.0 | | 68.2 |
| Sodium | 943 | Stainless Steel | 0.5 | II | 54.4 |
| | | | 1.0 | | 29.1 |
| | | | 1.5 | | 25.4 |
| | | | 2.0 | | 24.3 |
| Sodium | 943 | Stainless Steel | 0.5 | III | 28.6 |
| | | | 1.0 | | 16.0 |
| | | | 1.5 | | 14.6 |
| | | | 2.0 | | 14.5 |
| Sodium | 943 | Nickel | 0.5 | I | 173.1 |
| | | | 1.0 | | 75.3 |
| | | | 1.5 | | 49.8 |
| | | | 2.0 | | 54.8 |
| Sodium | 943 | Nickel | 0.5 | II | 24.6 |
| | | | 1.0 | | 17.1 |
| | | | 1.5 | | 18.4 |
| | | | 2.0 | | 19.6 |
| Sodium | 943 | Nickel | 0.5 | III | 12.8 |
| | | | 1.0 | | 9.4 |
| | | | 1.5 | | 10.6 |
| | | | 2.0 | | 11.7 |
| Sodium | 943 | TZM-Moly | 0.5 | I | 129.6 |
| | | | 1.0 | | 63.6 |
| | | | 1.5 | | 56.0 |
| | | | 2.0 | | 51.0 |
| Sodium | 943 | TZM-Moly | 0.5 | II | 18.4 |
| | | | 1.0 | | 14.4 |
| | | | 1.5 | | 16.6 |
| | | | 2.0 | | 18.2 |

TABLE 5-4. TEMPERATURE DROPS FOR VARIOUS HEAT PIPE INPUT AND OUTPUT METHODS AND MATERIALS (Continued)

| Working Fluid | Temperature (°C) | Wall Material | Diameter (in.) | Case No. | $\Delta T_i + \Delta T_o$ (°C) |
|---|---|---|---|---|---|
| Sodium | 943 | TZM-Moly | 0.5 | III | 9.6 |
| | | | 1.0 | | 7.9 |
| | | | 1.5 | | 9.5 |
| | | | 2.0 | | 10.8 |
| Lithium | 943 | TZM-Moly | 0.5 | I | 107.7 |
| | | | 1.0 | | 33.1 |
| | | | 1.5 | | 16.5 |
| | | | 2.0 | | 15.6 |
| Lithium | 943 | TZM-Moly | 0.5 | II | 12.4 |
| | | | 1.0 | | 4.9 |
| | | | 1.5 | | 3.6 |
| | | | 2.0 | | 3.5 |
| Lithium | 943 | TZM-Moly | 0.5 | III | 6.5 |
| | | | 1.0 | | 2.7 |
| | | | 1.5 | | 2.0 |
| | | | 2.0 | | 2.1 |
| Sodium | 627 | Stainless Steel | 0.5 | I | 351.8 |
| | | | 1.0 | | 85.9 |
| | | | 1.5 | | 49.7 |
| | | | 2.0 | | 40.0 |
| Sodium | 627 | Stainless Steel | 0.5 | II | 61.4 |
| | | | 1.0 | | 26.3 |
| | | | 1.5 | | 17.5 |
| | | | 2.0 | | 16.1 |
| Sodium | 627 | Stainless Steel | 0.5 | III | 32.0 |
| | | | 1.0 | | 14.5 |
| | | | 1.5 | | 10.0 |
| | | | 2.0 | | 9.6 |
| Sodium | 627 | Nickel | 0.5 | I | 129.1 |
| | | | 1.0 | | 40.3 |
| | | | 1.5 | | 25.0 |
| | | | 2.0 | | 26.1 |

TABLE 5-4. TEMPERATURE DROPS FOR VARIOUS HEAT PIPE INPUT AND OUTPUT METHODS AND MATERIALS (Continued)

| Working Fluid | Temperature (°C) | Wall Material | Diameter (in.) | Case No. | $\Delta T_i + \Delta T_o$ (°C) |
|---|---|---|---|---|---|
| Sodium | 627 | Nickel | 0.5<br>1.0<br>1.5<br>2.0 | II | 18.3<br>9.8<br>7.8<br>9.6 |
| Sodium | 627 | Nickel | 0.5<br>1.0<br>1.5<br>2.0 | III | 9.3<br>5.0<br>4.3<br>5.5 |
| Potassium | 327 | Stainless Steel | 0.5<br>1.0<br>1.5<br>2.0 | I | 410.3<br>170.4<br>[illegible].9<br>99.2 |
| Potassium | 627 | Stainless Steel | 0.5<br>1.0<br>1.5<br>2.0 | II | 69.6<br>43.2<br>37.1<br>37.2 |
| Potassium | 627 | Stainless Steel | 0.5<br>1.0<br>1.5<br>2.0 | III | 35.1<br>23.7<br>21.3<br>22.1 |
| Potassium | 627 | Nickel | 0.5<br>1.0<br>1.5<br>2.0 | I | 113.3<br>114.7<br>91.2<br>85.2 |
| Potassium | 627 | Nickel | 0.5<br>1.0<br>1.5<br>2.0 | II | 26.2<br>26.0<br>27.1<br>30.4 |
| Potassium | 627 | Nickel | 0.5<br>1.0<br>1.5<br>2.0 | III | 13.4<br>14.3<br>15.6<br>18.1 |

c. Evaporative Temperature Drops

In an operating heat pipe, the net evaporation rate is a difference between forward and backward evaporation rates in the heat input zone. This net evaporation rate is a function of the temperature difference between the liquid and the vapor when they interface in the evaporator.

The heat flux transfer, q, can be written:

$$q = \Delta H \, (\mu_1 - \mu_2) \tag{5-67}$$

where:

- q is heat flux (cal/cm$^2$/s)
- $\Delta H$ is latent heat of vaporization (cal/gm)
- $\mu_1$ is forward evaporation rate (mole/cm$^2$/s)
- $\mu_2$ is backward evaporation rate (mole/cm$^2$/s)

Since

$$\mu = \frac{P}{(2\pi \; mRT)^{1/2}} \tag{5-68}$$

q becomes

$$q = \frac{\Delta H}{(2\pi \; R)^{1/2}} \left[ \frac{P_1}{(M_1 T_1)^{1/2}} - \frac{P_2}{(M_2 T_2)^{1/2}} \right] \tag{5-69}$$

where:

- $P_1$ is equilibrium vapor pressure of the liquid in the capillary (dynes/cm$^2$)
- $P_2$ is pressure of the vapor within the evaporator (dynes/cm$^2$)
- $M_1$ is molecular weight of the liquid at $T_1$ (°K), (grams/mole)
- $M_2$ is molecular weight of the vapor at $T_2$ (°K), (grams/mole)
- R is gas constant $8.3 \times 10^7$ ergs/mole/°C

or

$$q = 1.83 \times 10^{-4} \, \Delta H \left[ \frac{P_1}{(M_1 T_1)^{1/2}} - \frac{P_2}{(M_2 T_2)^{1/2}} \right] \quad (W/cm^2) \tag{5-70}$$

This expression has been plotted for sodium in Fig. 5-40 where the evaporator heat flux is shown versus the evaporation temperature drop. Since input heat fluxes over 50 W/cm$^2$ induce excessive thermal conduction drops in the heat pipe wall, the normal operational level will be kept below this level.

By interpolation it can be seen that at this input heat flux the temperature drop at 627 °C is less than 2 °C and at 943 °C the drop is less than 0.15 °C. On this basis the evaporative and condensive temperature drops have not been considered significant enough to include in the overall heat pipe temperature drops.

d. Total Temperature Drop

The total temperature drop in the heat pipe has been plotted versus diameter in Figs. 5-41 through 5-48. Each of these plots is for a 12-in. long heat pipe of a given working fluid, wall material, and operating temperature conducting 550 W of throughput. The heat transfer area (Case I, II, and III) is plotted as the parameter. In addition, the temperature drop in a solid copper rod of the same dimensions and operating at the same input temperature is plotted for comparison. It can be seen that at this length the thermal conductivity of the heat pipe is always many times greater than the copper rod.

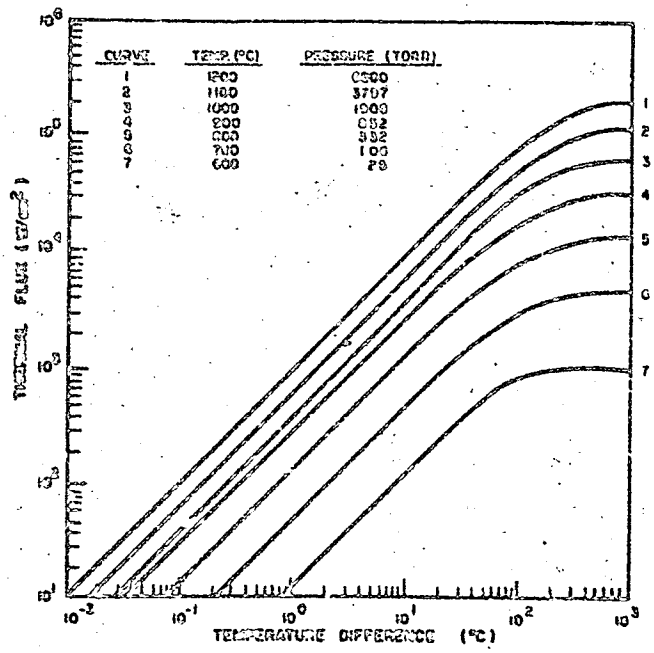



Fig. 5-40. Thermal flux characteristics of sodium.

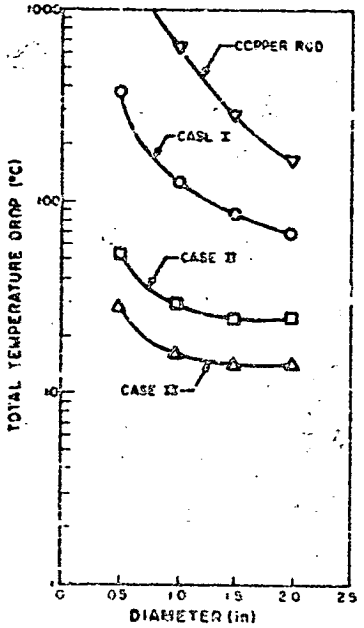



Fig. 5-41. Total temperature drop as a function of diameter with input and output method as a parameter for a 12-in-long sodium in stainless steel heat pipe and a copper rod with a throughput of 350 W at a temperature of 943°C.

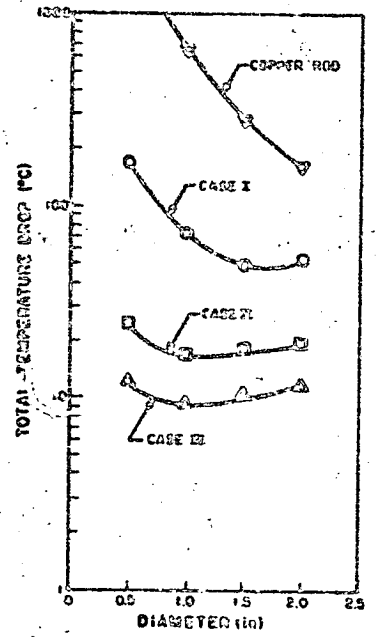



Fig. 5-42. Total temperature drop as a function of diameter with input and output method as a parameter for a 12-in-long sodium in nickel heat pipe and a copper rod with a throughput of 350 W at a temperature of 943°C.

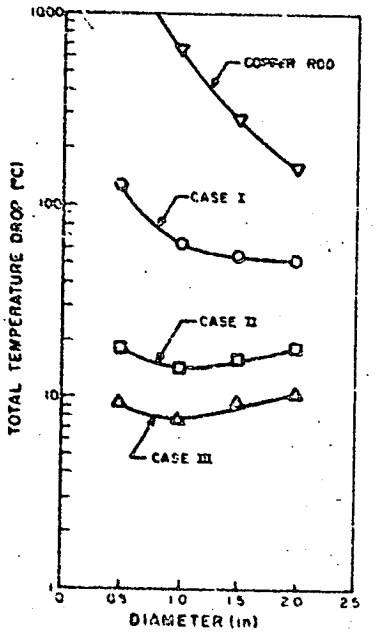



Fig. 5-43. Total temperature drop as a function of diameter with input and output method as a parameter for a 12-in-long in molybdenum heat pipe and a copper rod with a throughput of 350 W at a temperature of 943°C.

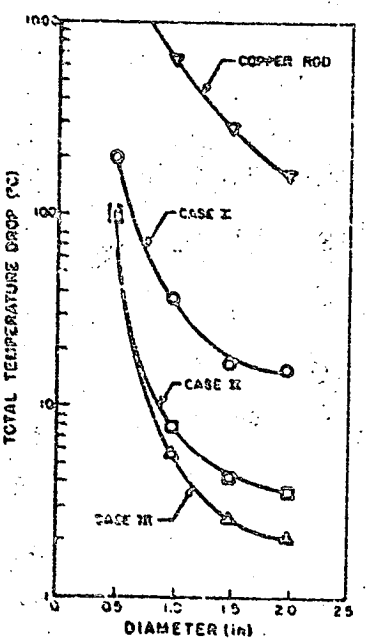



Fig. 5-44. Total temperature drop as a function of diameter with input and output method as a parameter for a 12-in-long lithium in molybdenum heat pipe and a copper rod with a throughput of 350 W at a temperature of 943°C.

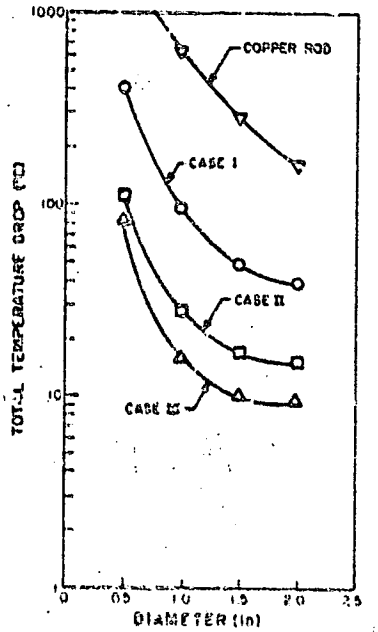



Fig. 5-45. Total temperature drop as a function of diameter with input and output method as a parameter for a 12-in-long sodium in stainless steel heat pipe and a copper rod with a throughput of 350 W at a temperature of 627 °C.

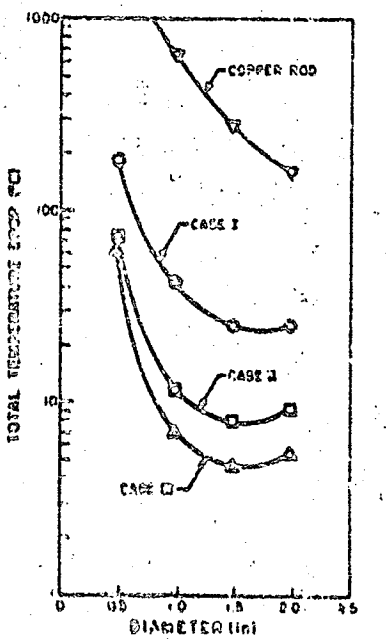



Fig. 5-46. Total temperature drop as a function of diameter with input and output method as a parameter for a 12-in-long sodium in nickel heat pipe and a copper rod with a throughput of 350 W at a temperature of 627 °C.

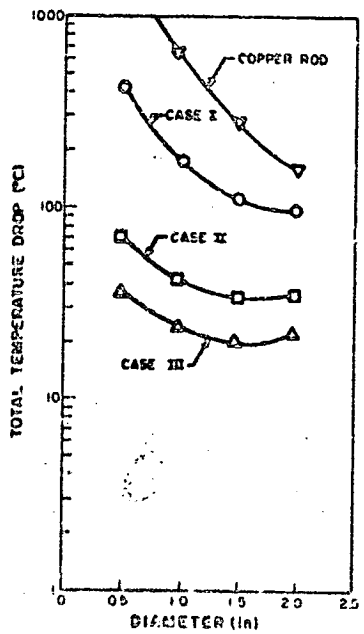



Fig. 5-47. Total temperature drop as a function of diameter with input and output method as a parameter for a 12-in-long potassium in stainless steel heat pipe and a copper rod with a throughput of 350 W at a temperature of 627°C.

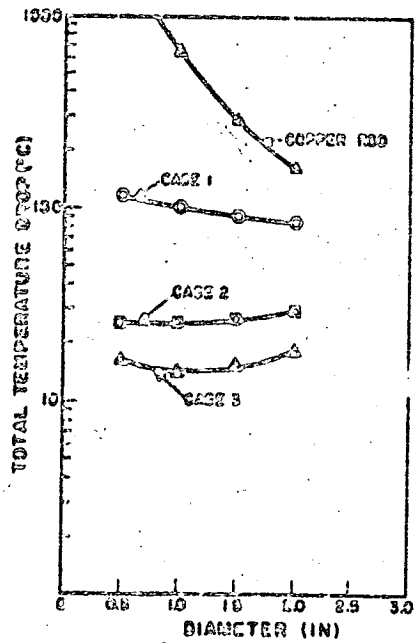



Fig. 5-48. Total temperature drop as a function of diameter with input and output method as a parameter for a 12-in-long potassium in nickel heat pipe with a throughput of 350 W at a temperature of 627 °C.

This difference has been further amplified by plotting overall ΔT (at 350 W) versus length for a 1-in-diameter copper rod and for two heat pipe designs of the same diameter as shown in Fig. 5-49. One heat pipe is a "worst case" one; i.e., potassium in a stainless steel vessel end fed. Even in this example the copper rod does not become superior until its length is reduced to approximately 3-in. When a "best case" heat pipe is considered; i.e., sodium in molybdenum at 943 °C, the copper rod does not become competitive until it is reduced to 0.1 in. long. The comparision is graphic; even the poorest heat pipe is superior to a copper rod for conducting heat the distance required by ICICLE.

## 8. Summary

In summary, the optimal heat pipe for thermally connecting the radioisotope output to the VM engine in the ICICLE concept appears to be sodium-TZM molybdenum with molybdenum wick heat pipe operating at 943 °C and radiatively coupled to the heat source and sink. If the device must operate in air before launch, molybdenum would not be satisfactory and nickel would be recommended for the wall and wick material. An alternative is an inert gas or vacuum protection for the molybdenum heat pipe when it is operated before launch. The heat pipe should be coupled to the isotope and engine by copper spreaders as depicted in Case III, Fig. 5-38, in order to reduce the temperature drops to a minimum.

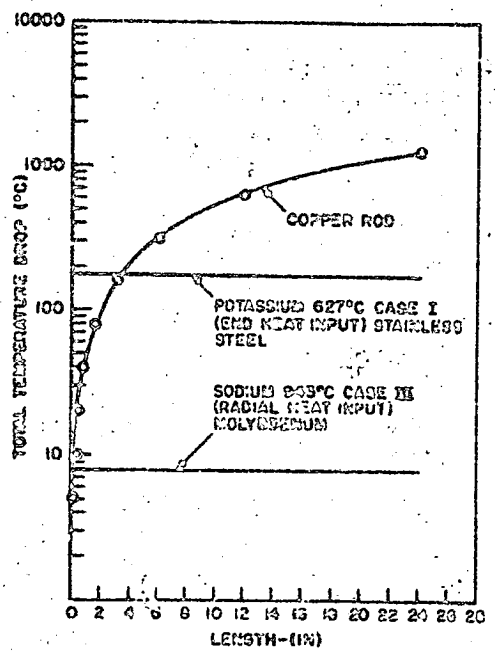



Fig. 5-49. Total temperature drop as a function of length for heat pipes and a copper rod with a throughput of 350 W.

## C. AMBIENT TEMPERATURE HEAT PIPES

The rejected heat from the VM engine must be disposed of to space by radiation at ambient temperature. The heat rejection system will employ a primary heat pipe to conduct heat from the output of the VM engine to a series of secondary heat pipes which make up a honeycomb radiator section. A right-angle bend will be made in the primary heat pipe to facilitate its integration into the TIROS-M satellite.

### 1. Primary Heat Pipe - General Description

The primary heat pipe will attach to the output cylinder of the VM engine through an annular metallic connection. The heat pipe will extend approximately 36 in. to the ambient temperature radiator. A right-angle bend is made just before the radiator. The primary heat pipe extends an additional 44 in. through the radiator. The total length, Z, of the primary heat pipe is 80 in.

The right-angle band is within the state of the art of heat pipes. RCA has made a number of heat pipes, both high temperature and low temperature which contain bends or sharp angles. In a series of tests performed on high-temperature sodium in nickel heat pipes operating at 800°C, no detectable temperature drop could be observed going around a sweeping bend having a radius of twice the pipe diameter.

In another series of tests performed on a flexible, low-temperature heat pipe containing acetone as the working fluid and operating at 80°C, no change in temperature distribution was observed when the heat pipe was bent 90° from the straight position. This flexible heat pipe contained a proprietary wick structure which permits the heat pipe to be bent more than 90° without adversely affecting the wick properties. This same wick design was used in a number of other low-temperature heat pipes which have permanent bends.

Another series of tests were performed on a water-stainless steel heat pipe operating at 100°C. This heat pipe had a mitred 90° corner in the middle. When heat was transferred at the rate of 1000 W/cm$^2$ of vapor space a 2.0°C temperature drop was observed at the mitred corner. Interestingly, there was almost a 1.0°C recovery of temperature on the heat sink side of the bend.

The experience indicates that the primary heat pipe in the ICICLE ambient heat rejection system can be made without serious loss in temperature.

### 2. Constant-Temperature Operation

The primary heat pipe will be of the constant temperature type so that the output of the VM engine will always operate into a uniform temperature. The constant

temperature mode of heat-pipe operation, which was an early development at RCA, employs an inert gas blanket to establish the temperature of operation. The system, as shown schematically in Fig. 5-50.A, employs a reservoir on the sink end of the heat pipe which contains an inert gas. The pressure of the gas, which is adjusted during initial processing, will establish the temperature of operation of the heat pipe. This is so since only one pressure can exist within the device, and the vapor pressure, and hence temperature, of the working fluid will be established by the preset gas pressure in the reservoir. As heat is added to the device the interface between hot vapor and cold gas will move until the heat rejection system removes the additional heat. Thus, the heat pipe becomes a device of nearly constant temperature which changes heat transfer area to accommodate heat input or exit changes.

The vapor of the working fluid, moving toward the heat sink, continuously drives the inert gas into the reservoir. Because of the short mean free path of vapor molecules at normal heat pipe pressures, the penetration into the inert gas is small and the interface has a very sharp temperature gradient. The heat pipe and reservoir walls are generally lined with a capillary structure to return any working fluid that does enter the inert gas domain. RCA has operated a heat pipe of this type for over 32,000 hours without any apparent mixing of the working fluid and inert gas. There is a small change in heat pipe operating temperature as the heat input varies from minimum to maximum. This occurs because of the change in volume in the inert gas section. This change in temperature is inversely proportional to the gas volume so that larger

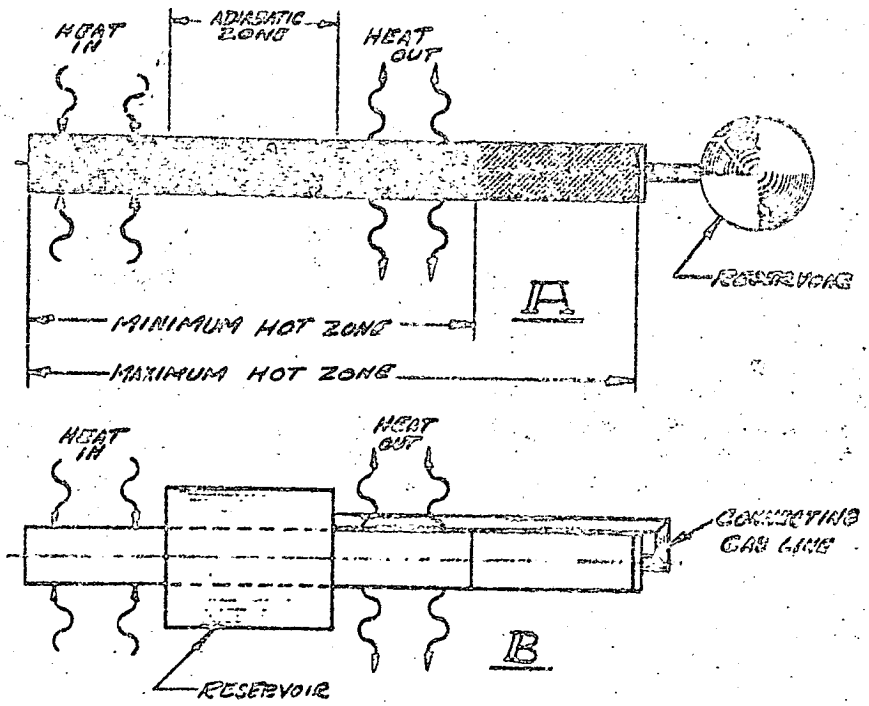



Fig. 5-50. Constant-temperature heat pipe system.

reservoirs will yield the most uniform heat pipe temperature. In the primary heat pipe for the SNAP-8 system the gas-vapor interface would be at the entrance to the radiator at minimum heat and would move to the other end of the radiator at the maximum heat load of 100 W. The reservoir volume required to maintain the heat pipe within the desired operating temperature limits may be found by rearranging the expressions for pure gases as follows:

$$V_R = \frac{\Delta V}{\frac{P_1}{P_2} - 1}$$

where

$V_R$ is reservoir volume

$\Delta V$ is heat pipe volume between minimum and maximum interface positions.

$P_1$ is vapor pressure of working fluid at maximum permissible temperature

$P_2$ is vapor pressure of working fluid at minimum permissible temperature

For an SNAP-8 primary heat pipe of 1 in. outside diameter with a 0.050-in wall and containing 0.170 in of capillary wick structure the change in volume, $\Delta V$, when the interface moves across the 44-in length of radiator is 10.870 $in^3$.

If the temperature of an ammonia heat pipe is to be kept between 27°C (300°K) and 32°C (305°K) the required reservoir volume, $V_R$, is 57.5 $in^3$.

This calculated value is valid if the average gas temperature remains nearly constant during a power excursion. A method to achieve this thermal stability is shown in Fig. 8-50. B. In this case the inert gas reservoir is thermally coupled to the heat pipe by making it coaxial with the adiabatic section. In this manner the reservoir gas is also kept at a uniform temperature. Thermal insulation is required outside the

reservoir to reduce heat losses to a minimum. The reservoir is connected to the sink end of the heat pipe by a small gas line. This line may be run inside the heat pipe or along the outside of the device.

Helium is recommended for the reservoir gas. Since it is inert, no reaction with heat pipe materials or working fluid can occur. In addition, its freezing point is below any temperature expected to be encountered on TIROS M operation. Other inert gases could present a freezing problem.

In addition to maintaining a uniform exit temperature at the VM engine, the constant temperature heat pipe has the further advantage of insuring smooth start ups after the radiator has fallen below the freezing point of the working fluid. Because of the presence of the inert gas, the heat pipe will start up in a progressive manner with the vapor-gas interface moving steadily down the heat pipe. The working fluid cannot suddenly flow to the far end and freeze out as can happen in a heat pipe without the gas addition.

3. Working Fluid

Ammonia has been selected for the working fluid for the ambient temperature heat pipes operating at 30°C. The vapor pressure and density of water at 30°C is low which would result in sonic limitations. The vapor pressure of ammonia is sufficiently high (approx. 180 psia) that the temperature drop due to vapor flow is negligible. Ammonia has a high heat of vaporization so that the evaporative temperature drop is low. The vapor pressure is not so high as to require inordinately heavy walls to contain the pressure. Such pressure vessels would result in increased weight and high temperature drops in the wall.

The compatibility of ammonia with aluminum has been demonstrated. Considerable care must be taken to assure that the ammonia is pure. Ammonia with a purity of 99.99% is available and has been tested with good results. Purities less than this value have been found to be corrosive in heat pipes, particularly if the residual impurities contain water vapor.

4. Material

Both the primary heat pipe and secondary heat pipe will be made from aluminum. 6061T4 or T6 has excellent strength characteristics so that minimal wall thickness can be used. The wick will be of pure aluminum, either in screen or powder form.

## 5. Thermodynamic Design

The ambient temperature heat pipes, both primary and secondary, were designed using the HPDP18 heat pipe design code described in the section on high-temperature heat pipes. For each diameter and length a series of wick structures was analyzed and the capillary structure was selected which optimized the power throughput. The weight was also calculated for each design. These data are plotted in Fig. 5-51. The upper part of the Fig. 5-51 shows the product of power throughput and length (QZ) versus the inside diameter of the heat pipe. There are three curves on this illustration; the upper one shows the characteristics of an ammonia heat pipe with a mesh wick under zero gravity conditions. The optimum mesh size and optimum number of wraps are shown in small numbers. The lower curve shows the data for an ammonia heat pipe with a mesh wick when a small acceleration force is placed on the pipe. In this case a gravity head equal to a fluid lift of one diameter was placed on the pipe. Because of the surface tension characteristics of ammonia the power transfer characteristics are markedly reduced when the small acceleration force is applied. Because such forces are likely to be encountered in service, the heat pipe design must account for them.

The middle curve in Fig. 5-51 is the performance data for a heat pipe with a sintered powder wick. This type of capillary structure has the advantage of having substantially lower input and output temperature drops than the mesh wick designs. This factor will be further amplified in the following section. The sintered wick also

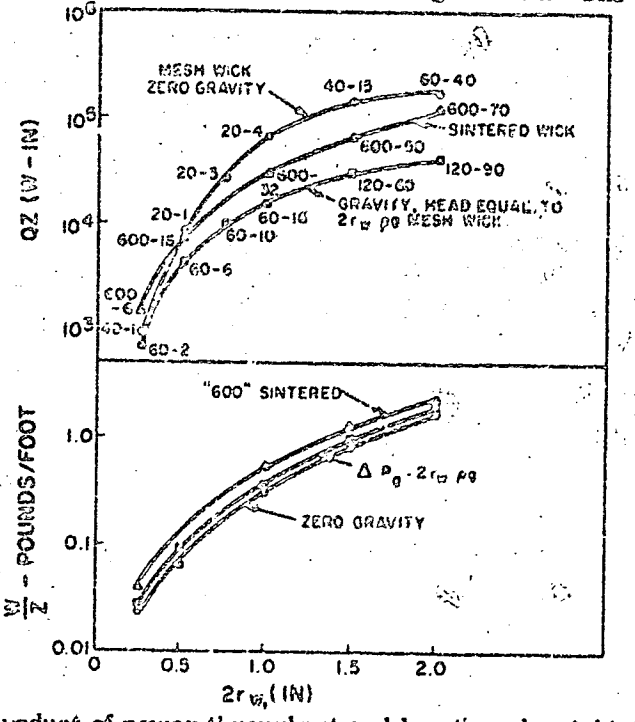



Fig. 5-51. Product of power throughput and length and weight-to-length ratio as functions of inside diameter for an ammonia heat pipe at a temperature of 30°C.

develops the much higher capillary pumping pressure so that there is only a slight reduction in performance when an acceleration equal to a diameter lift is applied. The difference is not large enough to show on the graph paper. The small numbers beside the data point indicate the code number (600) for the sintered powder and the thickness of wick in units of 0.01 in. The code number refers to the wick density and particle size.

The ratio of weight to length of the three types of heat pipes are shown in the lower part of Fig. 5-51. Heat pipes of optimum design which contain the sintered powder wick are somewhat heavier than those having the less dense screen wicks. However, the other advantages of the porous metal wick more than offset the penalty of additional weight.

6. Temperature Drops

The temperature drops encountered in the ambient temperature heat pipe are developed in the same regions as the high temperature heat pipe, as shown in Fig. 5-66.

The dominant difference in the low temperature heat pipe is due to the high temperature drops which develop when the heat passes through the low conductivity working fluid.

Because of the characteristics of ammonia at the operating temperature, the temperature drops due to evaporation, condensation and vapor transport are small and can be ignored. The expressions which were used to calculate the temperature drops differ somewhat depending on the wick structure. In the coarse-structured screen wicks it has been found that the metallic screen only increases the thermal conductivity of the wick about 20% over that of a pure liquid. Consequently, the temperature drops through low conductivity working fluids like ammonia can become inordinately high. This is the case with the screen wick structures evaluated by the following expression:

$$\Delta T_t = Q \left( \frac{t_w}{k_w A_i} + \frac{t_s N}{k_f A_i} + \frac{t_w}{k_w A_o} + \frac{t_s N}{k_f A_o} \right) \qquad (5\text{-}72)$$

where

$\Delta T_t$ is the total temperature drop (°C)

$Q$ is the heat transfer rate (cal/s)

$t_w$ is the wall thickness (cm)

$k_w$ is the thermal conductivity of wall material (cal/s/cm$^2$/°C)

$t_s$ is the thickness of one layer of screen (cm)

N is the number of layers of screen

$A_i$ is the input area ( cm$^2$)

$A_o$ is the output area (cm$^2$)

$k_f$ is the thermal conductivity of the working fluid (cal/s/cm$^2$/°C)

Based on an annular input area of 24.1 in$^2$ and an output area equal to the pipe diameter times the radiator length, each diameter heat pipe was evaluated for temperature drop at a throughput of 100W for the optimized wick structure.

The data is plotted in Fig. 5-68, along with the temperature drop calculated for a 6061-T4 aluminum rod 12 inches long. It can be seen that both screen wick heat pipe designs and the solid aluminum rod all have temperature drops which are excessively high.

A good alternative is a wick structure which employs a type 600 sintered powder wick. This material has been evaluated at RCA and found to have a thermal

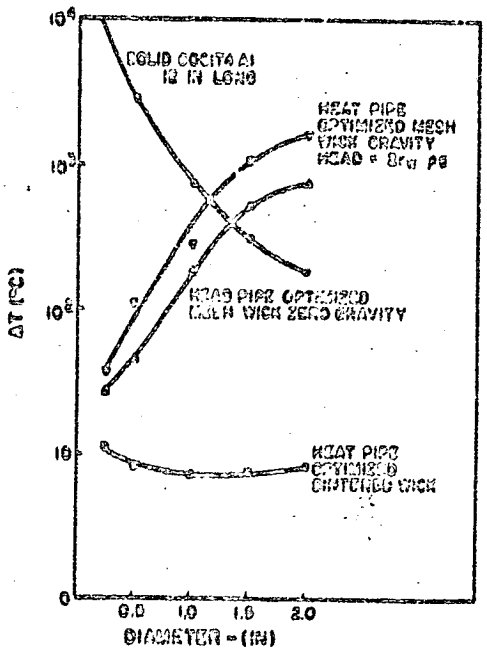



Fig. 5-62. Temperature drop as a function of diameter for solid aluminum and for ammonia in aluminum heat pipes with a throughput of 100W.

conductivity which is 40% of the solid metal. Consequently, the temperature drop in the wick is greatly reduced. The expression used to evaluate this design is:

$$\Delta T_T = Q\left(\frac{t_w}{k_w A_i} + \frac{t_p}{k_p A_i} + \frac{t_f}{k_f A_i} + \frac{t_w}{k_w A_o} + \frac{t_p}{k_p A_o} + \frac{t_f}{k_f A_o}\right) \quad (5\text{-}73)$$

where

$t_p$ is the thickness of powdered wick (cm)

$k_p$ is the thermal conductivity of powdered wick (cal/s/cm$^2$/°C)

$t_f$ is the thickness of working fluid film on the surface of the wick (cm)

Using Eq. 5-73 and assuming a 0.010-inch thick film of working fluid in both the evaporator and condenser, the temperature drops were calculated for each diameter heat pipe. The data is plotted as the lower curve in Fig. 5-52. It graphically shows the superior attributes of the sintered powder wick structure.

7. Summary

Based on the data calculated, both the primary and secondary heat pipes should be made of 6061T4 aluminum with pure sintered powder wick equivalent to RCA Type 600. Based on a QZ of 15,200W-in (190W x 80 in), a 1-in diameter heat pipe would be adequate for the primary heat pipe thermal power throughput requirements. A heat pipe of this design would have a total temperature drop of 7.2°C.

The secondary heat pipe will be 0.25-in. in diameter to fit within the honeycomb radiator. A QZ of 252W-in (12W x 21 in) is required which is well within the capability of the sintered wick design at that diameter. Based on an input area equal to the area formed where the secondary heat pipe crosses the primary heat pipe, the temperature drop in the secondary heat pipe evaporator is 11.0°C. This could be reduced by increasing the input area by using larger saddle-shaped heat spreaders.

D. BY-PASS HEAT PIPES

Short half-life higher power radioisotopes such as $Th^{226}$ (1.9 years), $Po^{210}$ (0.38 years), $Cm^{242}$ (0.45 years) and $Cm^{244}$ (18.0 years) can be used for longer mission life if means are provided for holding the isotope useful temperature at a nearly constant value even though its power generation rate is falling in an exponential manner. The

constant temperature, gas controlled heat pipe supplies this requirement since it can be used to clamp the isotope output temperature at a specific desired value. When used in this manner an excess amount of radioisotope is provided so that the minimum amount required to drive the VM engine is available until the end of mission life. At the start of life, the excess power is bypassed from the isotope and radiated to space. As the isotope output decays, the amount of power radiated will decrease exponentially, but the temperature will remain nearly constant. Rejection of the excess heat will occur automatically with no control required. A device of this type was tested at RCA as a means for obtaining uniform electrical output from a thermionic device designed to convert the heat from the radioisotope into electricity. In these tests an 8-to-1 power change (three half lives) was made with a negligible change in temperature and electrical output.

It is proposed to use this device in the ICICLE concept to maintain the input temperature constant over a 2-to-1 power change; i.e., 700 W at the beginning of life and 350 W at the end of life. A schematic of a heat pipe design to accomplish this objective is shown in Fig. 5-53. The heat pipe is connected to the radioisotope container and extends out 12 in. A 10-in length of this extension is used to radiate the excess power to space. The heat pipe diameter was established at 1 in. to obtain the correct heat transfer area to radiate an excess power of 350 W. At the beginning of life the hot zone of the heat pipe will extend the full 12 in; at the end of mission life the hot zone will have receded to 10-in. The heat pipe for this application was designed for minimum weight with a 1-in diameter. Using the HPDP18 computer program of RCA a

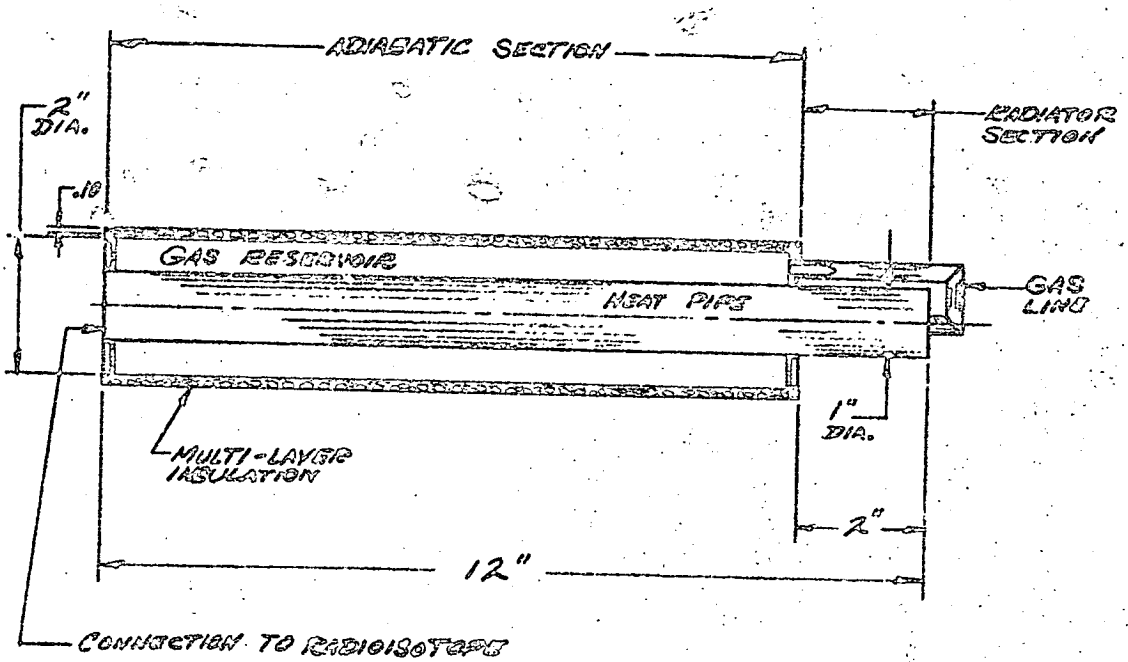



Fig. 5-53. By-pass heat pipe.

stainless steel-sodium heat pipe was designed for operation at 950 ± 15°C. A heat pipe with two wraps of 120 mesh would carry the required power with considerable safety factor (1000 watt capability). The weight of the heat pipe alone would be 0.604 lb in stainless steel or 0.774 lb in molybdenum.

The reservoir volume, $V_R$, required to hold a temperature tolerance of 935°C to 965°C (±15°C) found using Fig. 5-71, is 18.95 $in^3$ for a 1-in diameter heat pipe with a wall thickness of 0.05 in, a wick thickness of 0.029 in, and a length of 2 in.

If this volume is made as a concentric reservoir surrounding the 10-in-long adiabatic section, the outside diameter of the reservoir will be 2.0 in. with a 0.040-in wall. Multifoil insulation will be used around the reservoir to maintain this region nearly adiabatic.

Helium will be used to fill the inert gas reservoir because of its inert characteristics and its low freezing point.

A gas-controlled high-temperature heat pipe is an effective device for bypassing excess radioisotope power to permit longer periods of operation at uniform temperature input. The design, fabrication and operations of this type of heat pipe has been demonstrated at RCA.

## E. AMBIENT RADIATOR

### 1. Selection of Ambient Radiator Surface Finishes

The surface finish of an ambient temperature radiator must be compatible with the environment in which it must operate. A radiator which receives no external heat flux such as solar, earth self-emitted, earth reflected solar, and spacecraft self-emitted radiation should have a finish with the highest possible emissivity (such as black paint). Since such a condition is not likely to exist on a real spacecraft, the finish should be selected such that it can give maximum performance in the worst-case environment. The worst-case environment would have a combination of solar, earth, and spacecraft self-emitted heat fluxes. The worst-case solar heat flux would occur with the solar vector normal to the radiator surface. The worst-case earth heat flux would occur with the local vertical normal to the radiator. The worst-case spacecraft self-emitted heat flux depends upon the spacecraft physical configuration and the location and orientation of the radiator with respect to the spacecraft.

In a near-earth orbit, the maximum direct solar heat flux would be 0.93 W/in.$^2$. At a radiator temperature of 300°K with an emissivity, $\epsilon$, of 0.8, the maximum total heat flux that a 100-percent efficient radiator can dissipate is 0.237 W/in.$^2$, as shown in Fig. 5-54. Therefore, the amount of external heat absorbed must be less than 0.237 W/in.$^2$ in order for the radiator to radiate any net heat ($Q_{net} = Q_{emitted} - Q_{absorbed}$). Therefore, it is necessary to reduce the amount of solar energy absorbed by the radiator to a level which is well below 0.237 W/in.$^2$. This can be accomplished by choosing a location on the spacecraft which will minimize the solar heat flux on the radiator, by using a low solar absorptance finish, or a combination of both.

Until the particular flight spacecraft is known, the amount of solar energy impinging upon the radiator cannot be determined. Therefore, for the purpose of this study, a finish for the radiator should be chosen that will minimize the absorbed solar energy. The amount of solar energy absorbed by a radiator as a function of solar absorptivity and sun angle, $\phi$, (angle between the solar vector and radiator normal) is shown in Fig. 5-55. Inspection of Fig. 5-55 indicates that for a full sun load ($\phi = 0°$) the solar absorptance, $\alpha$, cannot exceed 0.255 (the radiator area for this case would be infinite) and a reasonable limit would be half of this value or 0.127. At a sun angle of 60°, $\alpha$ cannot exceed 0.51 with a reasonable limit of 0.255.

Undegraded white paints such as Z93 have values of $\alpha$ as low as 0.18 but upon exposure to the sun they will degrade to values of 0.3 to 0.5 within a year or less. Therefore, for many spacecraft applications, undegraded white paints are unacceptable on 300° K radiators. This conclusion is based on the fact that sun angles greater than 60° cannot be achieved on some spacecraft (such as the geostationary satellites) and are not likely to be achieved on many low-altitude, sun-synchronous satellites unless deployable radiators can be used (deployable radiators would require a flexible primary heat pipe).

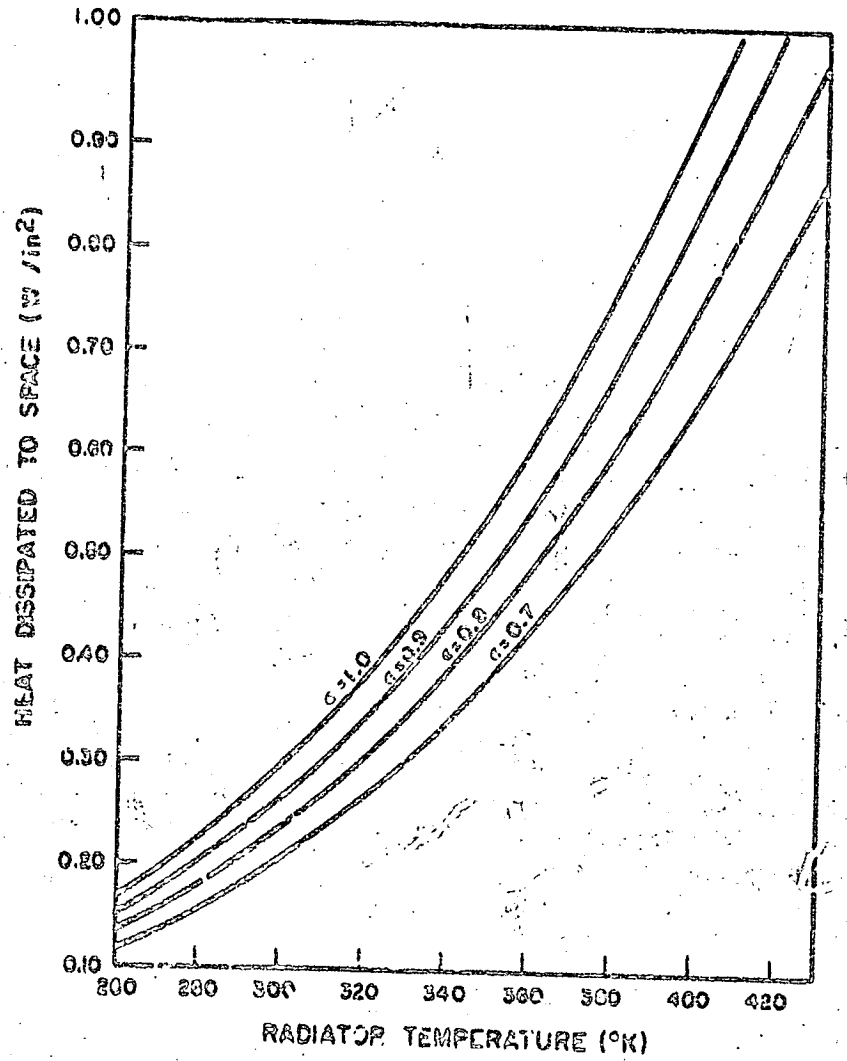



Fig. 5-64. Heat radiated to space as a function of radiator temperature for a 100-percent-efficient, isothermal radiator with emissivity as a parameter.

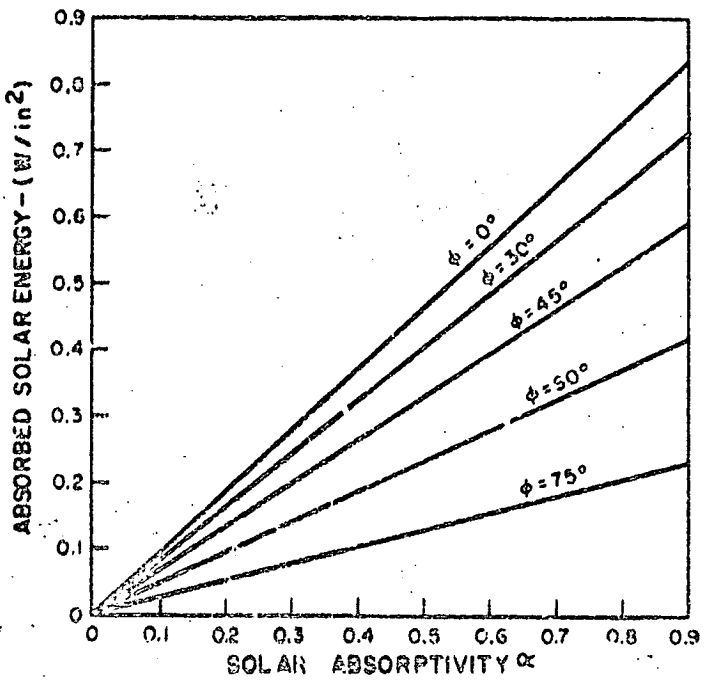



Figure 5-55. Solar energy absorbed by radiator as a function of solar absorptivity for a solar constant of 0.93 W/in.$^2$ with the angle between solar vector and radiator normal as a parameter.

Second-surface mirrors with an emissivity of 0.80, an undegraded solar absorptance of 0.06, and a degraded solar absorptance of 0.10 or less can be used as a radiator finish. This will give a maximum ($\alpha$ = 0.10) absorbed heat flux of 0.093 W/in.$^2$ at $\phi$ = 0° and a heat flux of 0.047 W/in.$^2$ at $\phi$ = 60°. These heat fluxes are within the limits chosen and are the lowest values which can be achieved within the present state-of-the-art.

The Astro-Electronics Division of RCA has recently developed a technique for applying a clear coating to solar cells which may eliminate the need to bond cover glasses on solar cells. A similar technique may be used to fabricate a radiator finish which has thermal properties very close to that of second-surface mirrors but would be much lower in cost, lighter in weight, and would be less susceptible to damage. This technique is presently under investigation but is not as yet a proven finish. Therefore, the recommended finish for radiators which must accept a high sun load is second-surface mirrors.

The earth and spacecraft self-emitted heat fluxes are not a factor in determining the radiator finishes since these heat fluxes will be absorbed and re-emitted with the same efficiency (IR absorptivity and emissivity are equal).

The earth reflected solar energy is a factor in determining the radiator finish but is not as critical as the direct solar energy since the maximum heat flux is 0.3 $W/in.^2$ at an altitude of 600 nautical miles and decreases rapidly as the altitude increases.

A finish which minimizes the absorbed direct solar energy will also minimize the absorbed earth reflected solar energy. Therefore, second-surface mirrors are also recommended for most radiators which face the earth at low altitudes but final selection would have to be made on the basis of spacecraft altitude and orbit parameters.

The recommended finish for radiators which do not receive direct solar energy or high values of earth reflected solar energy is any good space qualified white paint which has an emissivity of approximately 0.9.

2. Radiator Configuration

In order to mount second-surface mirrors on a surface, the surface should be flat and rigid. Rigidity is required in order to prevent cracking and/or falling off of mirrors during launch vibration. In addition, the design should permit construction of the lightest-weight radiator that is compatible with the surface area and rigidity requirement.

In order to meet these requirements, a honeycomb panel containing heat pipes, as shown in Fig. 5-56, is recommended.

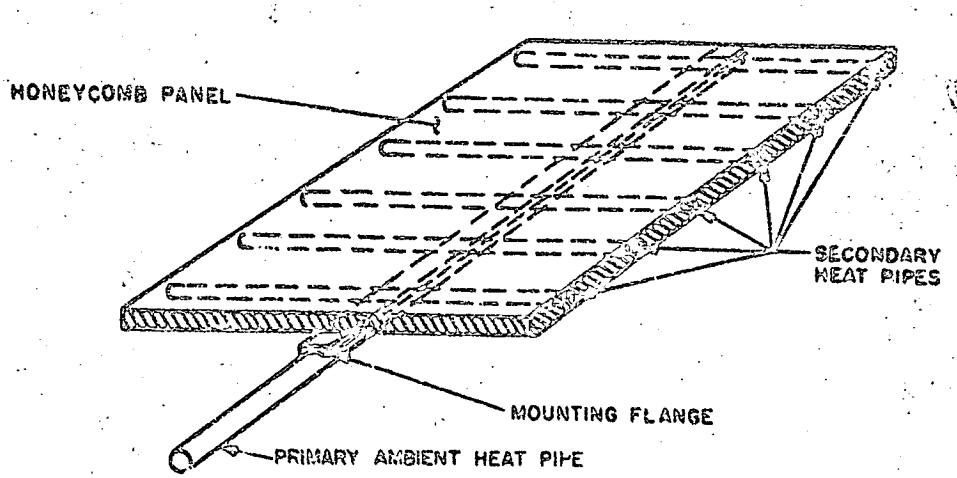



Fig. 5-56. Honeycomb heat pipe radiator.

Other configurations were considered and rejected because of their relatively high weight. A comparison of radiator weights is shown in Fig. 5-57 for a 350-W radiator at 300° K with PE = 0.3. (PE is the ratio of absorbed external energy to the total emitted energy of an isothermal radiator at the heat-pipe temperature.) PE = 0.3 corresponds to a second-surface mirror radiator with an incident solar input at an angle of approximately 45°. As shown in Fig. 5-56, the solid-aluminum radiator (1100 aluminum alloy) must be very large and long (and therefore impractical) before it can begin to compete with the minimum-weight heat-pipe radiator. A solid radiator with the same area as the minimum-weight heat-pipe radiator would weigh approximately 70 pounds as opposed to approximately 6 pounds for the heat pipe radiator. A radiator with a tapered cross section would be slightly lighter but still could not compete with the heat-pipe radiator.

The heat-pipe-honeycomb radiator consists of heat pipes embedded in a honeycomb core which has the same thickness as the diameter of the heat pipe. The skins are aluminum alloy bonded to the heat-pipe-honeycomb matrix. The second-surface mirrors are bonded to the radiating surfaces with RTV.

For a radiator which uses both the front and back surfaces for heat rejection (2-sided radiator), the skins will be identical in material and thickness. For a radiator which uses only one side for heat rejection (single-sided radiator), the skin on the radiating side should be the thicker of the two skins in order to minimize the amount of heat which must be conducted from the back skin to the front skin through the honeycomb. Since the radiating skin or skins are the primary heat transport mechanism, they should be made of an aluminum alloy with high thermal conductivity (1100 or 1145 aluminum alloy is recommended). The non-radiating skin could be made of a high-strength aluminum alloy (keeping the thermal conductivity times thickness product constant) since its primary purpose is to provide structural strength.

### 3. Thermal Analysis and Optimization

The honeycomb-heat pipe radiator is basically a series of identical rectangular fin radiators fabricated into a single unit as shown in Fig. 5-58. Therefore, the radiator can be analyzed on the basis of a single fin radiator which is uniformly heated along one edge. Since there are an infinite number of fin configurations (height and thickness) which will dissipate the required amount of heat, it is necessary to find the configuration which will yield the minimum weight for any specified external environment and size constraint.

This can be accomplished by generating a mathematical model which will permit a computer to calculate and select the design which results in the lightest weight

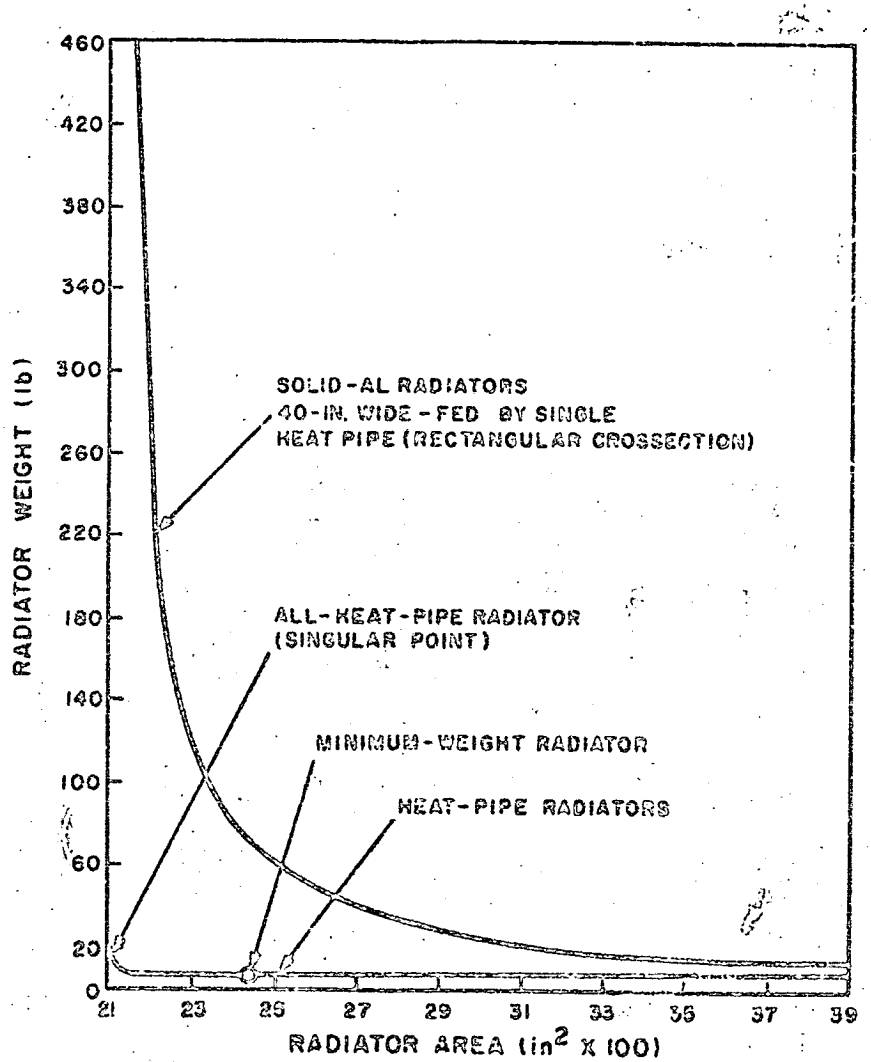



Fig. 5-57. Radiator weight as a function of area for single-sided solid-aluminum and heat-pipe radiators, a heat dissipation of 350W, and a PE of 0.3.

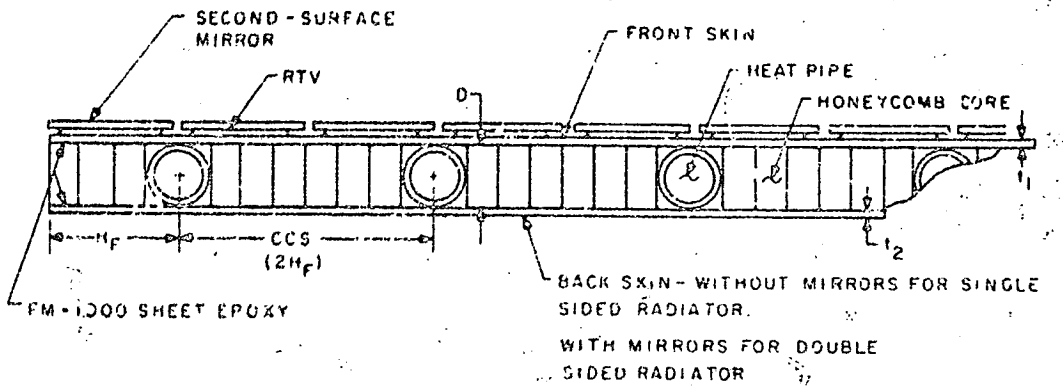



Fig. 5-58. Cross-section of heat-pipe radiator.

radiator for various environmental conditions and material thermal properties. The weight of a radiator is computed as follows:

$$W_r = A_r\left(\frac{D\,P_c}{1728\,S} - \frac{D^2\,P_c}{3456\,S\,H_f} + t\,P_s + W_{sf} + \frac{2W_e}{S}\right) + W_{hp}\,\Sigma \qquad (5\text{-}74)$$

where

$W_r$ is the weight of the radiator (pounds)

D is the thickness of honeycomb core (OD of heat pipe) (in.)

S is the number of radiating surfaces (1 or 2)

$P_c$ is the density of honeycomb core ($lb/ft^3$)

H is fin height (1/2 heat pipe spacing) (in.)

t is thickness of skin (in.)*

$P_s$ is thickness of skin material ($lb/in^3$)

*$t = (t_1 + t_2)$ for single-sided radiator; $t = t_1 = t_2$ for double-sided radiator.

$W_{sf}$ is unit weight of surface finish ($lb/in^2$)*

$W_e$ is unit weight of epoxy used to bond honeycomb ($lb/in^2$)

$W_{hp}$ is unit weight of heat pipes (lb/in of length)

Z is total length of heat pipes (in.)

$A_r$ is total area of radiating surfaces ($in^2$)

For a rectangular radiation fin, there exists a relationship between $H_f$ and t called the profile number. This relationship can be expressed as:

$$N_p = \frac{\bar{\epsilon}\,\sigma\,T_r^3\,H_f^2}{kt} \qquad (5\text{-}75)$$

where

$N_p$ is profile number

$\bar{\epsilon}$ is emissivity of radiating surfaces (average value)

$\sigma$ is Stefan Boltzman constant ($W/in.^2/°K$)

$T_r$ is radiator root temperature (°K)

k is the thermal conductivity of skin material ($W/in/°K$)

The effectiveness, $\Omega$, of the radiation fin is related to $N_p$ and the environmental parameter, PE, as shown in Fig. 5-55[10]. The effectiveness, $\Omega$, is defined as the ratio of the net heat radiated, $Q_n$, ($Q_n = Q_{rad} - Q_{abs}$) to the total heat that would be radiated from an identical radiator at a uniform temperature equal to the fin root temperature

$$\Omega = \frac{Q_{rad} - Q_{abs}}{A_r\,\epsilon\,\sigma\,T_r^4}.$$

PE is the ratio of absorbed external heat to the total heat that would be emitted by an isothermal radiator at the root temperature

$$PE = \frac{Q_{abs}}{A_r\,\epsilon\,\sigma\,T_r^4}.$$

*Includes all materials used to produce surface finish.

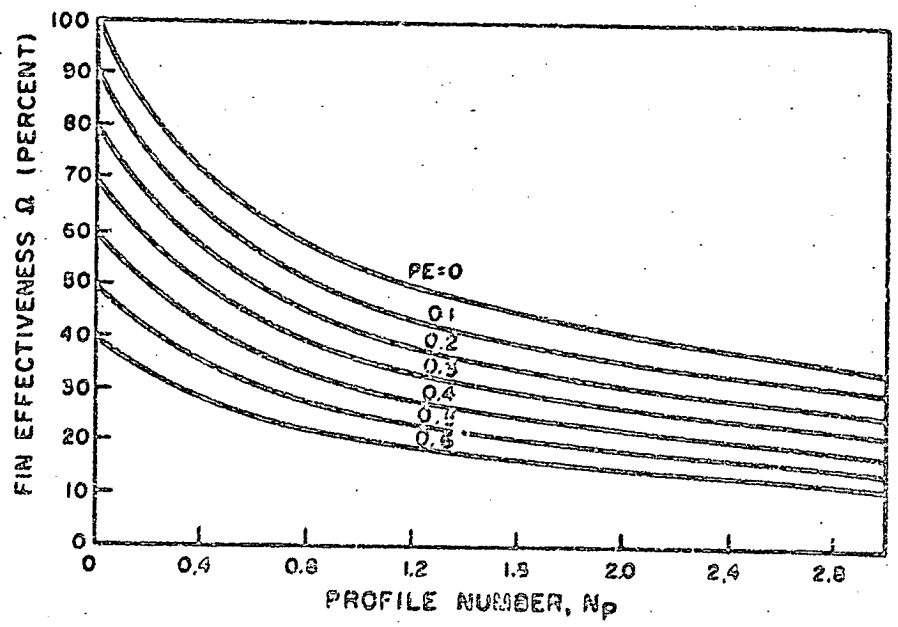



Fig. 5-59. Fin effectiveness as a function of profile number with PE as a parameter.

The total radiator area, $A_r$, is:

$$A_r = \frac{Q_r}{\sigma T_r^4 \Omega \tilde{\epsilon}} \tag{5-76}$$

The fin height is derived from Equation (5-75):

$$H_f = \left( \frac{N_p^2 kt}{\tilde{\epsilon} \sigma T_r^3} \right)^{1/2} \tag{5-77}$$

The required length of heat pipe is:

$$Z = \frac{A_r}{2 S H_f} \tag{5-78}$$

With the aid of a computer, Eqs. 5-74, 5-75, 5-76, 5-77, and 5-78, and the $N_p$ relationships shown in Figure 5-59 can be used to determine the radiator configurations which result in minimum radiator weight. This is accomplished by iterative calculations of $W_r$ at selected points on each of the environmental parameter, PE, curves of Fig. 5-59. The iterative calculations are performed by holding the profile number, $N_p$, and the effectiveness, $\Omega$, constant and varying the skin thickness, t, until the minimum weight configuration is found. A new point on the $N_p$-$\Omega$ curve is then selected and the process repeated. The results of these calculations are shown in Fig. 5-60 through 5-65. The following values were used in all calculations:

$Q_n$ = 350 W

D = 0.25 in.

k = 5.52 W/in/° K (1100 Al Alloy)

$\bar{\epsilon}$ = 0.8 (second-surface mirrors)

$P_c$ = 1.0 lb/ft$^3$ (light-weight aluminum honeycomb core)

$P_s$ = 0.1 lb/in$^3$ (1100 Al alloy)

$W_e$ = 0.0001735 lb/in$^2$ (FM-1000 sheet epoxy)

$W_{sf}$ = 0.00104 lb/in$^2$ (8-mil second-surface mirrors with 5 mils of RTV)

$W_{hp}$ = 0.00216 lb/in (estimated wt. of 0.25-in OD heat pipe)

Figures 5-60, 5-61, and 5-62 are for single-sided radiators at 300° K, 325° K, and 350° K, respectively. Figures 5-63, 5-64, and 5-65 are for double-sided radiators at 300°K, 325°K, and 350°K, respectively.

Each of the illustrations contain all of the information necessary to design a heat pipe-honeycomb radiator when constructed with the materials indicated. If it is desirable to use other materials, different size or weight heat pipes, and/or operate at other temperatures, it will be necessary to use Eq. 5-74 to find the optimum configuration for the new conditions. With the aid of a computer, this is a relatively simple process.

The radiator weights shown in Figs. 5-60 through 5-65 do not include any weight allowance for inserts required to mount the radiator or mate the primary heat pipe and the radiator since the quantity required will depend upon the final shape of the radiator.

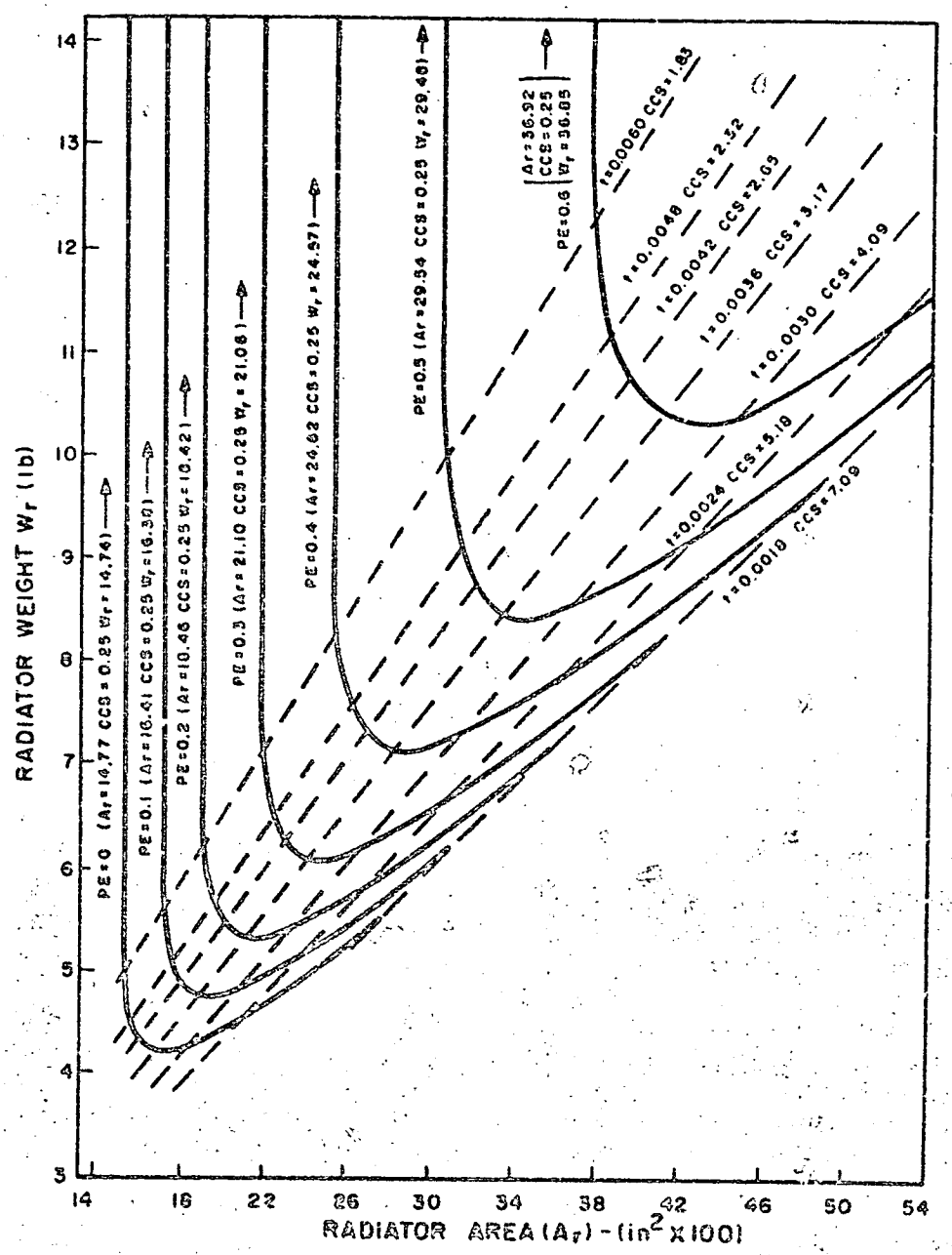



Fig. 5-60. Radiator weight as a function of area for a single-sided heat-pipe radiator with environmental parameter and skin thickness-heat-pipe spacing as parameters at a heat-pipe temperature of 300° K.

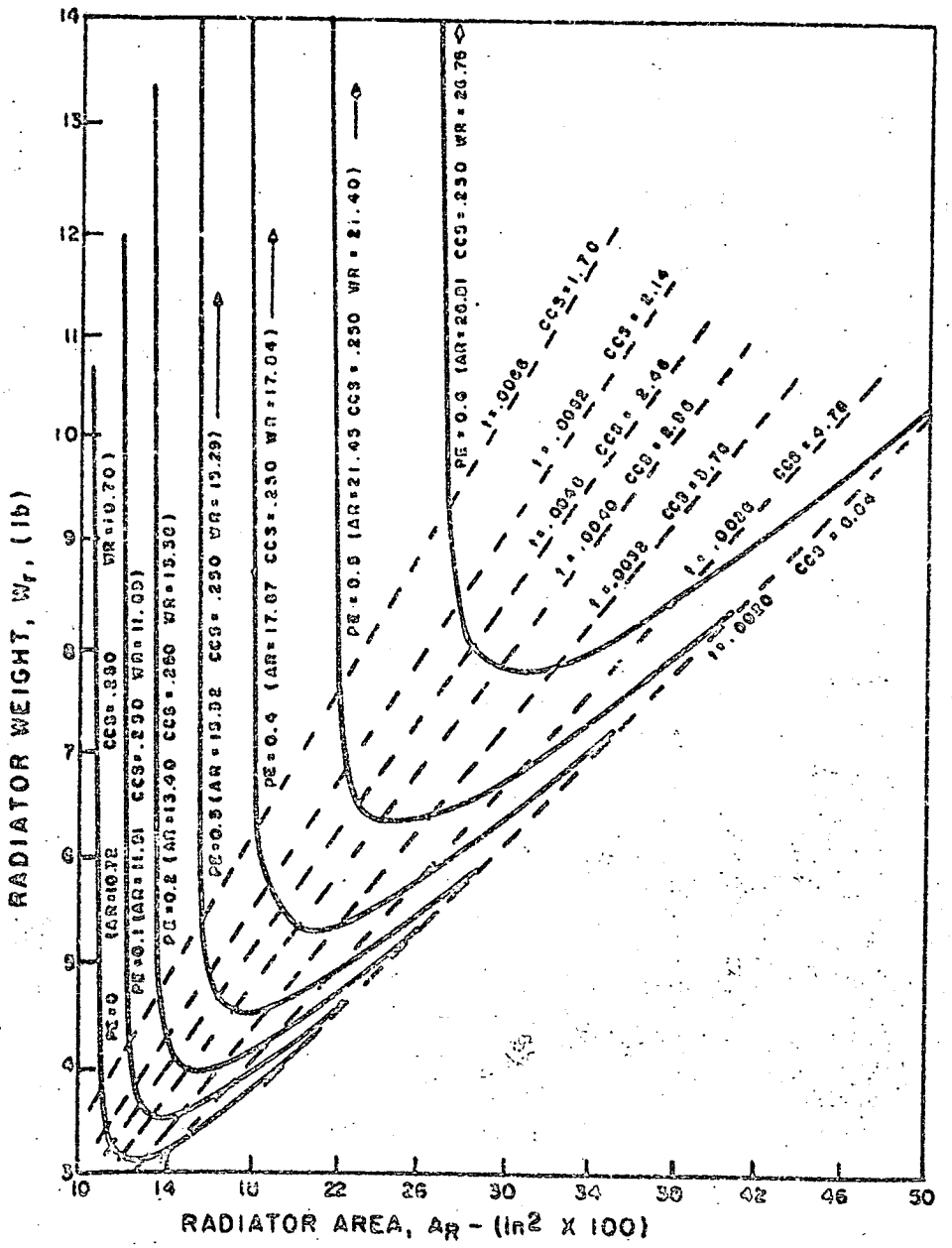



Fig. 5-61. Radiator weight as a function of area for a single-sided heat-pipe radiator with environmental parameter and skin thickness-heat-pipe spacing as parameters at a heat-pipe temperature of 325° K

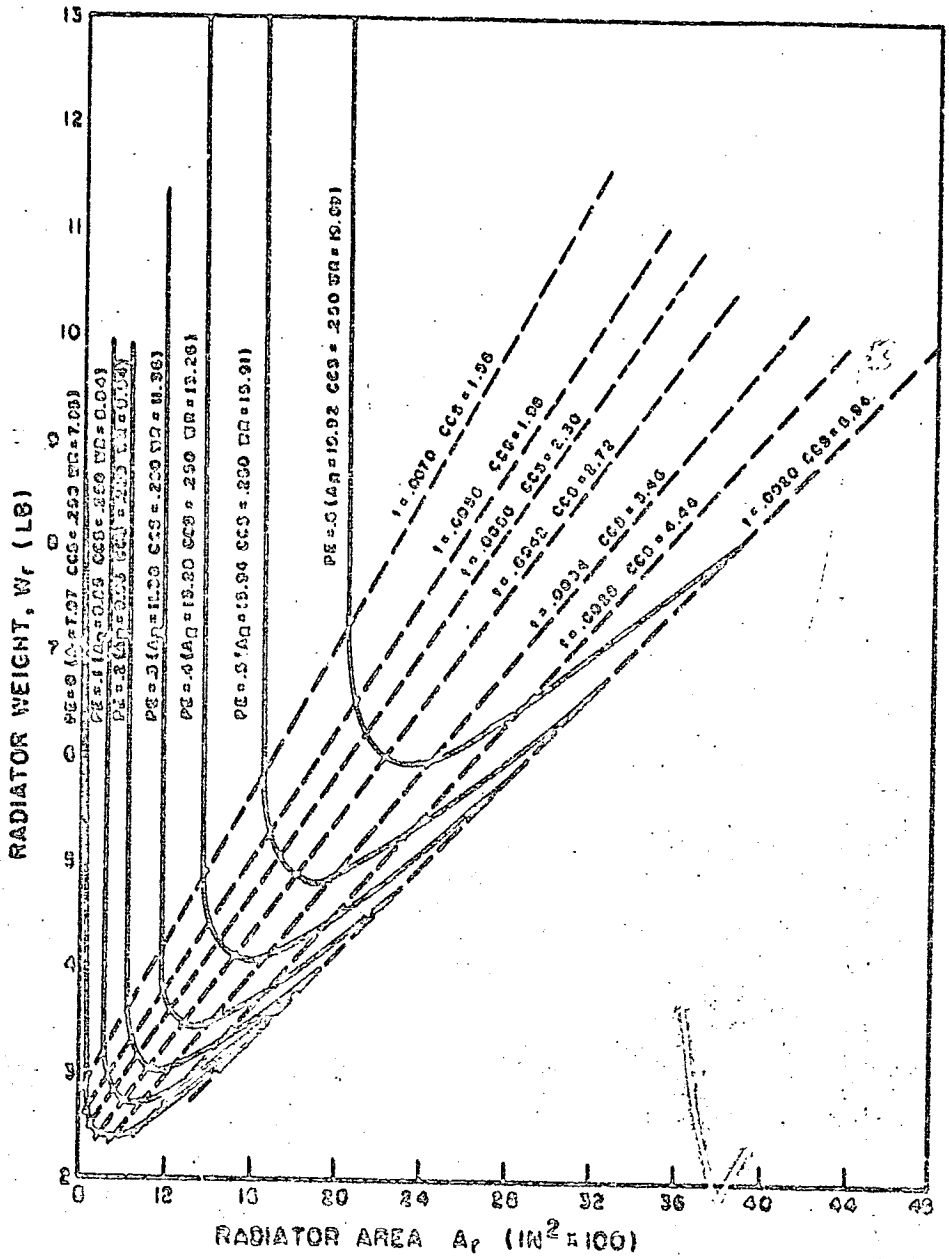



Fig. 6-62. Radiator weight as a function of area for a single-sided heat-pipe radiator with environmental parameter and skin thickness-heat-pipe spacing as parameters at a heat-pipe temperature of 350° K.

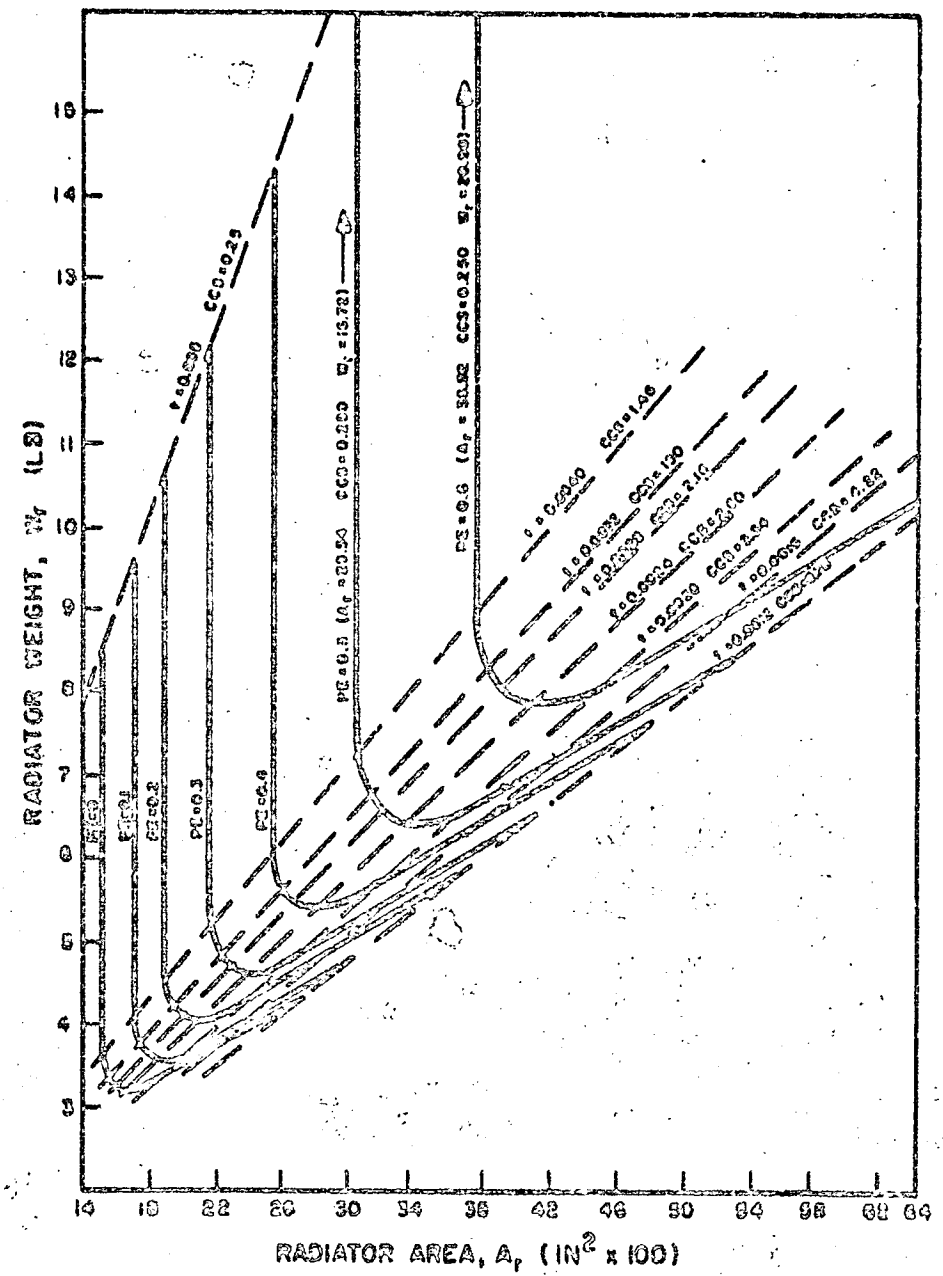



Fig. 5-63. Radiator weight as a function of area for a double-sided heat-pipe radiator with environmental parameter and skin thickness-heat-pipe spacing as parameters at a heat-pipe temperature of 300° K.

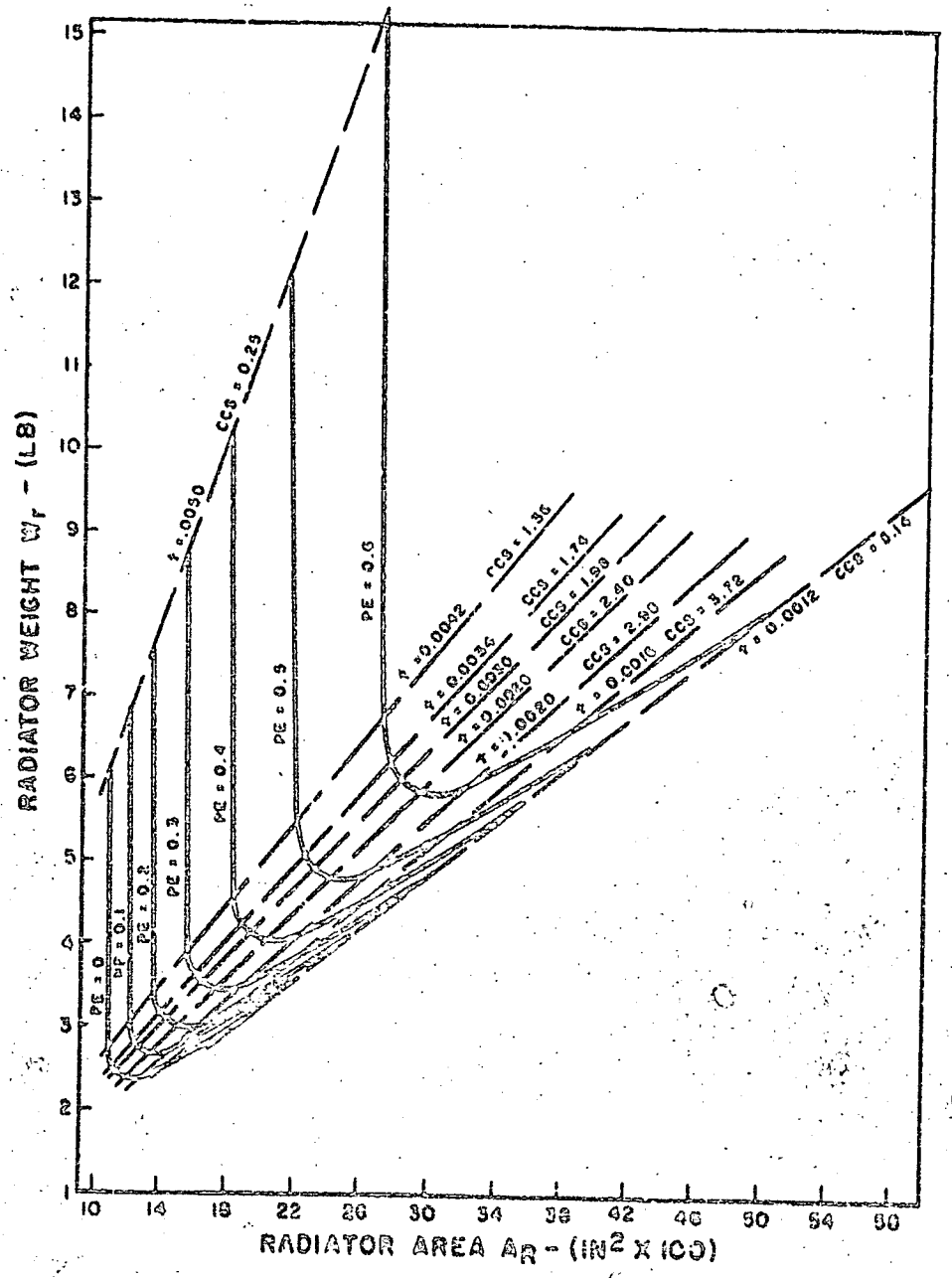



Fig. 5-64. Radiator weight as a function of area for a double-sided heat-pipe radiator with environmental parameter and skin thickness-heat-pipe spacing as parameters at a heat-pipe temperature of 325° K.

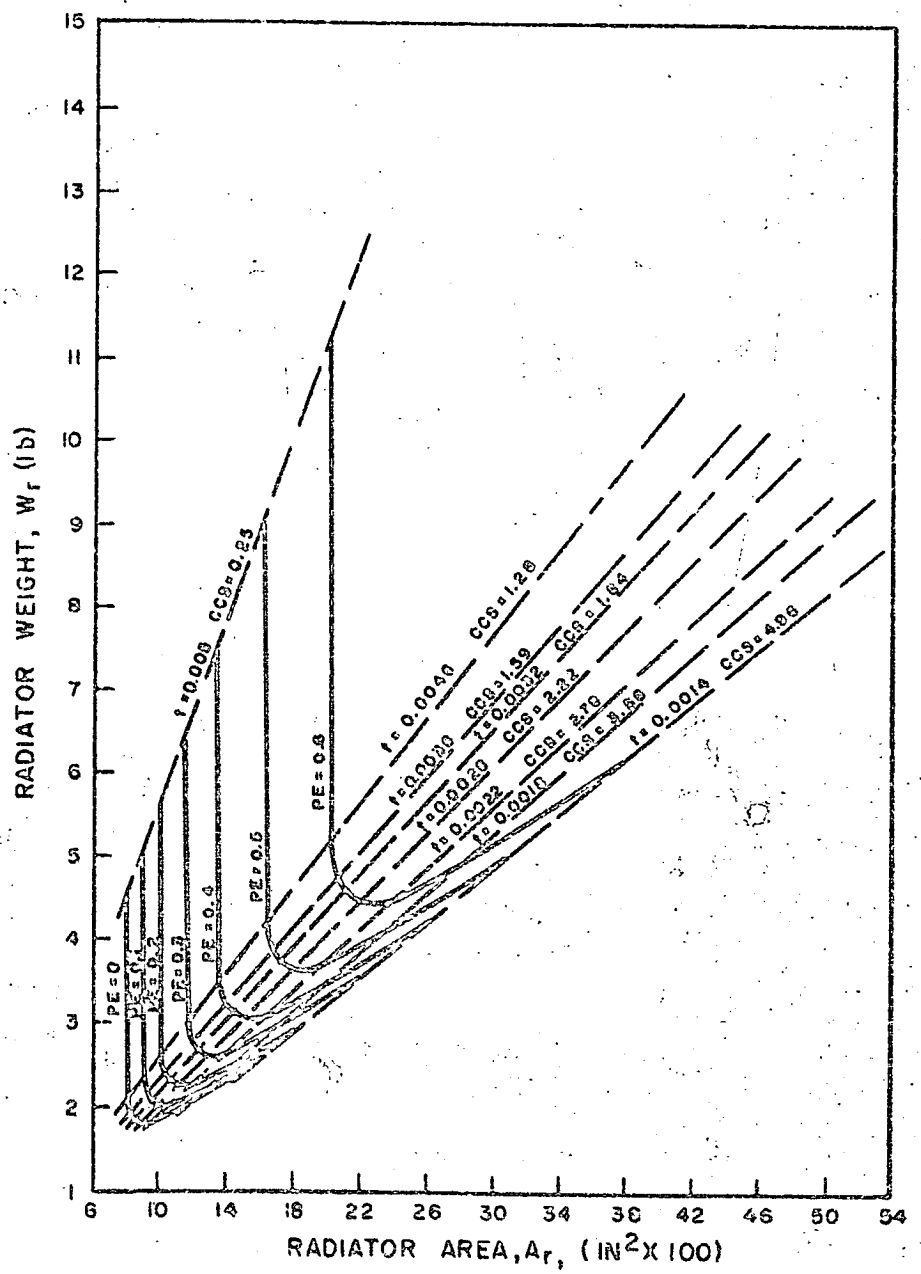



Fig. 5-65. Radiator weight as a function of area for a double-sided heat-pipe radiator with environmental paramoter and skin thickness-heat-pipe spacing as parameters at a heat-pipe temperature of 350° K.

Inspection of Figs. 5-60 through 5-65 show that a very sharp increase in radiator weight occurs as the minimum radiator area (maximum effectiveness) as approached. The radiator weights, areas, and heat-pipe spacings shown in parenthesis are for the minimum-area cases which do not fall on the graphs.

It should be noted that each point on each curve represents the minimum weight configuration (obtained by computer) for that particular radiator area. There exists an infinite number of other configurations for any particular radiator area but all are heavier than the configuration shown.

At first glance, it would appear that at each temperature, a particular skin thickness and heat-pipe spacing results in the minimum-weight radiator. This is not true but appears to be true because of the relative flatness of the curves at the minimum values. Figure 5-60 shows that a single-sided radiator with skin thicknesses totaling 0.0036 in. and a heat-pipe spacing of 3.17 in. will result in a near-minimum-weight radiator for all environmental conditions when operated at 300° K. If the area constraints of a particular system prohibit the use of this configuration, a heavier radiator with less area must be chosen or a double-sided radiator must be used. For the same environment parameter, the minimum-weight, double-sided radiator will be approximately half the size of the single-sided radiator and approximately 25 percent lighter.

The recommended double-sided radiator will have skin thicknesses of 0.0024 in. each and a heat-pipe spacing of 2.60 in.

The size, shape, weight, and design of a flight radiator will depend upon the flight spacecraft.

## F. LOW-TEMPERATURE HEAT PIPE

### 1. Fluid Selection

The selection of a working fluid for the cryogenic heat pipe is based on the following criteria: (1) fluid properties $\gamma$, h, $\rho_\ell$ $\rho_V$, $N_\ell$, $N_V$ such that maximum throughput is obtained for a given pipe length, diameter and wick thickness, and gravity field; (2) high $k_\ell$ to minimize input-output $\Delta T$s; (3) low value of $\rho_\ell$/MW to minimize internal pressure at ambient temperature; and (4) chemical compatibility of fluid with wick and container materials to insure to long undegraded life. An expression combining all four criteria into a single working fluid "figure of merit" does not exist and would be meaningless if it did since different applications would require each criteria be weighted differently. Each criteria is thoroughly examined in light of an ICICLE application in the following paragraphs.

#### a. Maximum Throughput Criteria

The maximum zero-g heat-pipe throughput equation was developed in Section 5. and is

$$Q|_{r_{co}} = Q_{max} = \frac{2\gamma h\, r_w^3}{\left[\dfrac{13.5\, b\, \eta_\ell\, \eta_V\, (Z+Z_a)^2}{\pi^2 \rho_\ell\, \rho_V\, e}\right]^{1/2}} \qquad \begin{matrix} Re_z < 1000,\ Re_r << 1, \\ \text{Homogeneous Wick} \end{matrix} \qquad (5\text{-}79)$$

$$\left(\frac{r_V}{r_w}\right)_o$$

The length term may be combined with the maximum throughput to yield:

$$Q(Z+Z_a)_{max} = \left(0.542\, r_w^3 \sqrt{\frac{e}{b}}\right)\left(\gamma h \sqrt{\frac{\rho_\ell\, \rho_V}{\eta_\ell\, \eta_V}}\right) \qquad (5\text{-}80)$$

The first bracketed expression is a function of the pipe and wick geometry; the second expression is a function of fluid properties only. The largest value of $\gamma h \sqrt{\rho_\ell\, \rho_V/(\eta_\ell\, \eta_V)}$, will, therefore, yield the largest $Q(Z+Z_a)$ product or in terms of a fixed ICICLE heat load, the maximum value of $\gamma h \sqrt{\rho_\ell\, \rho_V/(\eta_\ell\, \eta_V)}$ will yield the longest cryogenic heat pipe based on zero-g fluid-flow considerations.

The longest heat-pipe length means a more flexible ICICLE system since the system design should not be dictated by the length of the cryogenic heat pipe.

The fluid parameter $\left(\gamma h \sqrt{\rho_\ell\, \rho_V/(\eta_\ell\, \eta_V)}\right)$ for the maximum $Q(Z+Z_a)$ product in the absence of gravity forces is referred to as the working fluid figure of merit as is plotted in Fig. 5-3 for all candidate ICICLE working fluids. Good heat-pipe design practice calls for an analysis of the effects of acceleration on the pipe

design and fluid selection.* As the following paragraphs will detail, the exclusion of acceleration effects could result in the selection of a different working fluid or in a heat pipe design which cannot be tested on the launch pad, even in a horizontal orientation.

The maximum throughput length expression for operation in an acceleration field was developed in Section 5.A.

$$Q(Z+Z_a)\big|r_{co} = \frac{2\gamma\, r_{co} - C\, r_{co}^2}{A + B\, r_{co}^2} \qquad (5\text{-}81)$$

where

$$A = \frac{h\,\eta_\ell}{2\pi (r_w^2 - r_v^2)\rho_\ell\, he} \qquad B = \frac{4\,\eta_v}{\pi \rho_v\, r_v^4\, h} \qquad C = \rho_\ell\, gZ$$

The optimum pore size can be expressed in terms of the pipe geometry, wick geometry, fluid properties and gravity fields as:

$$r_{co} = \frac{-AC + \sqrt{(AC)^2 + 4\gamma^2\, AB}}{2\gamma B} \qquad (5\text{-}82)$$

The optimum wick-thickness ratio for zero-g conditions was shown to be 0.817 for a homogeneous wick and 0.834 for a channel wick. For both types of wicks, $r_v/r_w|_o$ is inversely related to the g field as might be expected, since additional flow area is required to support the gravitational pressure drop. Also, the $r_{co}$ is related to g field as shown in 5-82 above. Equations 5-80 and 5-81 were programmed into the computer and plots of $Q(Z+Z_g)$ vs. $r_w$ were generated for oxygen and nitrogen at 77°K and 90°K for several acceleration fields including zero g. (Methane and fluorine were eliminated from the detailed analysis because of their toxicity and corrosiveness.) Also the triple point of Methane (90.6°K) and Argon (83.5°K) precludes their use below these temperatures. The $Q(Z+Z_a)_{max}$ vs. $r_w$ plots are shown in Figs. 5-66 through 5-83. The effect of acceleration fields (expressed as a product of g, Z and $\sin\phi$) on the throughput-length term for the candidate fluids and temperatures and for two common wick geometries: homogeneous and channel wicks, are shown in Figs. 5-66 through 5-73. Fluid selection is facilitated by comparing both fluids at 77°K and 90°K for a particular g Z $\sin\phi$ product using Figs. 5-74 through 5-83. In all plots shown the pore size and wick thickness used in determining $Q(Z+Z_a)_{max}$ is optimum for the particular fluid, temperature, and g Z $\sin\phi$ product.

*Gravitational effects should be considered because of the requirement for ground testing where, even in a horizontal orientation, a significant gravitational liquid pressure drop would exist across the pipe diameter.

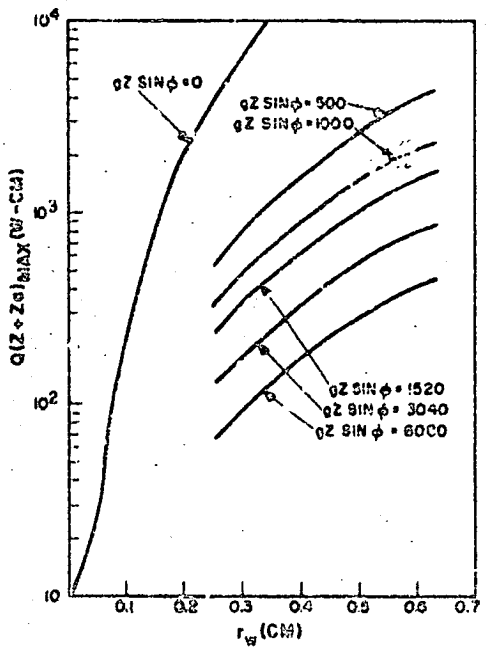



Fig. 5-66. Maximum $Q(Z+Z_0)$ product as a function of inner wall radius with gravitational field products as a parameter for an oxygen heat pipe with a homogeneous wick at a temperature of 90°K.

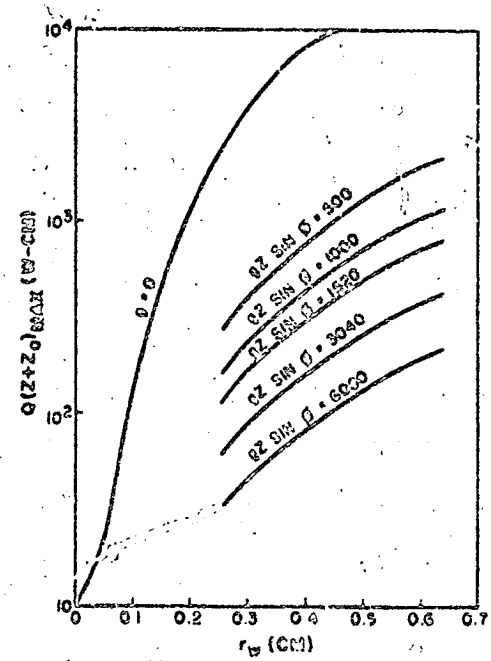



Fig. 5-67. Maximum $Q(Z+Z_0)$ product as a function of inner wall radius with gravitational field products as a parameter for a nitrogen heat pipe with a homogeneous wick at a temperature of 77°K.

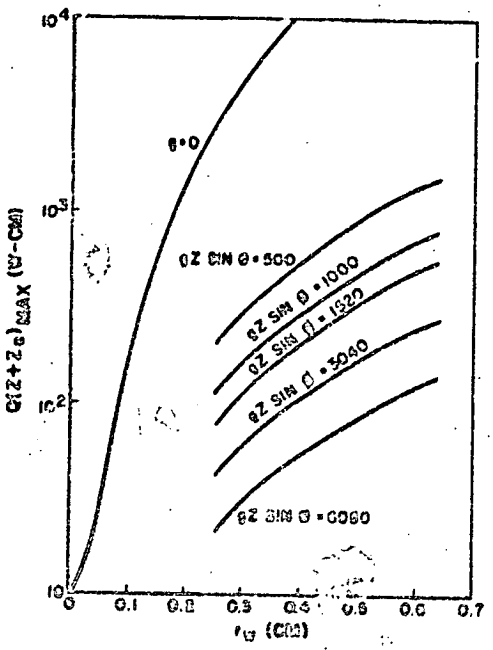



Fig. 5-68. Maximum $Q(Z+Z_0)$ product as a function of inner wall radius with gravitational field products as a parameter for a nitrogen heat pipe with a homogeneous wick at a temperature of 90°K.

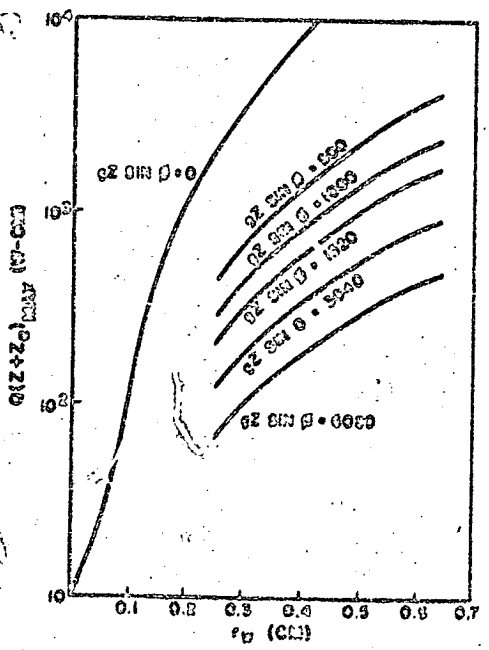



Fig. 5-69. Maximum $Q(Z+Z_0)$ product as a function of inner wall radius with gravitational field products as a parameter for an oxygen heat pipe with a homogeneous wick at a temperature of 77°K.

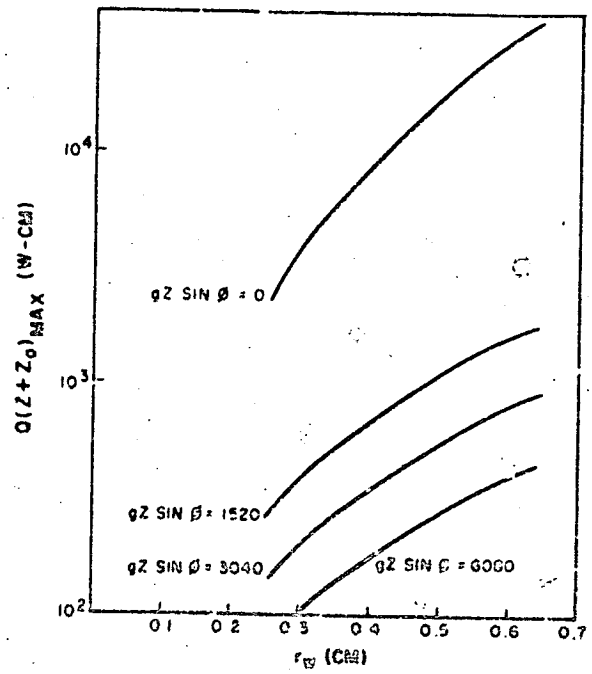



Fig. 5-70. Maximum $Q(Z+Z_0)$ product as a function of inner-wall radius with gravitational field products as a parameter for a nitrogen heat pipe with a channel wick at a temperature of 77°K.

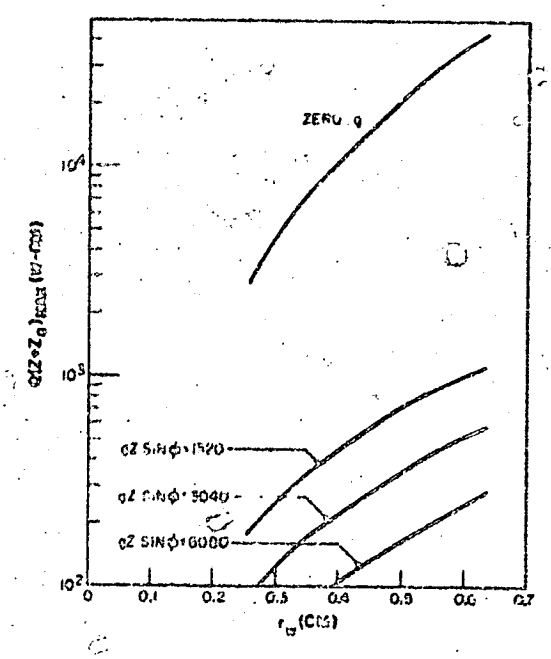



Fig. 5-71. Maximum $Q(Z+Z_0)$ product as a function of inner-wall radius with gravitational field products as a parameter for a nitrogen heat pipe with a channel wick at a temperature of 90°K.

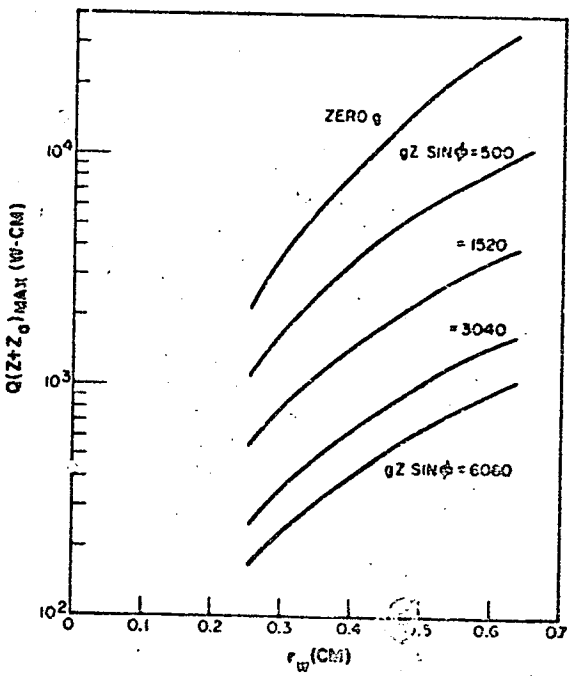



Fig. 5-72. Maximum $Q(Z + Z_0)$ product as a function of inner-wall radius with gravitational field products as a parameter for an oxygen heat pipe with a channel wick at a temperature of 77°K.

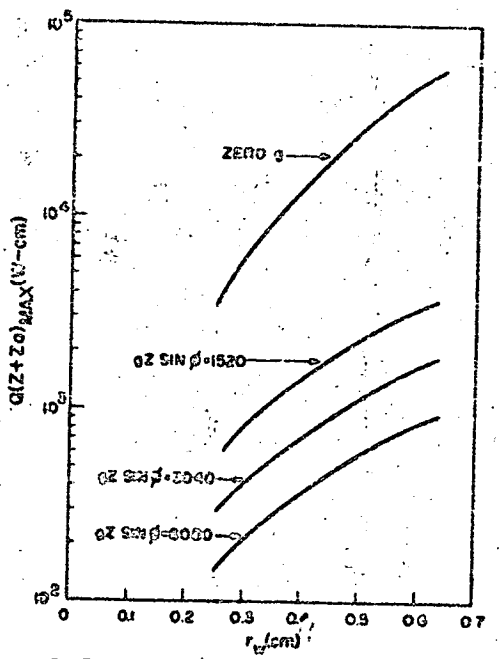



Fig. 5-73. Maximum $Q(Z + Z_0)$ product as a function of inner-wall radius with gravitational field products as a parameter for an oxygen heat pipe with a channel wick at a temperature of 90°K.

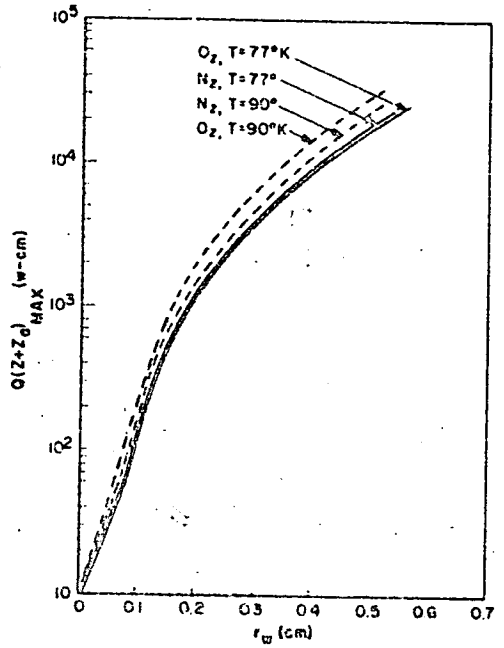



Fig. 5-74. Maximum $Q(Z+Z_0)$ product as a function of inner-wall radius with working fluid at temperature as a parameter for a zero-g field with $r_c$ optimized and $r_v/r_w = \sqrt{2/3}$ in a heat pipe with a homogeneous wick.

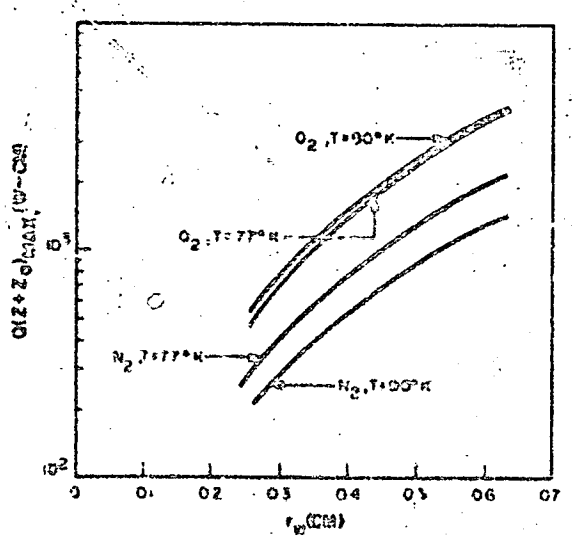



Fig. 5-75. Maximum $Q(Z+Z_0)$ product as a function of inner-wall radius with working fluid at temperature as a parameter for g Z sin$\phi$ = 500 $cm^2/s^2$ in a heat pipe with a homogeneous wick.

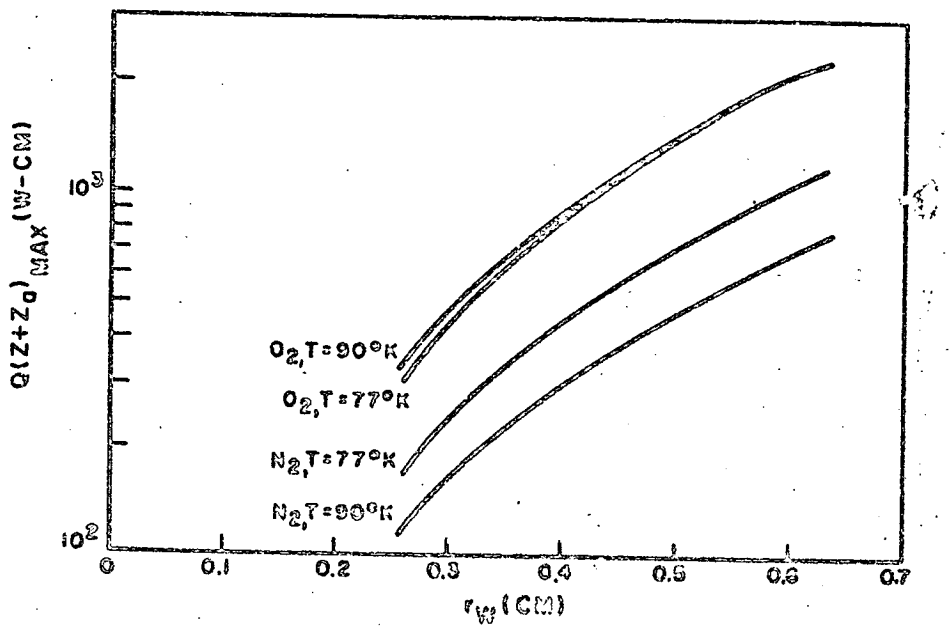



Fig. 5-76. Maximum $Q(Z+Z_0)$ product as a function of inner-wall radius with working fluid at temperature as a parameter for $g\ Z \sin\phi = 1000\ cm^2/s^2$ in a heat pipe with a homogeneous wick.

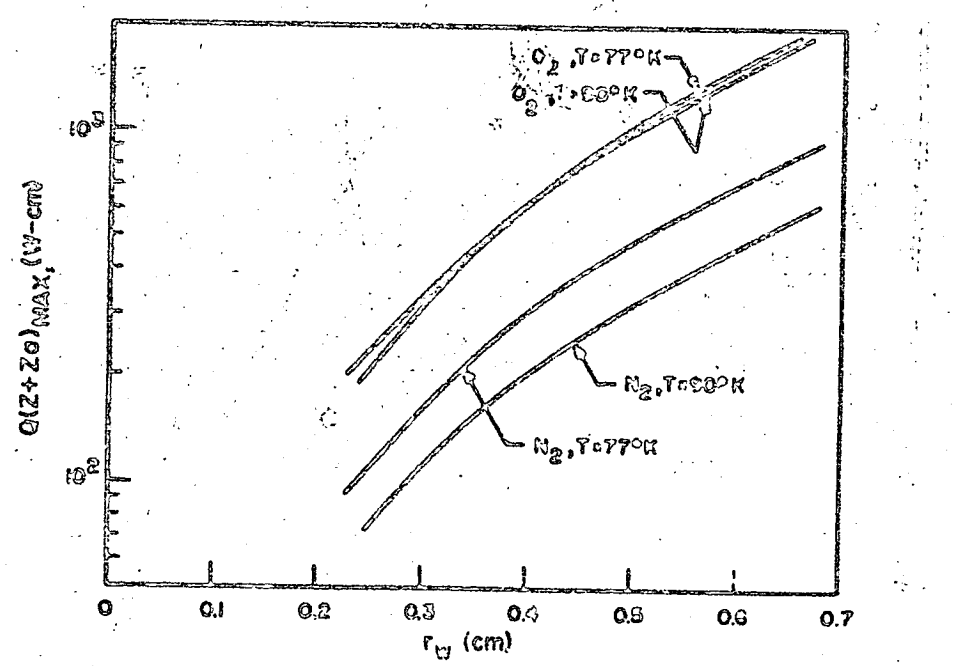



Fig. 5-77. Maximum $Q(Z+Z_0)$ product as a function of inner-wall radius with working fluid at temperature as a parameter for $g\ Z \sin\phi = 1520\ cm^2/s^2$ and optimum $r_c$ and $r_v/r_w$ in a heat pipe with a homogeneous wick.

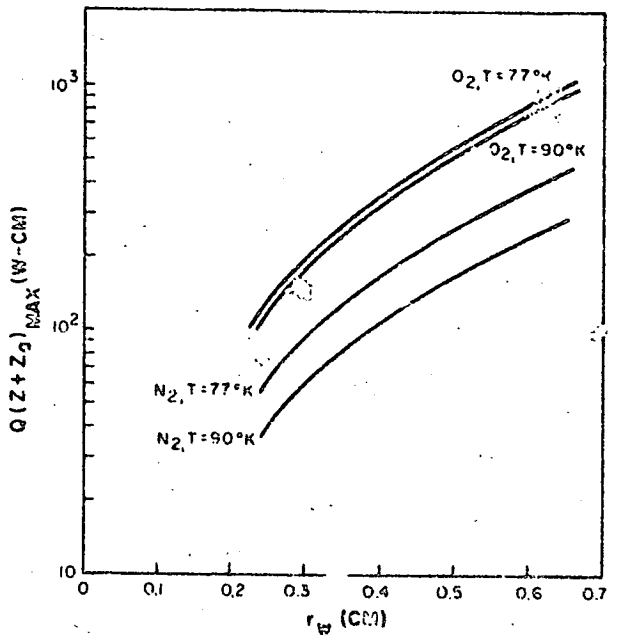



Fig. 5-78. Maximum $Q(Z+Z_g)$ product as a function of inner-wall radius with working fluid at temperature as a parameter for $\rho Z \sin\phi = 3040$ cm$^2$/s$^2$ and optimum $r_c$ and $r_v/r_w$ in a heat pipe with a homogeneous wick.

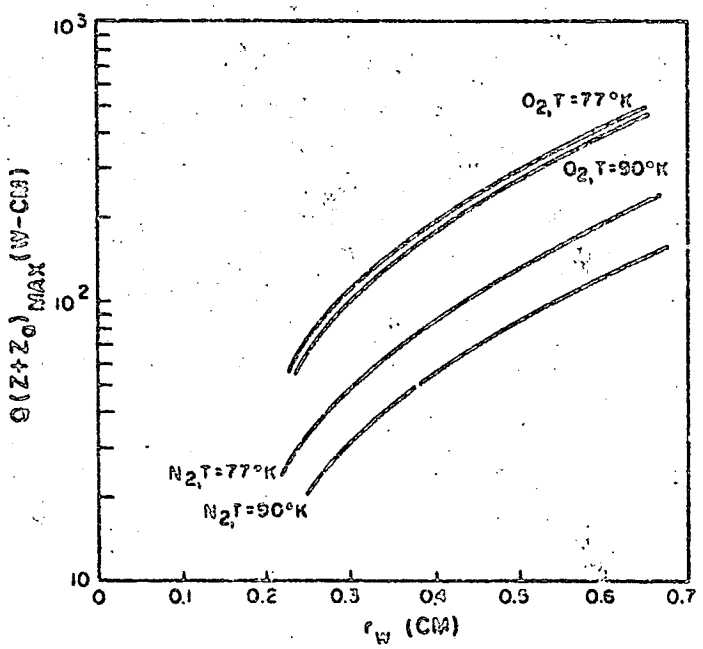



Fig. 5-79. Maximum $Q(Z+Z_g)$ product as a function of inner-wall radius with working fluid at temperature as a parameter for $g Z \sin\phi = 6080$ cm$^2$/s$^2$ and optimum $r_c$ and $r_v/r_w$ in a heat pipe with a homogeneous wick.

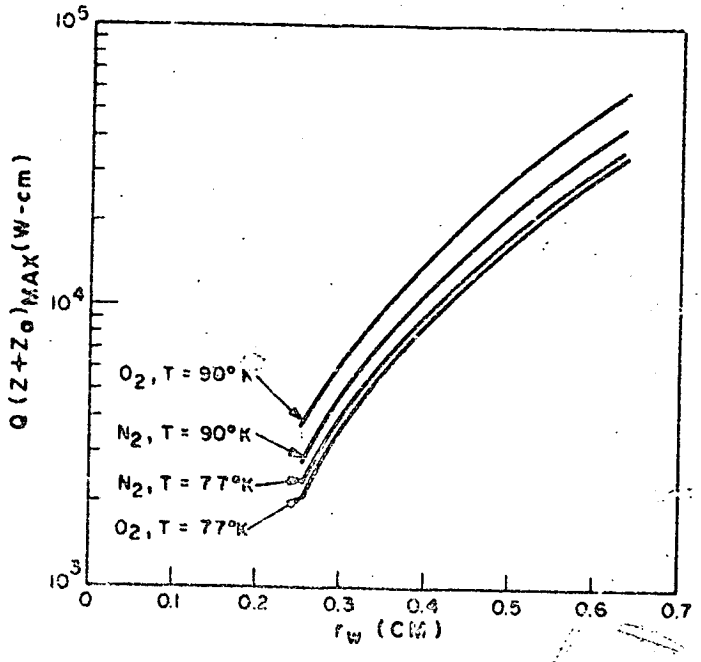



Fig. 5-80. Maximum $Q(Z+Z_o)$ product as a function of inner-wall radius with working fluid at temperature as a parameter for zero-g in a heat pipe with a channel wick.

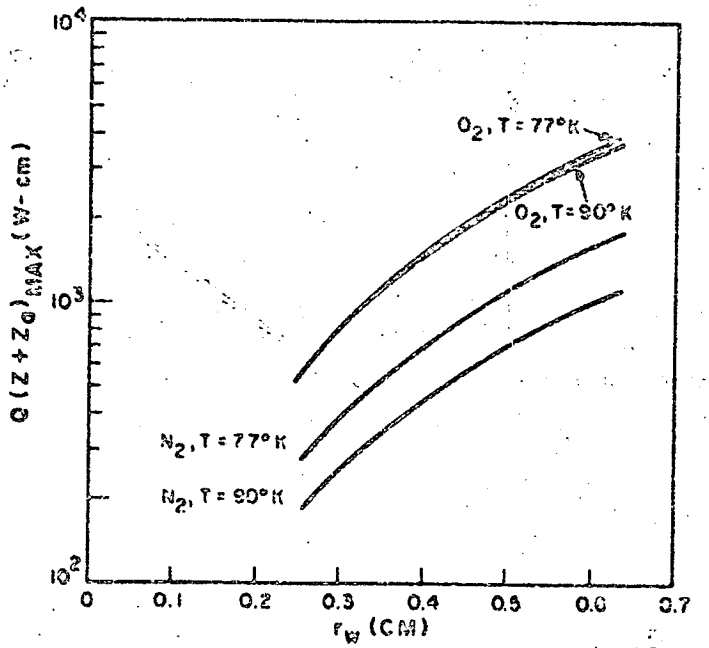



Fig. 5-81. Maximum $Q(Z+Z_o)$ product as a function of inner-wall radius with working fluid at temperature as a parameter for $g\ Z \sin\phi = 1520$ $cm^2/s^2$ in a heat pipe with channel wick.

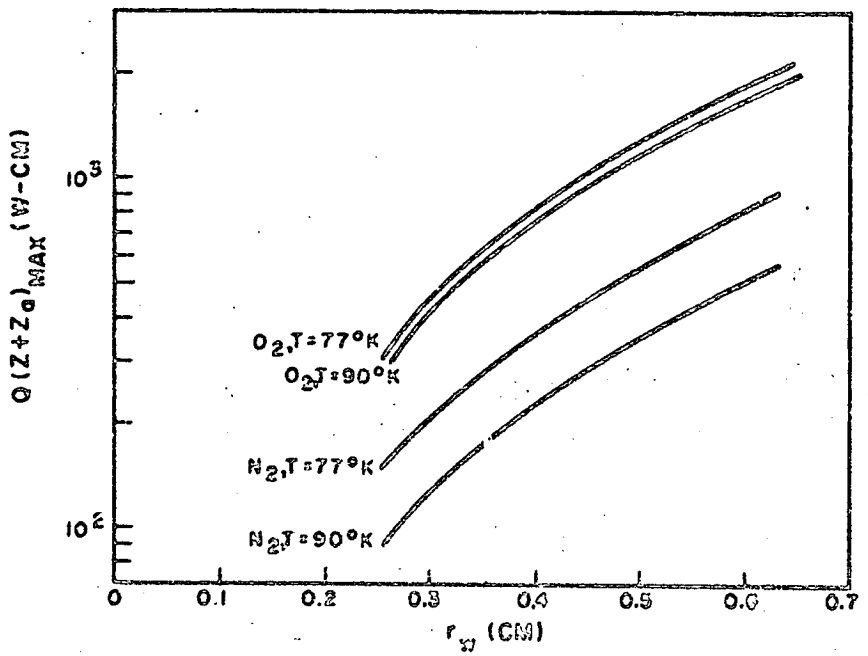



Fig. 5-82. Maximum $Q(Z+Z_a)$ product as a function of inner-wall radius with working fluid at temperature as a parameter for $g\ Z \sin\phi = 3040$ $cm^2/s^2$ in a heat pipe with a channel wick.

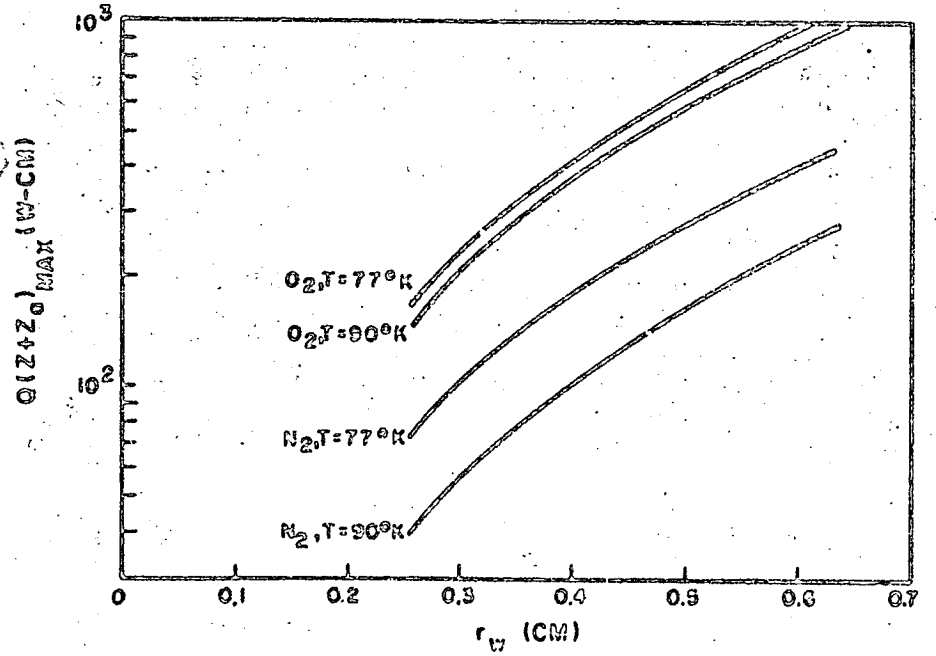



Fig. 5-83. Maximum $Q(Z+Z_a)$ product as a function of inner-wall radius with working fluid at temperature as a parameter for $g\ Z \sin\phi = 6080$ $cm^2/s^2$ in a heat pipe with a channel wick.

The graphs illustrate some important differences between $O_2$ and $N_2$. An examination of the zero-g curves, Figs. 5-74 and 5-80, reveals that at 77°K, $N_2$ yields about 5 to 10% higher $Q(Z+Z_a)_{max}$ product for the same $r_w$ at the optimum design conditions. The performance of $N_2$ and $O_2$, however, changes considerably when even a small g Z sin$\phi$ product is imposed on the heat pipe. Figures 5-77 and 5-81 show that the $Q(Z+Z_a)_{max}$ product for $O_2$ at 77°K is about 2:1 higher than $N_2$ at 77°K in a "g-field product" (g Z sin$\phi$) of 1520 $cm^2$. This product could represent a one-foot (30 cm) pipe operating in a gravity field of 0.05 g with sin$\phi$ = 1. Or, the condition could be a heat pipe with $2r_w$ = 1.5 cm oriented horizontally on earth. It should be emphasized that the liquid pressure drop due to gravity for a horizontal cryopipe in a 1-g field cannot be neglected, even for the small diameters of interest. The 2:1 ratio is also maintained for larger g Z sin$\phi$ products.

The degradation of $Q(Z+Z_a)$ with increasing temperature is greater with $N_2$ in a "g" field than with $O_2$. For example, Fig. 5-78 shows a 5-1/2% degradation for $O_2$ with a temperature rise from 77°K to 90°K. The same temperature rise in a nitrogen pipe results in a 35% drop in $Q(Z+Z_a)$. The throughput-length product, therefore, is relatively insensitive to temperature changes for an optimized oxygen heat pipe in the range 77°K - 90°K. For heat pipe designs which are optimized for zero-g conditions, Figs. 5-74 and 5-80 show an increase in $Q(Z+Z_a)$ for both $O_2$ and $N_2$ heat pipes as the operating temperature increases from 77°K to 90°K. It should be noted, that for optimized designs, the optimum pore size and the optimum wick thickness ratios are functions of fluid properties, gravity field, and $r_w$. The optimized wick designs therefore, are different at 90°K than at 77°K which can result in a throughput increase with a temperature increase even though fluid properties such as surface tension and latent heat are degrading with increasing temperature. On the basis of maximum throughput criteria, the preferred working fluid is in the 77°K to 90°K range clearly oxygen. The heat-transfer properties of each fluid are discussed in the following paragraphs.

b. Thermal Conductivity Criteria

Homogeneous wicks such as screen mesh and felt metals are typically 20% to 30% dense; when saturated with a working fluid, the liquid becomes the primary heat-transfer medium and therefore, the liquid thermal conductivity is the important parameter in determining heat transfer temperature drops in a heat pipe evaporator and condenser. The lower limit on thermal conductivity of a composite structure is given by Corring and Churchill[13] for a heat conduction in series:

$$\frac{k_e}{k_s} = \frac{1}{1 + e\left(\frac{k_s}{k_\ell} - 1\right)}$$

Assuming a nickel fiber metal wick filled with nitrogen, $\begin{cases} k_s = 0.62\ \text{W/cm/°K}, \\ k_\ell = 0.0014\ \text{W/cm/°K}, \\ e = .85, \text{ and } T = 77\text{°K}. \end{cases}$

The composite thermal conductivity for this structure is 0.00164 W/cm/°K or only 17% higher than the conductivity of the liquid. The assumption of ordinary thermal conduction through an all liquid layer, therefore, is a conservative one. A plot of cryogenic liquid thermal conductivity as a function of temperature is presented in Fig. 5-84. For identical, low-density wick structures, $O_2$ will yield lower conduction $\Delta T$s throughout the temperature range of interest. For densely packed wick structures, the composite thermal conductivity is independent of the liquid in the pores.

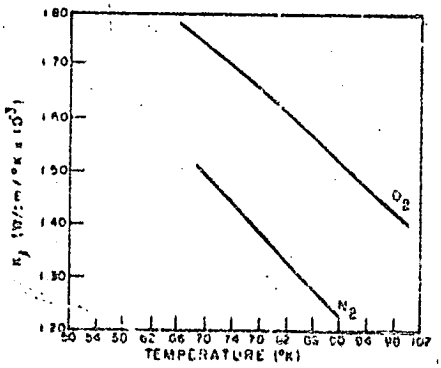



Fig. 5-84. Cryogenic liquid thermal conductivity as a function of temperature with working fluid as a parameter.

Boiling heat transfer in cryogenic fluids is highly empirical and most studies published to date contain data for nitrogen only. It is difficult to predict the onset of nucleate boiling of a cryogenic fluid in a wick since there are no published works on this subject. The heat transfer coefficient for cryogenic wick boiling as for boiling in general depends on the surface condition of the wick as well as the physical properties of the liquid. The effect of wick design on heat transfer will be explained later in this Section; the combination of physical properties which affect the boiling heat transfer coefficient is given in a general form by Allingham and McIntire[14] as

$$\left[\frac{h}{CG}\right]^a \left[\frac{C\eta}{\kappa}\right]^b \left[\frac{\rho_\ell \gamma}{p^2}\right]^c = \phi \left[\frac{D_e G}{\eta}\right]^d \qquad (5\text{-}83)$$

where

h is boiling film coefficient
C is specific heat of liquid
G is liquid mass flow rate

$\eta$ is liquid viscosity
k is liquid thermal conductivity
$\rho_\ell$ is liquid density
$\gamma$ is liquid surface tension
P is absolute pressure
$D_e$ is dimension parameter
a, b, c, d are constants.

Equation 5-83 is based on a physical model of nucleate pool boiling. The main differences between pool boiling and wick boiling are thought to be dependent on the mass flow rate, G and the dimension parameter, $D_e$. The combination fluid of properties yielding the highest heat transfer coefficient in boiling would be, from Eq. 5-83,

$$h_{max} \alpha \left[\frac{k_\ell}{CP\eta}\right]^b \left(\frac{C^a}{\eta d}\right) \left[\frac{P2}{\rho_\ell \gamma}\right]^c \qquad (5\text{-}84)$$

Note the inverse relationship between boiling coefficient and the liquid properties of density and surface tension. For maximum heat transfer based on fluid flow considerations, it is desirable for the liquid density and surface tension to be very large. Thus, a tradeoff is indicated between heat pipe fluid flow and boiling heat transfer. Since wick boiling $\Delta$Ts with cryogenic fluids can only be estimated and will probably result in lower $\Delta$Ts (at the same q) than for pure conduction through a liquid layer, a conservative, pure-conduction model will be employed for calculation of heat transfer $\Delta$Ts. The model is presented in Section 5.F.2.b.(2).

It is clear from Eqs. 5-83 and 5-84 that high liquid-thermal conductivity will result in low heat transfer $\Delta$Ts whether the transfer mechanism is conduction or boiling. In the temperature range from 77°K to 90°K, therefore, oxygen would be the preferred working fluid based on its highest thermal conductivity.

c. Minimum Pressure Criteria

Both $O_2$ and $N_2$ will exist as a high-pressure gas at ambient temperatures. For the same heat pipe ID and wick volume, the fluid which yields a lower pressure at ambient temperatures will require a thinner container wall and thus yield a lighter weight heat pipe. The perfect gas laws, with the appropriate compressability factor can be used to predict internal pressures, P, at ambient temperatures:

$$P = \frac{C\eta R T}{V_t}$$

where C = 1.08 for $N_2$ at 300°K and 3500 psia
C = 1.06 for $O_2$ at 300°K and 3500 psia
$V_t$ is total volume
R is universal gas constant
T is temperature, °K

$$\eta = \frac{m_\ell + m_v}{MW} \qquad \begin{matrix} m_\ell = \rho_\ell V_p \\ m_v = \rho_v V_v \end{matrix}$$

where

$V_p$ is the volume of the pores
$V_v$ is the volume of the vapor space
MW is molecular weight

$V_t = 1.47\ cm^3$ and $V_p = 0.47\ cm^3$ are assumed for the calculation.

The ratio $m_\ell/m_v$ is 81:1 for $N_2$ and 513:1 for $O_2$ at 77°K. Therefore, the contribution of $m_v$ to the total mass will be neglected and

$$P = \frac{C\, m_\ell}{MW} \frac{RT}{V_t}$$

The internal pressures $P_{N_2}$ and $P_{O_2}$ for $O_2$ and $N_2$, respectively occupying identical heat pipes at the same temperature may be compared thus:

$$\frac{P_{N_2}}{P_{O_2}} = \frac{\left[\frac{C\,\rho_\ell\, V_p}{MW}\right]_{N_2}}{\left[\frac{C\,\rho_\ell\, V_p}{MW}\right]_{O_2}}$$

$$\frac{P_{N_2}}{P_{O_2}} = \frac{(1.06)\ \frac{(0.31)}{28}}{1.06\left(\frac{1.2}{32}\right)} = 0.76$$

The internal pressure of $O_2$, therefore, will be about 13% higher than $N_2$ and the container wall thickness and weight will be higher by the same percentage.

Based on the criteria of minimum internal pressure at ambient temperatures, the preceding analysis has shown nitrogen to be the preferred fluid.

d. Chemical Compatibility Criteria

There is no experimental data available on life of $O_2$ or $N_2$ heat pipes. However, some of the properties of cryogenic heat pipes indicate that chemical compatibility should be much less of a problem with cryogenic heat pipes when compared to ambient and liquid metal pipes.

The first favorable property of cryogenic heat pipes is temperature. At cryogenic temperatures, the chemical reactions which might release a noncondensible gas such as hydrogen or cause the wick to partially dissolve in the liquid, proceed at a much slower rate. Another property favoring nitrogen is simply the fact that it is chemically inert and would not react with any materials. If in the fabrication and charging process, a small amount of gas is accidentally left in the cryogenic heat pipe, the $O_2$ and $N_2$ component will condense out of this gas leaving a noncondensible gas volume of less than 1% of the original gas volume. Nitrogen appears to be the preferred working fluid on a chemical compatibility basis, due to its inertness. There is need, however, for life data on nitrogen and oxygen heat pipes.

## 2. Design

The preferred design of a cryogenic heat pipe for an ICICLE system is the one which best satisfies the following criteria:

(1) Maximum throughput and length

(2) Minimum size and weight

(3) Minimum heat pipe temperature drop.

Criteria (1) and (2) can best be satisfied by utilizing the optimization technique which is based on fluid properties. In this section, optimum heat pipe designs will be generated for oxygen and nitrogen at 77°K and 90°K operating in the presence of several "gravitational field products" ($\rho Z \sin\phi$).*

Two common wick structures are examined: the homogeneous wick and the channel wick. The homogeneous wick is one in which the characteristic pore size for capillary pumping is equivalent to the pore size for liquid flow. The channel wick is one in which longitudinal channels serve as a smooth liquid return passage and the capillary pumping radius of curvature is formed in a single layer of screen mesh covering the channels. The capillary pumping capacity of the channel wick with channel width equal to screen opening is halved if the screen mesh covering is removed. The total heat pipe temperature drops which result from using these optimum wick designs with a representative value of heat load are examined and a recommended design is presented.

*When this quantity is multiplied by the liquid density, the resulting quality is the heat-pipe liquid pressure drop due to gravity.

a. Optimum Design Approach

The heat pipe optimization procedure which was presented in Section 5.A. will result in the largest throughput-length product $Q(Z+Z_a)$ of any heat pipe design for the same $r_w$. Equations for $Q(Z+Z_a)$ and optimum pore radius, $r_{co}$ are again presented below.

$$r_{co} = \frac{-AC + \left[(AC)^2 + 4\gamma^2 AB\right]^{1/2}}{2\gamma B}$$

where

$$A = \frac{b\eta_\ell}{2\pi\,(r_w^2 - r_v^2)\,\rho_\ell\, h\, e} \qquad \text{(homogeneous wicks)}$$

$$A = \frac{(2+x)\,\beta_\ell\,\eta_\ell}{2\pi\,\rho_\ell\, h\, r_v\,(r_w - r_v)} \qquad \text{(channel wicks)}$$

$$B = \frac{4\,\eta_v}{\pi\,\rho_v\, r_v^4\, h} \qquad \text{(homogeneous or channel wicks)}$$

$$C = \rho_\ell\, g\, Z \sin\phi$$

For the analysis, the following wick constants were assumed. (It should be cautioned, that good heat pipe design requires that these wick constants be experimentally determined.) For the homogeneous wick, $b/e = 17.5$. For the screen-covered channel wick shown in Fig. 5-85, the following constants were used.

$$x = y/r = 1$$

$$\beta_\ell = 0.75$$

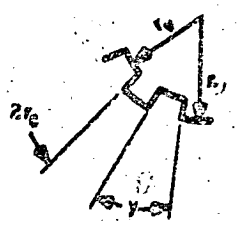



Fig. 5-85. Screen-covered channel wick geometry.

The maximum throughput-length product at the optimum pore size is:

$$Q(Z+Z_a)\big|_{r_{co}} = \frac{2\gamma r_{co} - Cr_{co}^2}{A + B r_{co}^2}$$

A computer iteration on $r_v$ is used to obtain the maximum $Q(Z+Z_a)$ product at the optimum $r_c$ and optimum wick thickness ratio, $r_v/r_w$. Plots of $Q(Z+Z_a)$ versus $r_w$ are presented in Figs. 5-56 through 5-83 for $O_2$ and $N_2$ in several acceleration fields and for both wick structures. In addition to facilitating fluid selection, these graphs allow the designer to rapidly select the design which will yield the maximum $Q(Z+Z_a)$ product for any given $r_w$. The utility and simplicity of these curves is evident from the wealth of information which they display. The gravity field optimization technique and the resulting performance curves represent a unique and important approach to cryogenic heat pipe design. For a typical ICICLE system, the values of Q and $Z+Z_a$ will be known and the $g Z \sin\phi$ product should be selected in order to satisfy the larger of these two constraints: (1) the gravitational field caused by a spin stabilized vehicle, or (2) a one-g field acting with the heat pipe horizontal, for testing on the ground.

Typical values of $g Z \sin\phi$ for case (2) range from 500 $cm^2/s^2$ for $r_w$ = 0.25 cm to $g Z \sin\phi$ = 1300 $cm^2/s^2$ for $r_w$ = 0.65 cm. It is recognized that an ICICLE system will probably operate in a true gravity-free environment but the inclusion of a small gravitational liquid pressure drop in the design will permit the cryogenic heat pipe to undergo ground testing at the full design heat load. A heat pipe with a design optimized to allow a horizontal ground test will have nearly twice the throughput or length capacity in a gravity free environment since the gravitational liquid pressure drop for the optimized designs is nearly 50% of the total capillary pumping pressure. A heat-pipe design which is based on a zero-g environment with a throughput reduction factor of two or three to one is adequate for high and ambient-temperature heat pipes, but with the cryogenic heat pipe, such an approach would result in a heat pipe design which could not be ground tested, even in a horizontal orientation at the design heat load.

The effect of wick structure on the maximum throughput-length product can be seen by comparing in Figs. 5-67 and 5-70. The wick structures being compared are the homogeneous type, which include screens, foils and powders and the channel type, which for this analysis is assumed to be covered with a screen whose openings are the same size as the channel width. Shown in Figs. 5-67 and 5-70 is an optimized $N_2$ heat pipe operating at 77°K under several $g Z \sin\phi$ products. The improvement in $Q(Z+Z_a)_{max}$ which the channel wick shows over the homogeneous wick is 2.34:1 for $g Z \sin\phi$ = 2500 $cm^2/s^2$, 2.22:1 for $g Z \sin\phi$ = 5000 $cm^2/s^2$ and 2.10:1 for $g Z \sin\phi$ = 8000 $cm^2/s^2$. For $O_2$ at 77°K under the same $g Z \sin\phi$ conditions, these ratios become 2.44:1, 2.27:1, and 2.28:1, respectively.

The effect of gravity or acceleration on the throughput of optimized cryogenic heat pipes is illustrated in Figs. 5-66 through 5-73. Figure 5-67 shows the relationships of $Q(Z+Z_a)_{max}$ to $g Z \sin\phi$ for $N_2$ at 77°K. The degradation in $Q(Z+Z_a)_{max}$ from zero-g to a $g Z \sin\phi$ product of 500 $cm^2$ is seen to be 90% for $r_w = 0.3$. For $O_2$ at 77°K under the same conditions, the decrease in $Q(Z+Z_a)_{max}$ is 81% (Fig. 5-69). An increase in $g Z \sin\phi$ from zero to 6080 $cm^2/s^2$ results in a $Q(Z+Z_a)_{max}$ decrease of 99% for $N_2$ at 77°K and 97% for $O_2$ at 77°K. It is clear from this comparison that a cryogenic heat pipe that is designed for the condition of zero gravity is not likely to function at all under the condition of a horizontal ground test where a $g Z \sin\phi$ product of about 600 $cm^2/s^2$ would exist. (For $g Z \sin\phi = 600$ $cm^2/s^2$, g is taken to be 980 $cm/s^2$, Z is replaced with 2 $r_w$ which is 0.6 cm and $\sin\phi$ is set equal to 1 for the horizontal orientation.)

The design of any heat pipe should include tolerances for variation in the properties of the wick or working fluid and also system tolerances which might cause the pipe to operate at off-design temperatures, thus changing the $Q(Z+Z_a)$ capability of the pipe. It was stated earlier that an important part of the heat-pipe design and fabrication procedure is an experimental determination of wick parameters such as the capillary pumping radius, $r_c$, and the wick friction $b/\epsilon r_c^2$ (for homogeneous wicks). Even when these parameters are experimentally determined, a slight variation in the properties of the working fluid or a non-zero liquid-solid contact angle can cause a significant decrease in the $Q(Z+Z_a)_{max}$ capability. Some excess capacity, therefore, must be designed into the heat pipe to account for the various tolerances. The excess design capacity for a given wick-fluid container combination is a direct function of the performance history of previous heat pipes of the same materials. Because of the embryonic stage of cryogenic heat pipe experimental programs, an overdesign or excess capacity of 2:1 is recommended. This means that the heat pipe should be designed for an operating point of two times the $g Z \sin\phi$ product required for a horizontal ground test. For optimized heat pipe designs, the liquid pressure drop due to friction is always 50% of the pumping capacity, $\Delta P_c$. The vapor pressure drops for optimum designs operating in a g field is typically less than 5% of $\Delta P_c$, which means that the total pressure drop for optimum heat pipes is almost entirely due to liquid pressure drops of which 50% is frictional ($\Delta P_{l_f}$) and nearly 50% is gravitational ($\Delta P_{l_g}$). This means that the C and Z parameters decrease linearly with increasing $\Delta P_{l_g}$. A doubling of the $g Z \sin\phi$ product, therefore, results in the $Q(Z+Z_a)$ being halved.

The optimization procedure described in this section will result in a heat-pipe design which achieves maximum throughput and length at a minimum size and weight. Since fluid-flow considerations form the basis for the optimization technique, the equally important heat transfer mechanisms must be thoroughly examined in light of minimizing the heat-pipe temperature drop before a design can truly be called optimum. The following paragraphs will detail the heat transfer in cryogenic heat pipe.

b. Cryogenic Heat Transfer Considerations

(1) Boiling Heat Transfer

Boiling heat transfer with cryogenic fluids is a highly empirical science, due to the wide variations in surface materials, surface roughness, and surface coatings, which have a strong influence on the superheat required for nucleate boiling. No experimenters to date have investigated the influence of a capillary structure on boiling in cryogenic fluids. There has been some investigation, however, into nucleate boiling of $O_2$ and $N_2$ from flat plates and wires. This information, together with the conclusions of Allingham and McIntire [14] on wick boiling with water, forms the basis for the following treatment of cryogenic wick boiling heat transfer. Reference 20 provides experimental heat transfer data in the form of heat flux, q versus superheat $\Delta T$ curves for $N_2$ and $O_2$ boiling from flat copper plates. Brentari and Smith [20] cite empirical formulas for $O_2$ and $N_2$ which correlate very closely with the experimental data. Figures 5-86 through 5-89, taken from Brentari and Smith compare data from several investigators for nucleate and film boiling of $O_2$ and $N_2$ at 1 atmosphere. Figures 5-87 and 5-89 show the boiling correlation of Kutateladze for $O_2$ and $N_2$ at various pressures.

The experimental data of Fig. 5-86 shows a wide variation in the superheat required for nucleate boiling of $O_2$ at 1 atm. For example, at a heat flux of 1 W/cm$^2$, the data of Malkov shows a 1.5°K superheat compared to a 7°K superheat measured by Mikhail. The 1 atm correlation of Kutateladze predicts an intermediate value of 4°K for q = 1 W/cm$^2$. The range of Kutateladze's correlations from pressures of 0.5 to 30 atm is illustrated in Fig. 5-27.

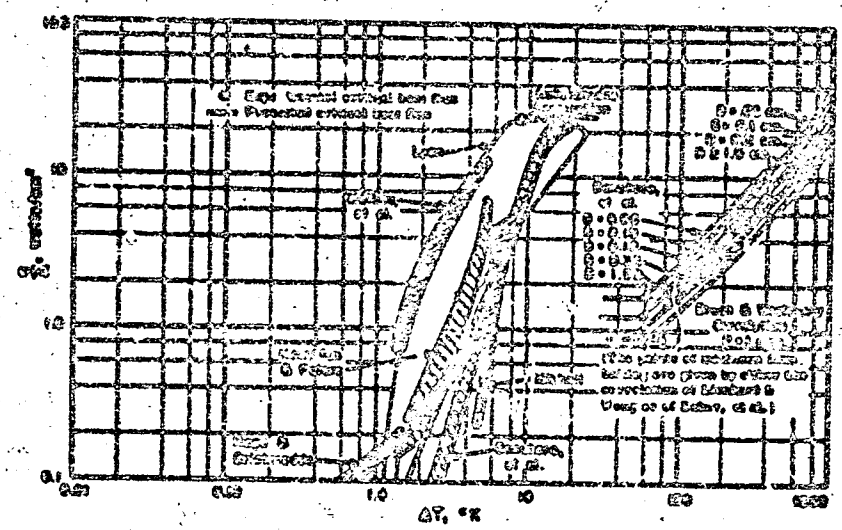



Fig. 5-86. Experimental nucleate and film pool boiling of oxygen at 1 atm compared with the predictive correlation of Kutateladze and Breen and Westwater. From Brentari and Smith[20].

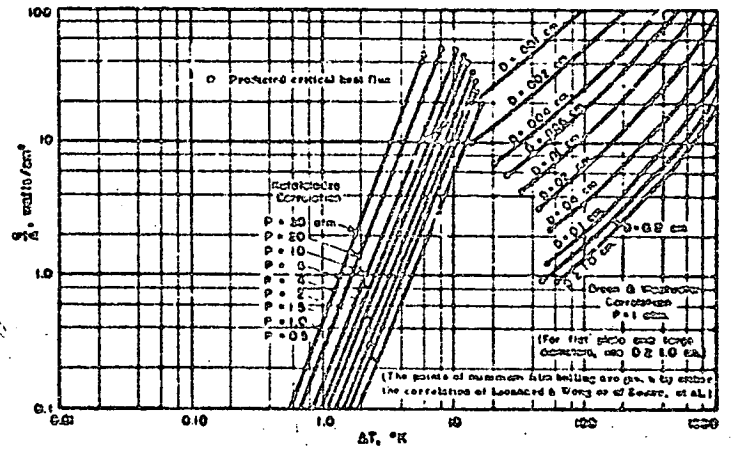


Fig. 5-87. Predictive nucleate and film pool boiling correlations for oxygen. From Brentari and Smith[20].

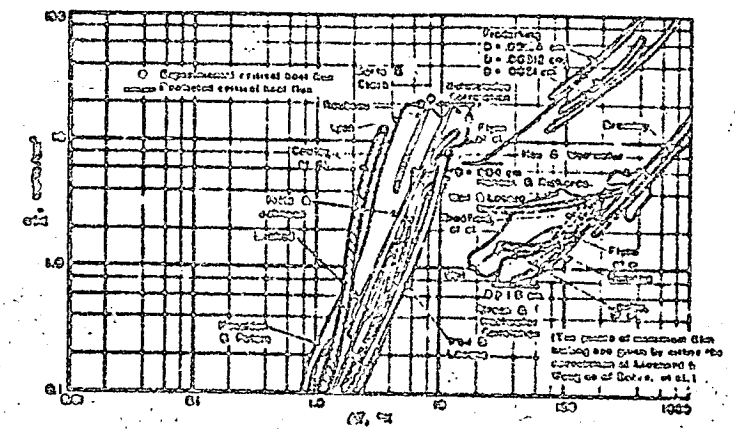


Fig. 5-88. Experimental nucleate and film pool boiling of nitrogen at 1 atm compared with the predictive correlations of Kutateladze, and Breen and Westwater. From Brentari and Smith[20].

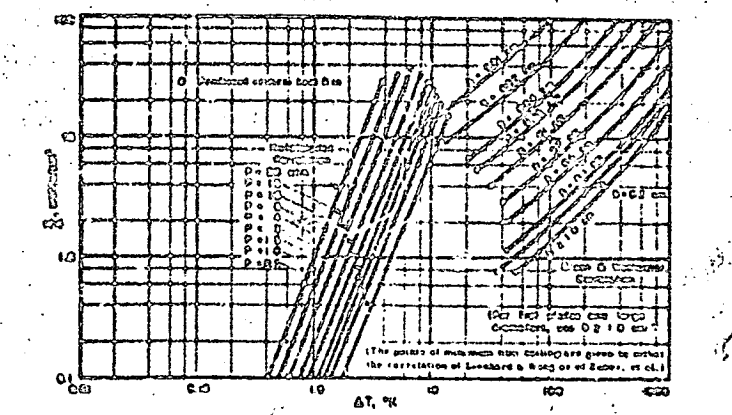


Fig. 5-89. Predictive nucleate and film pool boiling correlations for nitrogen. From Brentari and Smith[20].

At a vapor pressure of 0.5 atm which corresponds to a temperature of 84 °K for $O_2$, the correlation in Fig. 5-87 predicts a 5°K superheat at q = 1 W/cm$^2$. This heat flux might represent a heat load of 1.5 watts entering a heat pipe evaporator section with Rw = 0.254 and length = 1 cm. Operating $O_2$ at 77°K results in a vapor pressure of 0.184 atm which would indicate from Fig. 5-87 that a 6°K superheat would be required to initiate boiling. If we assume that a capillary structure influences $O_2$ wick boiling in generally the same way as it influences water boiling from a wick, then the boiling would occur at a lower ΔTs and the curves of Fig. 5-87 would be shifted to the left. As previously mentioned, the sterile cleaning procedures used to prepare heat pipes and wicks for assembly (e.g. high temperature vacuum bake-out) would tend to prevent rather than promote the boiling process because of the elimination of absorbed gas in the wick and dissolved air in the fluid, both which can serve as bubble nucleaters. The effect of heat pipe cleaning procedures would be to move the curves of Fig. 5-87 to the right. Considering the opposite effects of a capillary structure and cleaning procedures on boiling heat transfer and the lack of experimental data on cryogenic wick boiling, the prediction of heat pipe evaporator ΔTs in this section will preclude any effects of boiling in the wick. It is recognized, however, that the effect of wick boiling in the evaporator will be to reduce the heat transfer ΔT when compared to a pure conduction ΔT and that superheats in the range 2° - 10°K can initiate boiling in the wick.

(2) Conduction Heat Transfer Model, Homogeneous Wicks

For calculating temperature drops in cryogenic heat pipe evaporators, with a homogeneous wick, all the heat, Q, will be assumed to be conducted through the wick-liquid matrix with surface evaporation occurring at the liquid-vapor interface. The effective thermal conductivity of the wick-liquid matrix will be assumed equal to the liquid thermal conductivity. Condenser heat transfer is assumed to consist of film condensation at the liquid-vapor interface with ordinary conduction through the saturated wick whose $k_e$ equals $k_\ell$. This model is conservative because of: (1) the possibility of nucleate boiling which could lower the evaporator ΔT and (2) the fact that the effective thermal conductivity of a metallic wick-cryogenic liquid matrix with porosities of 0.8 to 0.9 is about 15% to 20% higher than the liquid thermal conductivity based on series thermal conduction. The heat transfer-temperature drops due to evaporation, condensation and vapor flow are neglected in this model because they are very small compared to the evaporator and condenser temperature drops. The vapor flow ΔT could be significant if the heat pipe is approaching sonic limitation where the vapor pressure drops (and temperature drop) increase considerably. For and ICICLE application, however, both $O_2$ and $N_2$ heat pipes would be operating well under their sonic limits.

The conduction model will be applied to the heat pipe homogeneous wick designs where the pore radius, $r_c$, and wick thickness ratio, $r_v/r_w$, are determined by the fluid flow optimization technique. By assuming a typical IR sensor load

of 500 milliwatts and evaporator and condenser lengths, $Z_e$ and $Z_c$ of 7.5 cm each, plots of total heat-pipe temperature drop versus heat pipe inner-wall radius can be generated for $O_2$ and $N_2$ heat pipes at 77°K and 90°K operating in the presence of various gravity-field products, $gZ\sin\phi$. Since the heat load or throughput is a fixed quantity in this model, a graph of total heat pipe length ($Z_{max}$) versus $r_w$ is made using the particular $Q(Z \div Z)_{max}$ versus $r_w$ curve and knowing that Q = 0.5 W and $(Z-Z_a)$ = 15 cm. This heat pipe length versus $r_w$ plot appears in Figs. 5-90 through 5-98. These plots facilitate comparison of optimized, homogeneous wick heat pipe and solid rod $\Delta T$s. The solid rod material selected for this comparison is high-purity (99.99%) aluminum which possesses the highest ratio of thermal conductivity to density of any metallic conductor. The heat pipe $\Delta T$s and the aluminum rod $\Delta T$s can thus be compared on an equal diameter and length basis. This comparison is illustrated in Fig. 5-85, which is the $\Delta T$ versus $r_w$ plot for an optimized nitrogen heat pipe at 77°K ($gZ\sin\phi = 500_{cm^2/s^2}$). At any point on the aluminum rod or heat pipe $\Delta T$ curve, the length dimension can be found by referring to the length versus $r_w$ curve at the top of the graph. Figure 5-85 shows a $\Delta T$ of 11°C for the heat pipe, with $r_w$ = 0.3 cm, and Z = 400 cm. For a solid aluminum rod of the same length and diameter (2 $r_w$), the curve shows a $\Delta T$ of 180°C. The heat pipe $\Delta T$ curves show a slight increase in $\Delta T$ with increasing $r_w$, due to the increasing wick thickness with increasing $r_w$. The solid rod $\Delta T$s are fairly constant with $r_w$, since the conduction $\Delta T$ is proportional to $Z/r_w^2$. Since the rod $\Delta T$ curves are based on one-dimensional conduction, the curves may be scaled in direct proportion to the throughput.

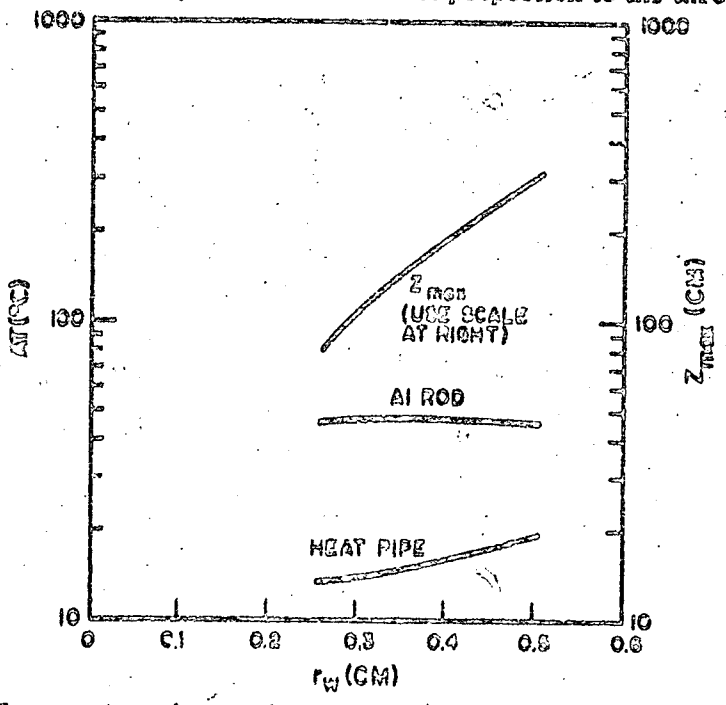



Fig. 5-90. Temperature drop and heat pipe length as functions of inner-wall radius for oxygen heat pipe at 77°K with Q = 0.5 W, $Z-Z_a$ = 15 cm, and $gZ\sin\phi = 6080\ cm^2/s^2$.

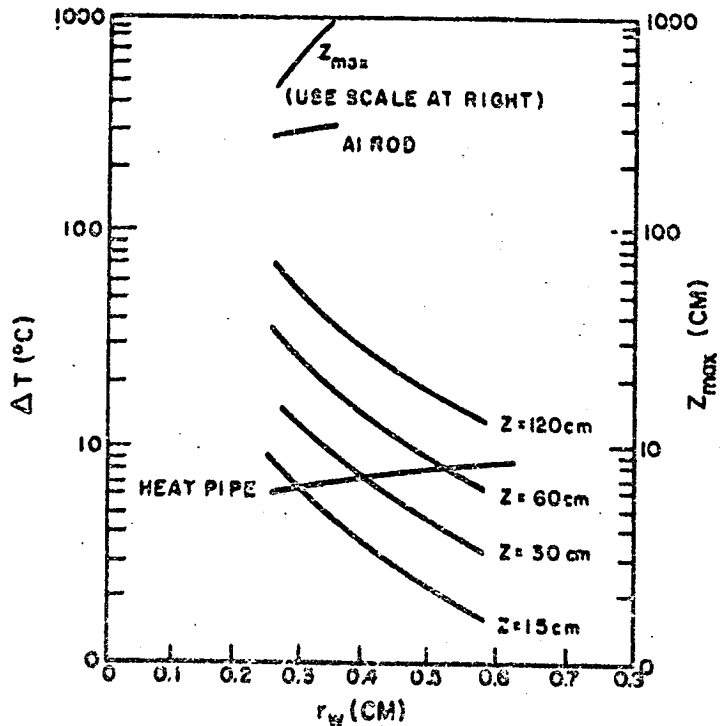



Fig. 5-91. Temperature drop and maximum heat pipe length as functions of inner-wall radius for oxygen heat pipe at 77°K with Q = 0.5 W, $Z-Z_a$ = 15 cm, and $gZ\sin\phi = 500\ cm^2/s^2$.

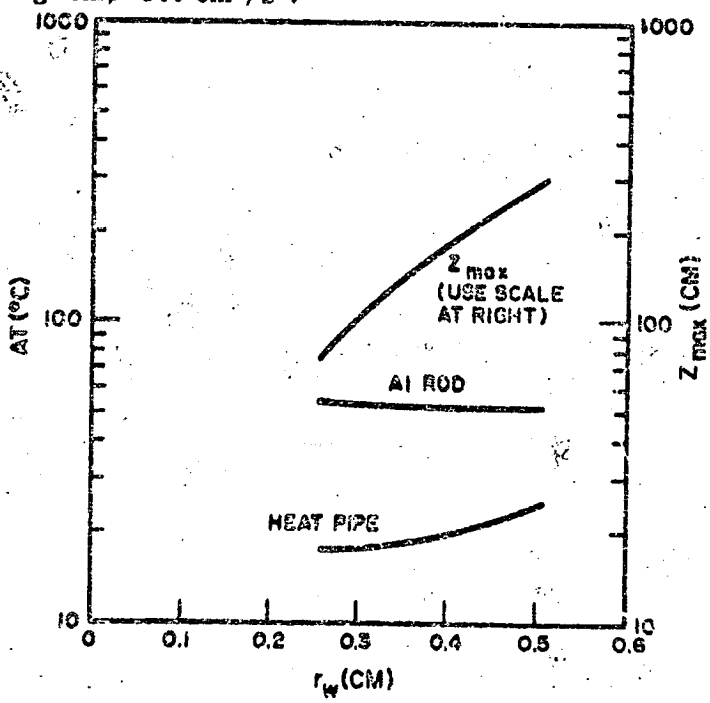



Fig. 5-92. Temperature drop and maximum heat pipe length as functions of inner-wall radius for oxygen heat pipe at 90°K with Q = 0.5 W, $Z-Z_a$ = 15 cm, and $gZ\sin\phi = 6080\ cm^2/s^2$.

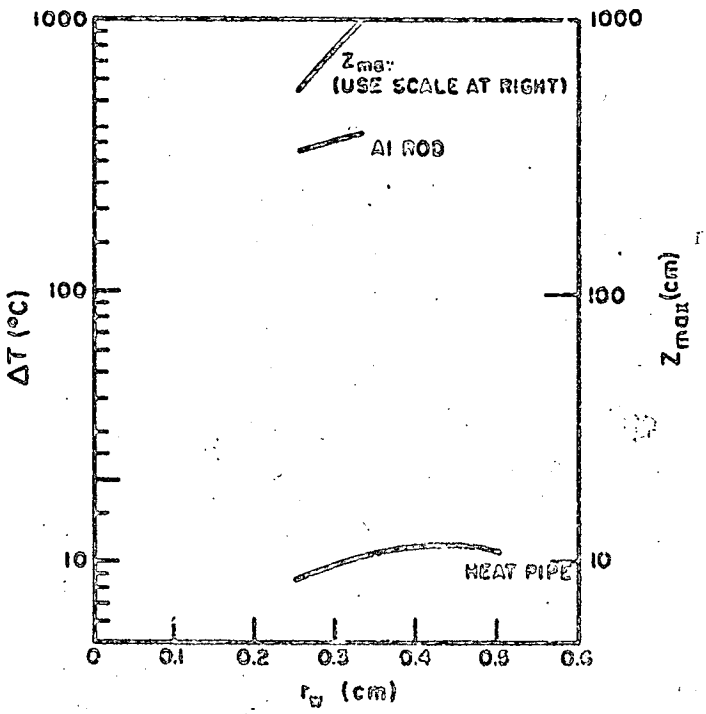



Fig. 5-93. Temperature drop and heat pipe length as functions of inner-wall radius for oxygen heat pipe at 90°K with Q = 0.5 W, $Z-Z_0$ = 15 cm, and $gZ\sin\phi = 500\ cm^2/s^2$.

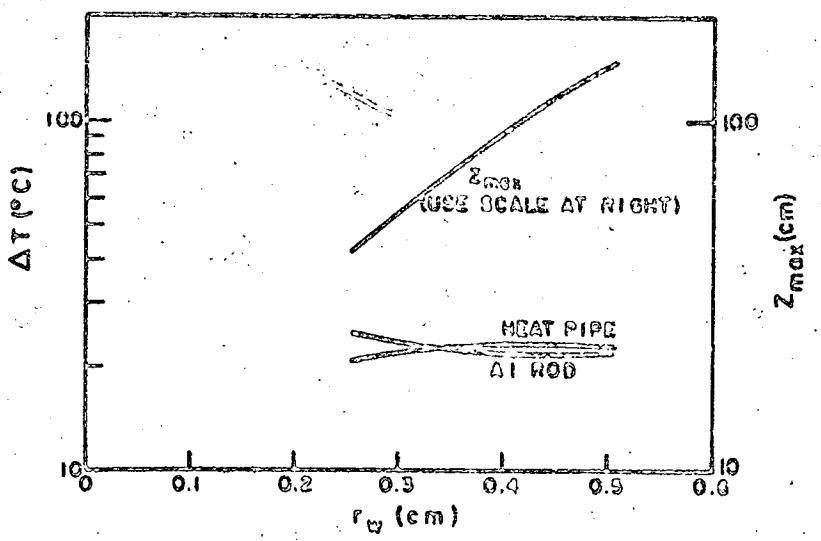



Fig. 5-94. Temperature drop and heat pipe length as functions of inner-wall radius for nitrogen heat pipe at 77°K with Q = 0.5 W, $Z-Z_0$ = 15 cm, and $gZ\sin\phi = 680\ cm^2/s^2$.

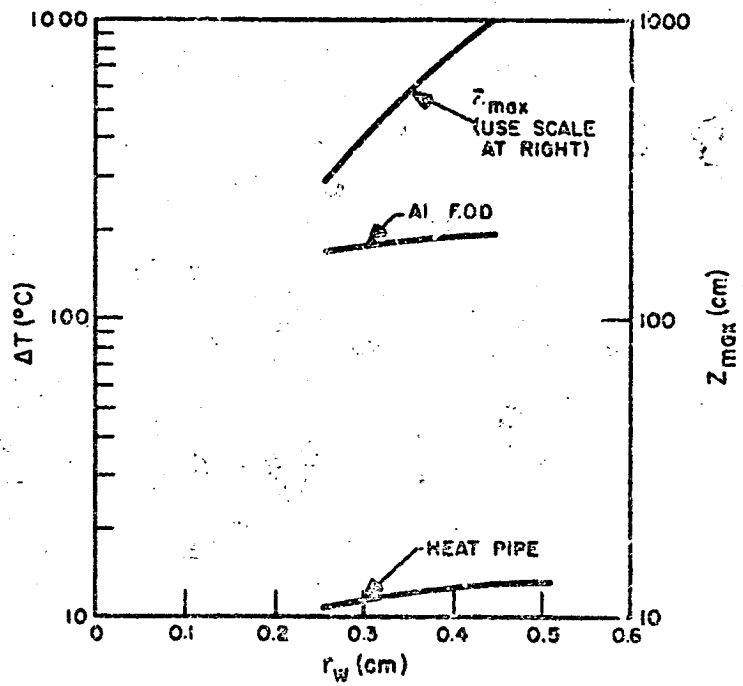



Fig. 5-95. Temperature drop and heat-pipe length as functions of inner-wall radius for nitrogen heat pipe at 77°K with Q = 0.5 W, $Z-Z_a$ = 15 cm, and $gZ\sin\phi = 500\ cm^2/s^2$.

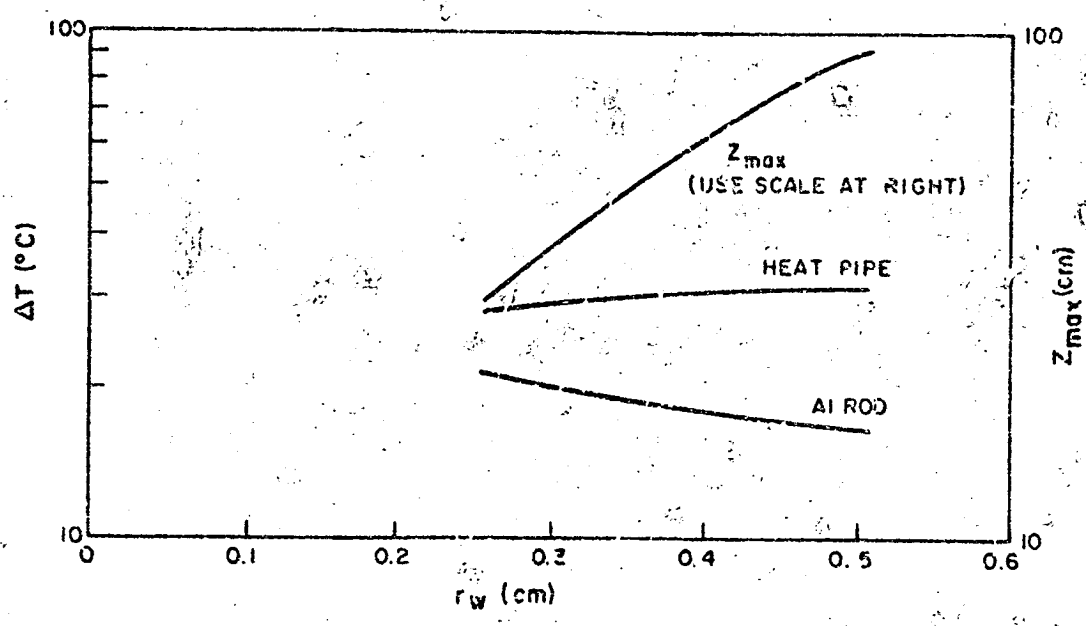



Fig. 5-96. Temperature drop and heat-pipe length as functions of inner-wall radius for nitrogen heat pipe at 90°K with Q = 0.5 W, $Z-Z_a$ = 15 cm, and $gZ\sin\phi = 6080\ cm^2/s^2$.

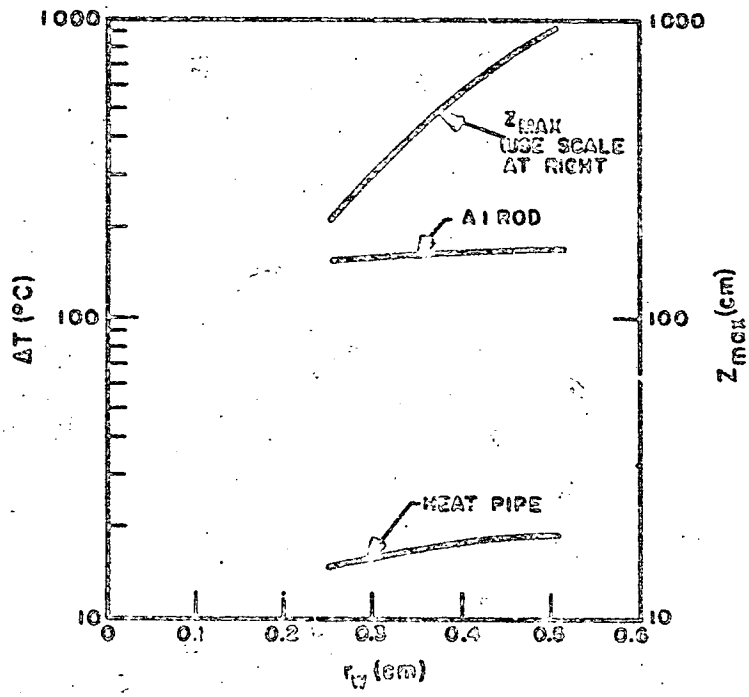



Fig. 5-97. Temperature drop and heat-pipe length as functions of inner-wall radius for nitrogen heat pipe at 80°K with Q = 0.5 W, $Z-Z_a$ = 15 cm, and $gZ\sin\phi = 500\ cm^2/s^2$.

The smallest total ΔT of all the designs examined in Figs. 5-90 through 5-96 is 6.2°K for oxygen, at 77°K with $gZ\sin\phi = 500\ cm^2/sec^2$ and $r_w$ = .25 cm and Z = 460 cm (Fig. 5-91). The design resulting in the largest ΔT (34°K) is shown in Fig. 5-94 for nitrogen at 80°K with $r_v$ = 0.5 cm and $gZ\sin\phi = 6080\ cm^2/s^2$. (This ΔT would result in $N_2$ being above its critical temperature.) A constant liquid thermal conductivity is assumed for all the temperature drop calculations. Actually, the degradation in $k_\ell$ from 77°K to 80°K is 12% for $N_2$ and 8.4% for $O_2$.

The optimized homogeneous wick designs examined in Figs. 5-90 through 5-96 result in very long lengths for a heat load of 0.5 W and $gZ\sin\phi$ products of 500 to 1000 $cm^2/s^2$. These high values of Z result in solid rod ΔTs in excess of 100°C. Another basis for comparing solid rod ΔTs to homogeneous wick ΔTs is an equivalent ΔT basis. For solid rod lengths of 2 ft (60 cm) and less, the rod ΔTs compare favorably with the heat pipes ΔTs even though the heat pipes have the capacity to transfer the 0.5 W a much greater distance than 60 cm. Temperature drop curves for two selected heat pipe designs compared with solid rods of 60 cm and less are shown in Figs. 5-91 and 5-96.

These comparisons for fixed-rod lengths indicate that at lengths up to 60 cm and radii of 0.5 cm and larger, the solid aluminum rod exhibits a lower overall temperature drop than any of the candidate optimum homogeneous wick heat-pipe designs. On a weight basis, the solid aluminum rods are generally twice as

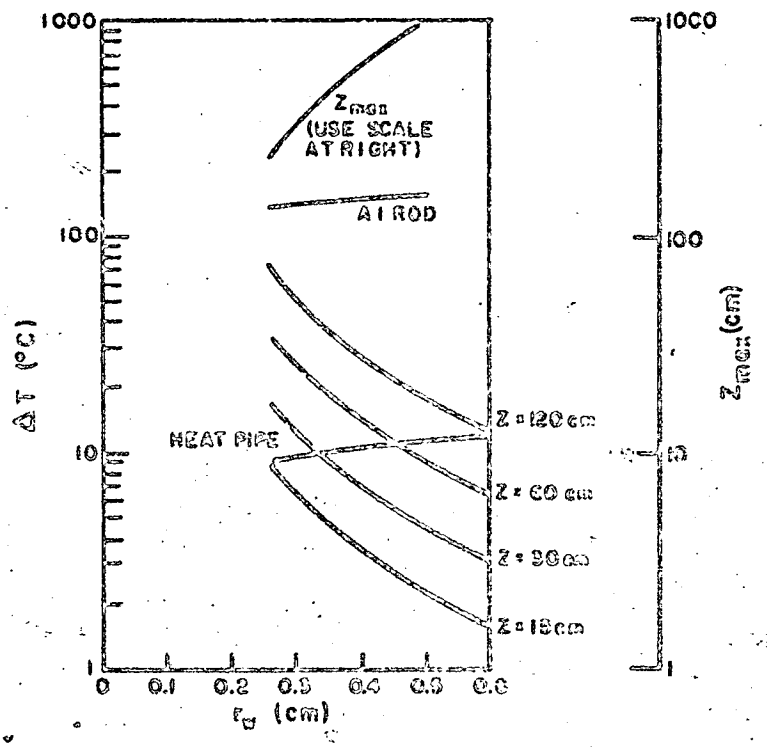



Fig. 5-98. Temperature drop and heat-pipe length as functions of inner-wall radius for oxygen heat pipe at 77°K with Q = 0.5 W, $Z-Z_a$ = 15 cm, and $gZ\alpha\ell\rho = 1520\ cm^2/s^2$.

heavy per foot of length as their heat pipe counterparts. For example, in Fig. 5-91 ($O_2$, T = 77°K, $\beta = 500\ cm^2/s^2$), the heat pipe ΔT curve intersects the solid rod curves at three points: (1) at ΔT = 6.5°C, $r_w$ = 0.29 cm and Z = 15 cm; (2) at ΔT = 7.3°C, $r_w$ = 0.38 cm and Z = 30 cm; (3) at ΔT = 8.2°C, $r_w$ = 5.3 cm and Z = 60 cm. The corresponding weights per foot for these three equi-ΔT points assuming aluminum material for rod, wall, and wick are: (1) ΔT = 6.5°C, heat pipe = 0.024 lbs/ft, rod = 0.048 lbs/ft; (2) ΔT = 7.3°C, pipe = 0.045 lbs/ft,

rod = 0.087 lbs/ft; (3) $\Delta T$ = 8.2°C, pipe = 0.087 lbs/ft, rod = 0.164 lbs/ft. On an equivalent $\Delta T$ basis, the solid aluminum rods, although twice as heavy as the homogeneous wick-heat pipe counterparts, are still very light when compared to the total ICICLE system weight and also have a decided advantage because of their ultra-reliability.

Reductions can be made in the homogeneous wick heat pipe $\Delta T$s by enlarging the pipe diameter while maintaining a constant wick cross-sectional area. Since the total temperature drop for this model is taken to be the sum of evaporator and condenser $\Delta T$s and ordinary radial thermal conduction is assumed in the evaporator and condenser, the heat flux entering the evaporator can be halved by doubling the inside diameter. If a constant wick area is maintained while the ID is increased, the wick thickness will decrease, resulting in a further reduction of $\Delta T$. For example, the $\Delta T$ for an $N_2$ pipe at 77°K with $gZ\sin\phi = 500$ cm$^2$/s$^2$ (Fig. 5-95) is 12°C for an $r_w$ of 0.382 cm. The wick thickness for this optimized design is 0.212 cm, the resulting cross-sectional wick area is 0.368 cm$^2$ and the evaporator surface area is 2.4 cm$^2$. If $r_w$ is doubled to 0.764 cm, the total $\Delta T$ is reduced by the ratio of ln (0.382/0.170)/ ln (0.764/0.680) = .807/.133 or 7.8 to 1(assuming radial conduction), thereby resulting in a $\Delta T$ decrease of from 12°C to 1.54°C for Q = 0.5 W. This reduction in total heat pipe $\Delta T$ is obtained, of course, at the expense of heat-pipe size and weight.

(3) Channel Wick Heat Transfer Model

The heat transfer in channel wick heat pipe is assumed to be a parallel mode of conduction through the metallic fin and cryogenic liquid to the liquid vapor interface where surface evaporation occurs. For simplicity, the fin thickness will be assumed constant; it is actually slightly thicker at the base in a circular heat pipe. Also, the heat transfer contribution of the screen mesh covering on channels will be neglected by assuming uncovered fins with insulated tips. This makes the conduction model slightly conservative. The channel wick conduction model is shown, in detail, in Fig. 5-99. The evaporator temperature drop is comprised of a $\Delta T$ from the skin of the pipe, down the fin to a point near the fin tip. Although the channel wick geometry permits a parallel mode of heat conduction, the large differences in thermal conductivity between fin and liquid (over 2000:1) cause essentially all the heat to be conducted down the fin with the liquid acting as an insulator. All of the heat is then assumed to be transferred into the liquid and conducted across the liquid to the liquid vapor interface. The heat conduction in the liquid to the meniscus is taken to be one dimensional with a characteristic heat flow area of $r_c \times \ell_\Theta$ and a heat flow length of $r_c/2$.

In the condenser, the heat flux is taken to condence evenly on fin tip and liquid as shown in Fig. 5-99. Two-thirds of the condensing heat flux is assumed to be conducted through the liquid using the same characteristic length and flow area as

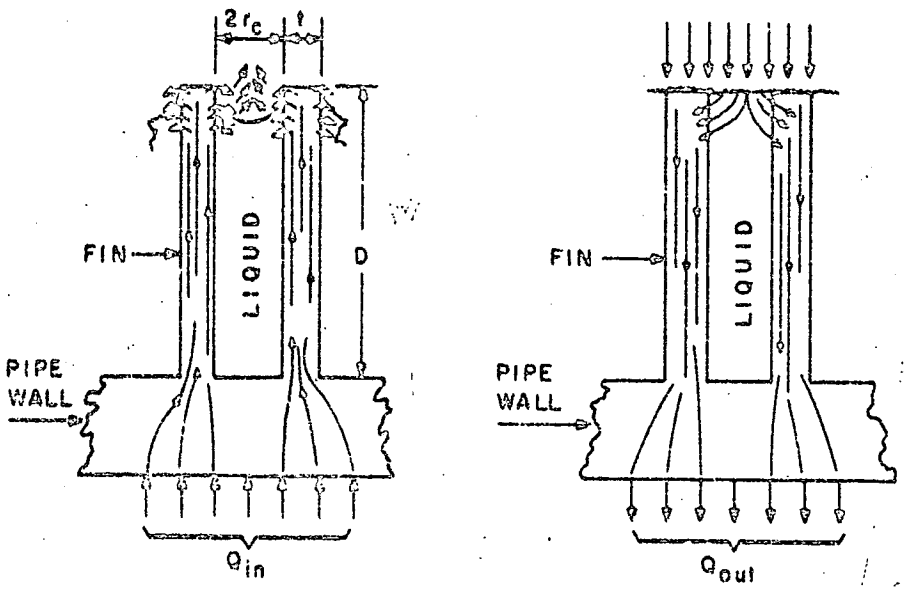



Fig. 5-99. Channel wick heat transfer model.

for the evaporator. This condenser conduction model is also conservative since the temperature of the liquid in the channel will probably exceed the fin temperature causing the vapor to preferentially condense on the fin tip. Typical $\Delta T$ calculations are presented below for the channel wick model.

For optimized $O_2$ heat pipe at T = 77°K, and $gZ\sin\phi$ = 1520 $cm^2/sec^2$ and $r_w$ = .382, $r_{co}$ = .0082 cm, channel depth = .163 cm and number of channels = 56.

As in the homogeneous wick model, Q = 0.5 W and $Z_e = Z_c$ = 7.5 cm

(1) Heat flow per fin = 0.500 W/56 fins = 9 mW/fin.

(2) $\Delta T$ from skin to fin tip (neglecting radial effects) = 0.0056°K.

(3) $\Delta T$ from fin edge to meniscus = 0.18°K.

(4) Evaporator $\Delta T$ = 0.185°K.

Doubling this $\Delta T$ results in a total heat pipe $\Delta T$ of less than 0.4 °K. A general expression for total $\Delta T$ in a heat pipe with channel wick where $y = r_c$ may be expressed:

$$\Delta T = 2\left[\frac{Q\left(\frac{r_{co}}{2}\right)}{r_{co}\, Z_e\, k_\ell}\right]$$

From the previous example $Q = 0.5$ W, $Z_e = 7.5$ cm, $k_\ell = 1.67 \times 10^{-3}$ W/cm/°K and an expression can be written for $\Delta T$ at $Q = 0.5$ W in terms of number of channels:

$$\Delta T = \frac{.5}{2N\,(7.5)\,(1.67 \times 10^{-3})} = \frac{20}{N}\ °K$$

The higher gravitational liquid pressure drops, which resulted in a thicker wick and larger $\Delta T$s in the homogeneous wick model, actually requires an increased number of fins in the optimum channel wick case, resulting in lower heat pipe $\Delta T$s for increasing gravitational fields. In this case, the deeper fin has negligible effect on the temperature drop. Total temperature drops for an optimized $O_2$ heat pipe with channel wick and homogeneous wick are contrasted with aluminum rod $\Delta T$s as shown in Fig. 5-100.

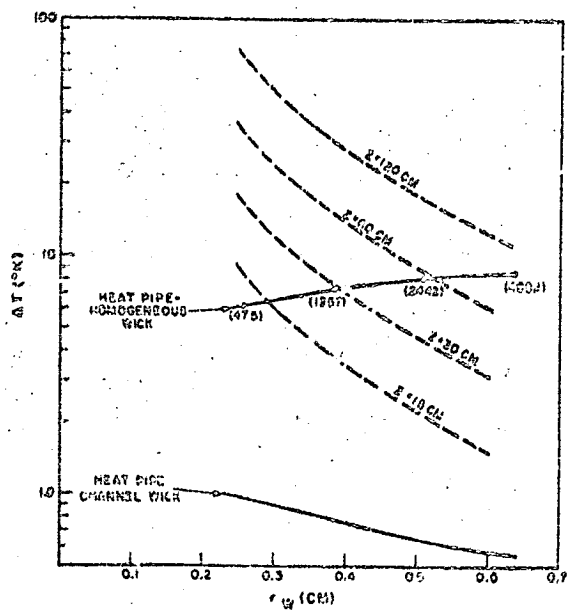



Fig. 5-100. Temperature drop as a function of inner-wall radius for oxygen heat pipes with channel and homogeneous wicks at 77°K with Q=0.5 W, $Z-Z_R$=15cm, and $gZ\sin\phi$=500 $cm^2/s^2$ contrasted with solid aluminum rods of fixed lengths.

(3) Pressure and Containment Considerations

At ambient temperatures, the cryogenic fluid will exist as a high pressure gas. The internal pressure can be predicted using the perfect gas law with the appropriate compressibility factor. The internal pressure can be approximated within about 15% by neglecting the mass of the vapor and the volume occupied by the wick material and compressibility effects. This approximate formula is

$$p = \rho_\ell \frac{V_p}{V_t} \frac{RT}{M}$$

where $\rho_\ell$ is the liquid density at the operating point.

For $N_2$ at 300°K with $\rho_\ell$ at 77°K and $V_p/V_t = 0.33$, p = 3460 psia. To contain this pressure in a 0.1 in-diameter pipe with a high-yield stress aluminum alloy such as 7072 where $\sigma_{yield}$ = 90,000 psi, a wall thickness of 0.0058-in will be required (3:1 safety factor),

$$t = \frac{pD}{2\sigma_{allow}} = \frac{(.1)(3500)}{(2)(30,000)} = .0058" \text{ Wall}$$

This wall thickness is typical for the internal pressures which result from the optimized heat pipe designs. For a constant pore volume, the wall thickness is roughly constant with increasing pipe diameter, since the internal pressure is decreasing in proportion to $V_p/V_\ell$. The wall thickness required for safe containment of the high-pressure cryogenic gas, therefore, is not excessive if high yield stress materials are used.

(4) Containment Materials

A check with two major supplies of cryogens, Air Products and Chemicals and Air Reduction revealed that industrial grade and high purity nitrogen and oxygen (liquid and gas) are routinely stored and shipped in stainless steel cylinders with copper or stainless piping. No problem with corrosion or oxide buildup on the container wall was reported. Long-term storage of ambient temperature $O_2$ or $N_2$ does not appear to be a problem, but there remains much testing to be done with cryogenic heat pipes to determine any effects of long-term, ambient-temperature storage and temperature cycling from ambient to cryogenic temperatures.

(5) Sonic Limitation

In the temperature range from 77°K to 90°K, both $O_2$ and $N_2$ heat pipes will not be sonic limited when transferring 1 W. However, $O_2$ at 77°K exhibits a vapor pressure of 0.2 atm and, for an $r_v$ of 0.3 cm, the sonic heat flow limit is

about 6 W. Because of possible sonic limitations, oxygen should not be used in a cryogenic heat pipe with an operating temperature below 77°K. By the same reasoning, a nitrogen heat pipe should not be operated below 65°K.

(6) Typical ICICLE Cryogenic Heat Pipe Designs

The following paragraphs describe four typical ICICLE heat pipe designs. These designs are optimized with respect to fluid properties and are selected because of minimum size and weight and minimum total $\Delta T$.

The following parameters are assumed:

$Q$ = 1 W

$Z$ = 120 cm

$Z_a$ = 105 cm

$Q(Z+Z_a)$ = 225 W-cm.

Design No. 1: oxygen, T = 77°K, $gZ\sin\phi = 1500\ cm^2/s^2$

Wick: Screen covered channel

Pipe inner wall radius: 0.25 cm

Pipe wall thickness: 0.034 cm

Heat pipe weight (no insulation): 0.043 lb.

Heat pipe $\Delta T$: 0.6°K (evaporator $\Delta T$ + condenser $\Delta T$)

Design No. 2: $O_2$, T = 80°, $gZ\sin\phi = 1500\ cm^2/s^2$

Wick: screen covered channel

Pipe inner wall radius: 0.25 cm

Pipe wall thickness: 0.034 cm

Heat pipe weight: 0.043 lb.

Heat pipe $\Delta T$ = 0.7°K

Design No. 3: $N_2$, T = 77°K, $gZ\sin\phi = 1500\ cm^2/s^2$

Wick: screen covered channel

Pipe inner wall radius: 0.32 cm

Pipe wall thickness: 0.034 cm

Pipe weight: 0.052 lb.

Pipe $\Delta T$: 0.6°K

Design No. 4: $N_2$, T = 90°K, $gZ\sin\phi = 1500\ cm^2/s^2$

Wick: screen covered channel

Pipe inner wall radius: 0.43 cm

Pipe wall thickness: 0.034 cm

Pipe weight = 0.4 lb.

Pipe $\Delta T$: 0.6°K

## G. REFERENCES


1. E.C. Phillips and J.D. Hinderman, "Determination of Properties of Capillary Media Useful in Heat Pipe Design." ASME paper #69-HT-16 presented at ASME Heat Transfer Conference, August 1969.

2. W.M. Kays, Convective Heat and Mass Transfer, McGraw-Hill, 1966.

3. M. Janssen, "Viscous Flow in a Rectangular Channel Heat Pipe." SPN-159, 1966.

4. T.P. Cotter, "Theory of Heat Pipes," Report #LA3246MS, Los Alamos Scientific Lab, Los Alamos, N.M.

5. H. Cheung, "Critical Review of Heat Pipe Theory and Applications," Report #UCRL-50453, Lawrence Radiation Lab., University of California, pg. 22.

6. E.K. Levy, "Theoretical Investigation of Heat Pipes Operating at Low Vapor Pressures," Aviation and Space Conference - ASME, Beverly Hills, Calif.

7. J. Kemme, "Heat Pipe Design Considerations," Report #LA-4221-MS, Los Alamos Scientific Lab, Los Alamos, N.M.

8. H. Cheung, "Critical Review of Heat Pipe Theory and Applications," Report #UCRL-50453, Lawrence Radiation Lab., University of California, pg. 26.

9. Y.Y. Hsu, "On the Size Range of Active Nucleation Cavities on a Heating Surface," Journal of Heat Transfer, August 1962.

10. A.I. Krakovlak, "Superheat Requirements with Boiling Liquid Metals, Report #ORNL-3305 Oak Ridge National Laboratory.

11. P.J. Marto and W.L. Mosteller, "Effect of Nucleate Boiling on the Operation of Low Temperature Heat Pipe" presented at the August, 1969 ASME Heat Transfer Conference, Minneapolis, Minn.

12. J. Schwartz, "Performance Map of the Water Heat Pipe and the Phenomenon of Noncondensible Gas Generation," presented at the August 1969, ASME Heat Transfer Conference, Minneapolis, Minnesota.

13. R. Gorring and S. Churchill, "Thermal Conductivity of Heterogeneous Materials," Chemical Eng. Progress, Vol. 57, No. 7, July 1961.

14. W. Allingham and J. McEntire, "Determination of Boiling Film Coefficient for a Heated Horizontal Tube in Water Saturated Wick Material," Journal of Heat Transfer, Feb. 1961.

15. W. Rohsenow and P. Griffith, "Correlation of Maximum Heat Flux Data for Boiling of Saturated Liquids," ASME Heat Transfer Symposium, Louisville, Kentucky, March 1955.

16. H. Kunz et. al., "Vapor Chamber Fin Studies," NASA Report #CR-812, June 1967.

17. J. Kemme, "Ultimate Heat Pipe Performance," presented at 1968 IEEE Thermonic Conversion Specialists Conference, Framingham, Mass.

18. Allegheny Ludlum Stainless Steel Handbook.

19. Mackoy, Dr. D.B., "Space Radiator Analysis and Design, Part I: Radiant Heat Transfer from Extended Surfaces in a Space Environment."

20. E. Brentari and R. Smith, "Nucleate and Film Pool Boiling Design Correlations for $O_2$, $N_2$, $H_2$ and He," Proceedings of 1964 Cryogenic Engineering Conference, Volume 10.

21. Mackoy, Dr. D.B., "Short Course on Thermal Management of Manned and Unmanned Spacecraft X401GH," Presented at University of California at Los Angeles, Sept. 5-15, 1961.

## Section 6

## THERMAL INSULATION REQUIREMENTS


*Summary*

*Thermal insulation is an important requirement in the ICICLE system because of the extremes in temperature involved. Heat leak from the heat source subsystem must be supplied by a larger isotope. Heat leak into the cryogenic subsystem creates a requirement for more refrigeration capacity which reflects as a requirement for more thermal power from a larger isotope.*

*While the requirement for insulation is more critical at the cryogenic temperatures, the quality of insulation required is much higher in the high temperature regions. Multiple radiation shields type of insulations are required at both temperatures to permit system performance at acceptable levels. Standard metalized Mylar blankets can be used with the cold subsystems to reduce thermal loads to less than 25 mW/ft of thermal line length. The best available multifoil and refractory powder blankets must be used around the isotope and hot heat pipe subsystems to reduce that heat leak to below 150 W for a 400 W heat source.*

*Careful consideration of such factors as edge losses, compressive loading, structural support, and multifoil quality control are required to achieve a satisfactory system configuration. Without careful application of this insulation technology, ICICLE is not feasible because of excessive power and size requirement. Close attention should be paid to this aspect of any system.*


The major nonideality in an ICICLE system is represented by heat losses or gains to the system from the environment. Heat load on the cold portions of the system is far more costly to the system than heat loss at the hot end since each additional watt of cooling required because of poor insulation requires 40 W of heat input into the system and a proportional amount of scaling in system size.

If a cryogenic heat pipe is utilized for heat transfer to the VM cold finger, the pipe should be polished and gold plated for low emissivity ($\epsilon$). A value of $\epsilon = 0.04$ is representative of a surface finish which can be used for heat load calculations. Figure 6-1 shows the heat leak occurring with a range of pipe sizes operating at 77°K in a 300°K surrounds. In the 1/4 in OD pipe required to transfer 500 mW 2 or 3 ft, the heat leak is over 100 mW per foot of length. This leak is unacceptably high. Using relatively simple insulation schemes as shown in Fig. 6-2, this leak cannot be reduced since the radiation coupling to the pipe is much weaker than the conduction

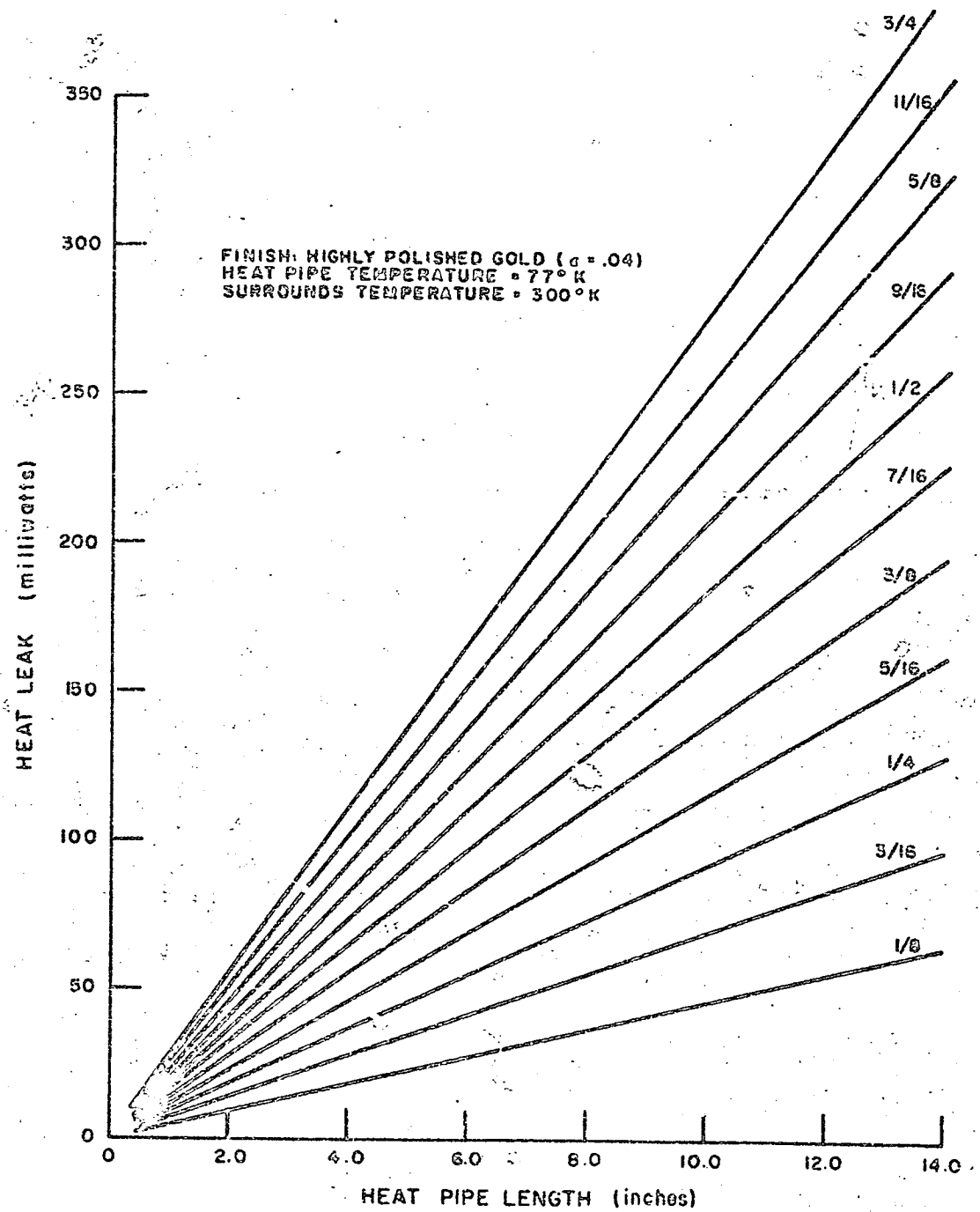



Fig. 6-1. Heat leak into heat pipes as a function of pipe length with pipe diameter as a parameter.

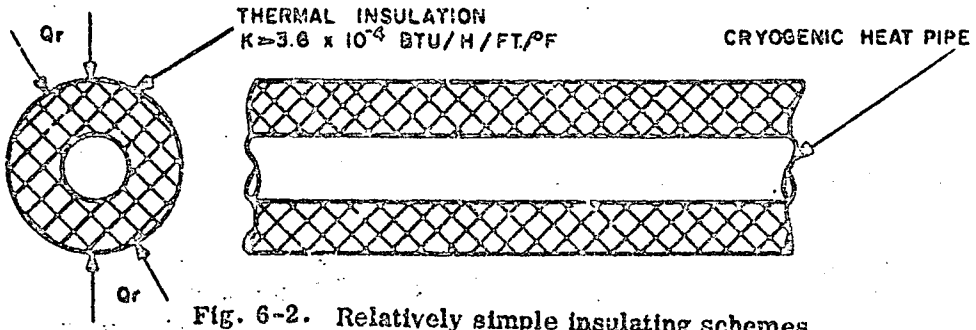



Fig. 6-2. Relatively simple insulating schemes.

coupling through even the best insulation materials available, and the increase in radiation area is more detrimental than the conduction insulation achieved. To get any reduction in cold finger loading requires an effective thermal conductivity of less than $3.6 \times 10^{-4}$ Btu/hr ft°F. The only approach to achieving such insulation levels is through the use of multifoil insulation blankets. The materials and techniques regularly used in spacecraft systems lead to heat loads which correspond to effective emissivity of the order of 0.01.[1*] Blankets of this type would lead to extraneous heat load of approximately 25 mW per foot of length. Recent measurements made on a sophisticated multifoil system of one hundred three 0.00025 in thick aluminum foils resulted in a heat leak of 0.20 Btu/hr $ft^2$ between 72°F to -320°F, corresponding to an effective emissivity (ε) of 0.0015.[2] The conclusion which can be drawn from this discussion is that multifoil insulation technology is necessary in the cryogenic areas of ICICLE to make the concept feasible. While the current level of this technology is adequate to meet the cryogenic insulation needs, application of the most recent developments in this field would be warranted if the full capability of such a system is to be exploited.

While the importance of good insulation is most important to ICICLE at cryogenic temperatures, the difficulty of the problem is most severe at high temperature. Recent work has been done to extend the operating temperature range and thermal conductivity of multilayer foils for use with radioisotope fuel capsules used in RTG systems. There are many types of systems in existence but the most attractive use refractory oxide particles to separate reflective radiation shields. The foils used range in thickness from 0.00025 in to 0.001 in, and the particle separators are in the 5-10 $\mu$m range. The systems which have been shown to be effective for long periods of time are aluminum-$ZrO_2$** at temperatures up to 500°C; copper-$ZrO_2$ up to 800°C; nickel-$ZrO_2$ up to 1000°C; platinum-$ZrO_2$ up to 1100°C; tantalum-$ThO_2$ up to 1200°C; molybdenum-$ThO_2$ up to 1800°F and tungsten-$ThO_2$ up to 1900°C. Investigation into the life, performance and design of these systems has resulted in data similar to the typical examples shown in Figs. 6-3 and 6-4.

*References for this section are at the end of this section.

**First is the foil material; second is the powder separator.

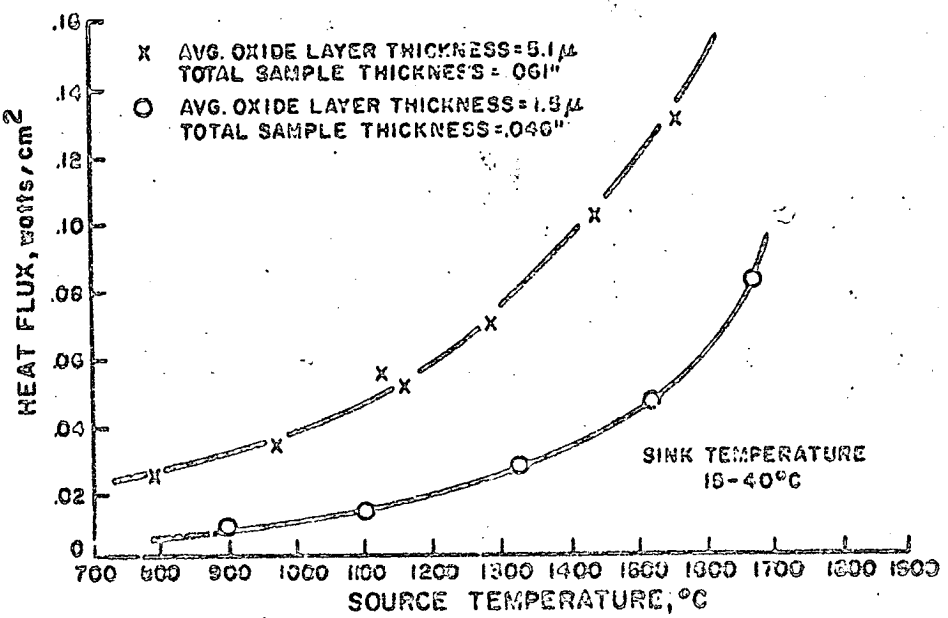



Fig. 6.3. 40-layer Mo-$ThO_2$ insulation samples — mixture 115 $ThO_2$ powder.

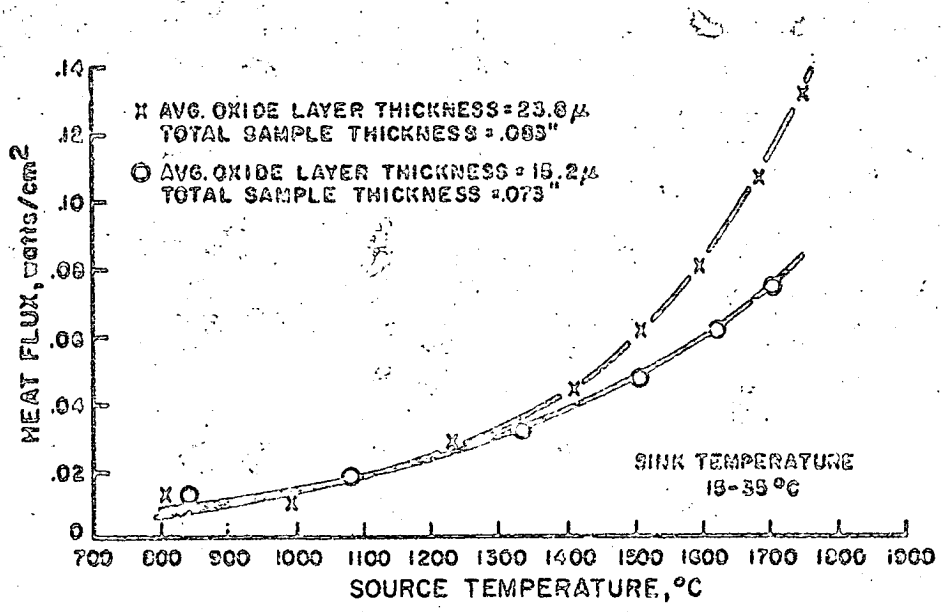



Fig. 6.4. 40-layer Mo-$ThO_2$ insulation samples — mixture 116 $ThO_2$ powder.

This performance, which is six to ten times better than competitive insulations, is necessary to make an ICICLE system practical. Four factors combine to degrade the performance of this type of system and should lead the designer to conservative use of the data presented. First, there is a great sensitivity of multifoil performance with insulation powder density. Figure 6-5 shows that there is a distinct minimum in heat leak as the amount of powder is varied. If too few particles are used, the chance of interfoil contact increases, resulting in an increase in heat flux. If too many particles are used, the conductive component of the insulation increases sharply, also increasing heat flux. By doubling the powder coverage from 0.0683 mg/cm$^2$ to 0.1575 mg/cm$^2$, the heat flux increases from 0.01 W/cm$^2$ to 0.05 W/cm$^2$. Since control of this parameter is not too precise, variation in samples can be substantial. A series of 6 $TaTh_{02}$ blankets were manufactured to the same specification and tested. The heat flux through these samples varied from 0.010 W/cm$^2$ to 0.017 W/cm$^2$.[3]

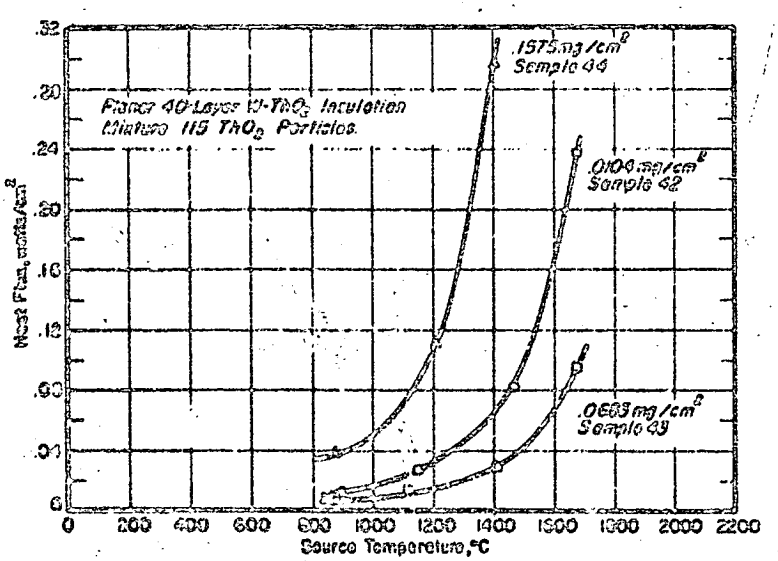



Fig. 6-5. Heat flux vs. source temperature — planar W-$ThO_2$ insulation.

A second degradation factor increases with operation at high temperature. Increasing heat flux with operating life can be caused by changing foil surface properties, gas evolution in the interspaces, or bonding between separator and the radiation foils. This latter factor appears to be the dominating factor with the powder type multifoils and for 2 to 5 year life would dictate the use of one of the refractory metals for the foil rather than the nickel, which might be preferred for short-term operation. If, in addition, launchpad operation is a requirement, then consideration should be given to a nontarnishing foil material like platinum or rhodium.

A third factor bearing on performance is the mechanical loading imposed on the insulation assembly. Multiple foils are not load carrying materials and should not be called upon for any structural requirements. In Fig. 6-6 is shown the effect of loading a 40 layer blanket of tungsten-$ThO_2$ with 1.21 psi and 2.10 psi. This small load increase causes a substantial heat loss increase. Great care must be taken to provide structural support of isotope container and heat pipe through zirconia mounting pins or fine wires of a material like rene 41. The heat leak through these members and the insulation penetration required can be significant if not carefully done.

A fourth degrading factor to foil thermal insulation is edge losses. Since the isotope source will probably be contained in a cylindrical package similar to that shown in Fig. 6-7, care is required at all joints. If cracks of 0.005 in existed, the heat loss would be 0.19 W per centimeter of joint. Overlapping joints must be designed with care since the material is very anisotropic and thermal short circuits are easily created. Three types of corner configurations have been investigated and are shown in Fig. 6-8. The data plotted in Fig. 3-9 shows that with care edge losses can be significantly reduced although they still remain a significant factor.

Representative of the fuel source which could be used for ICICLE is the package being qualified for Transit. This package is a modification of the LRHS capsule, which has a thermal output of 204 W. The Transit requirement is for 850 W, which is satisfied with the package shown in Fig. 6-10. This package is shown enclosed in an insulated thermal collector which would be suitable for the ICICLE application. The basic technology of this capsule can be utilized to build capsules with a linear relationship between capsule volume and thermal output. If the capsule is mounted as shown in Fig. 6-10, it represents a minor fraction of total heat source size. Heat losses can be calculated versus VM input requirement, using a variety of insulation types. These calculations are tabulated in Table 6-1. Data of the type shown in Figs. 6-11 and 6-12 is used to calculate losses. Notice that for a 0.85 in thick blanket with best materials available, container losses can be reduced to 35 W. When practical consideration of such things as cracks is made, these losses go to 65 W. Structural penetrations to support the capsule add another 15 W to the heat leak. Likewise, heat leak to the heat pipe is related to the thickness of the insulation.

The assumptions made concerning the insulation blankets have been conservative on balance. For instance, while no allowance has been made for losses due to the structural problem of mounting the isotope to the spacecraft and edge losses have been calculated only for the top and bottom of the container cylinder, the use of only 40 layers of foil has been assumed. The possibility of doubling this to 80 layers can be realized with an acceptable increase in system complexity and a significant decrease in thermal losses. There are several conflicting insulation and structural requirements which can be resolved only by detailed consideration of the system design. Suffice it to observe that the insulation technology

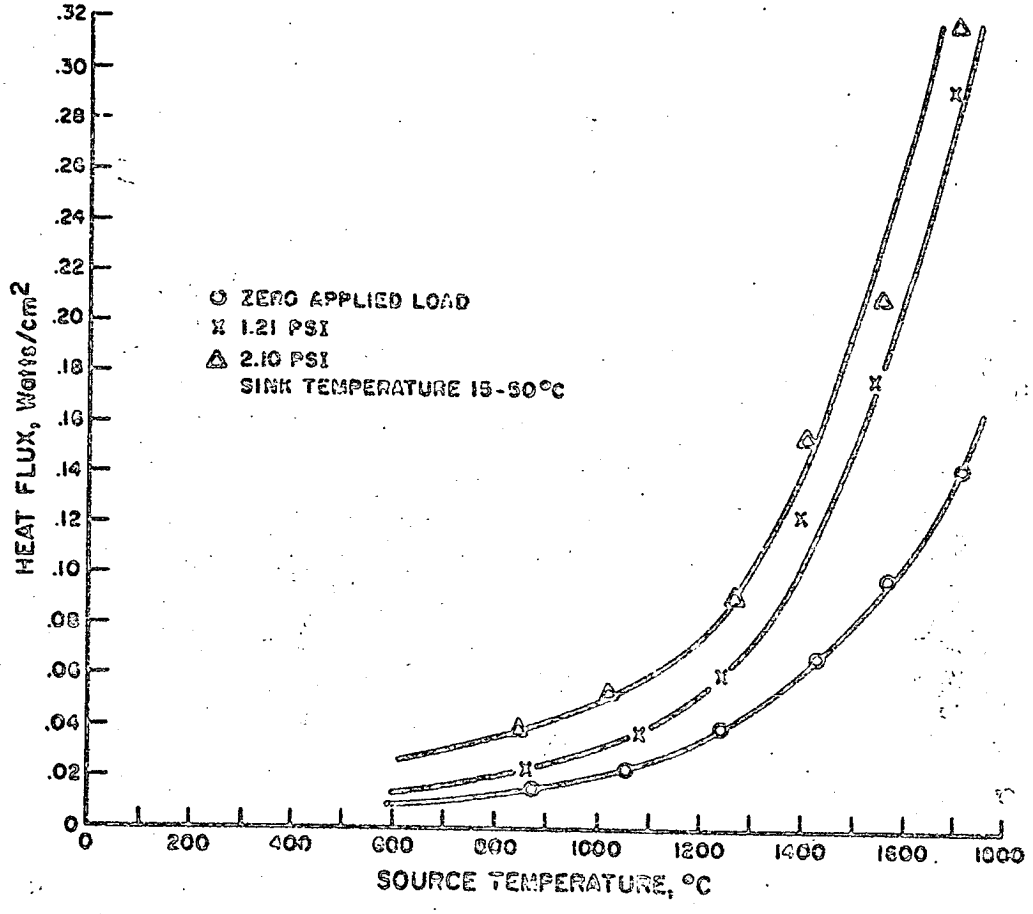



Fig. 6-6. Insulation performance as a function of the applied compressive load.

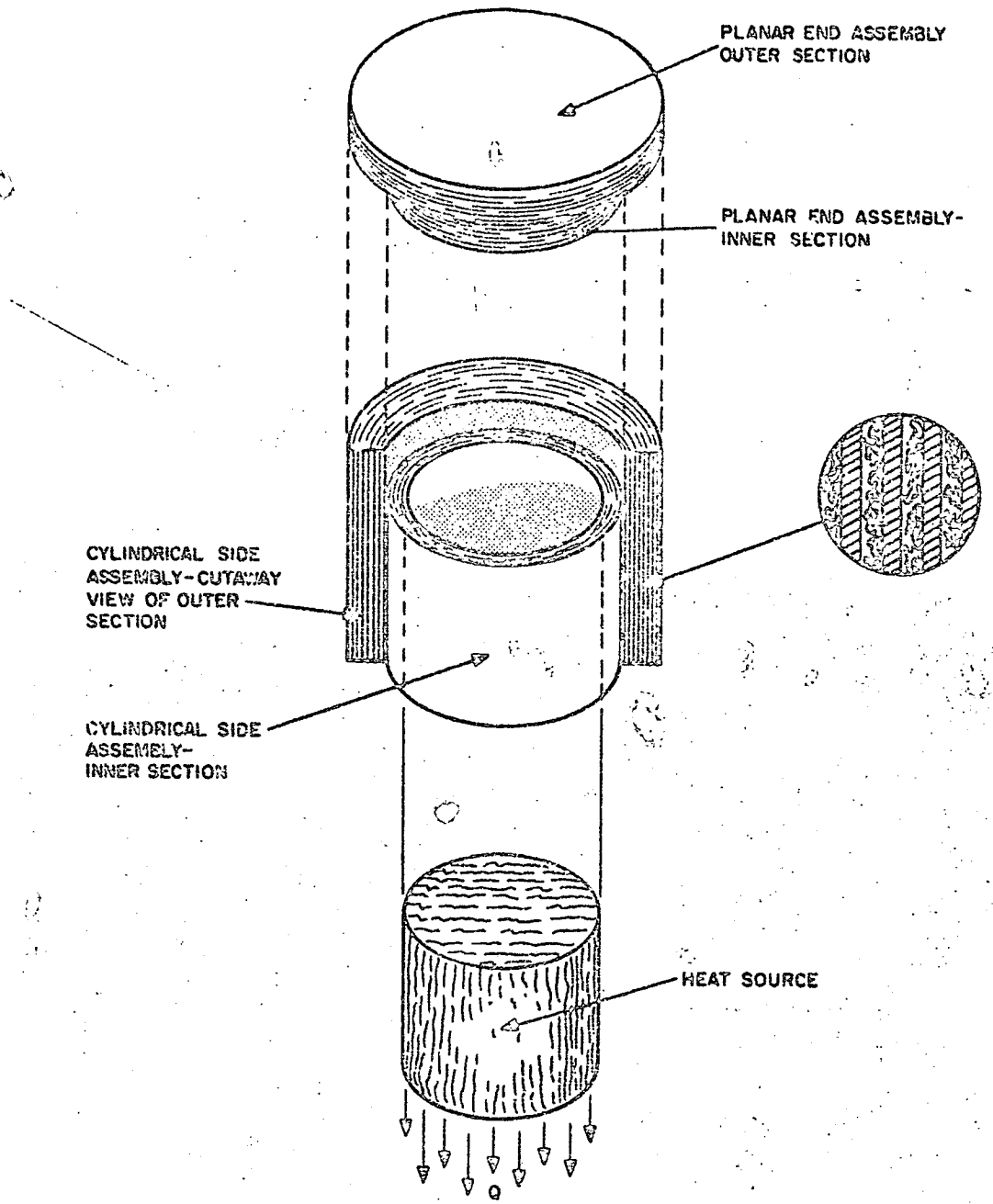



Fig. 6-7. Cylindrical-planar corner configurations around a radioisotope heat source.

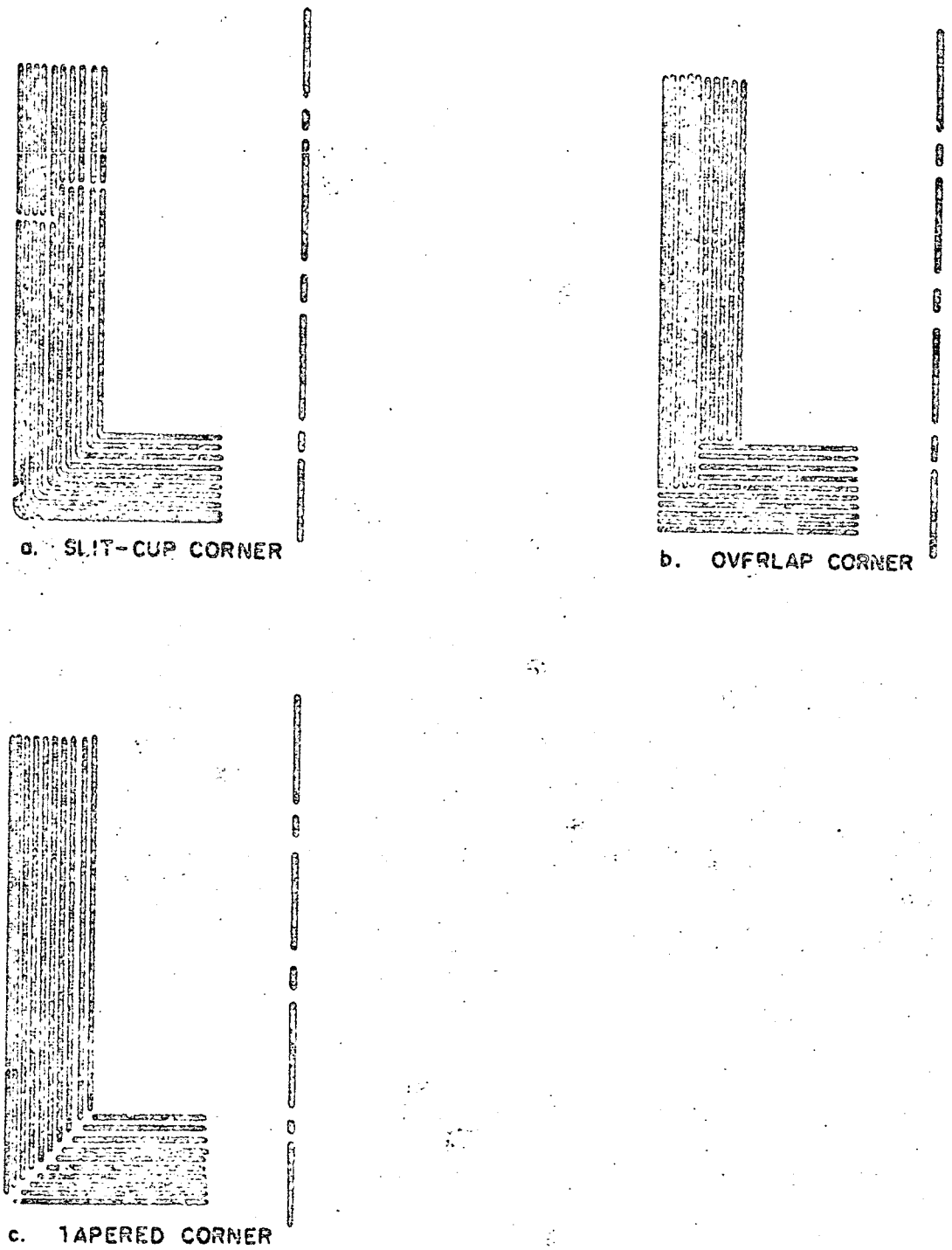



Fig. 6-8. Various corner configurations.

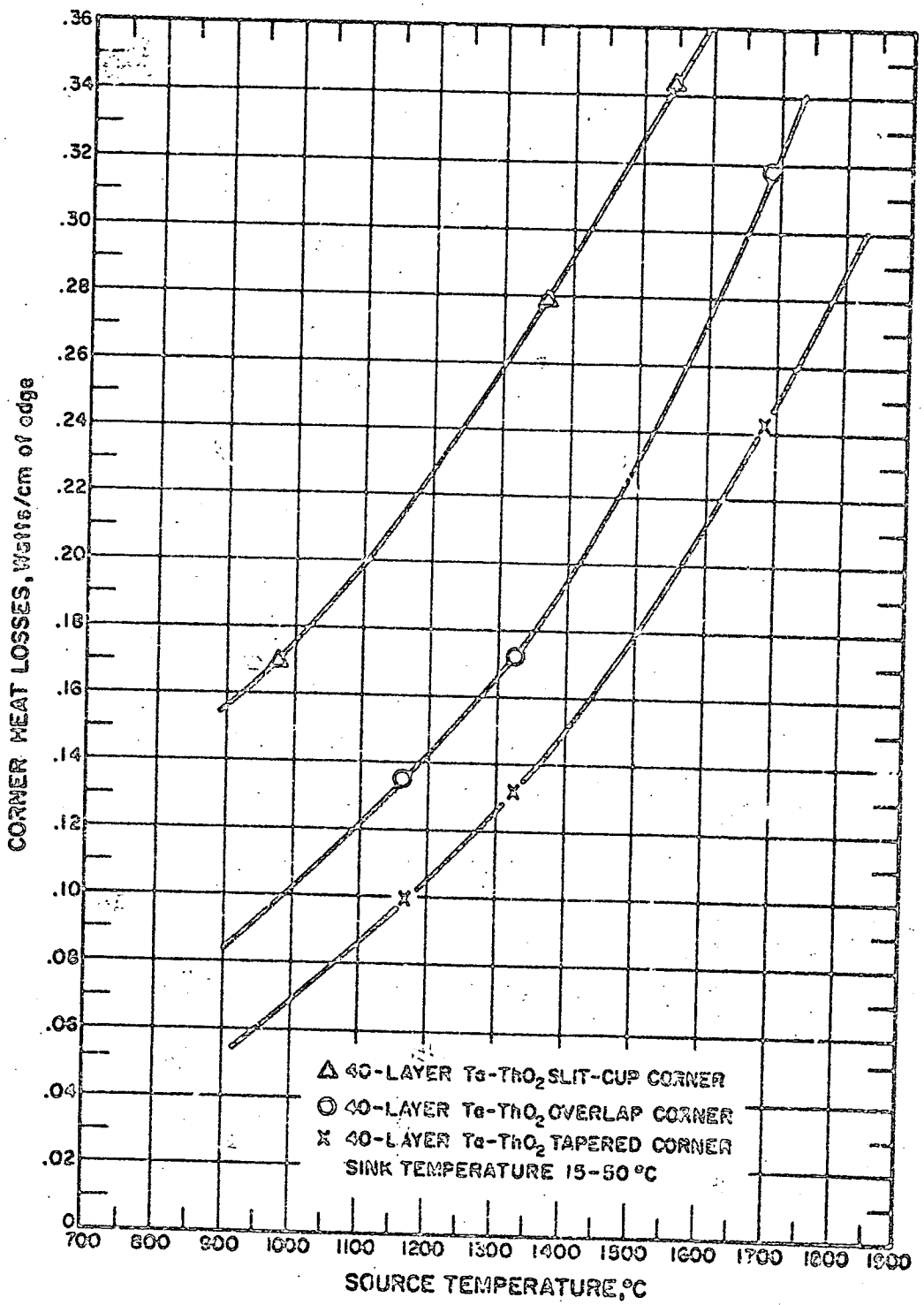



Fig. 6-9. Corner configuration performance comparison.

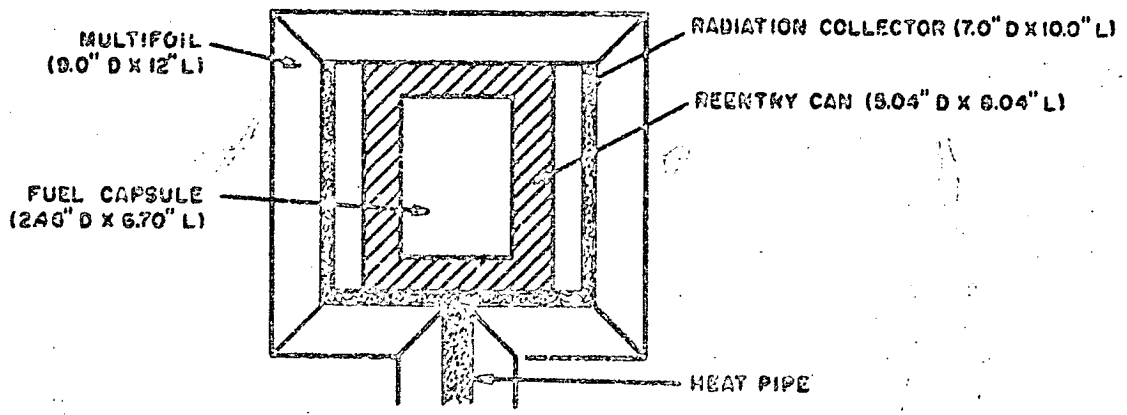



Fig. 6-10. Package being qualified for Transit.

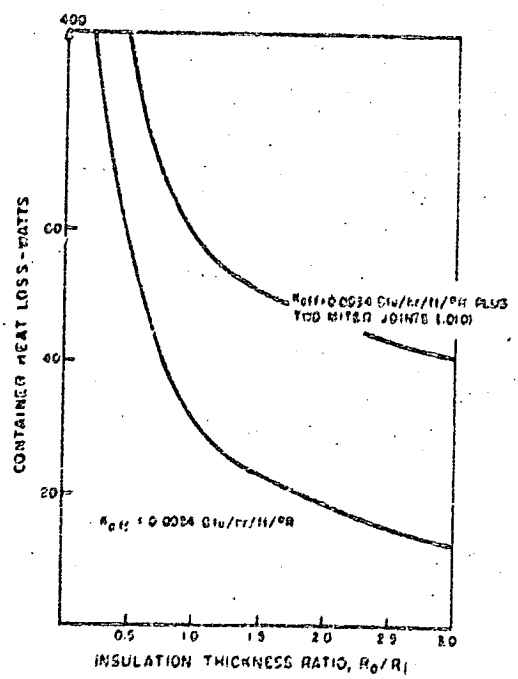



Fig. 6-11. Heat loss from isotope container (basic container has 6 in diameter and is 7.5 in long).

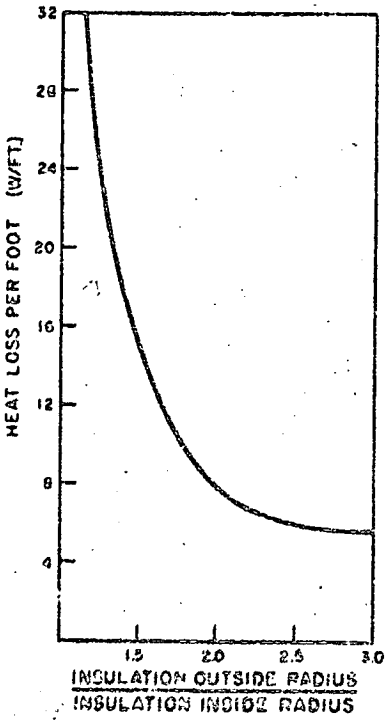



Fig. 6-12. Heat loss per foot of hot heat pipe length ($T_h$ = 950°C).

developed for RTG must be used in ICICLE. This is verified by the information shown in Table 6-1. The size of container which must be insulated is determined by scaling the radioisotope fuel capsule on the basis of Transit configuration. Since reentry can and thermal collector design is relatively insensitive to thermal output, the overall container size does shrink appreciably when gross isotope goes from 800 to 200 W. Thermal losses are calculated for three insulating techniques. The first uses the best properties reported and would not realistically account for repeatable quality and insulation degradation. An effective emissivity of 0.005 is realistic and would account for all the factors existing in a practical package design. The extreme right columns give a conservative estimate of losses using current conventional technology.

Two things are obvious from the data. Conventional multifoil blanket techniques are inadequate for effective insulation of the ICICLE heat source. Large heat sources utilize the heat generated in a fuel capsule much more efficiently. Based on these calculations, the isotope to drive a 5W VM will have a gross output of 350 to 400 W with 210 to 250 W net into the VM hot cylinder. The use of several smaller VM and isotope systems to accomplish the multiple load cooling would be clearly inefficient. In addition to any other reasons, this would more than provide adequate justification for a central refrigeration system approach.

TABLE 6-1. ISOTOPE CONTAINER HEAT LOSSES

| Isotope Output (W) | Container Size (diameter x length, in) | Losses (W) $\epsilon_{eff}$ = 0.0015 (Best Foil) | | | | Losses (W) $\epsilon_{eff}$ = 0.005 (Realistic) | | | | Losses (W) $\epsilon_{eff}$ = 0.01 (Conservative) | | | |
|---|---|---|---|---|---|---|---|---|---|---|---|---|---|
| | | Cont. | Heat Pipe | Switch | Total | Cont. | Heat Pipe | Switch | Total | Cont. | Heat Pipe | Switch | Total |
| 800 | 7x10 | 49.5 | 14.6 | 25.0 | 89.1 | 113 | 36 | 25 | 174 | 226 | 72 | 25 | 323 |
| 600 | 6.7x9.1 | 43.0 | 12.9 | 25.0 | 80.9 | 97 | 32 | 25 | 154 | 194 | 64 | 25 | 283 |
| 400 | 6.5x8.6 | 41.3 | 10.9 | 25.0 | 77.2 | 93 | 27 | 25 | 145 | 186 | 54 | 25 | 265 |
| 200 | 6.1x7.5 | 35.7 | 9.1 | 25.0 | 69.8 | 80 | 23 | 25 | 128 | 160 | 46 | 25 | 241 |

References for Section 6

1. Private communication, Ed Powers, NASA, GSFC.

2. M.L. Pacquin, "High temperature multi-foil thermal insulation," Proceedings of 1968 Intersociety Energy Conversion Conference, Boulder, Colorado.

3. Private communication, M.L. Pacquin.

Section 7

# ICICLE THERMAL CONTROL


*Summary*

*Thermal control of an ICICLE system will be required because of a combination of several factors which would cause variation in cold temperature. These factors are primarily degradation of system components and changes in environmental conditions. Control at each of the three heat transfer regions could be incorporated to provide the simplest and most reliable system.*

*Minor variations in refrigeration requirements and system degradation can be accommodated by a temperature controlled heater mounted on the experiment platform. A total of 2 to 4 W of such heating would be feasible since it would be required at the beginning of spacecraft life when excess electrical power is available from the solar cells.*

*Fluctuations of radiator temperature will cause varying refrigerator crankcase temperature, causing variations in system capacity as well as creating stress fluctuations in the refrigerator mechanism. Use of a gas controlled ambient temperature heat pipe will damp out temperature variation at the crankcase and thus stabilize the system.*

*The major control function of the ICICLE system must be to protect the isotope from excess temperature in the face of reduced demand by the refrigerator. This could occur because of hot heat pipe and/or refrigerator degradation, commanded shutdown of the system, or failure of the heat sink subassembly. The most effective method for accomplishing this is through the use of a temperature controlled flap on the isotope housing. This flap allows the isotope to have a variable view of space and thus keep its temperature below some high limit.*

*Because of the serious nature of an isotope failure, a failsafe protection device must be provided. A spring loaded fusible link could provide this function. Actuation of this protective device would result in system abort as this should be suitably interlocked with the rest of the system to assure that all other alternatives have been implemented.*

*Thermal control of an ICICLE system can be accomplished using existing technology. The system can be adequately protected against catastrophic malfunction.*


A complex thermodynamic system like ICICLE has a thermal control problem at three different temperatures. As described in this report these temperatures are 900°K, 300°K and 77°K. Since the reason for the thermal control is different at each temperature, the methods and control philosophy are different in each temperature range.

## A. THERMAL CONTROL REQUIREMENTS

### 1. Cryogenic Temperature Range

Temperature control requirements for the experiments likely to be supported by ICICLE are discussed in the requirements section of this report. Generally parametric amplifiers would want to operate at as low a temperature as is achievable although in some cases control to a known temperature might be desirable. Infrared detectors require control to at least 5°K and preferably closer. There are three kinds of conditions for which control might be necessary. First, the design capacity of the engine must be adequate to accommodate system variations which would affect the capacity demand on the refrigerator. These would include tolerances on heat pipe performance, variations in interface thermal resistances, or variations in the net capacity because of different experiments from spacecraft to spacecraft. This kind of thermal control requirement could best be satisfied by final adjustments of VM engine speed and/or charge pressure during final system testing.

A second control requirement would arise due to degradation of system components with life. At this phase of the program it is difficult to predict what this degradation will be. It seems clear that the refrigeration load on the system should be fairly constant since degradation of surface finishes due to condensation of contaminants will not affect thermal losses. This is one of the important reasons for using multifoil insulation on the cryogenic pipes rather than a high reflectivity finish. Degradation of the VM engine will probably account for the bulk of refrigeration loss during system life. If a small drop in refrigeration output must be accommodated during mission life, a temperature controlled heater located at the experiment would provide the most desirable control technique. The temperature coefficient of capacity for a 5 W machine is 7.5°K/W so that a machine which oversized by 2/3 W would remain within an acceptable temperature tolerance of 5°K without active control. Electric heaters of up to 2 or 3 W would probably be acceptable for most applications. If system degradation exceeds these values, initial sizing of the system to allow for design end of life capacity would begin to be unattractive. Temperature controlled heaters are the most attractive cold finger control systems to accommodate system degradation.

A third control problem at the cold finger is the short term fluctuation of thermal load caused when the cooled experiment is out of use or experiences a temporary change in thermal load. In this case the simplicity, response time, and efficiency of electric heater control make it the favored control technique.

### 2. Ambient Temperature Range

The widest temperature swings in an ICICLE system probably will be as its exposure to sun and earth loading changes. These temperature swings would reflect into the hot and cold cylinders as variations in temperature and heat load. In addition

to the temperature control problem, this would create a stress and wear factor which would be imposed on the crankcase mechanism operating with such temperature variations. Since a heat pipe appears to be indicated to transfer heat from the VM to the radiator, use of a constant temperature heat pipe in this application could lead to improved system thermal control and reliability. A constant temperature heat pipe will be used in all system descriptions. This passive device will permit the operation of the refrigerator crankcase at design temperature regardless of environment conditions.

3. High Temperature Range

Existence of a long life thermal source, such as an isotope, requires some method of handling the output when it is more than the demand of the system. This problem is just one of the aspects of thermal management in the ICICLE system. Protection of the spacecraft from the effects of ICICLE malfunction, control of system performance in the face of varying environmental and system parameters, and provision for remote commandable operation can be incorporated into a single system which we call a thermal switch.

The location of the thermal switch can be determined by an examination of the protection and control requirements of the system and a consideration of how they can be met. Typical of these requirements on ICICLE are the following:

a) Temperature control of the hot cylinder if the engine is not running.

b) Refrigeration capacity control.

c) Thermal input leveling from decaying isotope.

d) Launch pad temperature control.

e) Radiator freezeup protection.

f) Capability for commandable startup and stop.

g) Failsafe protection of isotope from system malfunction.

In all cases the requirements can be satisfied with a device for switching in the high temperature region. Few of the required functions can be provided by components at any other location so that a high temperature thermal switch is clearly indicated. Thermal control of the various components of the ICICLE system can be achieved by use of passive and/or active thermal control devices such as thermal switches (defined as on-off devices) and proportional thermal controllers (devices which have variable thermal resistance). Many of the thermal control devices can be operated by command as well as by self-actuation or sensor actuation.

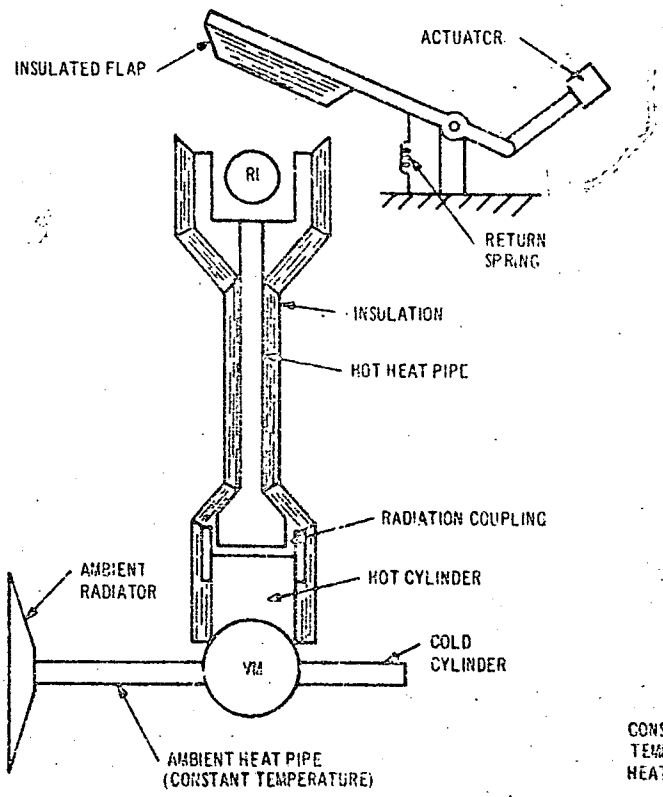
There are several approaches to doing thermal switching at high temperature. In order to select a preferred approach, the candidate techniques must be examined against a list of selection criteria; then the selection must be made on the basis of best overall qualification. The following paragraphs briefly describe the switching techniques investigated, the criteria used for selection, and the selection procedure.

Figure 7-1 shows seven different thermal control systems. System (a) controls the isotope, hot heat pipe, andVM hot cylinder temperature by controlling the radiation coupling of the isotope and isotope container to space. This is accomplished by means of an insulated flap whose position is controlled by an actuator. The flap can be positioned to dump any desired amount of heat to space up to the limit imposed by the maximum radiation coupling to space. For a 5 in diameter isotope container with no extended surfaces, the maximum coupling ($A \epsilon F$)* would be on the order of 17 $in^2$. With a 4 in diameter isotope sphere at 1150°K and a container temperature of 1100°K, the heat dumped to space would be approximately 1260 W. This exceeds the expected isotope heat generation. The average temperature of the isotope and its housing necessary to dump 350 W is approximately 860°K (assuming no heat input to VM hot cylinder). In practice this temperature would be less since some heat will be transferred to the VM hot cylinder. The thermal characteristics of the VM would have to be known in order to compute the actual isotope and isotope container temperatures. The heat leak in the closed position will be about 1 W per 0.001 in of crack width necessary for mating of the flap and container insulation.

System (b) controls the isotope, isotope container, and hot heat pipe temperatures to some predetermined value by means of a constant temperature heat pipe designed to "turn on" at the desired value. This concept is not capable of reducing the hot heat pipe temperature below the normal operating temperature unless the constant temperature heat pipe has a controllable inert gas reservoir. The reservoir would have to be maintained at the temperature of the hot end of the heat pipe in order to prevent the working fluid from collecting in the reservoir and thereby causing the heat pipe to fail due to lack of working fluid in the wick. In order to have minimum heat leak in the "off" condition (full length of the heat pipe filled with inert gas), the heat pipe should be as small and thin walled as practical. For a 0.35 in OD heat pipe with 0.010 in wall, 0.030 in wick thickness, sodium working fluid, 6.0 in insulated section, and 10.0 in long exposed section, the minimum heat leak would be approximately 10 W and the maximum heat handling capability would be approximately 700 W. The constant temperature heat pipe must be designed such that the cold end does not go below the freezing temperature of the working fluid in order to prevent capturing of all of the fluid at the cold end.

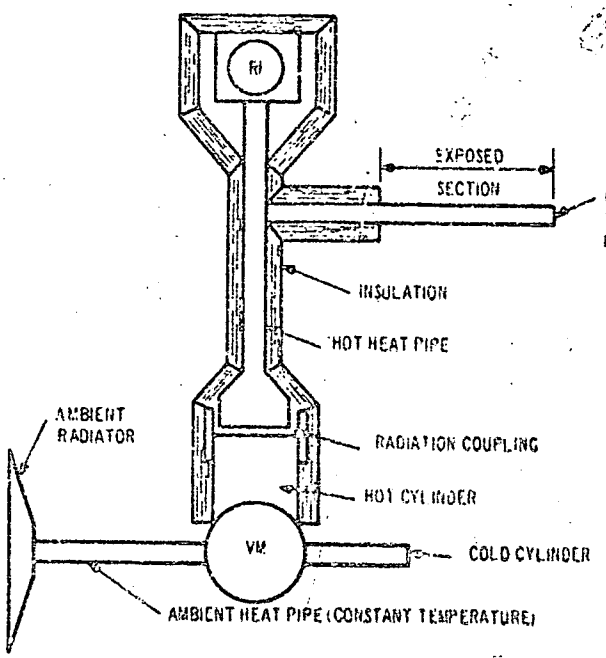
System (c) is similar to (b) but differs in that the bypass heat is dumped into the ambient temperature heat pipe-radiator system instead of directly to space. A thermal resistor must be placed in the thermal path in order to prevent freezing at the

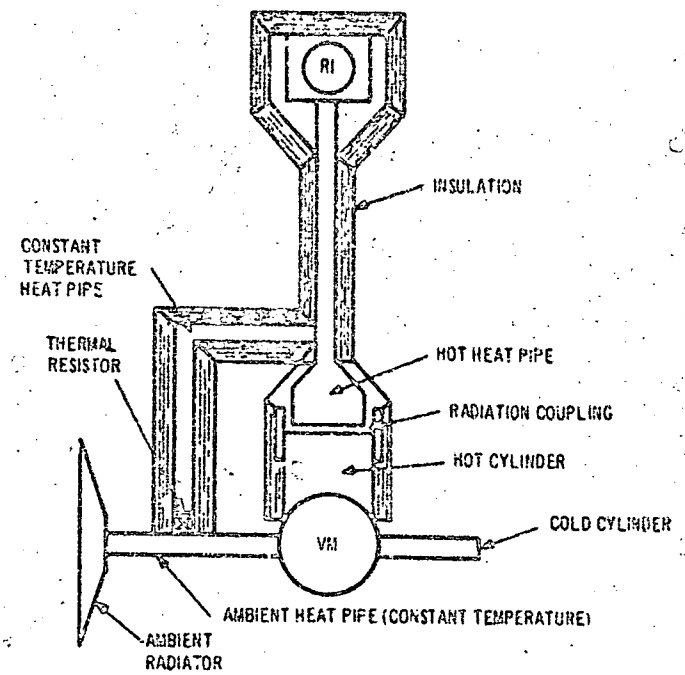
*A = radiating area; $\epsilon$ = emissivity; F = view factor.




(a)

(b)




(c)

FOLDOUT FRAME 1

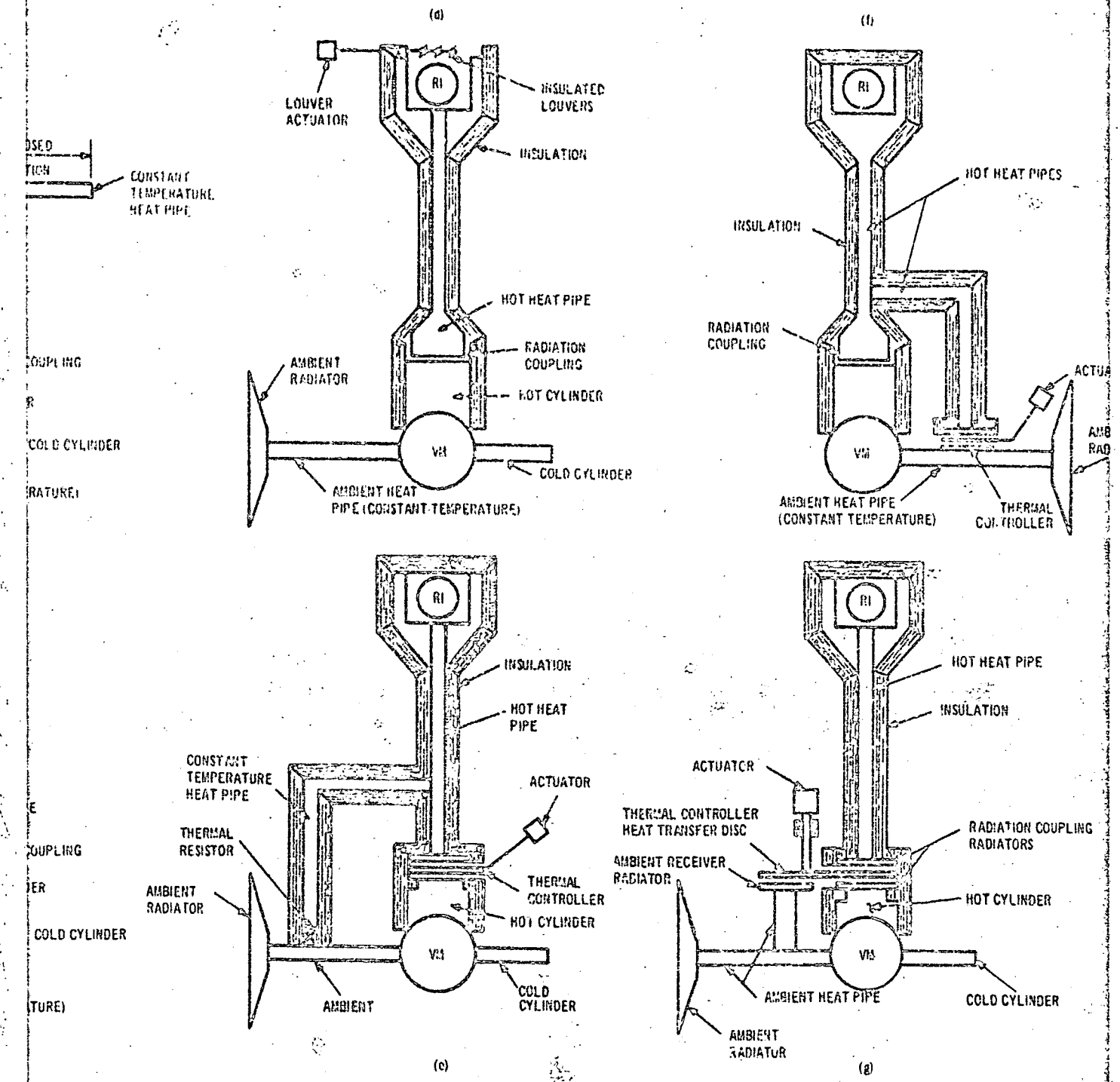



Fig. 7-1. Thermal control schematics.

ambient temperature interface. The resistor must be thermally sized such that in the "off" condition the heat leak from the hot heat pipe to the ambient heat pipe is sufficient to create a temperature gradient of approximately 100°C in the resistor (assuming a constant temperature sodium heat pipe). The required thermal resistance (Rt) can be calculated by dividing the desired thermal gradient in the "off" condition ($\Delta$Toff) by the "off" condition heat leak (Qoff). The "on" condition heat conductance (Qon) can then be determined by dividing the "on" condition thermal gradient ($\Delta$T on) by the $R_t$.

For example, the required $R_t$ with a Qoff of 10 W is 10°K per W. The Qon would then be the temperature of the hot heat pipe minus the temperature of the ambient heat pipe divided by $R_t$; that is, $Qon = T_h - T_a/R_t$. With the hot heat pipe at 1100°K and the ambient heat pipe at 300°K, the conducted heat is 80 W, or eight times the "off" condition heat leak. The Qon will always be Qon = $\Delta T/100$ X Qoff for a conduction type thermal resistor. This limitation can be eliminated by replacing the conduction thermal resistor with a radiation coupling of the proper size. In order to maintain a temperature of 400°K on the constant temperature bypass pipe, the radiation coupling will have an $A\epsilon$ value equal to the "off" condition heat leak (Qoff) divided by the $\Delta\sigma T^4$ ($\sigma T^4$ 400°K-$\sigma T^4$300°K). For a Qoff of 10 W, the $A\epsilon$ coupling value is 15.6 $in^2$. In the "on" condition the Qon (with a hot side temperature of 1100°K) would be 832W. At a Qon of 350 W the hot side temperature would be 885° K, which is less than the normal operating temperature of the VM hot cylinder (900°K). To achieve such a condition, a controllable inert gas reservoir held at the hot end temperature would be required. Otherwise the hot heat pipe will always be held at 1100°K. The actual operating temperature in the "on" condition would be less since the hot cylinder will absorb some heat. The thermal characteristics of the VM would have to be known in order to determine this temperature accurately.

System (d) is essentially the same as system (a) except insulated louvers are used in place of the insulated flap. The radiation heat leak of a closed louver system is relatively high due to the cracks and clearances necessary in a louver system. A closed louver system with an effective emissivity of 0.1 would be a good system. All louver systems presently in use have effective emissivities of 0.15 to 0.20. With an effective emissivity of 0.10 the closed heat leak would be on the order of 115 W. Due to this high closed heat leak and possible fabrication problems, this system is not recommended.

System (e) is identical to system (c) except that the hot heat pipe to VM hot cylinder thermal coupling has been replaced by a thermal switch or proportional controller. This system has all of the features of system (c), with the additional ability to control the heat flow from the hot heat pipe to the VM hot cylinder by means of ground control and/or temperature feedback from the VM hot cylinder. A well-designed radiation thermal switch or proportional controller should have an open position effective emissivity as low as 0.01. This would give an open position heat

leak of 0.53 W per square inch of coupling area with the hot heat pipe at 1100°K. To transfer 350 W from the hot heat pipe at 1100°K to the VM hot cylinder at 900°K would require 14.5 $in^2$ of coupling area with surface emissivities of 0.9. Therefore, the open position heat leak would be approximately 7.7 W.

System (f) is identical to system (c) except the constant temperature heat pipe is replaced by a standard hot heat pipe and the thermal resistor is replaced by a radiation thermal switch or proportional controller. This permits control of the hot heat pipe temperature by varying the radiation coupling between the hot heat pipe and the ambient temperature heat pipe. The larger the thermal controller the greater the temperature control range will be. The open position heat leak will be approximately 0.5 W per square inch of controller coupling area.

System (g) controls the hot cylinder temperature by controlling the radiation coupling from the hot heat pipe to the VM hot cylinder. This is accomplished by means of a heat transfer disk which can be rotated into the gap between the hot heat pipe and the hot cylinder and thereby reduce the radiation coupling. At the same time the heat transfer disk will receive heat from the hot heat pipe, will conduct this heat around the disk, and will then dump it into an ambient temperature receiver which is thermally coupled to the ambient temperature heat pipe. The amount of heat transferred from the hot heat pipe to the ambient heat pipe will be a function of the position of the heat transfer disk. This position can be controlled by the hot cylinder temperature, by ground command, or by a combination of both. The heat transfer disks can be either solid metal or a pancake type heat pipe. In order to transfer 350 W from the hot heat pipe to the VM hot cylinder with the hot heat pipe at 1100°K and the hot cylinder at 900°K, the radiation coupling radiators must have an area of 14.5 $in^2$ each with an emissivity of 0.9. The ambient receiver radiator would have an area of 87 $in^2$; the corresponding disk diameter would be approximately 12.5 in. In the "off" position the heat leak to the VM hot cylinder would be approximately 2 W. In the "on" position the heat leak to the surrounds (at 300°K) will be approximately 7 W, based on 0.010 in clearance on either side of the heat transfer disk.

The thermal resistors shown in Fig. 7-1(c) and Fig. 7-1(e), and the thermal controller shown in Fig. 7-1(f), could be replaced by a mechanical contact thermal switch; but, due to the high temperatures involved and the possibility of the mechanical contact sticking or welding shut, contact switches are not recommended. The possibility of using variable conductance insulation (vary conductance by injecting gas between the layers of multilayer insulation) is not recommended due to the relatively low switching ratio and the possible difficulties that could be encountered in building a gas tight insulation system that would not introduce large heat leaks into the system.

a. Types of Thermal Control Systems

The thermal control systems described in Fig. 7-1 fall into the following three basic categories:

1) Closed Loop Fixed Control

This type of system senses and maintains temperature at some point in the system, with no provisions for changing the initial set point. Systems (b), (c), and (e) fall into this category. Systems (a), (d), (f) and (g) would also fall in this category if the actuators are controlled directly by a temperature feedback. System (e) contains two independent control elements. The constant temperature heat pipe is fixed closed loop, and the thermal controller can be fixed closed loop.

2) Closed Loop Variable Control

This type of system senses and maintains temperature at some point in the system and has provision for changing the set point temperature value by means of ground command. All of the systems described in Fig. 7-1 can be of this type by providing ground control of the feedback circuit. In the case of the constant temperature heat pipes, or gas operated actuators, this means a variable volume inert gas reservoir such as a bellows, which can be shortened or extended by means of a ground controlled actuating mechanism. In the case of electrically actuated controllers, the signal (temperature) processing circuits could be ground controlled by means of variable or switchable circuit elements such as resistors.

3) Closed Loop Manual Link Control

This type of system has no feedback control which will maintain temperatures at some selected level but does have provisions for varying one or more of the thermal system characteristics (such as thermal resistances) by ground command. Temperatures will be monitored by telemetry, and ground control can increase or decrease temperatures by command. Systems (a), (d), (e), (f) and (g) could be designed to fall in this category.

b. Thermal Control Actuators

Thermal control actuators will fall in one of three general categories:

1) Electromechanical
2) Fluid expansion (gas or liquid)
3) Bimetallic

1) Electromechanical Actuators

An electromechanical actuator will generate a mechanical movement (linear or rotational) by means of an electromechanical component such as a motor or

solenoid. The electromechanical component will be controlled either by ground command or by a temperature sensing control which is fixed or variable by ground command. Figure 7-2 is the schematic of an electromechanical actuator system which is temperature controlled and variable by ground command. $RT_1$ is a temperature sensitive resistor such as a platinum temperature sensor; $R_3$ is a variable resistor which is controlled by ground command; $R_1$, $R_2$ and $R_4$ are field resistors. $R_1$, $R_2$, $R_3$, $R_4$ and $RT_1$ constitute a bridge circuit which provides a dc signal which is + or - depending upon whether the VM hot cylinder is hotter or cooler than the desired temperature. The signal is amplified and supplied to a motor control circuit which drives the motor forward or backward, depending upon the polarity of the signal. The motor provides a mechanical output which drives the thermal controller device through a speed reducer. The output speed must be low enough to permit the temperature sensor to respond to the change in the temperature controller without large overshoot. The motor control circuit should have sufficient hysteresis to eliminate hunting. This will permit the controller to find a position which provides thermal equilibrium near the desired VM hot cylinder temperature.

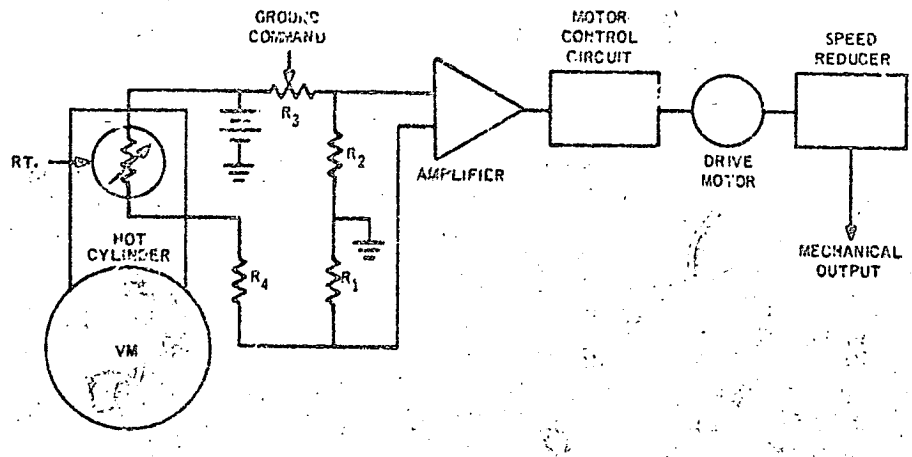



Fig. 7-2. Schematic of electromechanical thermal actuator.

2) Fluid Expansion Actuators

Constant temperature heat pipes are examples of fluid (gas) expansion actuation. Figure 7-3 is a schematic of a fluid expansion actuator which provides a mechanical output and is controllable by ground command as well as by temperature sensing. $RT_1$ is a temperature sensitive resistor which provides a signal $E_2$ as a function of temperature. When $E_2$ exceeds the breakdown voltage of the Zener diode, current is fed to the amplifier which operates a resistance heater on the fluid reservoir. The temperature at which $E_2$ reaches the turn-on voltage is determined by the values of $RT_1$ and $R_1$. $R_1$ can be varied by ground command and thereby vary the control temperature. The fluid reservoir is insulated such that the

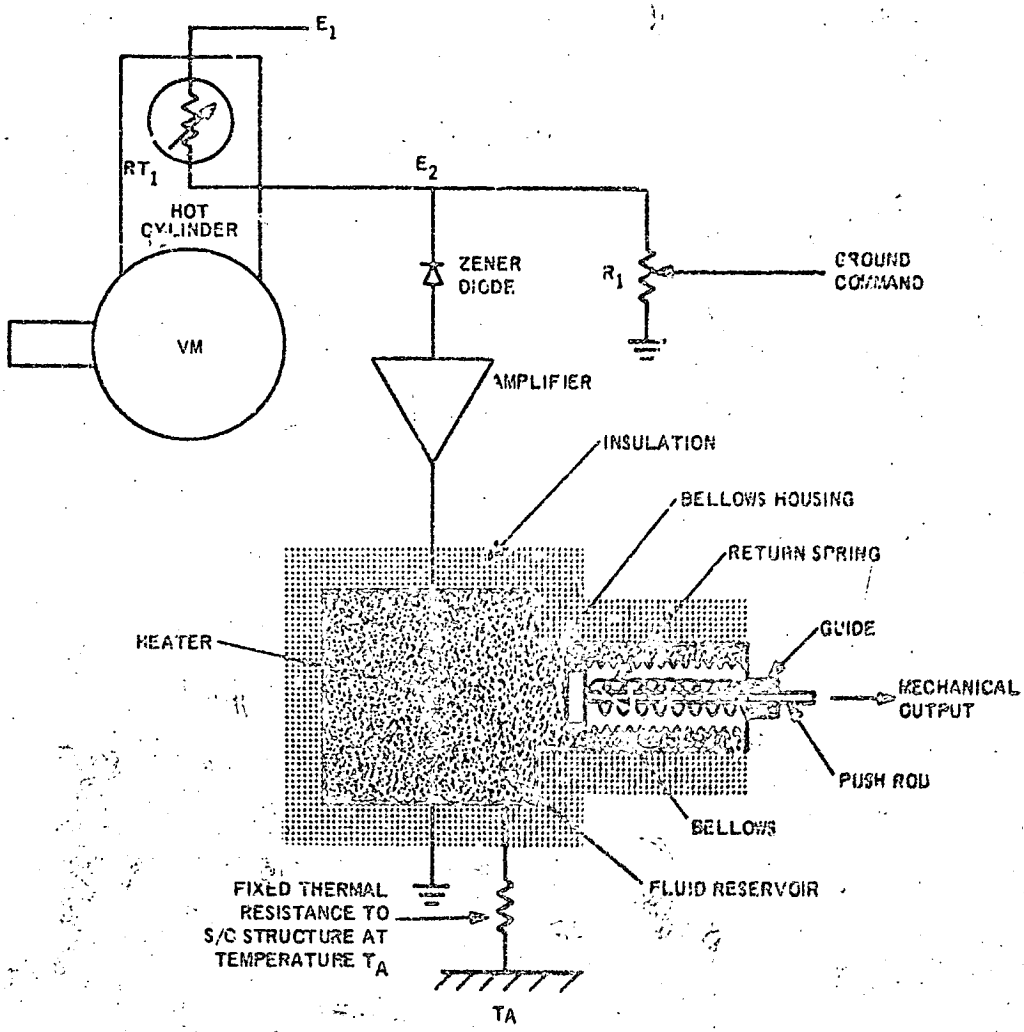



Fig. 7-3. Schematic of fluid expansion thermal actuator.

thermal coupling to the spacecraft is low, thereby permitting the fluid in the reservoir to increase in temperature when the heater is on. The increase in temperature creates an internal pressure either by liquid expansion or by change of phase from liquid to gas. The resultant pressure is transmitted to the spring loaded bellows, causing it to contract and to create a movement of the output shaft. In the case of liquid expansion, the sensitivity of the system is determined by the volume of liquid and the diameter of the bellows. In the case of phase change, the sensitivity is

determined by the vapor pressure-temperature characteristics of the working fluid, the spring constant of the bellows assembly, and the bellows diameter. The power consumption of the system is essentially equal to the heat leak of the fluid actuator assembly and should be 0.25 W or less. The maximum heater power should be limited so that the heating rate of the fluid is low enough to prevent large overshoots and oscillation. Similar fluid expansion systems have been flown on spacecraft for thermal control. The liquid expansion type has the ability to create large output forces which can overcome sticking and friction in the thermal controller if it should occur. A similar system could be built using a Bourdon tube to provide mechanical movement, instead of the bellows.

3) Bimetallic Actuators

Bimetal actuated louver systems are commonly used to control spacecraft temperatures in the region of 300°K. Due to the relatively high temperatures of the VM hot cylinder, it would not be advisable to use a bimetal to sense the VM hot cylinder temperature directly. An actuator which uses bimetal elements at ambient temperature (near 300°K) could be used. Figure 7-4 shows the schematic of a bimetal driven actuator which is temperature sensor controlled and ground commandable. The control portion of the schematic is the same as the control portion of the fluid expansion actuator. The bimetal element is mounted in an insulated housing which is temperature controlled by the resistance heater. The power consumption will be approximately the same as for the fluid expansion actuator (0.25 W or less). The torque or force output of bimetal elements depends on the spring constant of the bimetal. Large heavy elements can produce a reasonable output force or torque but are less temperature sensitive as the element thickness increases and the length decreases.

## B. THERMAL SWITCH SELECTION CRITERIA

Several reasons for high temperature thermal control have been discussed. All of these reasons do not apply to any one specific application, but each application may have one or more requirements for the function a switch can perform. The way that each type of switch impacts on an ICICLE system is by virtue of such parameters as

1) Efficiency - Thermal loss associated with the switch
2) Actuation power - Electrical power required to actuate, hold and deactuate the switch
3) Switching ratio - Ratio between the amount of heat rejected in the rejection mode to the heat leak in the insulated mode
4) Weight - Total weight of the switch
5) Reliability

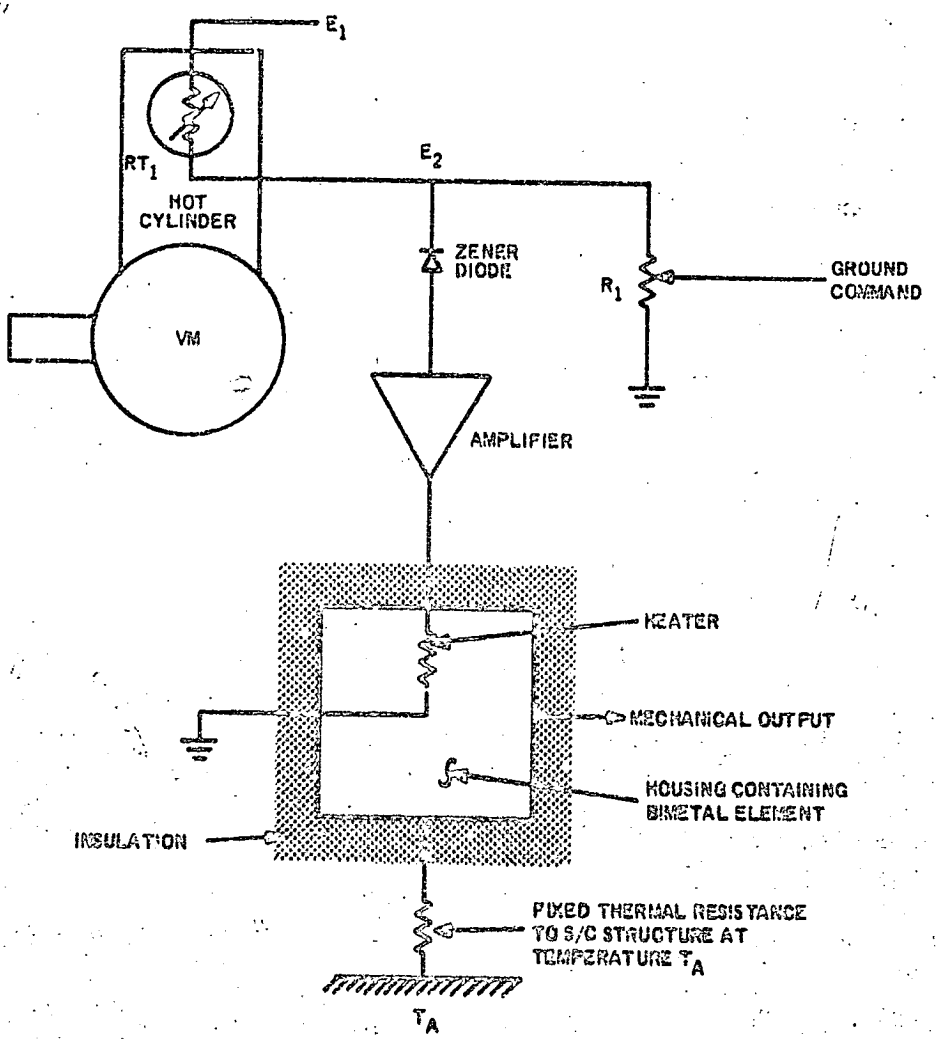



Fig. 7-4. Schematic of bimetal thermal actuator.

6) Commandability - Either programmed or by telemetry

7) System impact - Ease of integration into the spacecraft and ICICLE.

8) Life

9) Response time

Quantitative assessment of these factors for each type of switch is a time consuming design task which provides only marginally improved information over a qualitative evaluation. In Table 7-1 is a matrix display of each of the eight switching techniques described, rated for their suitability in the applications listed below:

1. Slow startup of ICICLE system
2. Use of short half life radioisotope
3. Requirement to conserve engine revolutions
4. Requirement to eliminate cooling
5. Conservation of spacecraft electrical power
6. Reset type of thermal protection device
7. Accommodation of out-of-tolerance thermal parameters
8. Requirement to conserve high temperature heat pipe life

On the basis of this subjective evaluation, a clear overall choice for thermal switch emerges. This choice is system (a), which is an insulated flap actuated in response to hot cylinder temperature. It should be noted that this choice is not the first choice for meeting all control requirements. The important requirement of shunting excess heat early in the operation of a short half life isotope could be accomplished by a simpler and more reliable hot constant temperature heat pipe (system (b)). System (e), which utilizes a temperature controlled radiation interrupter at the hot VM cylinder, is judged superior when control is required because the refrigerator is turned off and/or because cooling is not required. The choice in the latter instances is not completely clearcut, with the result that system (a) is a strong second choice.

Except for some special requirement not covered in this selection exercise, a temperature controlled isotope insulation flap is the preferred thermal switching technique.

TABLE 7-1. EVALUATION OF THERMAL SWITCH CONFIGURATION

| Control Requirement | Point Rating | | | | | | | | Total Point Count |
|---|---|---|---|---|---|---|---|---|---|
| | 1 | 2 | 3 | 4 | 5 | 6 | 7 | 8 | |
| System Description | | | | | | | | | |
| (a) Insulated Flap | 3 | 2 | 2 | 2 | 3 | 3 | 3 | 3 | 18 |
| (b) Constant Temperature Heat Pipe to Space | | 3 | | | | | | | 3 |
| (c) Constant Temperature Heat Pipe to Radiator | | | | | | | | | 0 |
| (d) Insulated Louvers | | 1 | | | | 2 | | 1 | 4 |
| (e) Constant Temperature Heat Pipe with Radiation Variable Control | | | 3 | 3 | 2 | | | | 8 |
| (f) Variable Radiation Coupling to Radiator | 2 | | | | | | 2 | 2 | 6 |
| (g) Variable Radiation Coupling to Radiator and VM | 1 | | 1 | 1 | 1 | | 1 | | 5 |

Point Scale:

Most Acceptable 3

⇩

Least Acceptable 0

## Section 8

# THERMAL INTERFACE DESIGN


*Summary*

*The ICICLE system consists of five major subassemblies. These are the isotope heat source, hot heat pipe, ambient temperature heat sink, VM refrigerator, and cryogenic heat pipe. Each of these subsystems must interface thermally and structurally in order to achieve the desired results.*

*Thermal interfaces must be selected on the basis of heat transfer capability, stability, and system impact. At high temperatures radiation coupling is very attractive since relatively effective thermal performance can be expected along with long term stability. Use of radiation coupling also eliminates the thermal stress induced in a rigid system experiencing such a temperature excursion.*

*Low temperature interfaces cannot be made through radiant thermal coupling because of the large temperature gradients required to transfer the required heat. In these instances, mechanically clamped joints are appropriate. By having properly designed mating surfaces with a soft interstitial material like indium, adequate values of thermal conductance can be achieved at both the cryogenic and ambient temperature interfaces.*

*The thermal interface requirements of an ICICLE system can be met, and this factor will not adversely affect the feasibility of the concept.*


## A. HOT HEAT PIPE TO VM HOT CYLINDER INTERFACE

There are two basic methods which could be used to transfer heat from the hot heat pipe to the VM hot cylinder. These are conduction coupling through a mechanical joint and radiation coupling between noncontacting surfaces.

In order to determine which coupling concepts are feasible, it is necessary to examine the thermal source and sink which must be connected by some thermal coupling method. Figure 8-1 shows a typical hot heat pipe condenser cross section which is the thermal source.

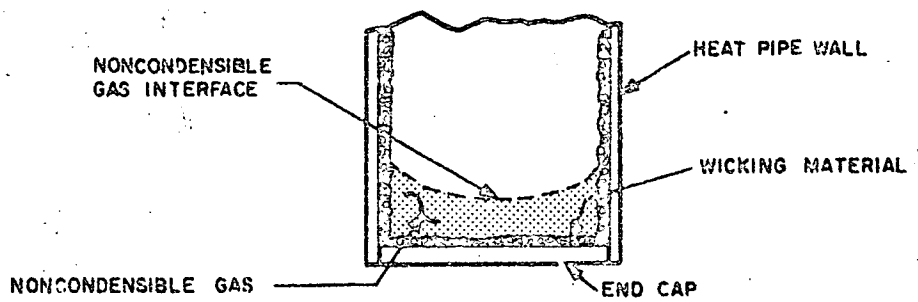



Fig. 8-1. Hot heat pipe condenser section.

Because of the possibility of noncondensible gas buildup during the life of the heat pipe, a thermal coupling design which depends upon heat removal at the end cap is not recommended. Figure 8-2 shows how the thermal conductance of the condenser liquid vapor interface varies with the presence of a noncondensible gas (the curve is for helium).[1*] The thermal conductance with non noncondensible gas present is approximately 48 W per square inch per °K and decreases very rapidly in the presence of helium (a noncondensible gas). An effective film thickness of 0.020 in reduces the conductance to approximately 3 W per square inch per °K, and a thickness of 0.05 in reduces the conductance to approximately 0.9 W per square inch per °K. This means that a helium barrier 0.050 thick would support a thermal gradient of 390°K for a flux density of 350 W per square inch. In a high temperature heat pipe, the gradient would not be this large since the liquid metal and heat pipe wall would provide a thermal conductance path which bypasses the gas barrier, but the gradient would still be significant since the wall conduction path is relatively poor compared to the direct path across the end of the pipe when no noncondensible gas is present. Also, the bypass conductance will change rapidly as the noncondensible gas film thickness increases.

Therefore, the heat should be removed from the heat pipe wall at a distance from the end sufficient to allow for noncondensible gas buildup.

Figure 8-3 shows a cross section of the top end of a typical VM hot cylinder. Most of the heat transfer between the working fluid and the hot cylinder takes place in the cylinder wall over a distance defined by the stroke.

Therefore, any hot heat pipe/VM thermal coupling system should remove heat from the hot heat pipe walls and transfer it to the VM hot cylinder stroke area by the most efficient method.

---

*References for this section are at the end of this section.

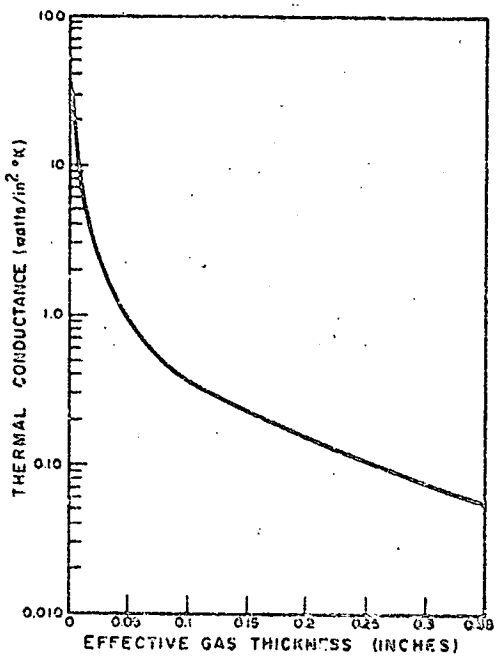



Fig. 8-2. Interface thermal conductance vs. noncondensible gas thickness (helium).

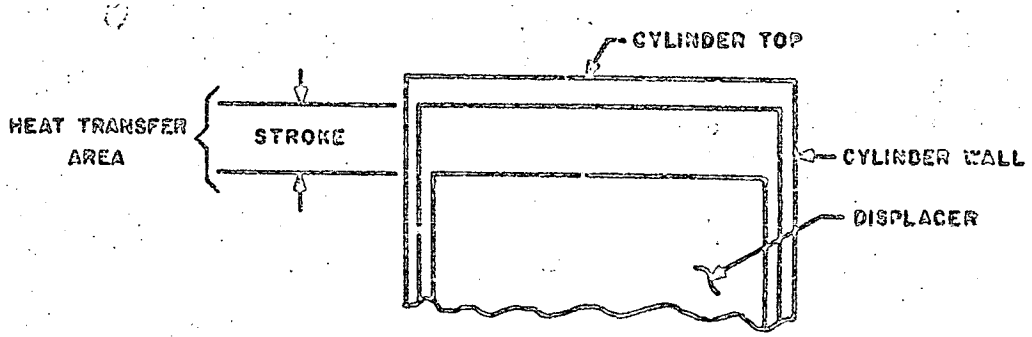



Fig. 8-3. VM hot cylinder.

## 1. Conduction Coupling

Conduction coupling between the hot heat pipe and the VM hot cylinder can be achieved by means of mechanical joints held together by means of bolts or a threaded nut. Care must be exercised in the design and fabrication of a reliable thermal

contact joint which will operate at the high temperatures required for the VM and which must maintain the high heat flux required with a reasonable thermal gradient.

Figure 8-4 is a design concept which could meet the requirements of a conduction coupling. No stress-related problems are anticipated in clamping to the VM in this manner since high strength Inconel is commonly used as the cylinder material.

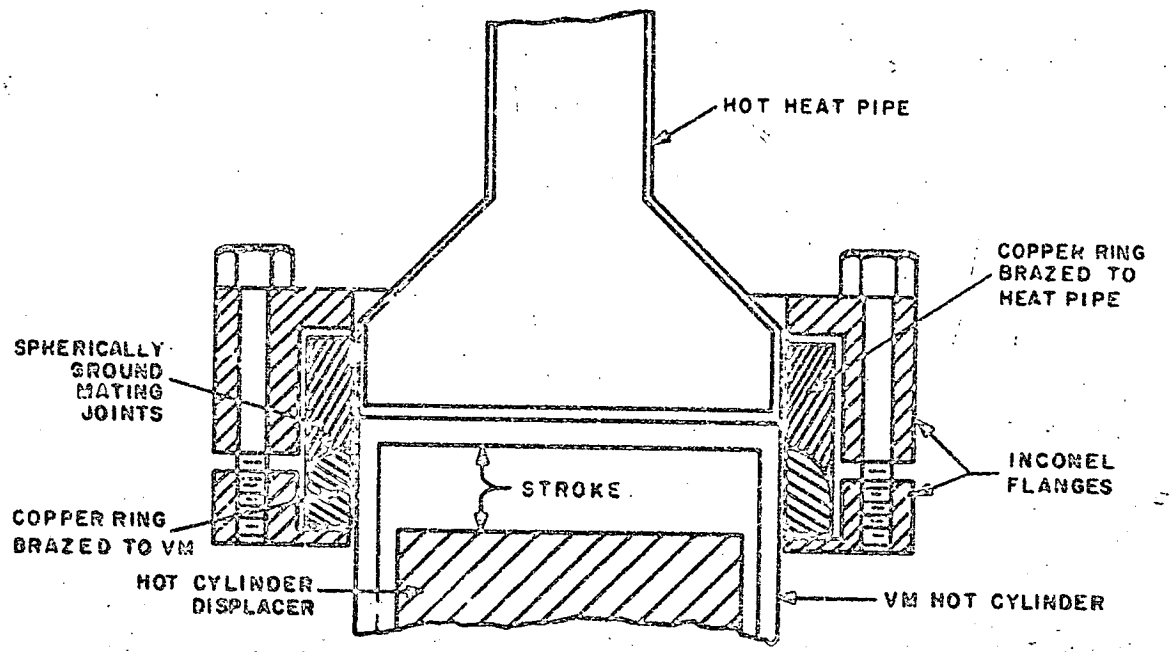



Fig. 8-4. VM hot heat pipe thermal coupling.

For a VM hot cylinder OD of 1.5 in and a copper ring thickness of 0.25 in, the cross sectional area of the ring is 1.38 $in^2$. The contact area for a flat joint would be 1.38 $in^2$ and larger for a spherical joint. The thermal gradient across the joint will be:

$$\Delta T = Q/CA$$

where:

$\Delta T$ = thermal gradient, °K

Q = conducted heat, W

C = joint conductance, $W/in^2 °K$

A = joint contact area, $in^2$

Table 8-1 shows joint conductance test results obtained by A.M. Clausing and B.T. Chao of the University of Illinois.[2] For annealed copper, joint conductances of 10 W per square inch per °K or better should be obtainable with a joint pressure on the order of 1000 psi. The thermal conductance of metal to metal joints is affected by the cleanliness of the mating surfaces. Heavy oxide films can greatly reduce the joint conductance due to the hardness and low thermal conductivity of the oxides. Therefore, the mating surfaces should be free of oxide films. Vapor depositing of gold on the mating surfaces should greatly retard the formation of an oxide film.

TABLE 8-1. CONDUCTANCE TEST RESULTS

| Material | Conductance | | | |
|---|---|---|---|---|
| | psi | Btu/h $ft^2$ °F | $W/in^2$ °F | $W/in^2$ °C |
| Brass | 200 | 400 | 0.8 | 1.44 |
| | 400 | 700 | 1.4 | 2.5 |
| | 1000 | 1300 | 2.6 | 4.68 |
| Magnesium | 200 | 2000 | 4 | 7.2 |
| | 400 | 4000 | 8 | 14.4 |
| | 1000 | 10000 | 20 | 36 |

With 350 W of conducted heat, the $\Delta T$ for the contact joint should not exceed 25 °K. The thermal gradient within the copper rings will not exceed 47 °K, based on a VM ring length of 0.5 in and a hot heat pipe ring length of 1.0 in, with all of the heat entering and leaving the rings at the ends. The actual gradient will be less since the heat effectively enters and leaves the rings somewhere between the ends. The total thermal gradient in the coupling will not exceed 72 °K.

The length of the hot heat pipe ring should be sized to allow for any non-condensible gas buildup in the heat pipe. The heat pipe is flared at the interface in order to minimize the length of the thermal conductance path. A spherical joint is shown as a possible solution to any angular misalignment problem since the spherical surfaces will mate properly without creating a torque at the joint.

At high temperatures and in a vacuum, the interface will tend to weld together after a period of time. This should increase the joint conductance although there appears to be a lack of test data which verifies this theory. No differential expansion problems are anticipated since identical materials are used and the $\Delta T$ across the joint is small.

A loss of thermal conductance at the mating surfaces of the couplings due to thermal cycling or other reasons could result in a system failure due to overheating of the hot heat pipe.

2. Radiation Coupling

Figure 8-5 shows a radiation coupling concept which is capable of transferring the necessary amount of heat from the hot heat pipe to the VM hot cylinder.

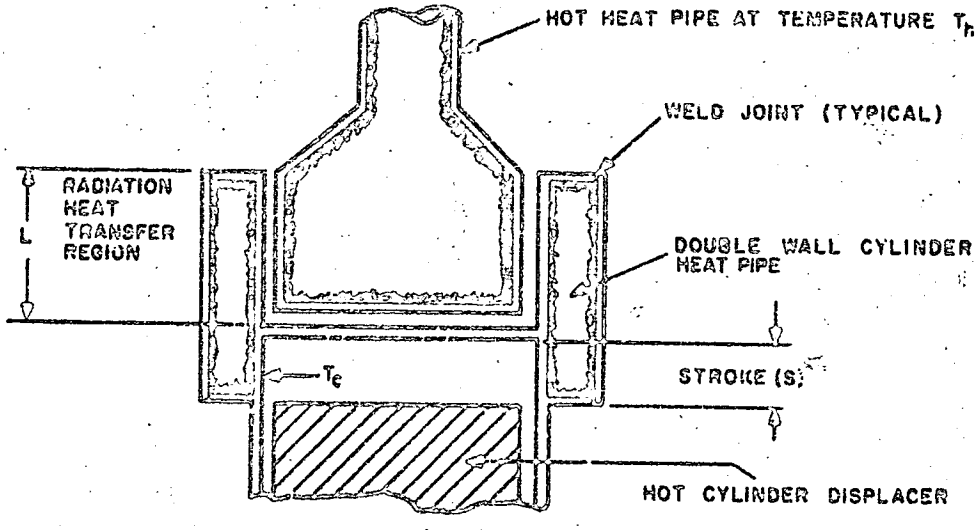



Fig. 8-5. Radiation coupler.

The radiation coupling consists of a hot heat pipe (which is flared at the end in order to provide greater radiation area) nested inside a secondary heat pipe which is a double wall cylinder which is closed at the ends and is lined with wicking material. The secondary heat pipe can be machined as part of the hot cylinder or brazed onto the hot cylinder. The secondary heat pipe is used in lieu of a copper cylinder or finned cap in order to eliminate the thermal gradients associated with thermal conduction.

The heat is transferred from the hot heat pipe to the secondary heat pipe by means of the thermal radiation coupling and then directly to the hot cylinder by the heat pipe action of the secondary heat pipe. Figure 8-6 is a plot of hot heat pipe temperature versus VM hot cylinder temperature for various levels of black body thermal flux (Q'). By choosing the desired VM hot cylinder temperature and the desired hot heat pipe temperature, the required Q' can be determined.

Figure 8-7 is a plot of radiation coupling height (L) versus the total heat flux to black body heat flux ratio (Q/Q') for various values of surface emissivity. The curves are based on a hot heat pipe OD of 1.4 in and a secondary heat pipe ID of 1.5 in. By knowing the desired VM heat input and dividing that by the required Q' at the chosen temperatures, the required coupling height can be found. For example, with a VM hot cylinder temperature of 900°K and a hot heat pipe temperature of 1150°K, the required Q' is 40. For a total heat transfer rate of 350 W, Q/Q' = 8.75. With a surface finish which has an emissivity of 0.9, the required radiation coupling height is 2.43 in. Flame (plasma) sprayed iron titanate has an emissivity of 0.9 at 1000°K and would be a suitable finish for the radiation coupling.

The secondary heat pipe could be replaced by a copper annulus. A copper annulus 0.25 in thick would have a thermal gradient of approximately 47°C from end to end, with a resultant increase in the hot heat pipe temperature from 1150°K to 1197°K. The hot heat pipe temperature can be decreased to 1150°K by increasing the length of the copper annulus by approximately 1/2 in. This increase in length results in an increase in radiative heat transfer area, thus lowering the heat pipe-to-copper annulus $\Delta T$ by 55° C. The thermal gradient in the copper annulus would be increased by 8° C to 55° C.

### 3. Recommendation

In view of the possibility of the conduction coupling failing due to thermal cycling and/or loss of joint pressure due to creep at high temperatures, the radiation coupling is recommended.

The radiation coupling employing the secondary heat pipe will be at least 1 lb lighter than the same coupling using a copper cylinder. Since the copper cylinder or secondary heat pipe must be supported by the VM hot cylinder, the secondary heat pipe is recommended since it will cause considerably less strain on the VM hot cylinder walls during launch.

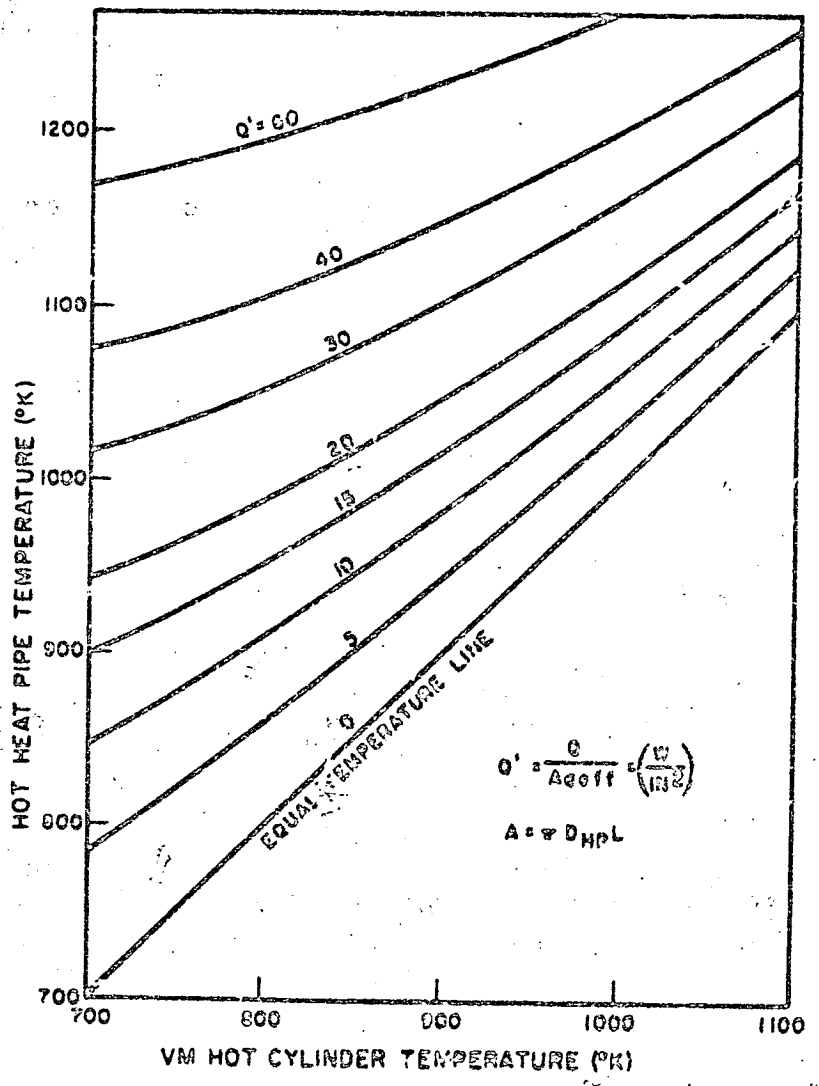



Fig. 8-6. Hot heat pipe temperature vs. VM hot cylinder temperature.

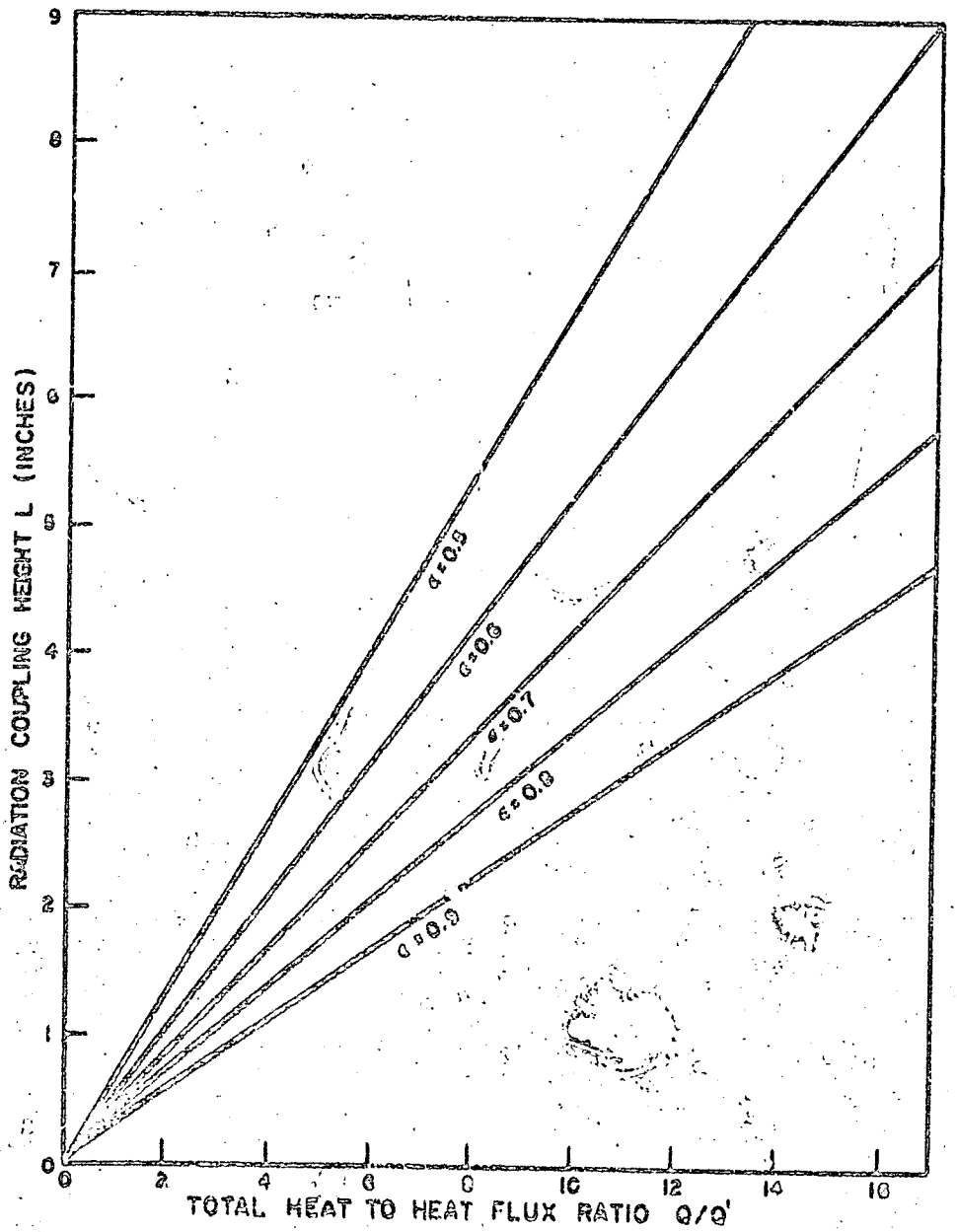



Fig. 8-7. Hot heat pipe to VM coupling height vs. total net heat transfer to net heat transfer flux ratio for various surface finish emissivities.

The VM hot heat pipe coupling techniques discussed here could also be employed for other VM configurations, such as a VM constructed with an external hot cylinder heat exchanger and regenerator.

## B. AMBIENT TEMPERATURE INTERFACE

There is a necessity to remove the heat input into the hot and cold cylinders from the crankcase of the VM refrigerator. The method of heat removal involves few alternative choices for interface techniques since a radiation coupling at temperatures of approximately 300°K is not practical. The only practical techniques for making this interface are by mechanical or metallurgical bonds between the refrigerator crankcase and the ambient temperature heat pipe.

### 1. Location of Interface

The thermodynamics of the crankcase is summarized in Fig. 8-8. The heat which must be rejected can be partitioned into three general sources. Seventy watts is rejected in the thermodynamic cycle. This heat is rejected uniformly in the swept and void ambient temperature volumes.

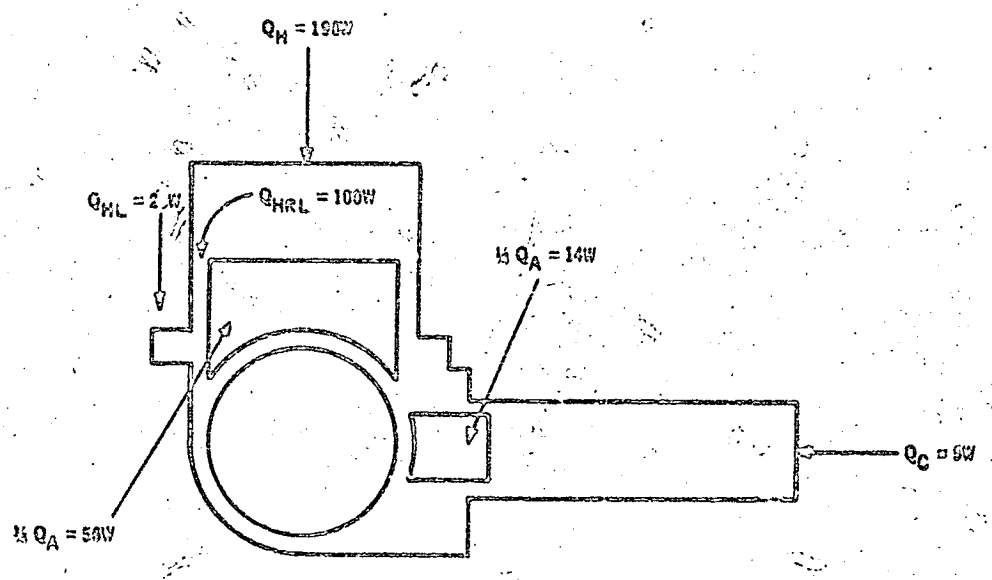



Fig. 8-8. Thermodynamics of the crankcase.

These volumes exist in a four to one ratio between the hot and cold cylinder location. This means that approximately 14 W of heat is rejected at the base of the cold cylinder and 56 W at the base of the hot cylinder. One hundred watts of heat is introduced in the exhaust from the hot regenerator due to the inefficiency of this

regenerator. Finally, 20 W are conducted down the hot cylinder walls to the crankcase. Clearly, the greatest percentage of the heat which must be rejected to the heat sink appears near the junction of the crankcase and the hot cylinder. Any interface should thus be located in this area. Two design considerations are necessary to ensure that all of the rejected heat is localized at such an interface flange. First, convection heat transfer must be promoted between the working fluid and the crankcase at the interface flange. Second, the conductance of the crankcase should be a maximum to assure effective transfer of heat from sources away from the flange.

## 2. Interface Techniques to Heat Sink Flange

Having located a heat transfer flange on the crankcase, an effective thermal contact with long life must be made to a heat pipe which is part of the heat sink. The only two realistic options are a bolted mechanical joint or a soft solder metallurgical joint. A soldering operation has definite negative aspects since raising the refrigerator and heat pipe to soldering temperature is a very difficult operation. Unless substantial performance benefit is derived, this approach should not be used.

The thermal resistance of a clamped interface is a function of the flatness, roughness, contact pressure, and flange materials since this resistance is made up of metallic conduction and gas conduction through the interstitial spaces. This thermal resistance would thus be worse in a vacuum than in a gas environment. Fried and Costello[3] have shown this relationship in the data shown in Fig. 8-9. As one would expect on the basis of information presented by Cetinkale[4] that magnesium (which is soft) would have high conductance even though it is relatively rough. As clearly shown, conductance increases with pressure, smoother finish, and improved flatness. The logical extension to this data would involve the use of a soft filler material to take up the effects of surface roughness and flatness. Richard Jansson[5] investigated such a possibility and the results are summarized by the data in Fig. 8-10. Use of the proper filler material (indium foil) can result in a 20-fold reduction of thermal resistance when used with 125 $\mu$in finish on aluminum.

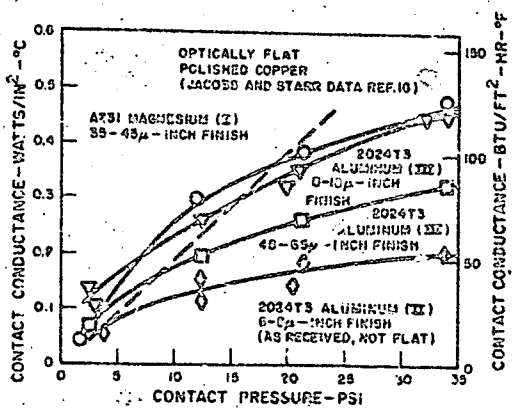



Fig. 8-9. Contact conductance vs. contact pressure for bare metal joints.

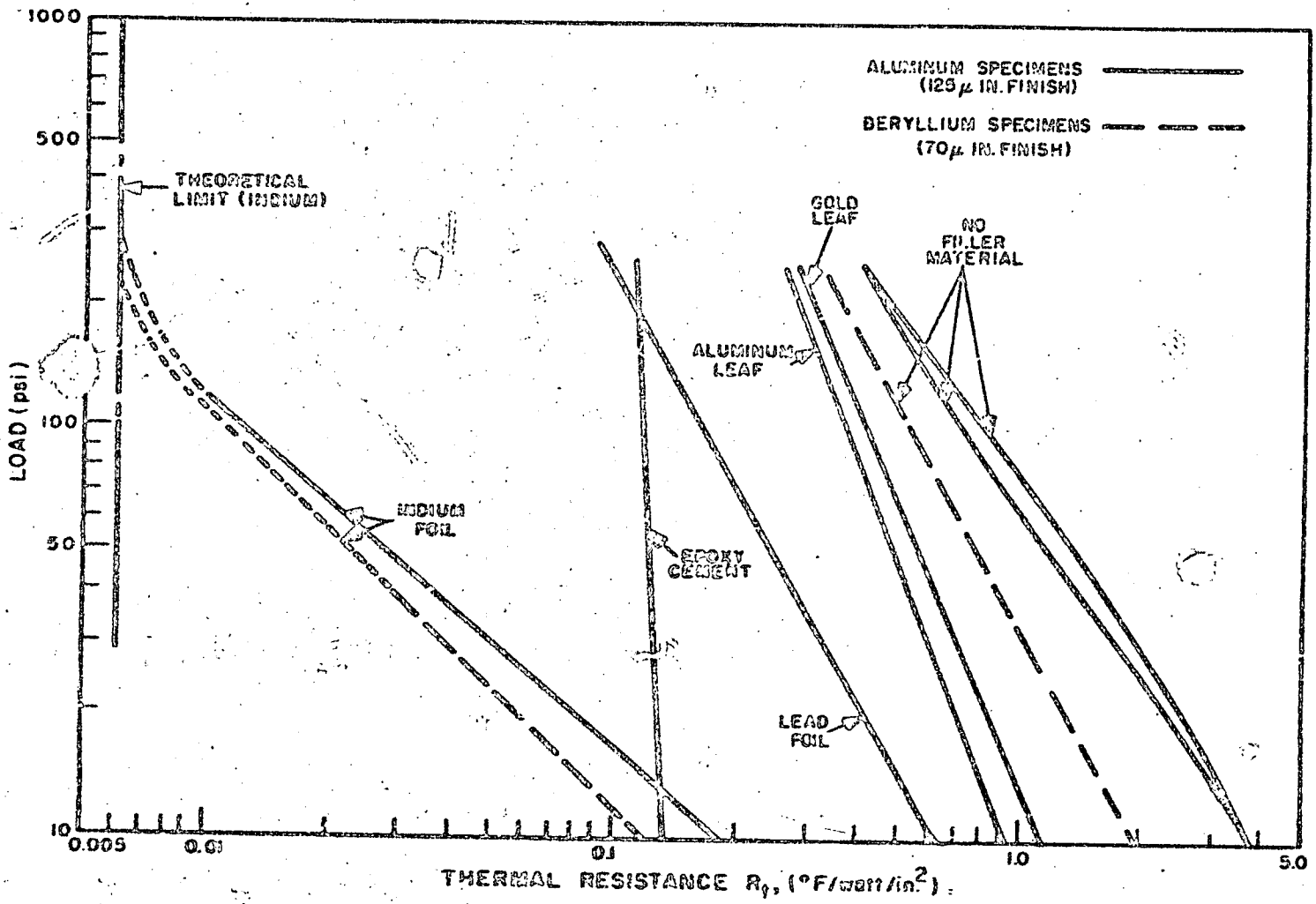



Fig. 8-10. Thermal resistances of metallic interface with various filler materials.

If a 1 in wide flange 1-1/2 in inside diameter is used to interface the refrigerator to the heat pipe, the heat flux for a 5 W system is approximately 20 W/in$^2$. A lightly loaded (20 psi) indium foil joint can operate with a temperature gradient of 2°F where the gradient would be 40°F without the filler. Other materials such as aluminum, gold, lead and epoxy are also shown. For the ambient temperature range indium foil is the indicated choice of material.

Solder joints are generally thought of as presenting negligible thermal resistance. However, incomplete oxide removal, flux and dirt entrapment, and soldering voids can lead to much higher resistance than one would predict from the bulk solder properties. Yovanovich and Tuarze[6] reported experimental results in which pure tin solder joints 15 μm thick from which one would theoretically expect a resistance of 0.00069°F/W/in$^2$ were actually tested to show 0.042°F/W/in$^2$ using normal soldering procedures. It is interesting to note that a modest clamping force of 30 psi on a 0.002 in indium foil could produce comparable thermal conductance.

The use of a mechanically clamped interface with 0.002 in indium foil filler is the preferred ambient temperature interface concept.

## C. CRYOGENIC TEMPERATURE INTERFACE

The interface problem at the cold finger is very similar to that at the crankcase except that temperature gradients are much more detrimental. There is some evidence that the thermal conductance of a thermal contact decreases with temperature. Fletcher et al.[5] cite data indicating a drop of up to 50 percent. This would result in a conductance of approximately 5 W/in$^2$°F for a well-made joint with an indium foil filler. A suggested method for interfacing several 1/4 in diameter heat pipes with a VM cold finger would be through a copper tee section soldered to the cold finger as shown in Fig. 8-11. The VM cold finger material should have a coefficient of thermal expansion which is close to that of copper to minimize thermally induced wall stresses in the cold finger. A copper sleeve is soldered to the pyro heat pipe to spread the heat input into the pipe to an acceptable level and then terminated in a tapered plug which interfaces with the tee. The heat flux through the foil interface is 7.5 W/in$^2$ for 1.5 W heat pipe throughput and 2.5 W/in$^2$ for 0.5 W heat pipe throughput. The junction gradient would be an acceptable 1.5°F and 0.5°F, respectively, for these cases. Without filler material, this temperature drop would go to 45°F and 15°F which is unacceptable. An alternative would be to make larger interface joints. With upward of six interfaces to make at the cold finger, the size of the structure increases rapidly with the interface size. The insulation complexity and losses at the interface must be evaluated against interface size.

The cryogenic interface appears to be limited by the same constraints as the ambient interface. Because of the uncertainty in values of interface thermal conductance at cryogenic temperatures and the sensitivity of system performance to this

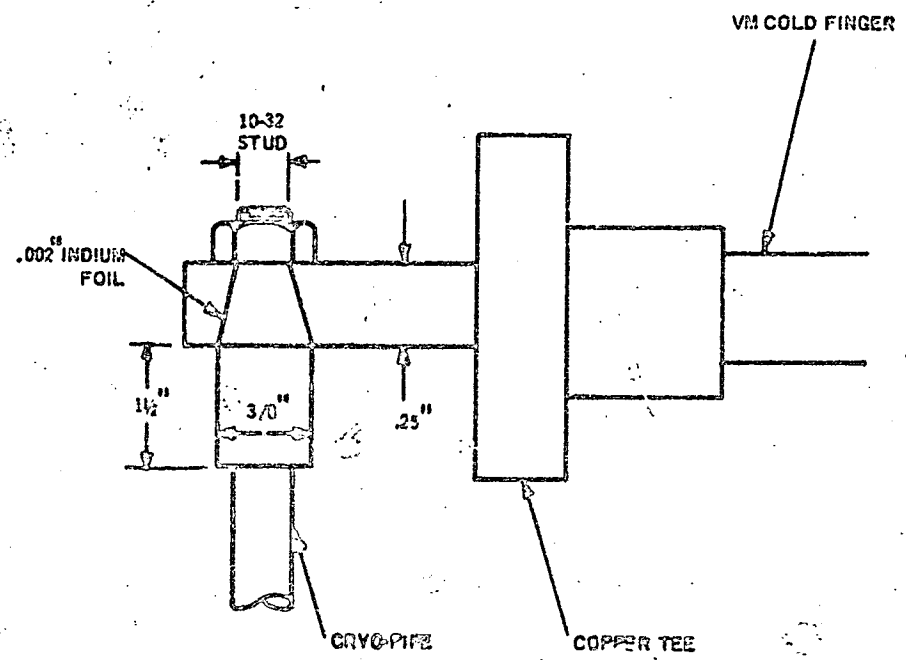



Fig. 8-11. Method for interfacing heat pipes with VM cold finger.

temperature gradient, experimental verification of this parameter would be desirable. Its value as a function of the relevant variables and its stability with life and environmental testing is of special interest.

## D. REFERENCES

1. MIT preprint number 859, "Condensation Heat Transfer in the Presence of a Non-condensible Gas," by Detlov G. Krager and Warren M. Rohsenow, Dept. of Mechanical Engineering.

2. A. M. Clausing and B. T. Chao, "Thermal contact resistance in a vacuum environment," Paper No. 64/HT-16, AI ChE - ASME Heat Transfer Conference and Products Show, Cleveland, Aug. 9-12, 1964.

3. E. Fried and F. A. Costello, "Interface thermal contact resistance problem in space vehicles," ARS Journal, vol. 32, Feb. 1937.

4. T. N. Cetinkale and M. Fishendon, "Thermal conductance of metal surfaces in contact," ASME, International Heat Transfer Conference, 1951, p. 271.

5. R. M. Jansson, "The Heat Transfer Properties of Structural Elements for Space Instruments," Report E-1173, MIT Instrumentation Laboratory.

6. M. M. Yovanovich and M. Tuarze, "Experimental evidence of thermal resistance at solder joint," J. of Spacecraft and Rockets, vol. 6, July 1969, pp. 855-857.

7. Fletcher et al., "Thermal contact resistance," AAIA Journal, vol. 7, July 1969, pp. 1302-1309.

## Section 9

# ICICLE SYSTEM INTEGRATION


*Summary*

*An important consideration in the determination of a preferred feasible ICICLE system design is the spacecraft in which the system will be integrated. The geometry and mission requirements of a given spacecraft have the greatest impact on the configuration and thus the performance.*

*An ICICLE system can be integrated into an ITOS spacecraft to assess the feasibility of such a system. ITOS DOE carried six radiometers, all of which could benefit from refrigeration to cryogenic temperatures although only two are presently refrigerated. In addition, a data link has been included in the integration exercise, although one is not presently planned in the missions.*

*With these experiments included at locations where they can perform their functions, the total heat load if the system operates at 77°K is 3.23 W. The refrigerator to service such a requirement would operate on the VM thermodynamic cycle, require 250 W of thermal power, 15 W of electrical power, and will weigh 7.0 lb. The heat sink will be a heat pipe radiator 42 in x 42 in, weighing 6 lb. The refrigerator will be coupled to the radiator using a 76 in long constant temperature ammonia heat pipe which weighs 3.7 lb. Six liquid nitrogen heat pipes will distribute refrigeration to each of the heat sources.*

*The heaviest part of the system will be the radioisotope heat source. This will be a 400 W fuel capsule of $Pu^{238}$ surrounded by appropriate structure and insulation. Total weight of the heat source subsystem will be 27.2 lb. The distance between the heat source and VM hot cylinder should be under 1 ft, which can be effectively thermally coupled using a 1 in diameter sodium heat pipe.*

*The total ICICLE system required to service an ITOS spacecraft easily integrates into the available space on the craft. The system can weigh under 50 lb and can require only 15 W of electrical power. The system will not have an excessive adverse impact on the dynamics, power budget, or weight budget of this spacecraft.*

*The key fact demonstrated by this exercise is that the flexibility of geometric configuration possible with the ICICLE concept makes it possible to integrate such a system into a variety of spacecraft with minimum compromise in system parameters.*


## A. GENERAL

An ICICLE system has been defined as a central thermal compression refrigerator interfaced with an isotope, spacecraft radiator, and spacecraft experiments through appropriate passive thermal links. In the parametric study of each of the

potential components described in the earlier sections, an isotope capsule using plutonium 238 was clearly indicated. Likewise, a thermal compression refrigerator based on the Vuilleumier cycle also is indicated. The thermal links, thermal switch, size of isotope, and size of refrigerator are all determined by system integration considerations.

Attempts to identify a preferred optimum ICICLE system degenerate into a trivial exercise when broad generality is attempted. Whether the criterion is minimum weight or maximum performance, an idealized system would optimize with zero length for each of the thermal links. Such a design would be trivial since no spacecraft could accept such a system. The spacecraft is an important part of ICICLE so that a preferred system can be selected only on the basis of use on a specific spacecraft and the constraints that this implies. The realities of spacecraft integration further dictate that the ICICLE configuration will be even more controlled by available space on the craft so that the preferred system will be one that fits that available space. The attraction of the ICICLE concept is that it lends itself very well to integration into a variety of system applications.

Although there is often little latitude permitted during spacecraft integration of ICICLE, some general guidelines should be followed if at all possible. These include:

1) The isotope should be located on the outside of the spacecraft in the form of an easily separable reentry body. It should be mounted and located so that it is not thermally coupled to the spacecraft. The isotope location should also permit easy capsule loading on the launchpad.

2) Hot heat pipes have the capability for pumping heat over the longest distances and thus should be favored for the longest runs.

3) Bends and irregular shapes should be minimized in the high temperature region to permit the most effective insulation configuration.

4) Multifoil insulation should be used in the high and cryogenic temperature regions. This insulation must carry no structural loading.*

5) Provision must be made to accommodate expansion and contraction in the thermal links.

6) All bends in heat pipes should be prefabricated.

7) The refrigerator should be located as close to the experiments as possible.

8) Failsafe protection should be provided against thermal runaway of the isotope fuel capsule.

---

*Insulation mounting techniques are detailed on page 6-6.

There are several spacecraft which would be likely candidates for use of an ICICLE system. Any vehicle which has an earth surveillance mission might have requirements for high resolution or IR information which would make refrigeration desirable. Other vehicles which might have reason to receive communication from another satellite could require a low noise receiver which could utilize a cooled varactor diode. An excellent example of a spacecraft which could have all of these requirements is the ITOS series of weather observation satellites.

Figure 9-1 illustrates how an ICICLE system could be integrated into an ITOS-D or ITOS-E spacecraft. The purpose of this drawing is to show the feasibility of incorporating an ICICLE system into a spacecraft of this type. For purposes of illustration, the VM engine is shown cooling all six radiometer detectors and a parametric amplifier. Present plans for the ITOS-D and ITOS-E spacecraft equipment include the mounting of two VHRR radiometers which are cooled to cryogenic temperatures by means of passive radiation coolers, two vertical temperature profile radiometers which are uncooled, and two scanning radiometers which are uncooled. No parametric amplifier is to be used, but one is shown in the illustration in order to show how one could be incorporated into such a spacecraft if it was desired for use with a Data Relay Satellite System.

The use of an ICICLE system on the ITOS-D or ITOS-E spacecraft would eliminate the need for passive radiation coolers on the VHRR radiometers and thereby eliminate the mounting location constraints imposed by the passive coolers. The ICICLE system would permit the use of cooled vertical temperature profile radiometers (which would greatly increase the obtainable vertical temperature profile resolution or accuracy) and cooled scanning radiometers (which could increase the resolution or accuracy by a factor of ten or more). The presently available mounting locations for the VTP and SR radiometers preclude the use of passive coolers for this purpose due to the stringent mounting location requirements for passive coolers (they must be mounted at the bottom of the spacecraft and must be facing parallel to the separation plane normal).

## B. INTEGRATION OF ICICLE COMPONENTS ON AN ITOS-D OR ITOS-E SPACECRAFT

### 1. Location

The location of the ICICLE components on an ITOS-D or ITOS-E spacecraft as shown in Fig. 9-1 is dictated by the location of the radiometers and the availability of space and areas for mounting the VM engine, ambient radiator, and isotope.

The VM engine is mounted directly behind the earth facing panel at the top of the spacecraft primarily in order to minimize the total length of cryogenic heat pipes required. In addition, the location chosen also leads to minimum hot heat pipe length and ambient heat pipe length.

The ambient temperature radiator is mounted on the antiearth side of the spacecraft since this is the only place a single piece radiator of this size (1760 $in^2$) could be mounted on this particular spacecraft. This location also minimizes the external heat inputs to the radiator since it is completely shielded from all earth heat inputs. The other sides of the spacecraft cannot be used for mounting this radiator since it would interfere with either the sensors or the active thermal control systems. During launch, the solar panel would be folded down and stowed over top of the ambient temperature radiator. Some cutouts would be required in the radiator in order to permit securing of the solar panel in place during launch. The ambient radiator would be capable of dissipating 265 W at 30[illegible] under worse case environmental conditions. The radioactive isotope is mounted externally on top of the spacecraft in order to provide an unobstructed view to space.

## 2. Weight

The ICICLE system as shown in Fig. 9-1 will weigh approximately 50 lb. The weight breakdown is shown in Table 9-1.

## 3. Refrigeration Load

The total cooling load requirement would consist of six radiometers cooled to approximately 90°K and the parametric amplifier cooled to approximately the VM cold cylinder temperature. This total cooling load would be approximately 3.2 W with the breakdown as shown in Table 9-2.

## 4. Spacecraft Dynamics

### a. Effects of Engine Vibration

A single VM engine with no counterbalance system will introduce a vibratory type input to the spacecraft. With the VM engine located as shown, a hot displacer weight of 1.0 lb, a cold displacer weight of 0.5 lb, and a speed of 400 rpm; a jitter rate of approximately $0.4 \times 10^{-3}$ rad/s with a maximum amplitude of approximately $10 \times 10^{-6}$ rad will be imposed on the spacecraft attitude control system. This is substantially greater than anything precently imposed on the system. A much more detailed analysis using actual displacer weights and an assessment of permissible rates and amplitudes would be required in order to determine the actual requirements for a counterbalance if any.

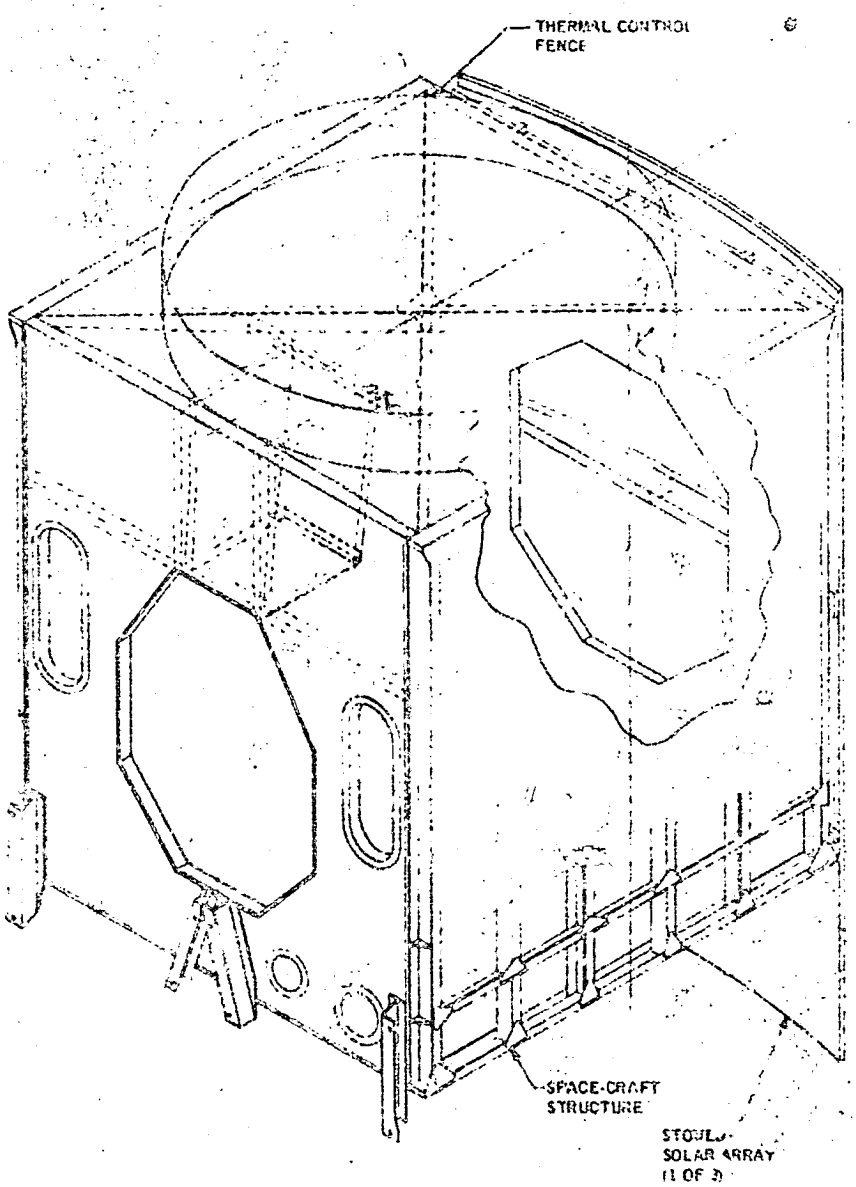
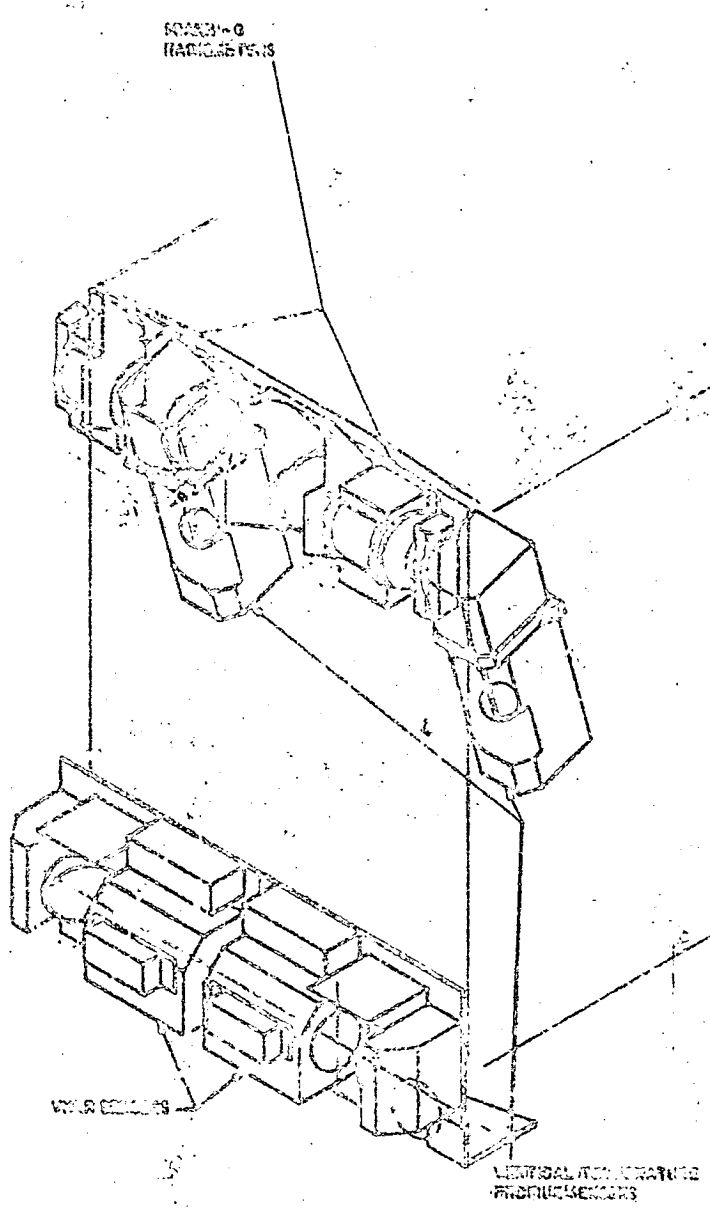
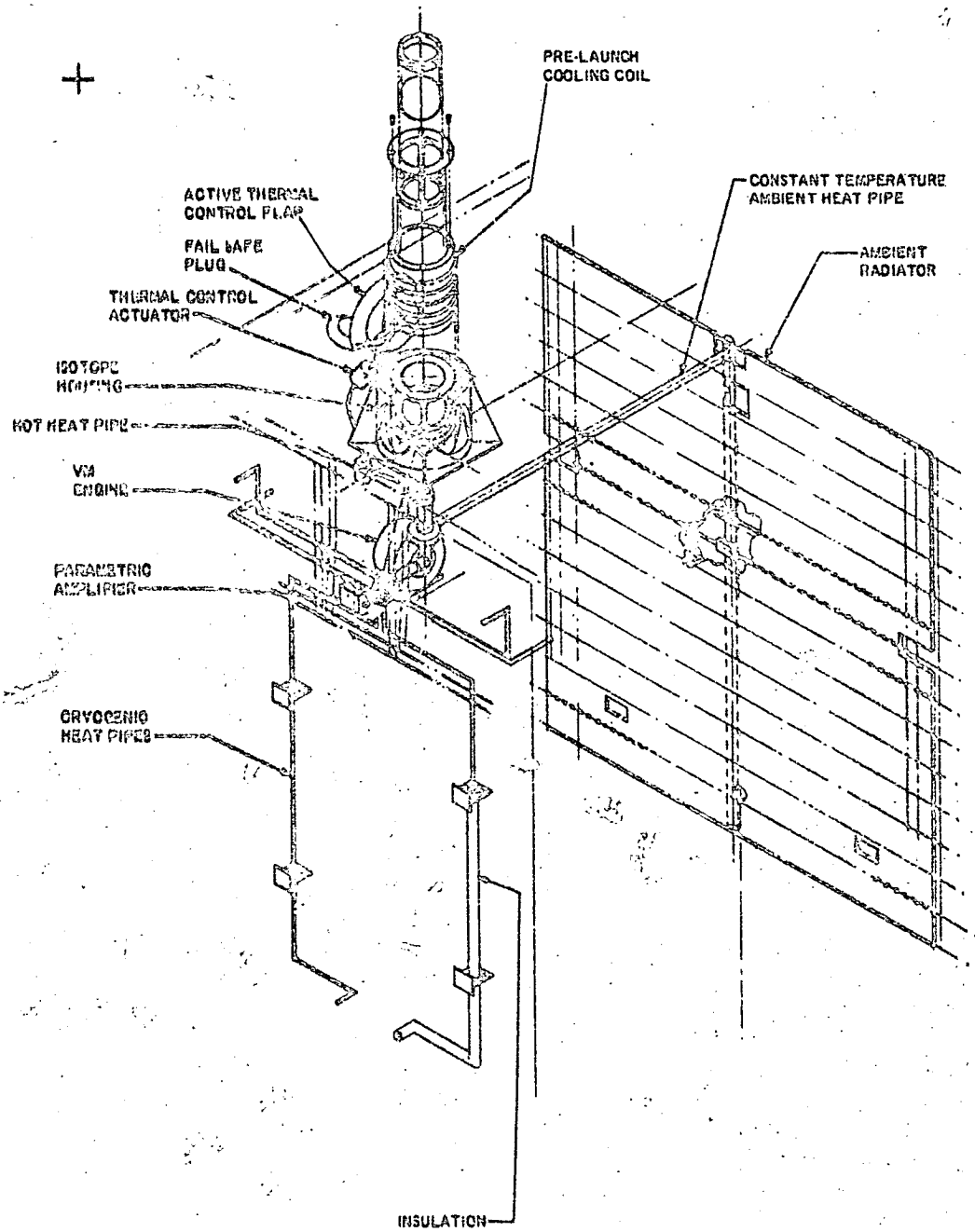



Fig. 9-1. ITOS spacecraft.



Infrared radiometry.




ICICLE system.

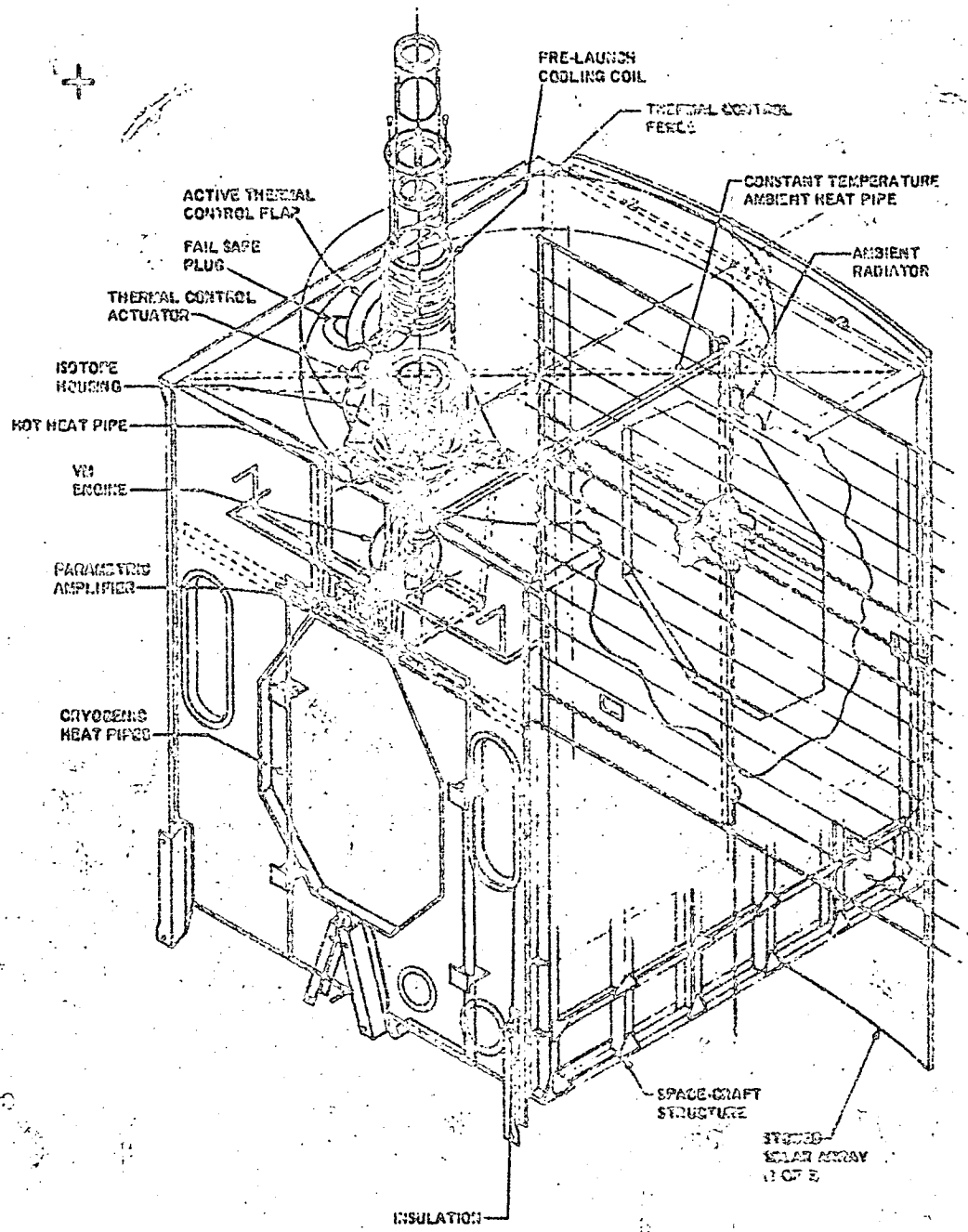



Fig. 9-1. ITOS spacecraft.

ICICLE system.

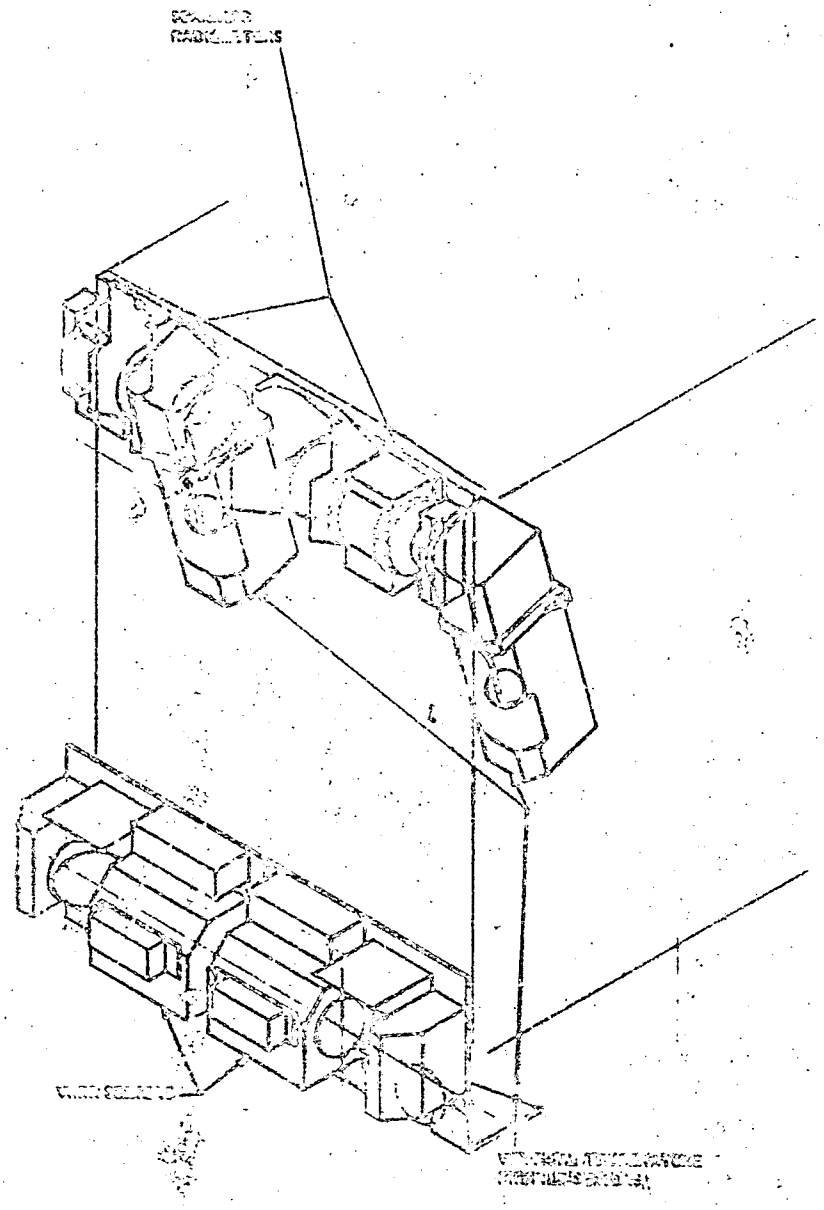
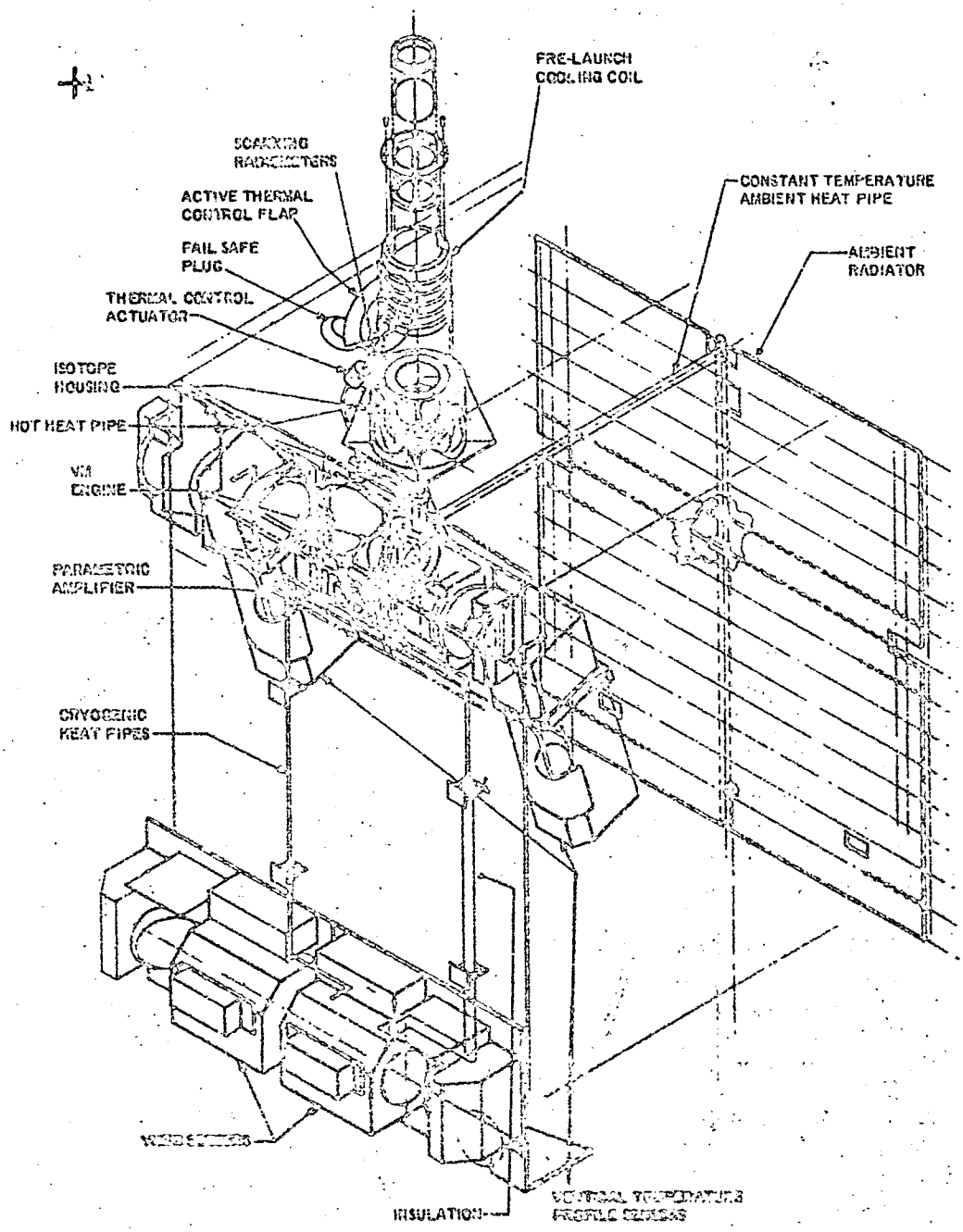


Fig. 2 Radiation Survey.




Infrared radiometry.
ICICLE system.

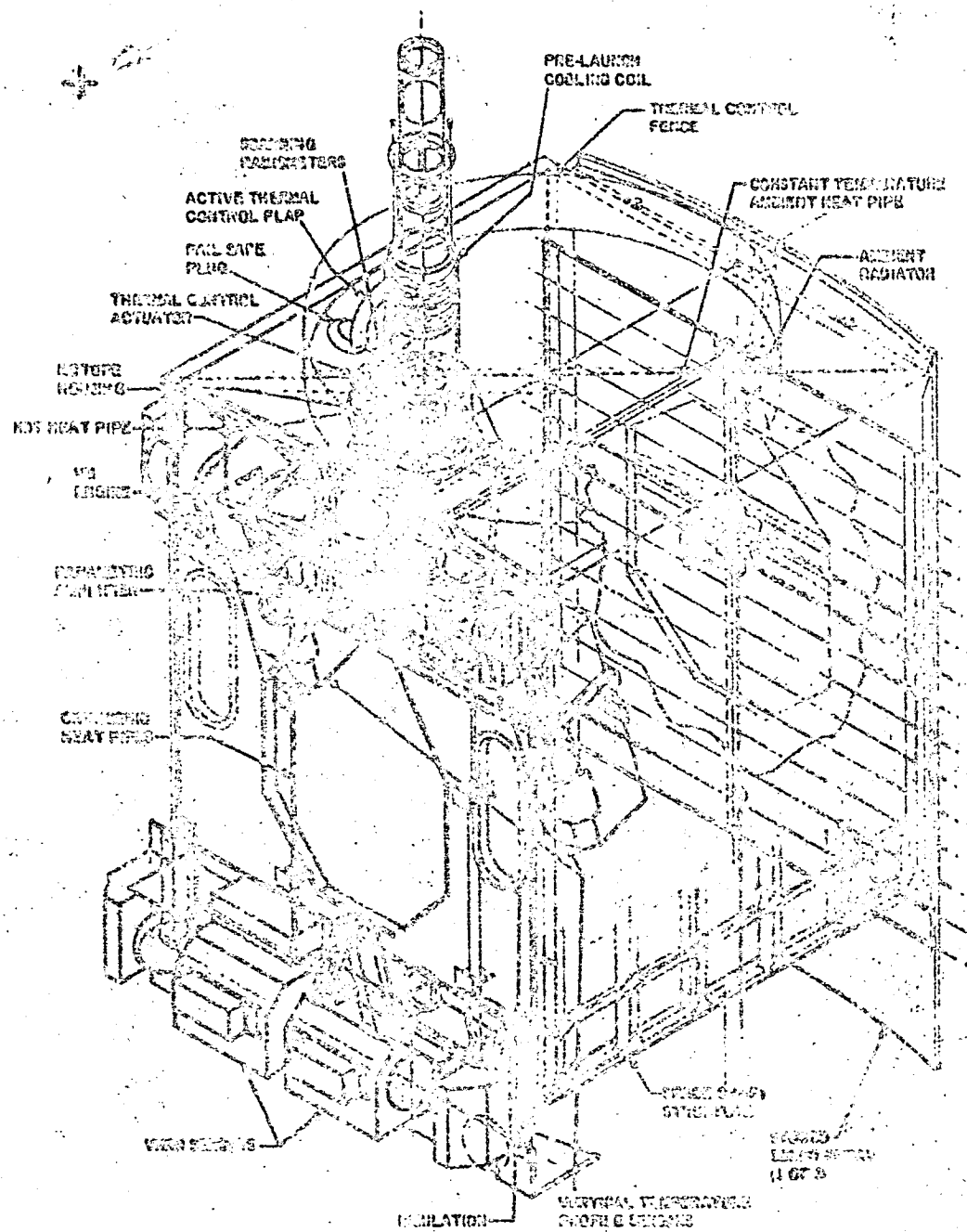



Fig. 3-1. ITOS spacecraft.
Infrared radiometry.
ICICLE system.

TABLE 9-1. WEIGHT TABULATION

| Component | Unit Weight | Quantity | Weight (lb) |
|---|---|---|---|
| Cryogenic heat pipes | 0.005 lb/in | 184 in | 0.9 |
| Cryogenic heat pipe insulation | 20 lb/ft$^3$ | 30 in | 0.3 |
| Cryogenic heat pipe supports | 0.1 lb | 6 | 0.6 |
| Cryogenic heat pipe flexible conductors | 0.03 lb | 6 | 0.2 |
| VM engine | 7 lb | 1 | 7.0 |
| Bracketry for VM engine | | As required | 1.5 |
| Hot heat pipe | 0.3 lb/ft | 6 in | 0.2 |
| High temperature insulation | 20 lb/ft$^3$ | 232 in$^3$ | 2.7 |
| Isotope | 10.0 lb | 1 | 10.0 |
| Isotope housing with cooling coil (heat pipe construction) | 10.0 lb | 1 | 10.0 |
| Isotope housing support | 4.5 lb | 1 | 4.5 |
| Ambient heat pipe | 0.6 lb/ft | 76 in | 3.8 |
| Ambient radiator | 6.0 lb | 1 | 6.0 |
| Active thermal control system | 0.5 lb | 1 | 0.5 |
| Hardware | | As required | 1.0 |
| Total | | | 49.2 |

TABLE 9-2. COOLING LOAD TABULATION

| Component | Quantity | Cooling Load (W) |
|---|---|---|
| VHRR radiometer | 2 | 0.23 |
| Scanning radiometer | 2 | 0.23 |
| Vertical temperature profile radiometer | 2 | 0.23 |
| Detector mounts | 6 | 0.32 |
| Flexible conductors | 6 | 0.15 |
| Cryogenic heat pipe supports | 10 | 0.58 |
| Cryogenic heat pipe insulation | 15.3 ft | 0.49 |
| Parametric amplifier | | 1.00 |
| Total | | 3.23 |

It is felt that a jitter below the calculated values would be desirable.

The natural frequency of the constrained heat pipes should be well above the VM vibrational frequency of 7.5 Hz to prevent resonance. The accelerations due to vibration must be accounted for in the heat pipe design since vibration will induce an additional liquid pressure drop in the heat pipe. If the vibrating frequency and maximum heat pipe deflections are known, then the maximum heat pipe acceleration can be determined, and the methods given in Sec. 5 can be used to determine the degradation in heat pipe performance due to those accelerations. At low frequencies, a properly constrained heat pipe would experience a liquid pressure drop due to acceleration which is much smaller than the gravitational liquid pressure drop which the heat pipe would experience in a horizontal position on earth.

b. Effects of Spin-Stabilized Spacecraft

The forces due to acceleration resulting from a spin-stabilized spacecraft will have a positive, or negative, effect on the performance of ICICLE heat pipes, depending on orientation. If a typical spin rate of 10 rpm and a heat pipe length of 60 cm are assumed, and if the pipe is aligned such that the liquid flow vector is 180°

from the inertial vector (worst case), and one end of the pipe is at the center of rotation, then the product of acceleration and the heat pipe length would be

$$a_r Z = r\,\omega^2 Z = 3940 \ \frac{cm^2}{sec^2}$$

where $a_r$ = radial acceleration

$Z$ = heat pipe length

$\omega$ = angular velocity

$r$ = radial distance from center of rotation.

This figure, when multiplied by the liquid density, results in the additional liquid pressure drop due to inertial forces on the heat pipe. Performance charts for cryogenic heat pipe which are presented in Sec. 5 can be used to determine the effects of inertial forces on heat pipe performance. The effect of inertial forces on the performance of high temperature and ambient temperature heat pipes will not be as severe as with the cryogenic heat pipes, but still must be accounted for in the heat pipe design.

## 5. Heat Leaks to Spacecraft

The only major heat leak to the spacecraft will be through the high temperature insulation. It is estimated that this heat leak to the spacecraft could be as high as 50 W. This would have some impact on the spacecraft thermal design, but can be compensated for by increasing the size of the fixed radiators. This should not be a major problem and could possibly be helpful in maintaining S/C thermal control.

The heat leak through the isotope housing support system will be approximately 14 W based on 16 rené-41 wires 0.062 in in diameter and 2 in long.

Most of the high temperature heat leak will be dumped directly to space since the isotope is mounted external to the spacecraft.

## 6. Electrical Interface

The VM engine will require on the order of 10 to 15 W of continuous electrical power. This is comparable to or slightly larger than the power consumption of an IR radiometer and is larger than the orbit average power consumption of most other electrical components in a spacecraft such as ITOS. This would have a major impact on the powor supply system of spacecraft which are already operating at maximum capacity. Early planning would be required in order to incorporate an ICICLE system into such a spacecraft.

This amount of electrical power should be available on most of the experimental spacecraft such as Nimbus and ATS since they are primarily designed as platforms for flight experiments.

If it was desirable to fly the first experimental ICICLE system using electrical power as a substitute for the isotope heat source, a very large source of electrical power (200 to 300 W) would be required. This would eliminate most of the operational spacecraft as potential hosts. If it is not possible to obtain this much electrical power from any of the experimental spacecraft, it would be possible to convert some existing spacecraft system to an ICICLE experimental spacecraft.

It would be possible to fly a short term ICICLE system experiment (using isotope heat source) on an operational spacecraft such as ITOS with little impact on the power supply since the undegraded solar arrays produce about 20 percent more electrical power at the beginning of life than at the end of life.

## 7. System Tradeoffs

The major system tradeoffs have been resolved by this study with only a few minor variables left which are not dictated by the integration of an ICICLE system into a particular spacecraft.

For the integration example presented in this study (ITOS-D and ITOS-E), the only obvious variable left is the VM cooling capacity versus ambient radiator size. Since the engine cooling capacity (5 W) exceeds the required cooling capacity (3.2 W), the engine crankcase could be operated at a higher temperature. This would result in a decreased cooling capacity and a decrease in the size of the ambient radiator. For example, operating the crankcase at 325°K would result in a cooling capacity of 1.5 W and a radiator size of 1275 $in^2$ (40 x 32 in). The weight saving would be approximately 2.2 lb as a result of reduced ambient heat pipe length as well as reduced radiator size. At a crankcase temperature of 335°K, the cooling capacity, radiator size, and weight saving would be 0 W, 950 $in^2$ (24 x 40 in), and 3.6 lb, respectively.

A decrease in the radiator size would make it somewhat easier to integrate into the spacecraft as well as to reduce the system weight. This tradeoff would have to be made for each particular spacecraft and its cooling requirements.

Since the bulk of the system weight is in the isotope, isotope container, and isotope container support bracket, this would be the major area of investigation in any attempt to reduce the system weight. On the order of 5 to 7 lb could probably be saved by using beryllium and/or lightweight heat pipe construction techniques for the isotope container and bracket.

This weight reduction, coupled with the weight reduction associated with operating the VM crankcase at 325°K, could result in a system weight on the order of 40 lb.

## C. ICICLE FAILURE MODE ANALYSIS

Any system which utilizes a radioisotope thermal source must be carefully analyzed from the point of view of failure modes. This is true not only because of launchpad and mission abort safety (which we cannot consider in this study) but also because of the impact of the ICICLE on the host spacecraft.

As described in this report, the ICICLE consists of four major subassemblies: the heat source, the heat sink, the refrigerator, and refrigeration distribution components. The effect of failure or degradation of each of these subassemblies on the spacecraft is different; thus protection against such events should be different in each case.

### 1. Heat Source

The most serious event that could occur in an ICICLE system would be the failure of the isotope capsule. Since these capsules are well-developed components and operate in a normal environment, the probability for failure would be very low. However, because of the method of application, other system component failures could cause conditions in which the isotope capsule could not exist. Figure 9-2 shows the heat source assembly.

Failure or degradation of the multifoil insulation would increase heat leak from the subassembly, making less heat available to the refrigerator. The capacity of the refrigerator will go down approximately 0.011 W per degree drop of hot cylinder temperature. Of more importance to the spacecraft may be the fact that more heat is coupled into the structure, thus raising its temperature. This fact may be important in determining the location on the spacecraft of the heat source.

A failure or degradation of the hot heat pipe would likewise degrade performance of the refrigerator, depending on the amount of heat pipe degradation. With less heat removed through the heat pipe, the capsule will begin to overheat. If the thermal switch responds to a signal to maintain a certain hot cylinder temperature, it will not sense increasing isotope temperature and will continue to operate since more heat is being called for at the hot cylinder. The isotope will ultimately fail due to overheat. Under no circumstances is this an allowable situation. Thus, a hot heat pipe failure could cause a catastrophic spacecraft situation. Because of this possibility, a fail-safe mechanism against this eventuality is essential. We are proposing that one such mechanism would center around a fusible link which would melt at a predetermined temperature. This would allow a spring loaded flap to open, exposing the isotope to a view of space which would allow all the heat of radioactive decay to be radiated at a safe isotope temperature.

Likewise, the fusible fail-safe device would protect against failure of the thermal switch or its activation mechanism.

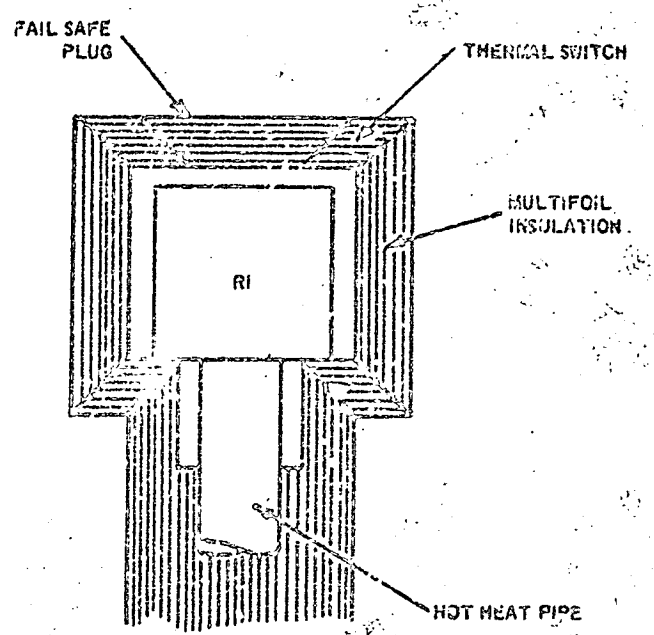



Fig. 9-2. Heat source assembly.

2. Heat Sink Assembly

The heat sink assembly consists of a space radiator and an ambient temperature heat pipe link. Failure of either of these components will cause rapid degradation of refrigerator performance. While data indicates a 10 percent reduction of gross refrigeration when the crankcase temperature rises from 300°K to 325°K, the change in net capacity is much more severe. Over a 50°C range a good approximation of gross refrigeration degradation is 0.4 percent per degree centigrade. Losses which are roughly proportional to the temperature gradient from cold finger to crankcase increase approximately 0.45 percent per degree centigrade rise of crankcase temperature. Typically, internal losses amount to 75 percent of gross capacity so that net capacity as a function of crankcase temperature can be approximated by the following expression:

$$Q_N = Q_C \left[1-0.004\,(T_A-300)\right] - Q_L \left[1+0.0045\,(T_A-300)\right]$$

$$\text{If } Q_L = 0.75\ Q_C,\quad Q_N = Q_C \left[1-0.004\,(T_A-300)\right] - 0.75Q_C \left[1+0.0045\,(T_A-300)\right]$$

Figure 9-3 is a plot of this relationship, showing that net capacity goes to zero when the crankcase temperature rises to 334°K.

In addition to the loss of capacity, degradation of the system heat sink will cause a rise in hot cylinder temperature which should be accommodated by the thermal switch assembly. As was the case with heat source protection, fail-safe protection for failure of the thermal switch must be provided.

Another failure mode in the heat sink would occur if a penetration of the heat pipe occurred. The radiator contains 13 individually sealed pipes each containing 2.5 g of ammonia. This gas could cause 250 g-s of impulse which could interfere with the spacecraft mission. The main heat pipe could cause even more problems since it contains 150 g of ammonia which would supply 15,000 g-s of impulse to the spacecraft.

Other miscellaneous degradation factors, such as change in radiator surface properties and interface contact resistance, would cause performance degradation along the lines shown in Fig. 9-3.

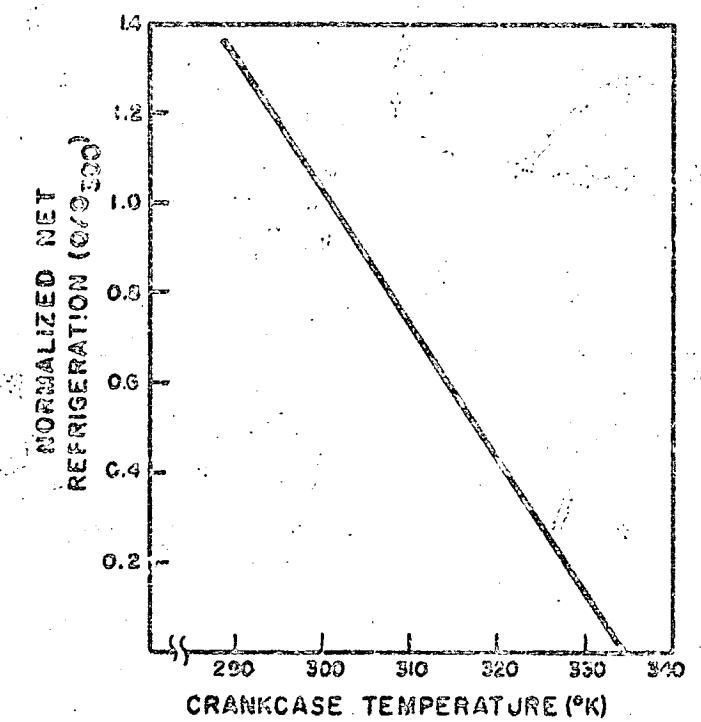



Fig. 9-3. Normalized net refrigeration vs. crankcase temperature

### 3. Refrigerator

A major concern in achieving 2-year system life is the performance of the refrigerator. With a 2-year refrigerator under development, potential failure modes will be better understood. Several of these modes can already be projected. Degradation of the machine due to contamination or loss of working fluid will reduce cooling capacity and thus not allow affected spacecraft systems to operate properly. In addition, such a failure mode would result in reduced demand for heat at the hot cylinder and would result in overheating. The remedy for this situation has already been discussed. Reduction of cycle speed will have similar effect to that of working fluid loss.

Other failure modes in the system center on the drive motor. Failure of the bearings of the motor could cause stall and increased electrical power draw. Dynamic unbalance could create vibration problems in the spacecraft. In both of these eventualities, provision must be made to terminate motor operation, and thus, system operation when these malfunctions are sensed.

Since the refrigerator will have potential for substantially less life than any other system component, provision must be made for accommodating the other subsystems when ICICLE becomes inoperative. This accommodation can be for as long as 80 years (isotope half life). Again, the fusible fail-safe link fits the requirement of best meeting this need.

### 4. Cryogenic Subsystems

Failure in the cryogenic subsystems will not have catastrophic impact on the spacecraft. With the exception of a structural penetration of the heat pipe which would impose unwanted thrust on the spacecraft, all other potential failure modes would be localized loss of cooling, damage to the affected experiment, or vibration of the experiment would have direct impact on the cooled experiment but would not significantly affect the spacecraft itself.

Degradations in the cryogenic subsystem which will have significant effect on its ability to achieve design temperatures include changes in vacuum insulation properties, interface at the cold finger or detector, and thermal expansion effects. These effects can be accommodated only by careful design and awareness of the problem.

The main conclusion of the failure mode analysis is that potential exists in the ICICLE system for serious failure problems. One safety device can protect the spacecraft against this failure mode. This device must be fail-safe and have extremely long life. A fusible link has been determined to best meet these needs.